CFD Simulation of Reactive Flow in Lime Shaft Kilns using Porous Media Model and Experimental Validation

Dissertation

zur Erlangung des akademischen Grades

Doktoringenieur

(Dr.-Ing.)

vorgelegt von

M.Sc. Kamyar Mohammadpour

geb.am 12.09.1980

in Mashad-Iran

genehmigt durch die

der Fakultät für Verfahrens-und Systemtechnik

der Otto-von-Guericke-Universität Magdeburg

Gutachter:

Prof. Dr.-Ing. Eckehard Specht

Institute of Fluid Dynamics and Thermodynamics, University Magdeburg

Prof. Dr.-Ing. Dominique Thévenin

Institute of Fluid Dynamics and Thermodynamics, University Magdeburg

Dr.-.Ing. Siegmar Wirtz

Institute of Energy Plant Technology, University Bochum

Abstract

Performing experiments in a real lime shaft kiln plant are quite complicated. A lime shaft kiln has typically a large geometry, including usually a height of 15 meters and a diameter of 3 meters, and is filled with large stones moving in a vertical direction. Within the kiln, measurements are difficult or, measuring instruments are damaged.

Due to these difficulties, modeling of physical and chemical processes is required for having a better understanding of the process and optimizing the parameters. The simulation techniques using Computational Fluid Dynamics (CFD) modeling are particularly beneficial for systems such as shaft kilns.

The main objective of this research study is to illustrate the key parameters affecting the flame behavior and temperature profiles in CFS and PFR kilns. For this aim, the CFD method of porous media model (PMM) was introduced. The results of the CFD porous media model were compared with the experimental measurements of packed bed in two types of injections (radial and parallel flows). The PMM model results showed reasonable accuracy with experimental validations.

The advantage of the PMM model is that it can be used in the simulation of kilns with a real dimension of about 10 meters in height without limitation in the number of nodes and computational times.

In PFR kilns, the flame length was calculated at about 5.2 meters when methane was injected from 18 burners. The flame length can be in the range of 4.8 to 6.1m depending on fuel velocity, particle diameter, types of fuels, number of burners, and arrangements.

In CFS kilns, a part of the combustion air was not pressed through the cooling zone but was injected horizontally with the fuel. Therefore, the influence of mixing parameters on penetration depth was studied. When the ratio of combustion air to cooling air was increased from 0.4 to 2, the penetration depth was increased from 0.4 to 0.6 meters. The flame length was calculated in the case of CFS kiln at about 6 meters when methane was injected from 8 burners. The flame length can be in the range of 6 to 8 m depending on the ratio of combustion air to cooling air, fuel velocity, particle diameter, types of fuels, number of burners and arrangements, burner depth.

Zusammenfassung

Experimente in einer echten Kalkschachtofenanlage durchzuführen ist recht kompliziert. Ein Kalkschachtofen hat normalerweise eine große Geometrie mit einer typischen Höhe von 15 Metern und einem Durchmesser von 3 Metern und ist mit großen Steinen gefüllt, die sich in vertikaler Richtung bewegen. Innerhalb des Ofens sind die Messungen schwierig oder die Messinstrumente sind beschädigt.

Aufgrund dieser Schwierigkeiten ist die Modellierung physikalischer und chemischer Prozesse erforderlich, um den Prozess besser zu verstehen und die Parameter zu optimieren. Die Simulationstechniken unter Verwendung der CFD-Modellierung (Computational Fluid Dynamics) sind besonders vorteilhaft für Systeme wie Schachtöfen.

Das Hauptziel dieser Forschungsstudie ist es, die Schlüsselparameter zu veranschaulichen, die das Flammenverhalten und die Temperaturprofile in CFS- und PFR-Öfen beeinflussen. Zu diesem Zweck wurde die CFD-Methode des porösen Medienmodells (PMM) eingeführt. Die Ergebnisse des CFD-Modells für poröse Medien wurden mit den experimentellen Messungen des Festbetts bei zwei Arten von Injektionen (radiale und parallele Strömungen) verglichen. Die Ergebnisse des PMM-Modells zeigten mit experimentellen Validierungen eine angemessene Genauigkeit.

Der Vorteil des PMM-Modells besteht darin, dass es bei der Simulation von Öfen mit einer tatsächlichen Abmessung von etwa 10 Metern Höhe ohne Beschränkung der Anzahl der Knoten und der Rechenzeiten verwendet werden kann.

In PFR-Öfen wurde die Flammenlänge mit etwa 5,2 Metern berechnet, als Methan aus 18 Brennern injiziert wurde. Die Flammenlänge kann im Bereich von 4,8 bis 6,1 m liegen, abhängig von Brennstoffgeschwindigkeit, Partikeldurchmesser, Brennstofftypen, Anzahl der Brenner und Anordnungen.

In CFS-Öfen wurde ein Teil der Verbrennungsluft nicht durch die Kühlzone gepresst, sondern horizontal mit dem Brennstoff eingeblasen. Daher wurde der Einfluss von Mischparametern auf die Eindringtiefe untersucht. Wenn das Verhältnis von Verbrennungsluft zu Kühlluft von 0,4 auf 2 erhöht wurde, wurde die Eindringtiefe von 0,4 auf 0,6 Meter erhöht.Die Flammenlänge wurde im Falle eines CFS-Ofens bei etwa 6 Metern berechnet, wenn Methan von 8 Brennern injiziert wurde. Die Flammenlänge kann im Bereich von 6 bis 8 m liegen, abhängig vom Verhältnis von Verbrennungsluft zu Kühlluft, Brennstoffgeschwindigkeit, Partikeldurchmesser, Brennstofftypen, Anzahl der Brenner und Anordnungen, Brennertiefe.

Nomenclature

	Description	Unit
A	Area	m^2
C_p	Specific heat capacity	$\dfrac{KJ}{Kg.\,K}$
d_p	Particle diameter	mm
d_f	Burner diameter	mm
$d_{c.a}$	Combustion air diameter	mm
D	Kiln diameter	m
D_h	Hydraulic diameter	m
E	Energy input	$\dfrac{m^3_{Fuel}}{Kg_{Lime}}$
H	Height	m
$\dfrac{h}{r}$	Penetration depth	
h_u	Lower heating value	$\dfrac{KJ}{m^3_{Fuel}}$
L	Length	m
L_f	Length of flame	m
L_b	Burner depth	m
n	Number of burners	
T.I	Turbulence Intensity	-
$U_{c.a}$	Combustion air velocity	$\dfrac{m}{s}$

U_j	Injection velocity	$\dfrac{m}{s}$
U_m	Mean air velocity	$\dfrac{m}{s}$
V_f	Fuel volume flow	$\dfrac{m^3}{s}$
V_j	Combustion air volume flow	$\dfrac{m^3}{s}$
V_m	Cooling air volume flow	$\dfrac{m^3}{s}$
Y^+	Near-wall region	-

Greek Symbols

α	Viscous resistance	$\dfrac{1}{m^2}$
Δ_p	Pressure drop	P_a
ε	Turbulent dissipation rate	$\dfrac{m^2}{s^3}$
K	Turbulent kinetic energy	$\dfrac{m^2}{s^2}$
λ	Excess air number	
μ	Dynamic viscosity	$\dfrac{Kg}{m.s}$
ρ	Density	$\dfrac{Kg}{m^3}$
ϕ	Porosity	
ω	Specific turbulence dissipation rate	$\dfrac{1}{s}$

Abbreviations

CFD	Computational Fluid Dynamics
CFS	Counter Flow Single Shaft Kiln
PFR	Parallel Flow Regenerative Shaft Kiln
PMM	Porous Media Model
BCC	Body Center Cubic
SC	Simple Cubic

Chapter 1

Introduction

1.1 Lime Shaft kilns

A large variety of lime shaft kiln designs have been used over centuries around the world. The two most essential kilns are:

1. Counter Flow Single Shaft Kiln (CFS), and

2. Parallel Flow Regenerative Shaft Kiln (PFR).

Lime burning is a high-temperature process where the reactive materials are packed in vertical positions. Via the virtue of gravitational force, these materials move downward to pass three process zones before reaching the final product quality. In shaft kilns, the fuel is introduced by injection from burners either in the radial direction (as in CFS) or in the axial direction (as in PFR), depending on the kiln type. The CFS shaft kiln is used for hard burnt lime and the PFR one for soft burnt lime.

1.2 Counter Flow Single Lime Shaft kiln (CFS)

As shown in Figure 1.1, a single shaft kiln is a vertical shaft where limestone is charged at the top of the kiln, and quicklime is discharged at the bottom. To generate the heat to calcify the limestone, fuel is introduced with air radially from outside through burner systems at different heights in the kiln. Additionally, the air is blown at the discharge of the kiln to cool the product in a counter-current manner. The limestone is preheated by the combustion gases in a counter-current mode to about 800°C before it reaches the burning zone. In this zone, the limestone is heated to a temperature between 900°C and 1500°C, which is sufficiently high to liberate carbon dioxide (CO_2) and obtain the derived lime [1].

$$CaCO_3 + \text{Heat} \rightarrow CaO + CO_2 \quad \Delta H_{298} = +178 \frac{KJ}{mol}$$
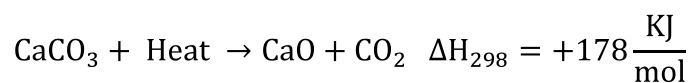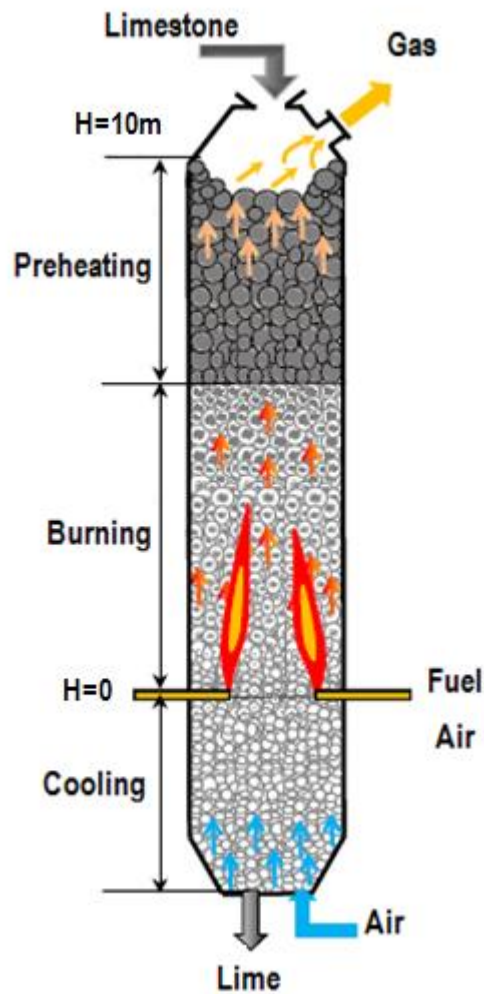
Figure 1.1: Schematic of a counter flow single lime shaft kiln (CFS) [2].

An essential factor in a shaft kiln is the burner system, which is shown in Figure 1.2. It is reasonable for proper fuel distribution in the cross-section and in addition to that for a high-temperature homogenization in the cross-section. Multiple burners were arranged in the circumferential distance at two levels of kiln height. In every level, the burners have a different penetration depth. Another critical parameter is the flame length, which determines the axial temperature profile and there with the quality of the product.
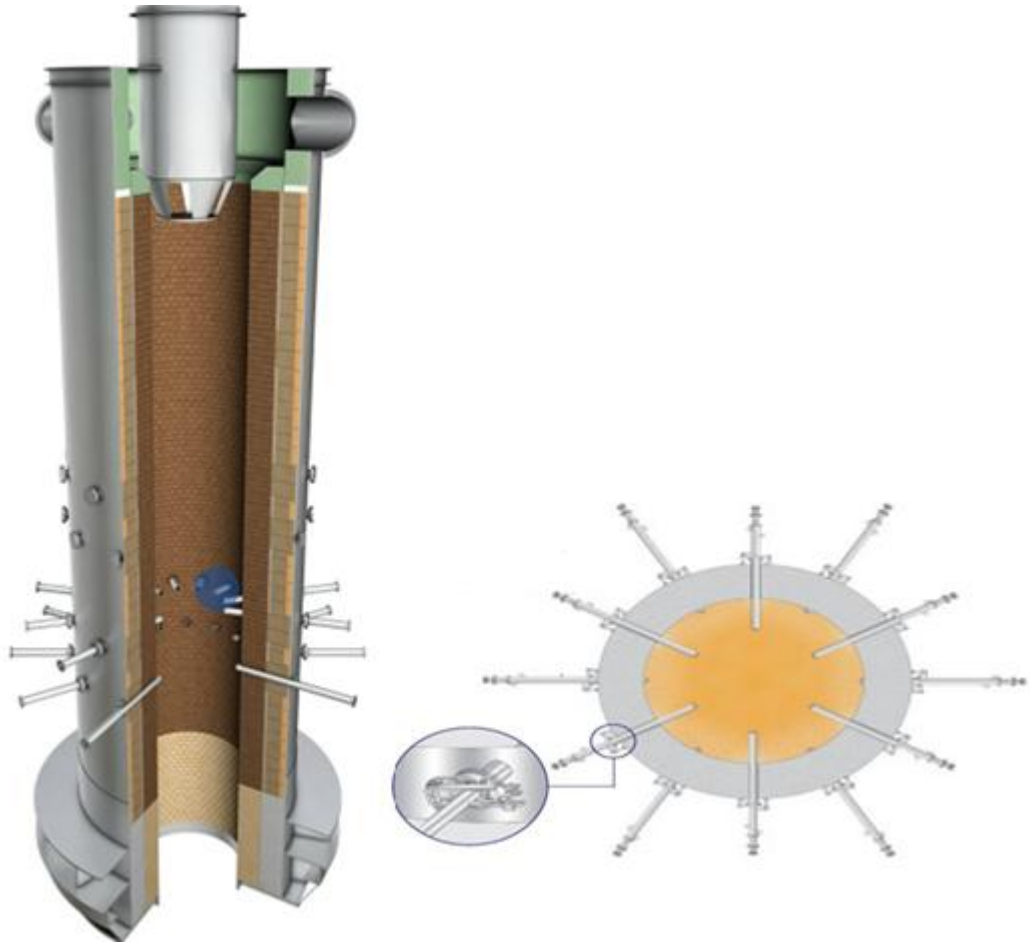
Figure 1.2: Burner arrangements in a CFS lime kiln [3].

The following factors in burner system design influence the temperature distribution in the cross-section and flame length in axial direction:

- Number of burners
- Fuel velocity (Burner diameter)
- Burner depth in the packed bed
- Combustion air/ cooling air

Process parameter, including:

- Kind of fuel (NG, coal, liquid fuel, etc.)
- Excess air number
- Particles of different sizes.

1.3 Parallel Flow Regenerative Shaft kiln (PFR)

The PFR kiln, as shown in Figure 1.3, is another type of design in which two single shaft kilns connected through a crossover channel in a typical geometry, such as rectangular or circular (Figure 1.4). It utilizes the regenerative process for lime calcination. The main features of PFR shaft kilns are:

1.   A parallel flow of stone and combustion gases in the burning shaft of the kiln.
2.   Regenerative preheating of packed bed in the non-burning shaft of the kiln.
3.   The counter flow of lime and fuel and air with a cooling zone

This kind of setup is ideal for producing soft, burnt reactive lime. The parallel flow of stone and combustion gases gives lower temperatures. During the operation, the two shafts are alternately loaded from the top with pre-weighed limestone charges. The fuel is introduced at the upper side of the burning zone. Combustion gases travel downward in parallel flow with the stone, leaving the burning shaft through the crossover channel, and move upward in counterflow with the stone in the non-burning shaft [2].
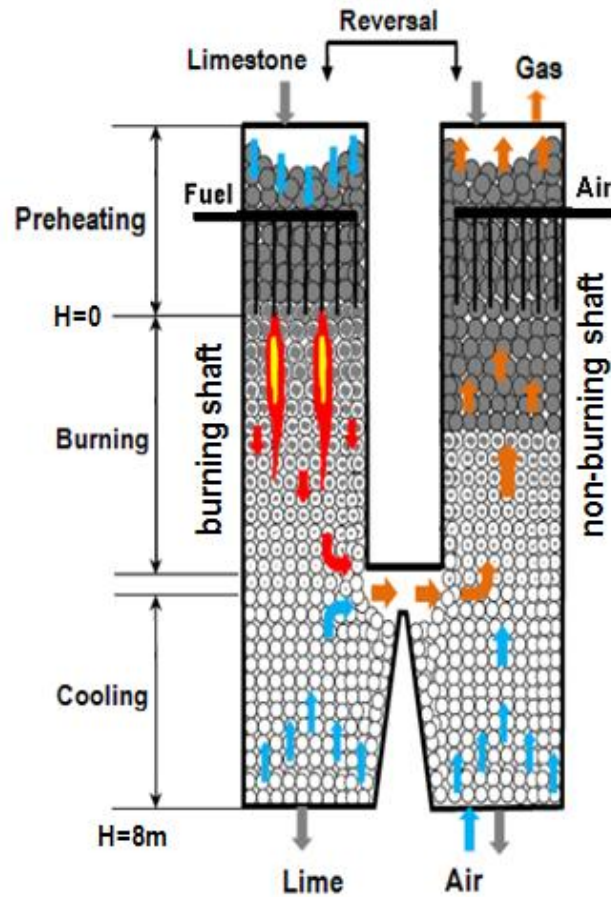
Figure 1.3: Schematic of a parallel flow regenerative shaft kiln (PFR).

The off-gases heat the stone, which acts as a regenerator in the non-burning shaft. This heat is reclaimed by the combustion gases when the non-burning shaft becomes the burning shaft. The off-gases leave the shaft at an average temperature of 100°C, thus transferring most of their residual heat. The shifting between the burning and non-burning modes is called inversion or reversal period and takes place at regular 15-minute intervals. In PFR shaft kilns, the fuel is introduced at the upper end of the burning zone, causing the material to absorb most of the heat released by the burners [3]. In other words, the usable sensible heat waste with the off-gases in a CFS shaft kiln, .In the case of PFR kilns this sensible heat is retained by the stones and ultimately goes to the non-burning shaft
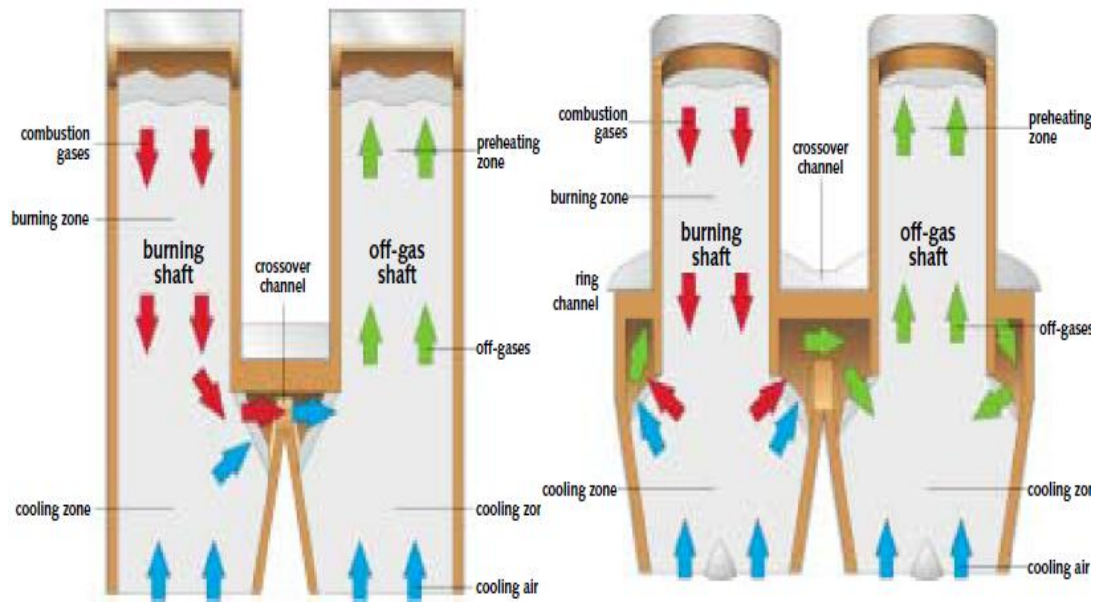
Figure 1.4: Rectangular (left) and circular (right) PFR shaft kilns [2].

The following factors in a burner system design influence the temperature distribution in the cross-section and flame length in axial direction:

- Number of burners
- Fuel velocity (Burner diameter).

Process parameters, including:

- Kind of fuel (NG, coal, liquid fuel, etc.).
- Excess air number
- Particles of different sizes
- Geometry of PFR kilns.

1.4 Temperature Measurements

Measurements in CFS and PFR shaft kilns confirm that the temperature distribution in the burning zone is not uniform. Figure 1.5 shows the temperature measurement profile in CFS and PFR shaft kilns. In the CFS shaft kiln, as it is evident, thermocouples T1, T2, T3, T4, and T5 have measured different temperatures [3]. The area, within the 900°C and 1400°C temperature range, is the burning zone, which is about 5 meters. The temperature in the radial direction is not homogeneous, and the thermocouple damaged near the burner levels Measurement in PFR shaft kilns conducted more quickly. The burning area is measured to be between 6 to 8 meters [4-15].
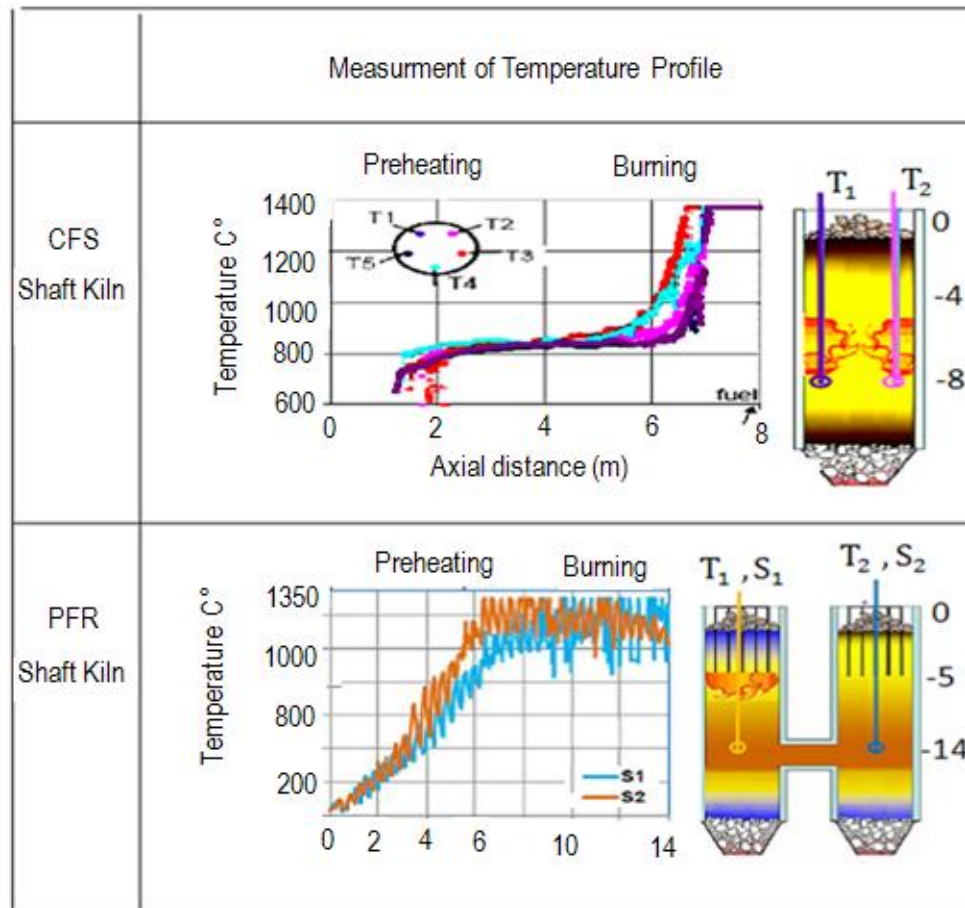
Figure 1.5: Temperature profile measured for CFS and PFR shaft kilns [3].

1.5 Problems and Objective of Modeling Lime Shaft kilns

To optimize the calcination process for lime quality and energy consumption, the length of the flame and fuel distribution in the cross-sections must be known. The combustion behavior and thus, also the heat release determines the calcinations rate. The fuel distribution determines the temperature homogenization in the cross-section. Measurements of temperature and concentration are not possible. The packed beds have a diameter of up to 6 m and a height of up to 18m. Because of the movement of the bed, no measuring devices can be stuck through the wall and the center of the bed. The combustion behavior influenced by several parameters, such as the particle diameter, velocity of fuel, air-fuel ratio, outlet velocity of the burners, and the number of burners. The influence of theses parameters can only be researched using computational fluid dynamics. However, the simulation of the actual flow between the particles requires a very fine mesh, which results in a high computational time. As a consequence, the packed bed has to be approximated as a porous medium. This assumption is used in this study to model the reactive flow in the kilns. Before that, experimental validation of this assumption conducted on a section of the packed bed.

7

Chapter 2:

Literature Review

A large number of research papers have been published in the field of lime production. Therefore in the current chapter, the modeling of flames and flow in a lime shaft kiln is reviewed. In the first place, the principles of modeling shaft kilns using CFD clarified. After that, modeling aspects for a packed bed of spheres, such as packing arrangement, mesh structure, and flow regimes discussed. Then, modeling of packed bed as a porous media model presented. Finally, flame propagation in both packed bed and porous media addressed with a general review about non-premixed flame**.**

2.1 Modeling of a Shaft Kiln using CFD

CFD is the science of predicting fluid flow, heat transfer, chemical reactions, and the related phenomena by numerically solving mathematical equations that govern these processes through a numerical method. Some of the research studies which have conducted so far are listed below: 1) Zhiguo Xu developed 2D and 3D geometries to investigate the temperature distribution of a radial gas mixing in the burning zone of a lime shaft kiln. He considered various factors such as burner depth, burner diameter, preheating of combustion air, and burner arrangement. The results found show that the flow structure in the jet expanding zone is independent of the height of the bed. Also, he proved that the jet flow pattern slightly influenced by the heat transfer between the solid and gas phases. Based on these simplifications (as shown in Figure 2.1), he created a 3D geometric model with 30° segments and a bed height of about 0.8 meters. Also, he illustrated an increase in the lance depth might be helpful to protect the refractory wall from being overheated. It has only a slight effect on the overall radial temperature distribution. Furthermore, he noted that the mixing between the combustion gas and the cooling air could be improved by reducing the burner diameter or preheating the combustion air. However, his model still has some limitations. For example, he used porous media conditions at the inlet and outlet of the domain during the 3D geometry creation, which could have affected the flame.

   Besides, his 3D discrete particle model is verified based on the pressure drop accuracy which May not influence flame distribution [15]
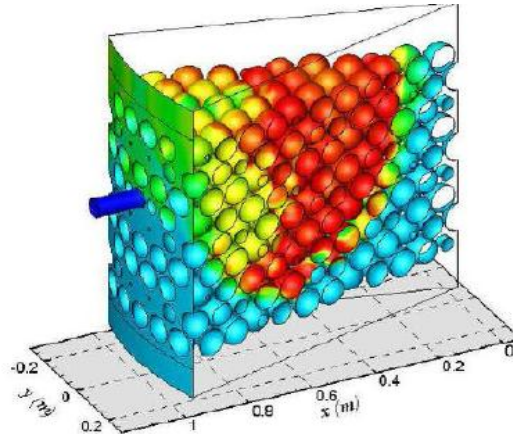
Figure 2.1: Temperature contours in case of diffusion burner [15].

2) Mikulcica and Von Berg presented a numerical model for the calcination process by implementing a commercial CFD code. That is detailed enough to contain the relevant physical and chemical processes such as pressure limitation, diffusion resistance, porosity, pore size, and pore efficiency. They carried out a simple 3D geometry of a pipe reactor, which used for numerical simulations. The numerical predictions compared with the experimental data given in the literature. The code can be used to simulate the turbulent flow field, the temperature field, concentrations of the reactants and products, as well as the interaction of the particles with the gas phase. However, no flame simulation was conducted in their model, even though they need calcination devices [16].

3) Rasul and Saotayanan developed a 2D model to simulate thermodynamic processes for a shaft kiln of magnesia briquettes. The combustion, particle-gas dynamics, and heat transfer processes that occur inside the shaft kiln modeled by the Eulerian multiphase model and species transport with the finite volume chemical reaction model. The results show a discrepancy in the model for gas-particle dynamics with a non-accurate prediction of gas and particle interactions. Moreover, these results predict that the temperature within the kiln is exceptionally high, making it far from working conditions [17].

2.2 Modeling of a Fixed Packed Bed of Spheres

The packing can be either structured or randomly unstructured. In the case of random or unstructured packing particles, there are no known mathematical descriptions to describe the orientation and position of particles. If a packing regime is considered to be structured, the coordinates of each particle will have a full mathematical description and constant porosities and packing densities. Also, packed beds can be loosely or densely packed based on the number of particles packed into a known volume.

4) Eisfeld and Schnitzlein developed a new model for the fluid flow within packed-bed reactors by formulating the Navier Stokes equations for statistically-described domain geometry. This technique gives an additional term to representing the fluid-solid interaction due to the particle boundaries in the packing. Their model validated concerning predictions of pressure drop and radial profiles of the axial velocity. Concerning the pressure drop, a maximum deviation of 16.4% predicted. They found that these large deviations only occur at deficient Reynolds numbers and very low aspect ratios. The velocity predictions compared to experimental works. And a good agreement is how that the pressure drop is influenced by the aspect ratio and small Reynolds numbers, which must be carefully designed [18].
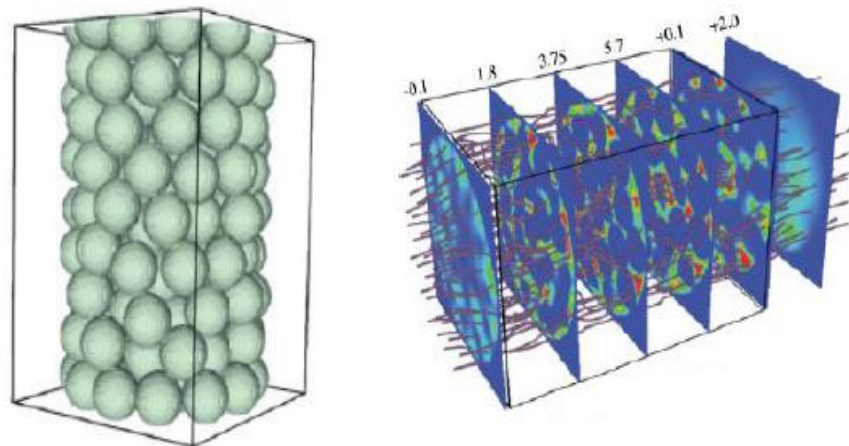
Figure 2.2: Image of the simulated random packing (uniform, spherical particles).

5) Ali Al-Khalaf researched about comparisons between experimental measurements in radial and axial flow injections in a packed bed and CFD simulations. In Figures 2.3 and Figure 2.4, the CFD Real Particle Model in three cases introduced. The results show reasonable accuracy when compared with experimental validation in the RPM model [19].
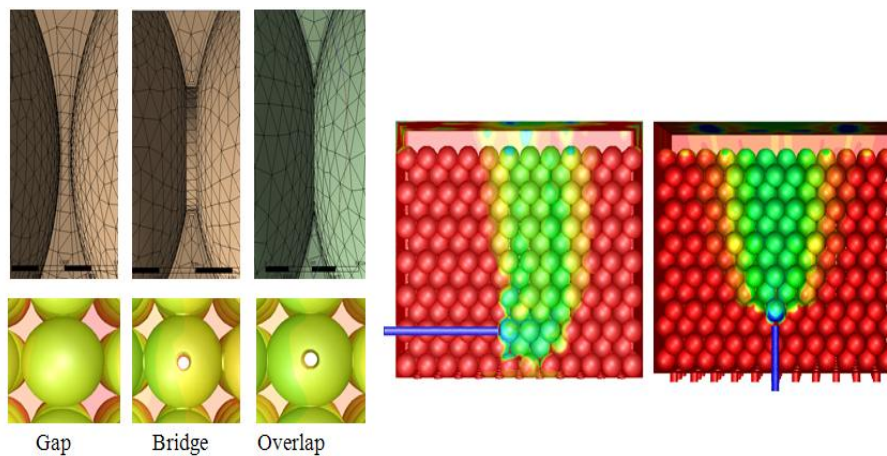
Figure 2.3: Three methods for contact point treatment [19].
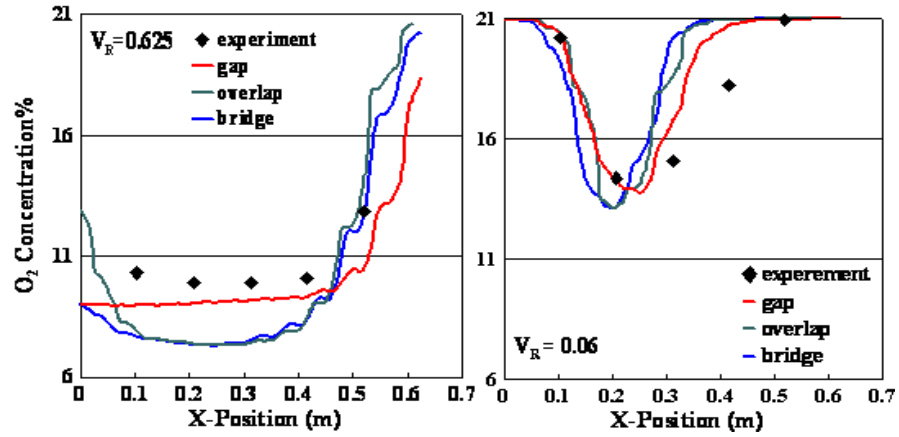
Figure 2.4: Comparison of the three methods for RPM and experimental data.

2.3 Modeling of a Packed bed using Porous Media Model (P.M.M)

In the CFD approach, there are two main methods to create the geometry for a packed bed: The porous medium approach and the real particle approach. In a porous approach, the geometry of the packed beds represented as an effective porous medium [20]. This approach used for a wide variety of single-phase and multiphase problems, including the flow through packed beds, filter papers, perforated plates, flow distributors, and tube banks. The widely-applied resistance model for flflow through porous media proposed by the Ergun model. This model, which is called the Ergun equation, is often used to analyze the resistance or pressure drop for flow through porous media. The Ergun equation considered in the area of porous media for the past decades [21-26]. This equation expressed as follows:

$$\frac{\Delta P}{L} = 150 \cdot \frac{1-\phi}{\phi^3}^2 \cdot \frac{\mu \cdot U}{d_p^2} + 1.75 \cdot \frac{1-\phi}{\phi^3} \cdot \frac{\rho \cdot U^2}{d_p} \qquad (2\text{-}1)$$

The first term on the right represents the viscous energy loss in laminar flflow when the modified Reynolds number is below 10.

The second term on the right denotes the kinetic energy loss primarily in turbulent flflow when the modified Reynolds number is above 100. The Ergun equation examined from its dependence on the flflow rate, properties of flfluids, porosity, orientation, size, shape, and particles' surface. According to Ergun, the direction of the Randomly packed beds do not influence by exact mathematical formulations.

$$Re = \frac{d_p \cdot \rho \cdot U}{\mu} \quad 1 - \phi^2 . \qquad (2\text{-}2)$$

6) Mac Donald and ElSayed [27] have shown that using ϕ=0.36 instead of ϕ=0.3 in the Ergun equation would better fit the experimental data. Moreover, they realized that the two coefficients of 180 and 1.8, respectively, are more accurate for the beds packed. Hicks [28] thought that the

11

two coefficients 150 and 1.75, in the Ergun equation are not constants but a function of the Reynolds number. Bradsha and Myers [29] found that their measured values for the pressure drop of a bed of cylindrical packing were half of those calculated by the Ergun equation. Handly and Heggs [30] found that the Ergun equation is not applicable when predicting the pressure drop across irregular beds packed with spheres, cylinders, or plat. Nemec and Levec [31] concluded that the Ergun equation is mainly applicable to spherical particles in the porosity range of 0.35-0.55. Also, the two empirical constants of 150 and 1.75 were found to have different values at different porosities, but the mechanisms of these constants are still not precise. 6) Wu and Yu [32] developed a new model for resistance of flow through porous media. Their model expressed as a function of porosity, the ratio of pore diameter to throat diameter, the diameter of particles, and fluid properties. The two empirical constants, 150 and 1.75, in the Ergun equation, are replaced by two expressions that are explicitly related to the pore geometry. Every parameter in their proposed.

7) Hellstörm and Lundstörm [33] modeled the flow through porous media considering the effect of inertial force. They used empirically derived Ergun equation to describe the mechanisms of the stream. They performed a micromechanically-based study to moderate Reynolds flow between parallel cylinders via the CFD approach. The CFD simulations are performed using the commercial software ANSYS CFX at high quality using grid refinement techniques, and the iteration error is sufficiently small. Their principal findings are that the Ergun equation fits well to simulated data up to Re=20 and that inertial effects must be taken in to account when Re exceeds 10.

2.4 Flames in a Lime Kiln

2.4.1 Types of flames

Diffusion and non-premixed flames are the main types of flames used in lime shaft kilns. A non-premixed flame model applied in a large number of industrial systems for numerous reasons. In contrast to premixed flames, diffusion burners are simpler to design and build since they require no perfect reactant mixing. Furthermore, diffusion burners have longer flames and lower flame temperatures, which prevent local overheating near the burner and make it more suitable for a wide variety of fuels. Therefore, flames in a packed bed of spheres and porous media are presented and studied in this work.

2.4.2 Flames in a packed bed

In literature, the knowledge about the flame behavior in packed beds is limited. Most researchers have studied the turbulent premixed combustion using methane-oxygen mixtures to examine the flame propagation, such as the flame speed in a packed bed over different pressures and flow velocities (Masaki and Suzuki [34], Johansen and Ciccarelli). However, only a few have studied the diffusion flame experimentally and theoretically [35].

8) Kamiuto and Miyamoto examined the diffusion flame profile theoretically and experimentally. They developed a flame sheet model within a packed bed to quantify the effects of several system parameters on the shape and height of flames in a packed bed. Moreover, they made experiments for methane oxygen diffusion combustion in a plane-parallel packed bed of alumina spheres to estimate actual flame shapes in the packed bed. The analysis was done by examining the photographs taken from the upper surface of the packed bed.
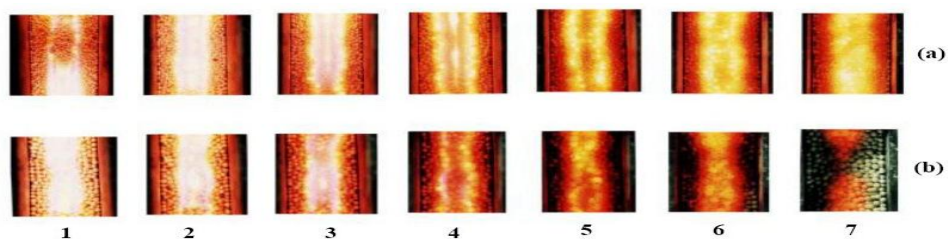
Figure 2.4: Photographs of the upper surface of the plane-parallel packed bed (a) Γ=8.663 and $R_e = 88.5$, (b) Γ=5.5, Γ is a ratio of the half-width of a combustion chamber to the packed sphere diameter [36].

The results showed that the flame height in packed beds is fifinite, and the flame shape elongates as the ratio of bed width to particle diameter increased. Also, they found that the flame form shrinks with an increase in the mean porosity

2.4.3 Flames in porous media

Numerous studies have been published over the past two decades, describing the combustion of gaseous fuels in the Porous Media Model. The flame in a porous medium differs from the flame in an open area due to the different heat transfer mechanisms it causes. Many researchers have theoretically and experimentally studied the combustion and flame propagation within porous media. Liu and Dong [37] demonstrate that the porous structure can enhance the mixing feature and intensify turbulent flow quantities.

Zhiguo Xu developed 3D geometries using PMM to simulate a flflame in a shaft kiln. His simulations were performed for three different porosities of 0.4, 0.6, and 0.8, respectively, as illustrated in Figure 2.5. He found the penetration of the combustion gas is under-predicted for the porosity of 0.4. Therefore the porosity must be larger in order to achieve deeper penetration. From Figure 2.5, it can found that penetration changes slightly with the porosity, increasing from 0.4 to 0.6 until it reaches 0.8. He has presented a packed bed as a porous medium before simulating the flflame. Although this flflame does not match the realistic model, his work provides a basis for further studies of flflame simulation in PMM [15].
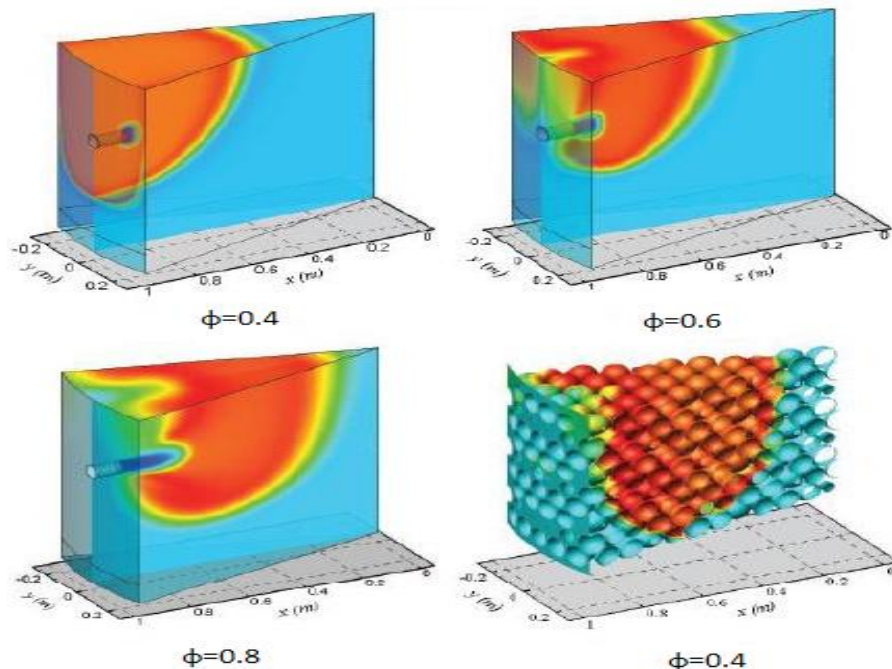
Figure 2.5: Comparison of temperature contours using P.M.M and D.P.M.

2.5 Conclusion of Literature Review

A large number of mathematical models have so far been developed to characterize lime shaft kiln operations. These models mainly deal with one-dimensional numerical equations to describe the lime burning process like core and surface temperatures of the solid particle, gas temperature, pressure drop, and so on. Nevertheless, these models still have many limitations, such as the inability to predict the temperature distributions in the radial direction, which assumed in many cases as a uniform distribution. Therefore, applying the CFD approach to study the physical and chemical processes within lime shaft kilns is essential to investigate the parameters which are difficult to predict by mathematical models. According to the literature, spherical particles are the most common shapes used to model a packed bed. When spheres are in contact with each other, they produce an infinitely small contact point, which is difficult for a mesh generation.

This phenomenon becomes a significant issue when analyzing packed beds using CFD approaches. Attempts have been made to eliminate this phenomenon by reducing the particle volumes and leaving a constant gap between particles, but the geometric continuity will be lost this way. The literature further shows that a structured packed bed has advantages in terms of simplification of the geometry creation, as well as that of problems in mesh generation. The BCC packing has typically a porosity of about $\phi=0.32$. However, the knowledge about the flame behavior in packed beds is limited, and only a few papers have examined the diffusion flames in packed beds theoretically or experimentally. Most of them have studied the turbulent premixed combustion using methane-oxygen mixtures to explore the flame propagation, such as the flame speeds over different pressures and flow velocities. In the case of simulation of a flame by PMM, researchers have mainly presented the combustion efficiency and flame propagation speeds.

To demonstrate that the porous structure can enhance the mixing features and the turbulent flow quantities. For this aim, most papers use the Ergun equation to predict the resistance or the pressure drop for flow through porous media.

Nonetheless, simulating a flame through PMM is completely different from the ones modeled by a packed bed or discrete particle model. Therefore, the Ergun equation must be modified so that the porosities or the two empirical constants of 150 and 1.75, which have no physical meaning, become almost similar to a real packed bed. However, the mesh and computational time needed for CFD simulations using PMM are considerably less than those needed for simulations using the discrete particle approach.

Computational Fluid Dynamics (CFD) and Porous Media Model (PMM)

3.1 Introduction

Computational Fluid Dynamics (CFD) is the science of predicting fluid flow, heat transfer, mass transfer, chemical reactions and the related phenomena by numerically solving the mathematical equations which govern these processes using a numerical process. Numerical methods are rising to prominence since the computer technology is advancing continuously and the computational power is getting higher. The physical feature for any fluid flow is governed by the fundamental principles of mass, momentum and energy conservation with chemical species for the gas flow. These principles can be expressed in terms of non-linear partial differential equations. For designing systems such as industrial shaft kilns, various tests with different parameters are needed to obtain a general trend for the response of the system. It is very costly and time-consuming to build such a massive model for testing purposes. Therefore, in this study, a CFD program is used to describe the reactive flow process through a packed bed. Generally, using a CFD model has both advantages and disadvantages. The main advantage of this model is its relatively low cost, as using physical experiments and tests to get essential engineering data for design can be expensive. CFD simulations can be executed in a short period and can simulate real conditions. The flows and heat transfer processes cannot easily be measured. On the other hand, there are some limitations to CFD models as well. In the real world, the CFD solution s can only be as accurate as of the physical models on which they are based, such as turbulence, compressibility, chemistry, and multi-phase flow. Solving equations on a computer is associated with numerical errors, parts of which are due to approximations in the numerical models. Also, mesh refinement is one way to eliminate these errors. Furthermore, the accuracy of the CFD solution is affected by the initial or boundary conditions provided to the numerical model. Generally, all CFD codes contain three main elements, including pre-processing, solver, and post-processing. The pre-processing involves many steps starting from building at the model within a Computer-Aided Design (CAD) package, creating or applying a suitable computational mesh, and setting up the flow boundary conditions and fluid material properties. This step performed by software tools such as Gambit, Workbench, and Star CCM, which used in this study. The CFD solver carries outflow calculations and produces results such as ANSYS Fluent. That can use different physical models such as incompressible or compressible, inviscid or viscous, laminar or turbulent, etc. Usually, ANSYS Fluent uses a finite volume method to solve the governing equations for the fluid flow [38-39].

3.2 Computational Domain and Assumptions
3.2.1 Chosen geometry

A kiln diameter of 2 m was chosen, which a small diameter is, but it is used here because of the limited computational time of 3D reactive flows for PFR or CFS kilns. However, this diameter is sufficient to research the influence of all parameters. The height of the packed bed is between 8 to10 m, which is a typical height for the burning zone. It assumed that the combustion air enters the burning zone with uniform velocity and temperature. Heat transfer to the packed bed excluded. Otherwise, the whole calcination process must be included, which requires a lot of computational time. The calcination process does not influence the reactive flow. Therefore, it is not necessary to consider the process of heat transfer. The geometry and dimensions of the two types of lime shaft kilns are shown in Figure 3.1.
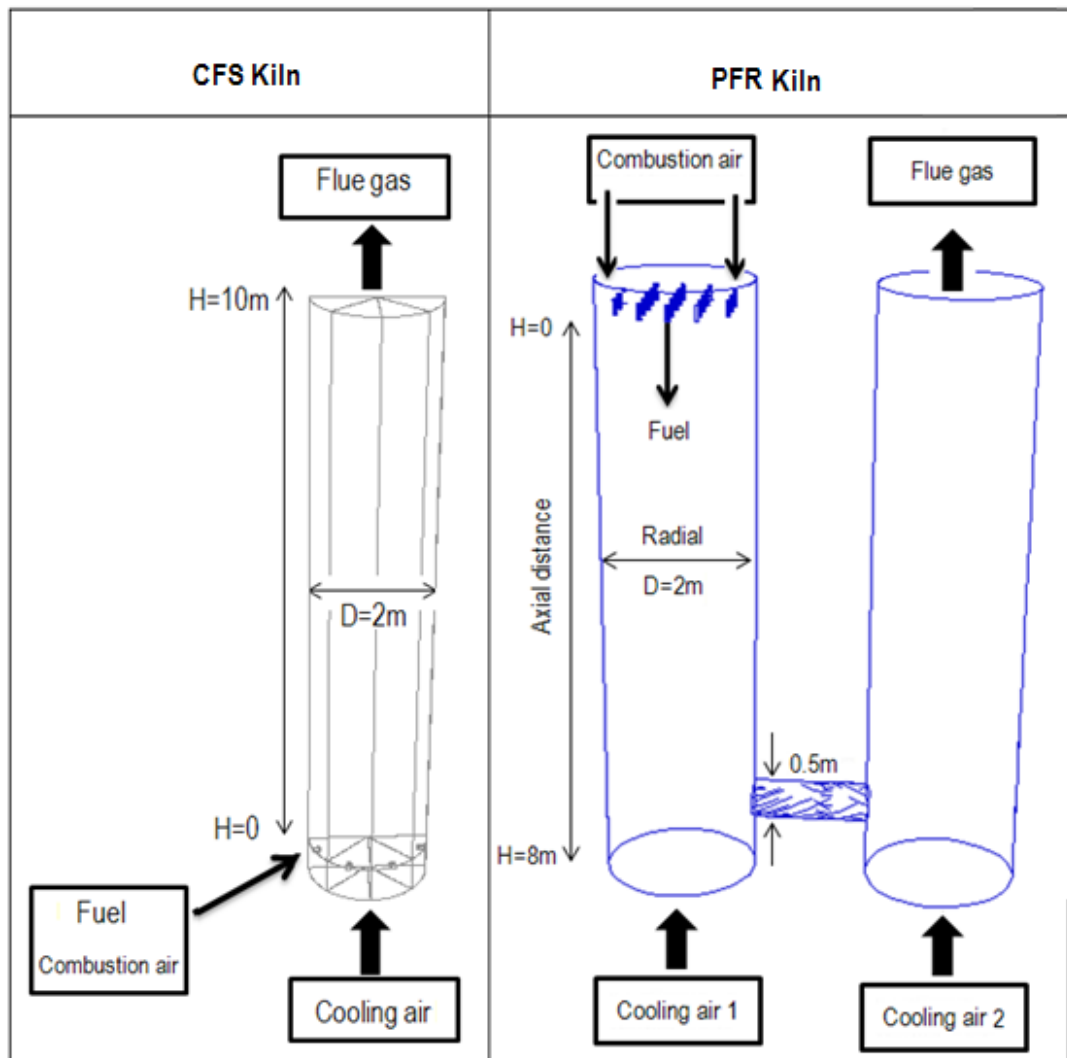
Figure 3.1: Geometry and domain of shaft kilns.

Validation of simulations with experimental results is done using a sample of a packed bed and injecting different gases into the packed bed. The experimental measurement done for the two

types of the structured packed bed is shown in Figure 3.2. The particles arranged in two types: BCC and SC, where two gases are injected in radial and parallel direction. The results were compared with the CFD simulation from PMM.

Radial flow injection

Parallel flow injection
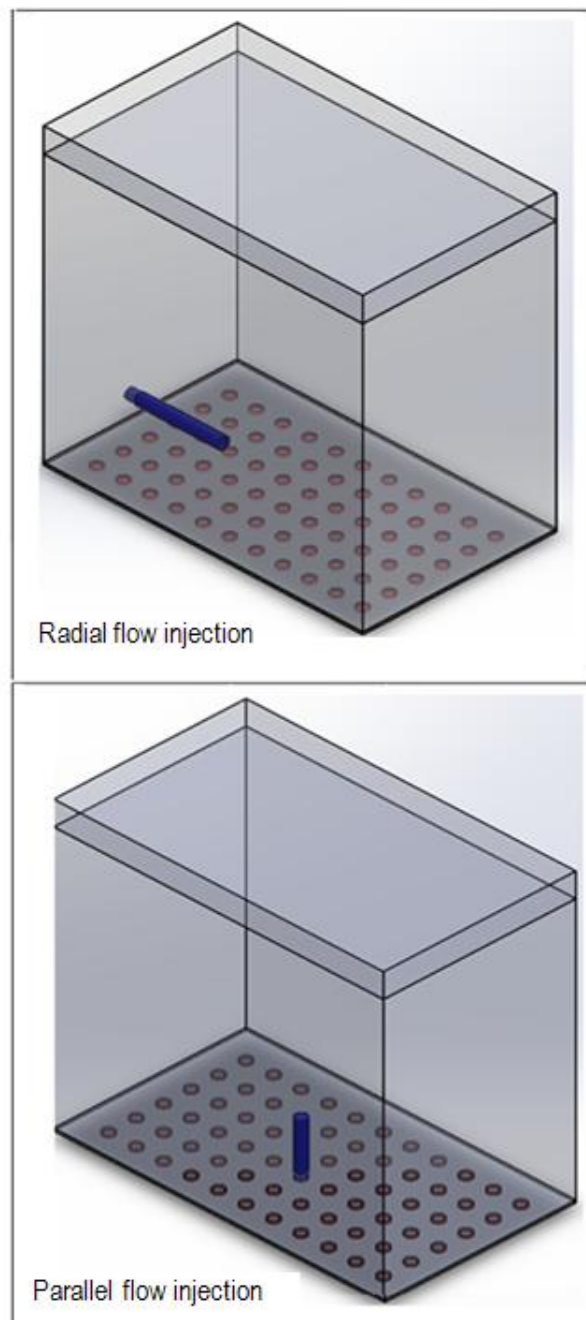
Figure 3.2: Geometry and domain of experiment packed bed.

3.2.2 Mesh-grid generation

Mesh generation is an essential part of the CFD approach, particularly for complex geometries such as packed beds. The accuracy of the simulation is strongly affected by the mesh structure. In general, a fine mesh reduces numerical errors which will improve the efficiency of the solution. However, a fine-mesh requires vast memory, and if the computer power is limited, it becomes difficult to run the simulations. Therefore, a mesh study has been performed in this work to find a

proper mesh density that provides a balance between a fine enough grid for acceptable accuracy and computing time. In this section, a discussion about mesh independent study for the flame in the packed bed presented. Figure 3.3 and Figure 3.4 shows the mesh-grid generation for CFS and PFR kilns [38].
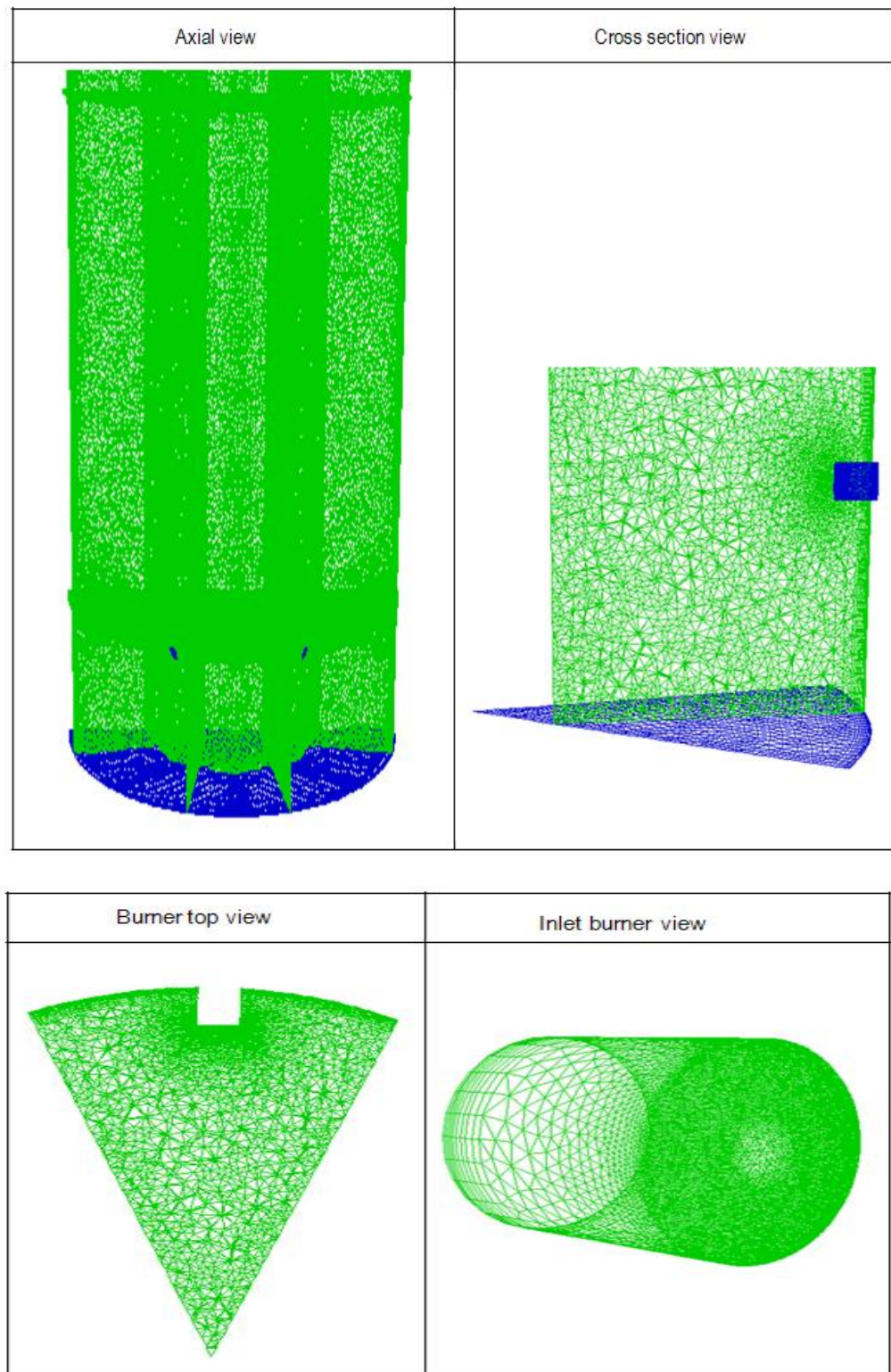
Figure 3.3:   Mesh-grid generation for a CFS Kiln.
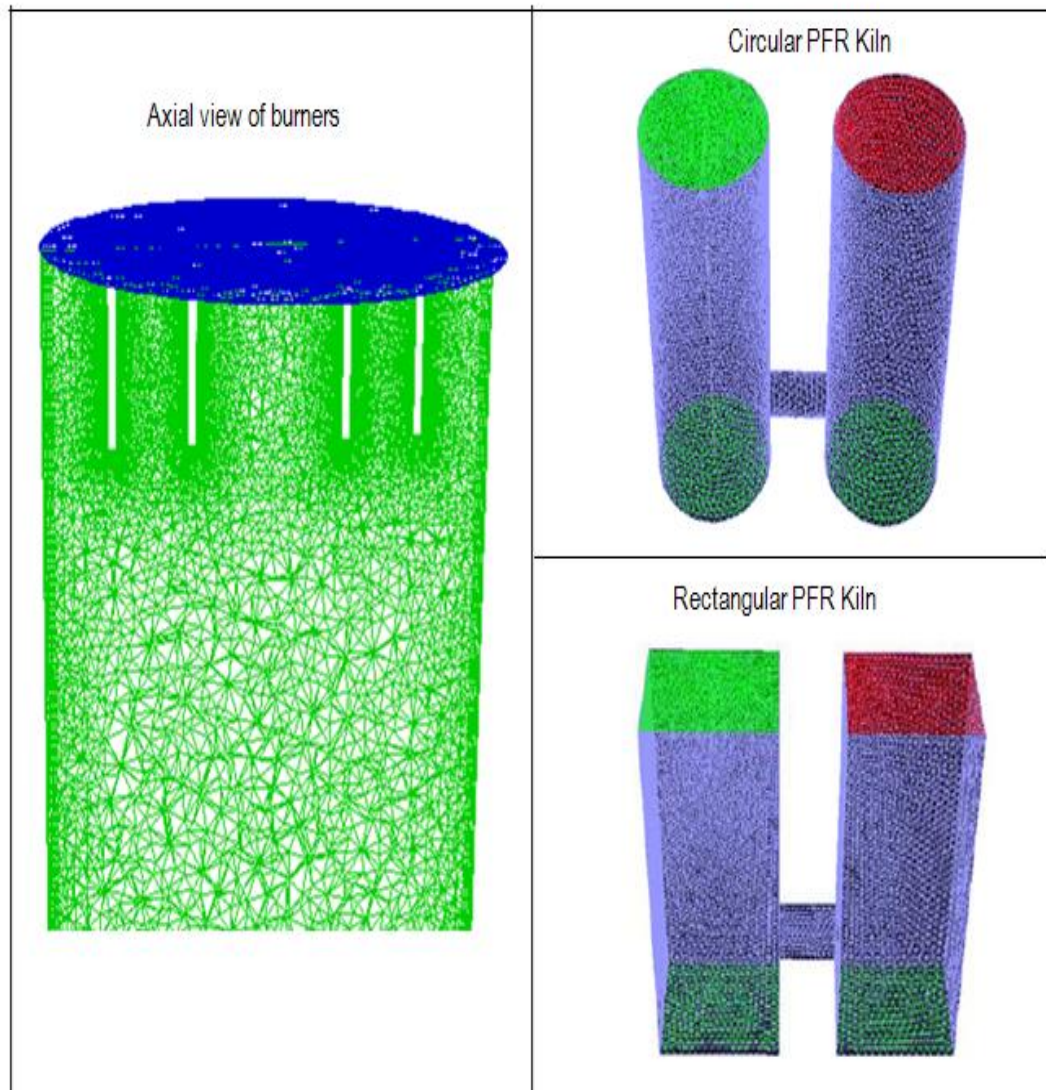
Figure 3.4: Mesh-grid generation for a PFR kiln.

The very fine mesh generated for the geometry of test packed beds shows in Figure 3.5. Mesh generation performed in ANSYS workbench and Gambit mesh tools. The tetrahedral cell used for all domains. Mesh kept fine enough to obtain adequate results, as shown in Figures 3.3 to Figure 3.5. Special attention has been given to the Y+ value. This value should be near 30, as turbulence models with standard wall functions can predict flows accurately only if the Y+ is within the range of 30. Table 3.1 shows the mesh generation for all geometries[38].
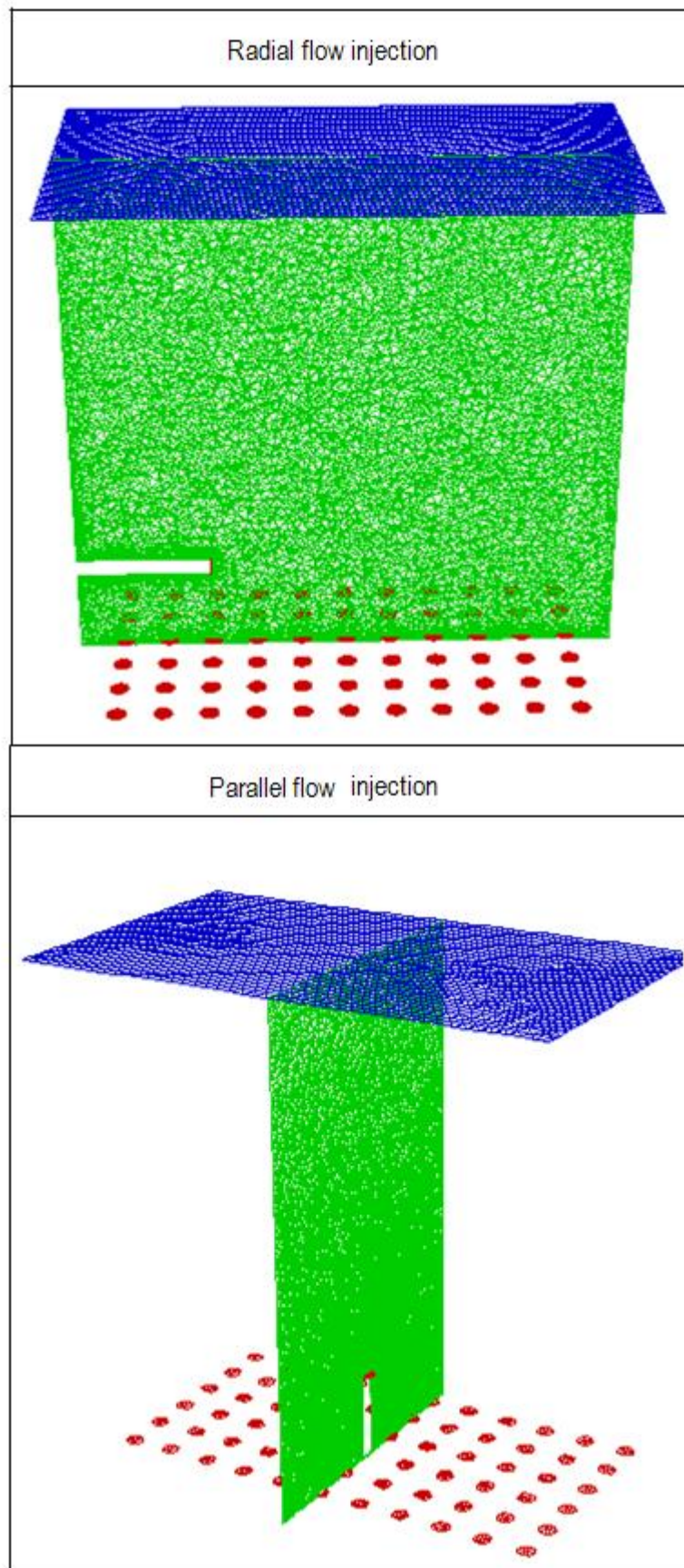
Figure 3.5: Mesh-grid generation for an experimental   packed bed.

Table 3.1: Mesh-grid generation reports.

Type of Geometry	Type of Mesh	Model of Mesh	Nodes	Faces	Cells
PFR Kiln	Tetrahedral	Porous Media Model	616,573	79,890	2,911,500
CFS Kiln	Tetrahedral	P.M.M	339,080	3,026,512	1,491,080
Parallel flow injection In packed bed	Tetrahedral	P.M.M	194,918	2,200,000	1,064,569
Radial flow injection In packed bed	Tetrahedral	P.M.M	319,188	3,687,988	1,855,051

3.2.3 Near-wall treatment

The near-wall modeling significantly impacts the numerical solutions. In packed beds, spheres surface presumed as walls, and these are the main source of mean vortices and turbulence. Therefore, accurate representation of the flow in the near-wall region determines successful predictions of wall-bounded turbulent flows. Numerous experiments have shown that the near-wall region can be subdivided mainly into three layers. In the innermost layer, called the viscous sublayer, the flow is almost laminar, and the viscosity plays a dominant role in momentum and heat and mass transfer. In the outermost layer, called the fully-turbulent layer, turbulence plays a significant role. Lastly, there is an interim region between the viscous sublayer and the fully-turbulent layer where the effects of molecular viscosity and turbulence are equally important. Figure 3.6 illustrates these subdivisions of the near-wall region.
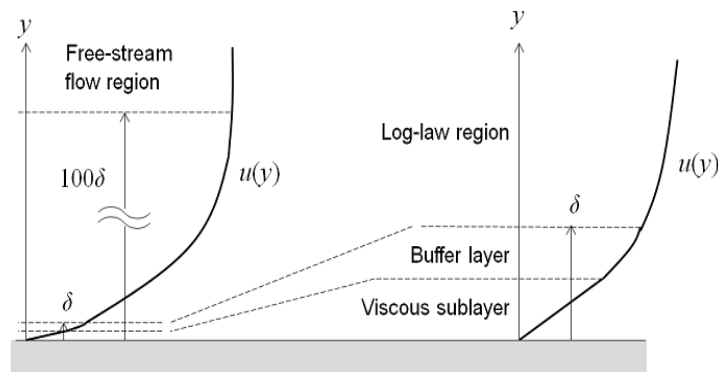
Figure 3.6: Subdivisions of the near-wall region [38-39].

There are two approaches to modeling the near-wall region. In one approach, the viscosity-affected inner region (viscous sublayer and buffer layer) not resolved. Instead, semi-empirical formulas called "wall functions" are used to bridge the viscosity-affected region between the wall and the fully-turbulent region. Using wall functions prevents the need to modify the turbulence models to account for the presence of the wall. In another approach, the turbulence models modified. This method enables the viscosity-affected region to resolve with a mesh to the wall, including the viscous sublayer. For the purpose of the discussion, this will be termed the near-wall modeling approach [38]. These two approaches are depicted schematically in Figure 3.7 below.
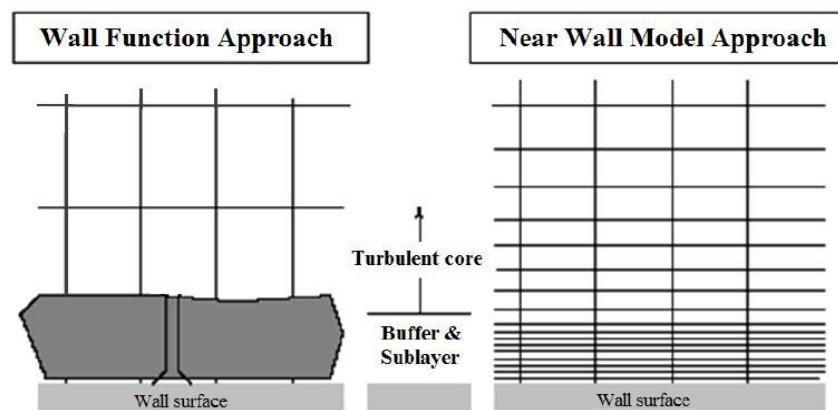
Figure 3.7: Schematic of the mesh for a wall function and a near-wall mode approach.

Near-wall Region Y+

Y+ is one of the most important parameters when modeling turbulent flows. It is related to the meshing. The wall Y+ is a non-dimensional distance similar to local Reynolds number, often used in CFD to describe how coarse or fine a mesh is for a particular flow. It is the ratio between the turbulent and laminar influences in a cell. Accurate presentation of the flow in the near-wall region determines the successful prediction of wall-bounded turbulent flows. Values of Y+ in the range of (Y+≈30-50) are most desirable for standard wall functions, whereas the ones with Y+≈1 are most desirable for near-wall modeling [41]. The wall function concept and different boundary layers near the wall shown in Table 3.2.

Table 3.2: Near-wall region.

Y^+	Near wall region
$Y^+ \approx 5$	Viscus sub layer
$5 < Y^+ < 30$	Buffer layer or blending region
$Y^+ > 30 - 60$	Fully turbulent

3.2.4 Boundary conditions and assumptions

It is essential to specify the boundary conditions according to the fluid or solid after geometry and mesh generation. The boundary conditions determine the flow and thermal variables on the boundaries of the physical model. There are a number of classifications of boundary conditions, such as flow inlet and exit boundaries: (pressure inlet, velocity inlet, inlet vent, intake fan, pressure outlet, outflow, outlet fan, exhaust fan), wall and repeating boundaries: (wall, symmetry, periodic axis); and Internal cell zones: (fluid, solid). Before applying these boundary conditions, some assumptions and simplifications required. In most cases, it is impossible to describe a real process mathematically correctly.

Therefore, in this work, the flow model is presumed as a steady state and incompressible. The boundary conditions are assigned as the velocity−inlet for the inlet section and the pressure−outlet(P_{gauge}=0) for the outlet section. Symmetry boundary condition is assigned to the lateral faces. The wall prism layer is shown in Figure 3.8.
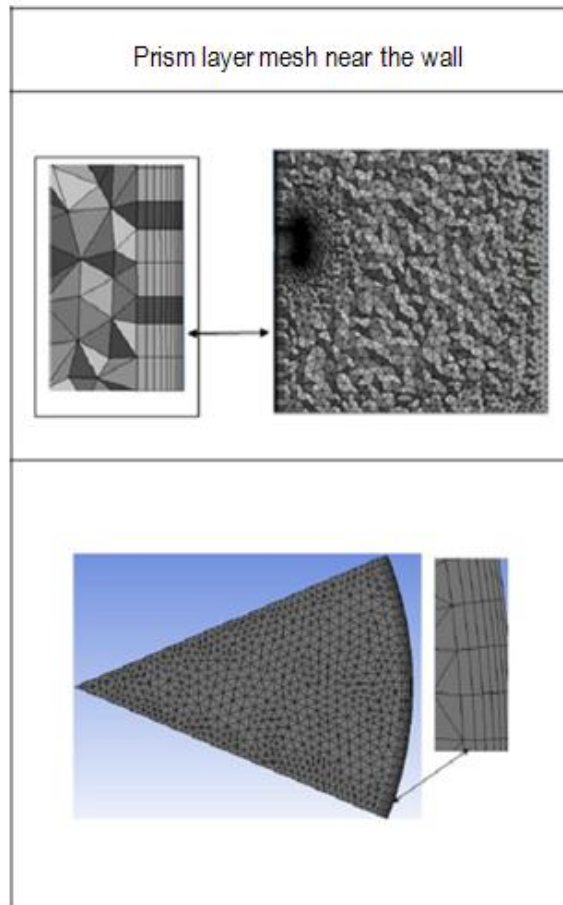
Figure 3.8: Prism layer mesh near the wall (CFS kiln).

The exterior parts of the packed spheres defined as wall boundaries. The wall boundaries separate the fluid zone from the solid zones (solid spheres). Since there are no solid reactions, solid spheres' boundaries not considered. No-slip boundary conditions applied at the surface of particles. After using the boundary conditions, the physical model defined, and the numerical solution can determine.

3.2.5 Solving the CFD problem

When the mesh completed and all the other complications resolved, the actual computational part of the CFD. At this point, the completed geometry imported into the solver, and the CFD simulations begin. Again, a series of steps performed. First, the boundary conditions of the system set. Next, the process iteration parameters should set. With the boundary conditions defined, the simulation performed. There are two main iteration parameters to be set before starting the simulation. First is the relaxation factor with which the iteration step-change multiplied before it applied to the result for the next iteration step. When this factor is larger than one, the process is called "over-relaxed." In an over-relaxed process, the step change is significant, and the convergence reached faster. However, it is not recommended to over-relax a procedure unless it is very stable. In a less stable or non-linear system such as turbulent flow, over-

relaxation may lead to divergence of the process. When the relaxation factor is less than one, the process is called "under-relaxed," which used in our simulations. In this case (under-relaxed), the iteration process is slower because the step change is small but not likely to diverge. The second important parameter is the residual value that determines when a solution has converged. The residual value is the difference between the current and the former iteration values and taken as a measure for convergence. Usually, the residuals will go to zero as the process converges. Therefore, in this study, all the convergence criteria are set below 10^{-3}. These cut-off values are for convergence placed for all elements in the model, temperature, densities, pressures, flow, velocities, species transport, or the mean mixture fraction. In some cases, such as pressure drop prediction, the convergence criteria are needed to be set below 10^{-6} to get a more accurate prediction. However, this might lead to significantly increased computational times. Navier stoke equations and species transport equations solved only by numerically discretized. A variety of techniques can be used to perform this numerical discretization, such as the finite volume method. The finite volume method (FVM) has been developed specifically to solve the equations of heat transfer and fluid flow and is the most popular method used in CFD. ANSYS Fluent adopts this method for the numerical discretization [39]. The final step in obtaining the desired data is the post-processing of the data in which the desired data sets took from the simulation data. All the computational work is carried out using commercial software ANSYS Fluent 14. The fluent solver uses an FVM procedure, which converts the governing differential equation to algebraic forms, together with the SIMPLE (Semi Implicit Method for Pressure Linked Equations) algorithm. The discretization algorithm is standard for pressure, and the first-order upwind for momentum, the SIMPLE scheme, has been employed for pressure-velocity coupling.

3.2.6 Governing equations

The momentum and continuity equations solved for a CFD simulation. The equation of the conservation of mass or continuity can be written as follows [38-39]:

$$\frac{\partial \rho}{\partial t} + \nabla. \ \rho u \ = S_m. \tag{3-1}$$

S_m is the mass being added to the continuous phase from the dispersed phase. The conservation of momentum in a stationary reference frame can be described by:

$$\partial \ \frac{\rho u}{\partial t} \ + \nabla. \ \rho u u \ = -\nabla p + \nabla.\tau + \rho g + F. \tag{3-2}$$

P is the static pressures (Pa), represents the stress tensor, and is the gravitational and external body forces, respectively. F also contains the model-dependent source terms such as porous media.

$$\tau = \mu \left[\nabla u + \nabla u^T \right] - \frac{2}{3} \nabla . uI \; . \qquad (3\text{-}3)$$

Here, μ is the molecular viscosity, I is the unit tensor, and the second term is the effect of volume dilation. One of the forms of the energy equation is as shown below:

$$\frac{\partial \rho E}{\partial t} + \nabla . \left(u(\rho E + p) \right) = \nabla . \left[(k + kt) \nabla T - \sum_j h_j J_j + (\tau . u) \right] + Sh \qquad (3\text{-}4)$$

Kt is the turbulent thermal conductivity. Jj is the diffusion flux of species j, and h is the enthalpy of ideal gases. The first three terms on the right-hand side represent energy transfer due to conduction, species diffusion, and viscous dissipation, respectively. Sh includes the heat of chemical reactions [40].

3.2.7 Turbulence models

>No single turbulence model is universally accepted as being superior for all classes of problems. The choice of turbulence model will depend on considerations such as the physics included in the flow, the specific type of issue, the level of accuracy required, the available computational resources.

Turbulence models separated into two classifications. The first one is the classical models and is based on the averaged Reynolds equations. These condors based on space-filtered averaging such as Large-Eddy simulation. In this study, Reynolds-Average Turbulence Models (RANS) presented. Usually, RANS is employed to the Naiver-Stokes equations so that the small-scale turbulent fluctuations could not directly be simulated. Therefore, the RANS approach dramatically reduces the required computational effort and is widely adopted for practical engineering applications. ANSYS Fluent offers different kinds of turbulence models based on the RANS approach. Here, six different types have been studied, including Standard k-ε, RNG k-ε, Realizable k-ε, Standard k−ω, SST k−ω, and Transition SST. In ANSYS documentation [38], there is more information regarding equation details and empirical constant that can be used for each model. Below is a brief introduction for each model:

> **Standard k−ε Model:**

It is the simplest complete turbulence model with two-equation models.

This model allows the turbulent velocity and length scales to be independently determined. This model has one differential equation for the turbulent velocity scale and another for the turbulent length scale. The variables modeled are the turbulent kinetic energy, k, and the rate of

dissipation of turbulent kinetic energy, ε. The standard k− ε model has become the workhorse of practical engineering flow calculations for 40 years.

➢ **RNG k−ε Model:**

The model has been derived for 25 years from the instantaneous Naiver-Stokes equations, using (RNG) methods. It is similar in form to the standard k−ε model but includes some refinements such as it has a new equation that significantly improves the accuracy for rapidly strained flows and the effect of swirl on turbulence, which is included in the RNG model. These features make the RNG k−ε model more accurate and reliable for a more comprehensive class of flows than the standard k−ε model.

➢ **Realizable k−ε Model:**

The realizable k−ε model is a relatively recent development by Shih (1995). This model is different from the standard k−ε model in two important ways: first, the realizable k−ε model contains a new formulation for turbulent viscosity; and second, a new transport equation for the dissipation rate. The term "realizable" means that the model satisfies certain mathematical constraints on the Reynolds stresses, consistent with the physics of turbulent flows. Neither the standard k−model nor the RNG k−ε models are realizable. The advantage of the realizable k−ε model is to provide superior performance for flows involving rotation, boundary layers under strong pressure gradients, separation and recirculation.

➢ **Standard k−ω Model:**

This model is based on the model transport equations for the turbulence kinetic energy (k) and the specific dissipation rate (ω) developed by Wilcox (1998). The standard k−ω model has modifications for low Reynolds number effects, compressibility and shear flow spreading. This model is applicable for the free shear flow spreading rates that are in close agreement with measurements for far wakes, mixing layers, and around plane.

➢ **Shear-Stress Transport SST k−ω Model**:

The shear-stress transport (SST) k−ω model developed by Menter to effectively blend the robust and accurate formulation of the k−ω model in the near-wall region with the free-stream independent of the k−ω model in the field. The SST k−ω model is similar to the standard k−ω model. It includes the following refinements: the modeling constants are different, and the definition of the turbulent viscosity is modified to account for the transport of the turbulent shear stress [42].

➢ **Transition SST Model**:

The model based on the coupling of the SST k-ω transport equations with two other transport equations in terms of the momentum-thickness Reynolds number. An empirical correlation by Langtry and Menter has been developed to cover standard bypass transition as well as flows in

low free-stream turbulence environments. [43].In the derivation of the k-e model, it assumed that the flow is fully turbulent, and the effects of molecular viscosity are negligible. The standard *k*-e model is, therefore, valid only for fully turbulent flows.

Transport Equations for the Standard K-ε Model:

Turbulent Kinetic Energy k:

$$\frac{\partial}{\partial t}\left(\rho k\right) + \frac{\partial}{\partial x_i}\left(\rho u_i k\right) = \frac{\partial}{\partial x_i}\left[\left(\mu + \frac{\mu_t}{\sigma_k}\right)\frac{\partial k}{\partial x_i}\right] + G_k + G_b - \rho\epsilon \qquad (3\text{-}6)$$

Dissipation rate ε:

$$\frac{\partial}{\partial t}\left(\rho\epsilon\right) + \frac{\partial}{\partial x_i}\left(\rho\epsilon u_i\right) = \frac{\partial}{\partial x_i}\left[\left(\mu + \frac{\mu_t}{\sigma_\epsilon}\right)\frac{\partial\epsilon}{\partial x_i}\right] + C_1\frac{\epsilon}{k}\left(G_k + C_3 G_b\right) - \frac{C_2\rho\epsilon^2}{k} \qquad (3\text{-}7)$$

G_K is the turbulent kinetic energy generated due to velocity gradients and G_b is turbulent kinetic energy due to buoyancy. These are defined as follows:

$$G_k = -\rho u_i u_j \frac{\partial u_j}{\partial x_i} \qquad (3\text{-}9)$$

 To buoyancy, which are defined as,

$$G_b = \beta g_i \frac{\mu_t}{Pr_t}\frac{\partial T}{\partial x_i} \qquad (3\text{-}10)$$

$$\beta = -\frac{1}{\rho}\frac{\partial\rho}{\partial T} \qquad (3\text{-}11)$$

$$\mu_t = \rho.C_\mu.\frac{K^{''}}{\epsilon} \qquad (3\text{-}12)$$

Pr_t is the turbulent Prandtl number for energy and g_i is the component of gravitational vector in the direction, β is the coefficient of thermal expansion. $C_1, C_2, C_\mu, \sigma_k$, are constants.

3.2.8 Combustion model

For gas-phase combustion models, a set of coupled partial differential equations describe the motion of the fluid, species reactions, transport processes like conduction of molecular heat diffusion and thermal radiation. The choice of combustion models typically depends on the available empirical or experimental data and the expected accuracy of the solution. ANSYS Fluent provides five approaches for modeling gas or solid-phase reacting flow generalized finite-rate model, non-premixed combustion model, premixed combustion model, partially premixed combustion model, and composition probability density function (PDF) transport model. The fact that the combustion model in shaft kilns is mostly non-premixed combustion; this means that both the fuel and oxidizer flow injected into the combustion zone in separate streams. Only the non-premixed model introduced in this work

Non-Premixed model

Definition of the mixture fraction

The non-premixed combustion model and Probability Density Function (PDF) choose for chemical reaction simulation. The non-premixed modeling approach offers many benefits over the finite rate formulation. This model allows intermediate (radical) species prediction, dissociation effects, and rigorous turbulence chemistry coupling. The method is computationally efficient in that it does require the solution of a large number of species transport equations. When the underlying assumptions are valid, the non-premixed approach can be used only when the reacting flow system meets several requirements. First, the flow must be turbulent. Second, the reacting system includes a fuel stream, an oxidant, or a non-reacting stream. Finally, the chemical kinetics must be rapid so that the flow is near chemical equilibrium. Owing to fluctuating properties of a turbulent mixing process, the Probability Density Function, PDF is a preferred method for the cases containing the combustion process and turbulent flow. PDF defined by two parameters of mean scalar quantity and its variance. Due to the difficulty in solving the transport equation for each species, the mixture fraction, f in the presumed PDF wrote in terms of mass fraction of species i, ,Z_i

$$f = \frac{Z_i - Z_{i,ox}}{Z_{i,fuel} - Z_{i,ox}} \quad . \tag{3-13}$$

The subscripts "ox" and "fuel" denote the value at the oxidizer and fuel streams inlets, respectively. It has a value of (f=1) in the fuel stream, zero value (f=0) in the oxidizer stream and it takes values between zero and one (f=0-1) within the flow field. The transport equations of mean mixture fraction,$\bar{f}$ and its variance,$\overline{f'^2}$, are:

$$\frac{\delta}{\delta t}(\rho f) + \nabla * \ \rho * v * f \ = \nabla * \ \frac{\mu t}{\sigma t} * \nabla * f \ + Sm + S_{User} \ . \tag{3-14}$$

The source term S_m is due to the transfer of mass into the gas phase from liquid fuel droplets or reacting particles (e.g. Coal). S_{User} is any user-defined source terms, which are both not considered in this study. In addition, ANSYS Fluent solves a conservation equation for the mixture fraction variance, f^2

$$\frac{\delta}{\delta t}(\rho f^2) + \nabla(\rho \overline{V} \hat{f}^2) = \nabla(\frac{\mu_t}{\sigma t} \ \nabla \hat{f}^2) + C_g \mu_t (\nabla \overline{f})^2 - C_d . \rho . \frac{\varepsilon}{k} \ \hat{f}^2 + S_{User} \tag{3-15}$$

Where $f = f - f$. The default values for the constants σt, Cg, and Cd are 0.85, 2.86, and 2.0, respectively. The power of the mixture fraction modeling approach is that the chemistry is reduced to one conserved mixture fraction. The mixture fraction definition can be understood in relation to common measures of reacting systems. Consider a simple combustion system involving a fuel stream (F), an oxidants stream (O) and a product stream (P) symbolically represented at stoichiometric conditions as

$$F + rO \rightarrow \ 1 + r \ P \tag{3-16}$$

Where r is the air-to-fuel ratio on a mass basis and the equivalence ratio as λ is [39]:

$$\lambda = \frac{(\frac{fuel}{fair})actual}{\frac{fuel}{air} \ stoichiometric} \ . \tag{3-17}$$

Their action in Eq. (3.16) under more general mixture conditions can be written as:

$$\lambda F + rO \rightarrow \ \lambda + r \ P \ . \tag{3-18}$$
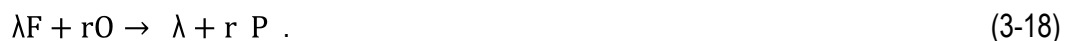
Looking at the left side of this equation, the mixture fraction for the system as a whole can then be deduced to be

$$f = \frac{\lambda}{\lambda + r} \ . \tag{3-19}$$

Eq (3.16) allows the computation of the mixture fraction at stoichiometric conditions (λ=1), or at fuel-rich conditions (λ>1), or fuel-lean conditions (λ<1) [44].

Enabling the Rich Flammability Limit (RFL) Option

To specify the mixture fraction limits f (Eq.3-13), the software provides a fuel stream Rich Flammability limits (RFL) option. RFL is often more accurate than the assumption of chemical equilibrium for rich mixtures and also avoids complex equilibrium calculations, speeding up the preparation of the look-up tables. The appropriate RFL value is approximate twice the

stoichiometric mixture fraction [38]. For the methane-air mixture, the stoichiometric mixture fraction is about f_{st} =0.091, so that, the RFL is about 0.18

3.2.9 Mesh convergence studies and validations

Here, the mole fraction of oxygen in an experimental packed bed (radial and parallel flow injections) was measured. The results were compared with three CFD simulations having various mesh element sizes. Therefore, the mesh convergence study and independency must be studied. The results were reported for three mesh element numbers. The velocity profile and computational time were monitored for three cases. The details are presented in Tables 3.3 and Table 3.5. The mesh numbers range from the coarsest mesh with around 881,000 element sizes to the finest mesh with 1,855,000 element sizes, for radial flow injection packed bed.

Table 3.3: Convergence study and mesh reports for radial flow injection in experimental packed bed.

Grid	Size of element (mm) (Interval)	Element No Cells	Computation Time(min)	Iteration No	Density Cell/cm3	Velocity (m/s) H=0.468m
Mesh 1	0.5	1,855,051	180	420	13.6	0.350
Mesh 2	1	1368128	100	280	10.04	0.345
Mesh 3	2	881205	30 min	141	6.46	0.33

The CFD simulation for three mesh elements was compared with the experiment results shown in Figure 3.9. The mesh 1 shows more accuracy with the experimental results as it is a fine mesh.
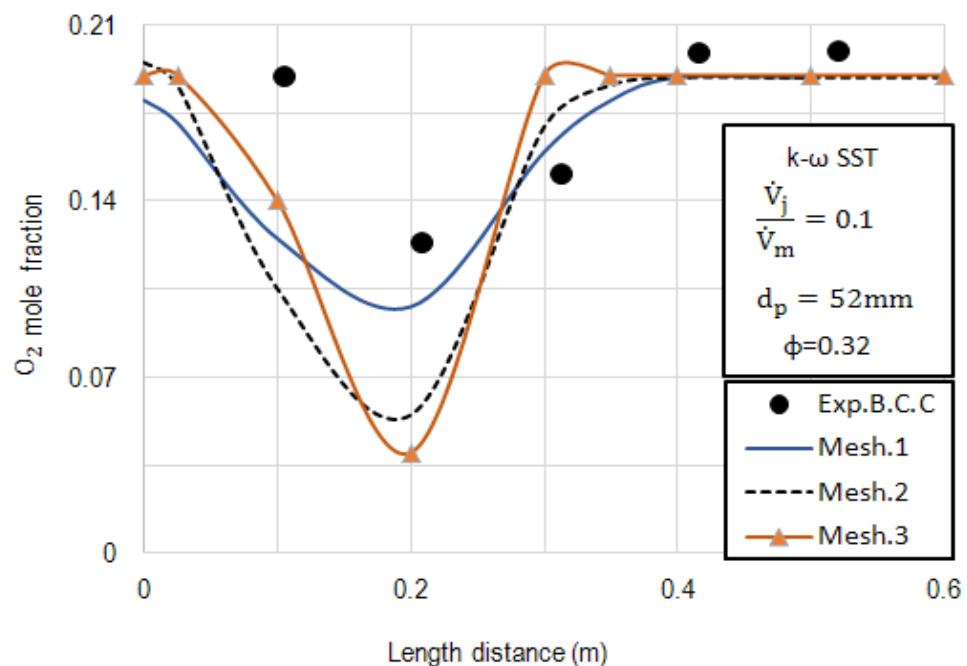
Figure 3.9: Mesh study and validation for radial flow injection in an experimental packed bed.

Figure 3.10 shows the histogram distribution of the cell equivolume skew. The mesh contains a few highly skewed elements. A bell-shaped diagram usually presents a normal distribution. The high skew reaches a maximum value, returns to a minimum before reaching zero. These kinds of histogram distributions belong to very fine meshes with optimum mesh elements numbers. The Y^+ is a region near the solid walls and is a non-dimensional distance value that is important in turbulence modeling to determine the proper size of cells near walls. In the current research study, as shown in Figure 3.10, the Y^+ is less than 5 in near-wall surfaces. Therefore, these histogram diagram and wall Y^+ values result in a CFD simulation program code with less computational time and an optimum number of meshes [38].

| Radial flow injection in experiment Packed bed Histogram distribution | |
| Wall Y plus function | |
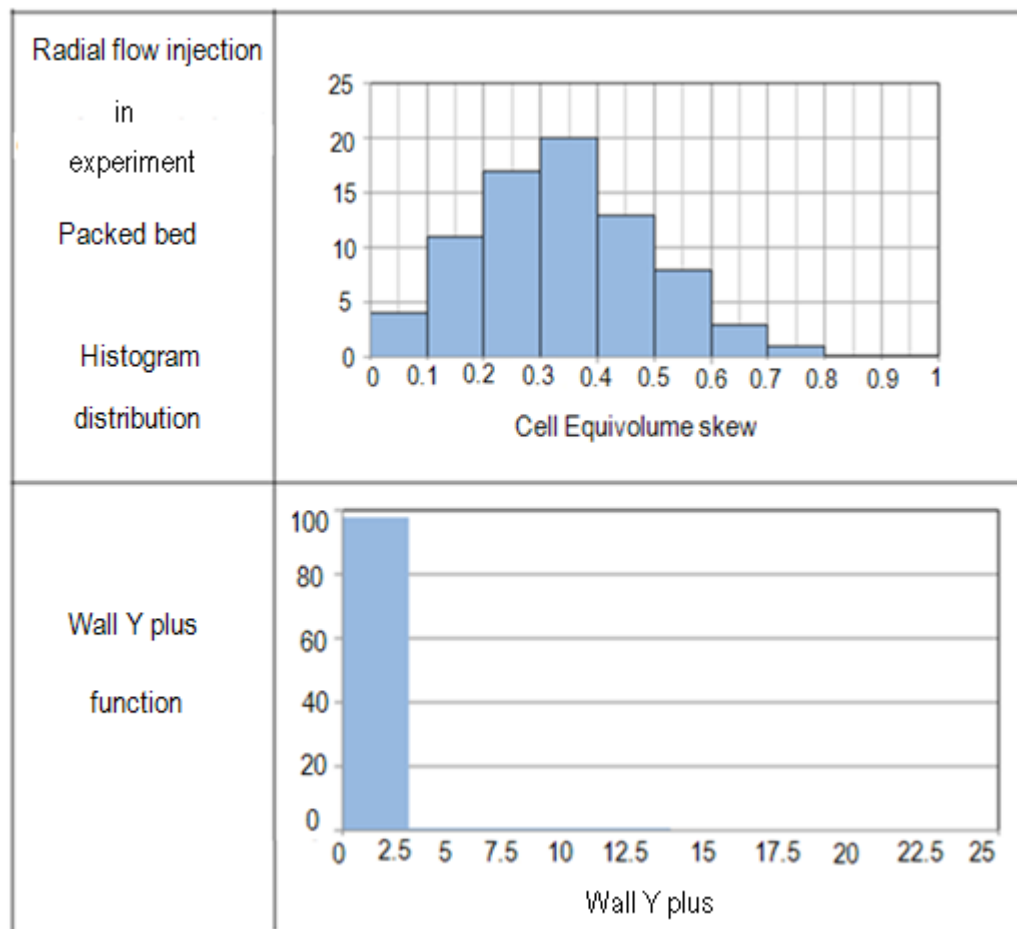
Figure 3.10: Histogram distribution and Y^+ values for the wall region in radial flow packed bed.

The mesh convergence study performed for parallel flow injection in experiment packed bed. The mesh report shows in Table 3.4.

Table 3.4: Convergence study and mesh reports for parallel flow experiment packed bed.

Grid	Size of element (mm) (Interval)	Element No Cells	Computation Time(min)	Iteration No	Density Cell/cm3	Velocity (m/s)
Mesh 1	0.5	1,064,569	140	280	7.8	0.30
Mesh 2	1	922887	85	120	6.77	0.295
Mesh 3	2	781205	25	135	5.73	0.28

The validation results with fines mesh are also shown in Figure 3.11 with high accuracy.
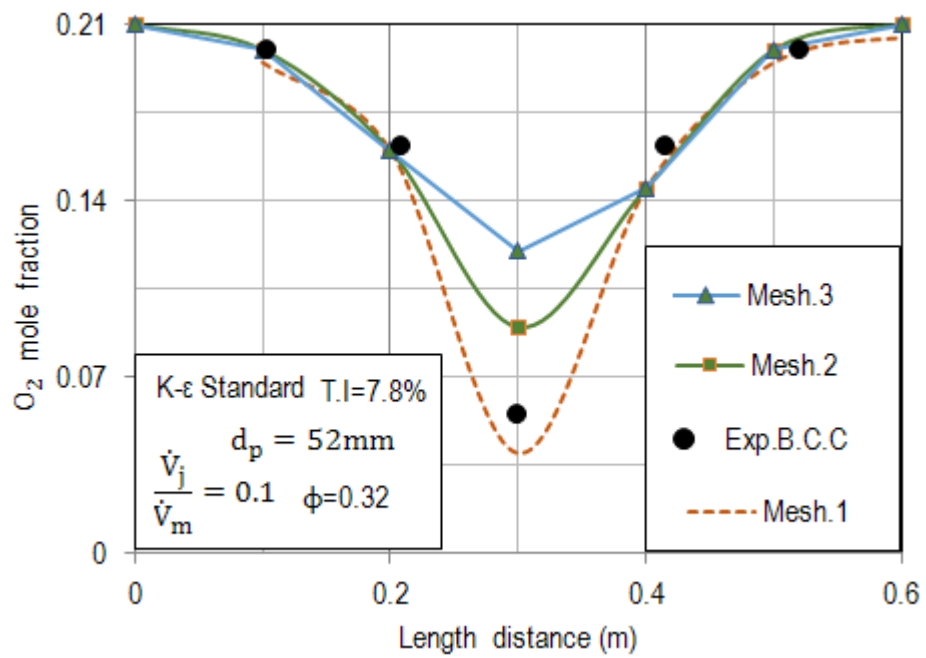
Figure 3.11: Mesh study and validation for a parallel flow injection in an experimental packed bed.

Parallel flow injection in experiment Packed bed Histogram distribution	
Wall Y plus function	
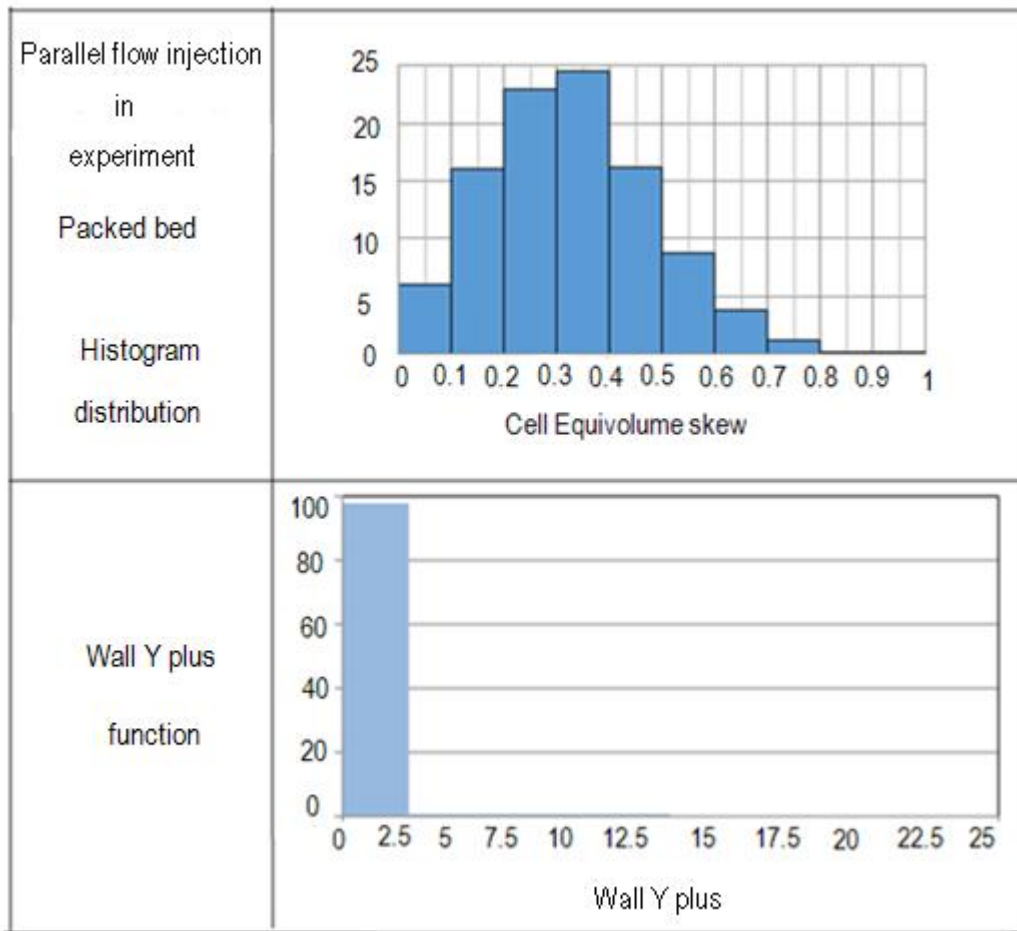
Figure 3.12: Histogram distribution and Y^+ values for the wall region in a parallel flow packed bed.

Figure 3.13 shows the length of flame related to the cell number for PFR kilns. It can be seen that the mesh number varied from 500,000 to around 3,200,000, where the coarse mesh is associated with a significant variation on the length of the flame. Moreover, the figure demonstrates that increasing mesh to more than 2,911,000 cells leads to a relatively constant flame length. Consequently, to minimize the computational time and an optimum number of cells with high accuracy, the mesh with 2,911,000 cells was selected to carry out all the cases of non-premixed simulation of PFR shaft kiln [40].
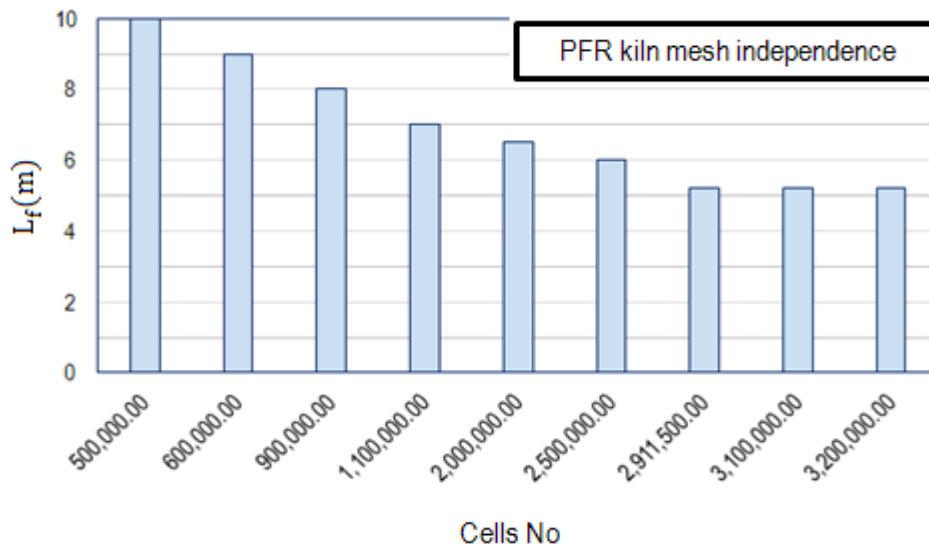
Figure 3.13: Mesh independence study for length of flame (PFR kiln).

In the current research study, as shown in Figure 3.14, the Y^+ is less than 5 in near-wall surfaces. Therefore, these histogram diagram and wall Y+ results CFD simulation program code with less computational time and an optimum mesh.
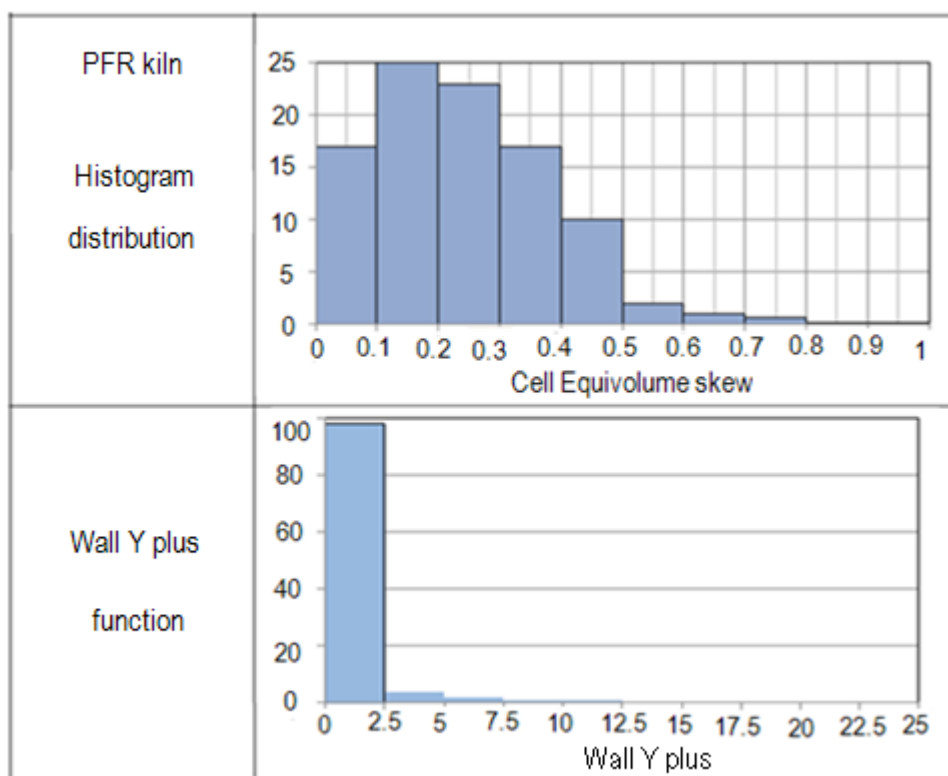
Figure 3.14: Histogram distribution and Y^+ values for the wall region in PFR kiln.

Figure 3.15 shows the length of the flame related to the cell number. It can be seen that the mesh number varies from 500,000 to around 1,900,000, where the coarse mesh is associated with a significant variation in the length of the flame. Moreover, the figure demonstrates that increasing

mesh to more than 1,500,000 cells leads to a relatively constant length of the flame. Consequently, to minimize the computational time and optimize the number of cells with high accuracy, the mesh with 1,500,000 cells was selected to carry out all the cases of non-premixed simulations of CFS shaft kilns.
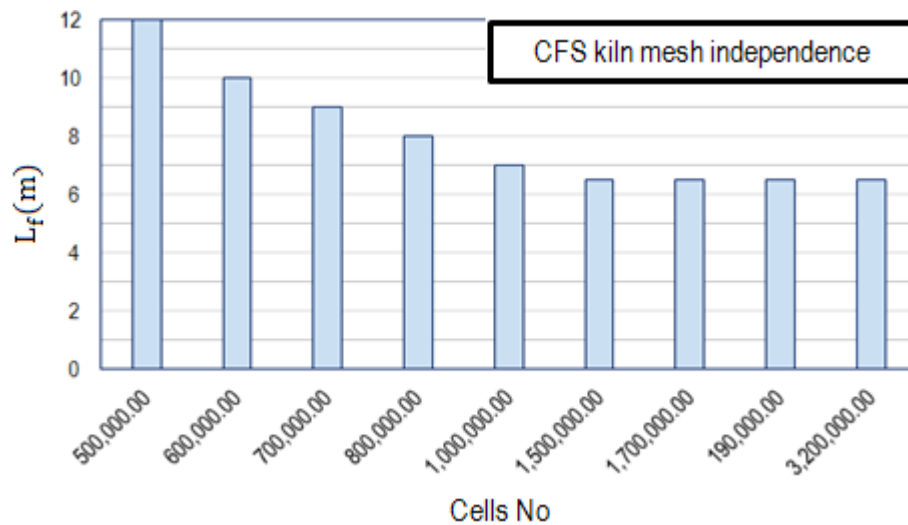
Figure 3.15: Mesh independence study for flame length.

As shown in Figure 3.16, the Y^+ is less than 5 in near-wall surfaces and all porous zones. Therefore, these histogram diagram and wall Y^+ values results a CFD simulation program code with less computational time and optimum number of mesh [45-46].
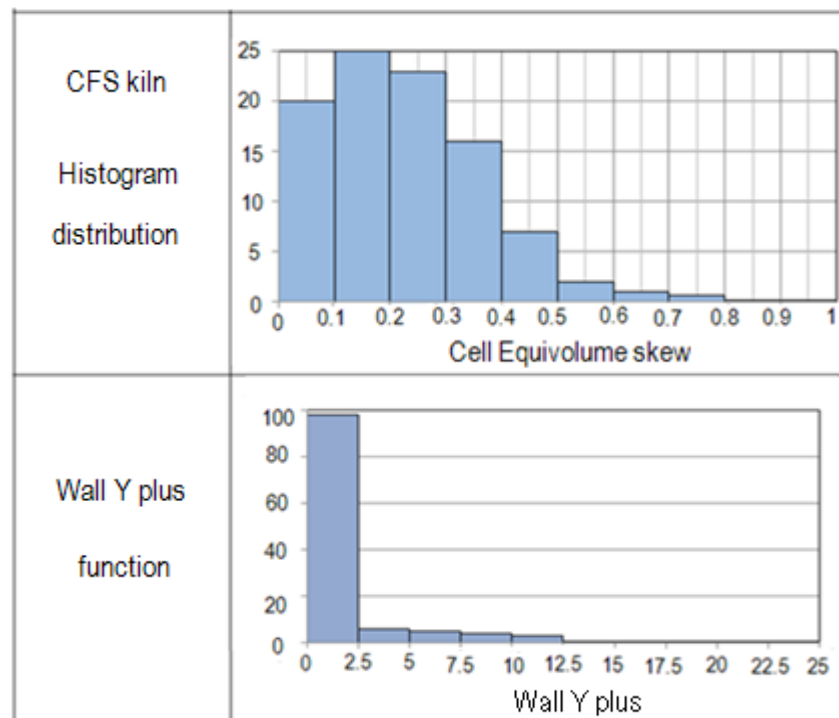
Figure 3.16: Histogram distribution and Y+ values for the wall region in CFS kiln.

3.3 Porous Media Model (P.M.M)

In recent decades, the porous media model has been widely used in numerous parts of the engineering industry and in the natural system for solving various problems including flows through packed beds. To use this model, it is necessary to define a cell zone in which PMM is applied. The pressure loss in the flow is determined by boundary conditions [38]. A porous medium is a body composed of a persistent solid part, solid matrix and the remaining void space that can be filled with one or more fluids. In a multiphase system, the void space is filled with two or more fluids that are immiscible with each other. They maintain a distinct boundary between them in order to derive mathematical methods for fluid flow in porous media.

3.3.1 Basic porosity

Porosity in packed bed defined to relations:

Particle porosity:

$$\phi_p = 1 - \frac{\rho_p}{\rho_s} \tag{3-20}$$

Bed porosity:

$$\phi = 1 - \frac{\rho_{bed}}{\rho_p} \tag{3-21}$$

$$\rho_{bed} = \ 1 - \phi \ . \ 1 - \phi_p \ . \rho_s \tag{3-22}$$

Where ϕ is bed porosity, ϕ_p is particle porosity, ρ_p is particle density ($\frac{kg}{m^3}$ total), ρ_s is solid density ($\frac{kg}{m^3}$), and ρ_{bed} is bed density ($\frac{kg}{m^3}$Total). ϕ and ϕ_p are variables that could be manipulated for quality [50-51].
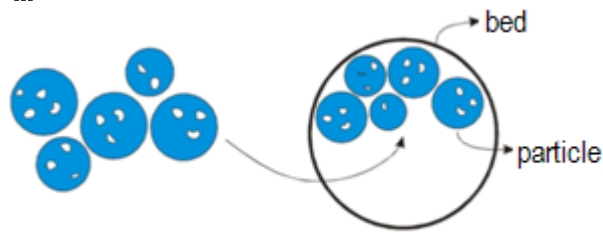
Figure 3.17: Packing of porous particles.

Compact structure   Hollow structure
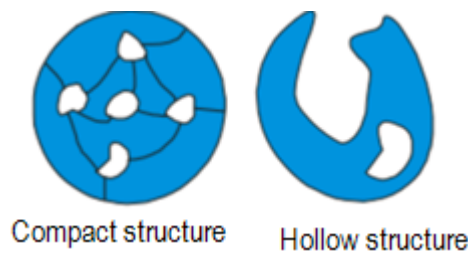
Figure 3.18: Categories of packing porous structures.

In the current research study, the particles are assumed to be homogeneous in diameter and particle porosity. The packed bed porosity (void fraction) is also calculated in following section as well.

3.3.2 Porosity

A packed bed is characterized by the void fraction ϕ which is defined as:

$$\phi = 1 - n.\frac{V_p}{V_{bed}}$$

(3-23)

The sphere particles arranged in a cylinder kiln. In the case of experiment measurement, the packed bed is cubic [47-48].

The porosity φ influenced by the following factors:

1.   The packing (random or regular, lose or dense);

2.   Particle shape (sphere, cylinder, etc.); and

3.   Particle size distribution

For infinitely extended, regular packing of equally-sized, large spheres, the porosity is:

ϕ=0.476 Simple Cubic Packing (S.C arrangement); and

ϕ=0.32 Cubic Space Centered Packing (B.C.C arrangement).

For random packing of equally-sized, large spheres, the void fraction is:

Loose packing ɸ=0.4-0.42; and

Dense packing ɸ =0.36-0.38

Two practical arrangements can be used in experiment packed bed is mentioned in Figure 3.19.
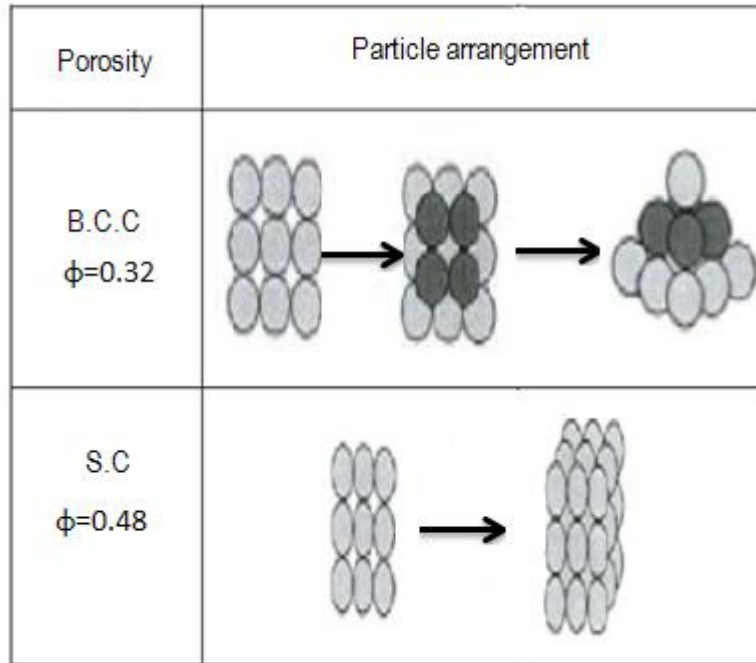
Figure 3.19: Schematic of B.C.C and S.C particle arrangements.

3.3.3 Porous media model applications

Due to difficulties of modeling the shaft kilns using a discrete particle model (DPM), therefore it is essential to adopt another approach. In this research study, a packed bed is modeled using a porous media model (PMM) to visualize a 3-D non-premixed flame model in a lime shaft kiln. In the Ansys Fluent porous media model, for the single-phase and multiphase, the porosity assumed to be isotropic. The pressure drop across the packed bed is calculated by a modified Ergun equation. In the next section, the governing equations of fluid flow through porous media will be introduced.

3.3.4 Governing equations

Porous media are modeled by adding a momentum source term to the standard fluid flow equations. The source term is composed of two parts: a viscous loss term (Darcy, the first term on the right-hand side of Eq. (3-24) and an inertial loss term (the second term on the right-hand side of Eq. (3-24) :

$$S_i = -(\sum_{j=1}^{3} D_{ij}\mu v_j + \sum_{j=1}^{3} C_{ij}\frac{1}{2}\rho \, v \, v_j \,) \qquad (3\text{-}24)$$

Where S_i is the source term for the i (x, y, and z) momentum equation v is the magnitude of the velocity and D and C are prescribed matrices. This momentum sink contributes to the pressure gradient in the porous cell, creating a pressure drop that is proportional to the fluid velocity (or velocity squared) in the cell. In the case of a simple homogeneous porous media (isotropic media), it could be written as:

$$S_i = -(\frac{\mu}{\alpha}v_i + C_2 \frac{1}{2}\rho \, v \, v_j)$$ (3-25)

Where, α is the permeability and C_2 is the inertial resistance factor, D and C are simply specified as diagonal matrices with $\frac{1}{\alpha}$ and C_2 respectively, on the diagonals (and zero for the other elements). Or, it is demonstrated by pressure drop per unit length:

$$\frac{\Delta P}{L} = - \ \frac{\mu}{\alpha}v_i + C_2 \frac{1}{2}\rho \, v \, v_i$$ (3-26)

To model a porous region without considering heat transfer, the main additional inputs for the problem setup are the definitions of the porous zone and specifications of the porosity of the porous medium, as well as the setup of the viscous resistance coefficient $\frac{1}{\alpha}$ and the inertial resistance coefficient C_2.

3.3.5 Darcy's law in porous media

In laminar flows through porous media at low Reynolds numbers, the pressure drop is proportional to the velocity and the constant C_2 can be considered to be zero, as shown in Eq. (3-25). By applying local averaging techniques or homogenization, it can be shown that under appropriate assumptions the momentum conservation of the Navier–Stokes equation reduces to the Darcy–Law (3-27) on the macroscopic level. Ignoring convective acceleration and diffusion, the PMM then reduces to Darcy's Law as below:

$$\nabla p = -\frac{\mu}{\kappa}q$$ (3-26)

$$u = -\frac{K}{\mu} \ \nabla p - \rho g \ .$$ (3-27)

Darcy's Law is valid for the slow flow of a Newtonian fluid through a porous medium with rigid solid matrix, where the inertial effects can be neglected.

P (x,t): fluid pressure in [Pa]=[N/m²]. This will be the unknown function to be determined by the flow model.

g: gravity vector pointing in the direction of gravity with size g (gravitational acceleration). Dimension is [m/s²]. When the z-coordinate points upward, we have g=9.81.

K(x): symmetric tensor of absolute permeability with dimension [m²]. It is only a parameter of the solid matrix and may depend on the position in case of a heterogeneous porous medium. Furthermore, K may be anisotropic if the porous medium has a preferred flow direction.

μ(x,t): Dynamic viscosity of the fluid given in [Pa.s]. In the applications considered here, μ is either constant or a function of pressure.

q: the volumetric fluid flow through the (homogeneous) medium.

In fact, Eq. (3-27) is calculated from empirical experiments on steady flow in a vertical homogeneous sand filter. The pressure drop is computed mathematically in each of the three (x, y, z) coordinates within the porous region:

$$\nabla p_x = \sum_{j=1}^{3} \frac{\mu}{\alpha_{xj}} v_j \Delta n_x \tag{3-28}$$

$$\nabla p_y = \sum_{j=1}^{3} \frac{\mu}{\alpha_{yj}} v_j \Delta n_y \tag{3-29}$$

$$\nabla p_z = \sum_{j=1}^{3} \frac{\mu}{\alpha_{zj}} v_j \Delta n_z . \tag{3-30}$$

Where $\frac{1}{\alpha_{ij}}$ are the entries in the matrix D in Eq. (3-23), V_j is the velocity components in the x, y, and z directions, and Δn_x, Δn_y and Δn_z are the thicknesses of the medium in the x, y, z directions.

3.3.6 Inertial losses in porous media

With the increase in the flow velocity, the constant C_2 in Eq. (3-25) is a new correcting factor for inertial losses in the porous medium. This could be served as a loss coefficient per unit length along the flow direction. Thus, it is wise to allow the pressure drop to be specified as a function of dynamic head, yielding the following simplified form of the porous media equation:

$$\nabla p = - \sum_{j=1}^{3} C_{2ij} \frac{1}{2} \rho \, v \, v_j \tag{3-31}$$

or in the coordinate form:

$$\nabla p_x \approx \sum_{j=1}^{3} C_{2xj} \Delta n_x \frac{1}{2} \rho \, v \, v_j \tag{3-32}$$

$$\nabla p_y \approx \sum_{j=1}^{3} C_{2yj} \Delta n_y \frac{1}{2} \rho \, v \, v_j \tag{3-33}$$

$$\nabla p_z \approx \sum_{j=1}^{3} C_{2zj} \Delta n_z \frac{1}{2} \rho \; v \; v_j \, .$$ (3-34)

3.3.7 Using ergun equation for a packed bed

Considering the modeling of a packed bed, the appropriate constants can be derived by the Ergun equation, from which a semi-empirical correlation is applicable to many kinds of packing structures [27-28]:

$$\frac{\Delta P}{L} = 150 \cdot \frac{(1-\phi)^2}{\phi^3} \cdot \frac{\mu \cdot U}{d_p^2} + 1.75 \cdot \frac{1-\phi}{\phi^3} \cdot \frac{\rho \cdot U^2}{d_p} \, .$$ (3-35)

Where d_p is the mean diameter of the particle. Comparing equations 3-25 and 3-35, the permeability and inertial loss coefficient in each component direction can be identified as [38]:

$$\alpha = \frac{d_p^2 \, \varphi^3}{150 \, (1-\varphi)^2} \, ,$$ (3-36)

$$C_2 = \frac{3.5 \, (1-\phi)}{d_p \varphi^3} \, .$$ (3-37)

As can be seen in Eq (3-36) and (3-37), both coefficients are determined by geometry parameters. Moreover, in Fluent, the viscous resistance is illustrated as $\left(\frac{1}{\alpha}\right)$, and it is quite necessary to notice this change [32-33]. The calculation of different porosities for the particle diameter d_p= 100 mm and 52 mm are presented in Table 3-5 and Table 3-6. Also the calculation of different particle diameters when the porosity is constant presented in Table 3.6.

Table 3.5: Calculations of viscous and inertial resistance for various porosities when $d_p = 100$mm.

ϕ	0.32	0.395	0.476	0.6	0.7	0.8	0.99
$\frac{1}{\alpha}\left(\frac{1}{m^2}\right)$	211670	89087	38189	11111	3936	1172	1.5
$C_2\left(\frac{1}{m}\right)$	726.3	344	170.1	64.8	30.6	13.7	0.4

Table 3.6: Calculations of viscous and inertial resistance for various porosities when $d_p = 52$mm.

ϕ	0.32	0.48	0.6	0.8
$\frac{1}{\alpha}\left(\frac{1}{m^2}\right)$	7828443	135652	41091	4333
$C_2\left(\frac{1}{m}\right)$	1400	316	124	26

Table 3.7: Calculations of viscous and inertial resistance for various particle sizes when φ=0.4.

d_p (mm) ϕ=0.4	15	25	55	85	100	155
$\frac{1}{\alpha}\left(\frac{1}{m^2}\right)$	3750000	1350000	278925	116782	84375	35120
$C_2\left(\frac{1}{m}\right)$	2187	1312	597	386	328	212

3.4 Aspect Ratio

The primary dimensionless property used to characterize a packed bed is the ratio between the container diameter (D) and the equivalent diameter (d_p) of the particle. This is referred to as the aspect ratio given below [22]:

$$A_{ratio} = \frac{D}{d_p}.$$

(3-38)

Packed beds are categorized as either being low or high ratio. A tube of sand would be considered as high aspect ratio, a tube of snooker balls would be considered low aspect ratio (Figure 3.20).
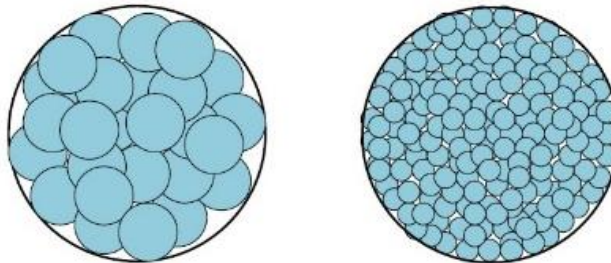
Figure 3.20: Left, low aspect ratio bed. Right, high aspect ratio bed.

However, an aspect ratio of 50 is often suggested as a reasonable value to distinguish between a low and high aspect ratio bed. In a shaft kiln the ratio can be between 60 to 80, which is significantly high [22]. Table 3.7 shows the range of aspect ratio for kilns and experiment packed bed.

Table3. 7: Calculation of aspect ratio for different types of packed beds.

CFS and PFR shaft kilns	$D=2m$ $d_p = 20-150mm$	$A_{ratio} = 13-100$
Experiment packed bed	$L=0.6m$ $d_p = 52mm$	$A_{ratio} \approx 12$

3.5 Flow Regimes and Reynolds Number:

A.Dybbs and R.V.Edwards have experimentally obtained the characteristics of turbulent flow through a porous media using laser anemometry and flow visualization techniques, and found the linear relationship between the pressure drop and flow rate. As the Re_p increases, the "core" flows enlarge in size and their influence becomes more and more significant to the overall flow picture. This steady non-linear laminar flow regime persists up to Re_p ~150. The third flow regime detected is an unsteady laminar flow field in the Reynolds number ranges of 150 to 300. At Re_p ~ 250, the first evidence of unsteady flow is observed in the form of laminar wake oscillations in the pores. These oscillations take the form of travelling waves characterized by distinct periods, amplitudes and growth rates. In this flow regime, these oscillations exhibit preferred frequencies that seem to correspond to growth rates. Vortices are formed at Re_p ~ 250 and persist up to Re_p ~300.

Finally, a highly unsteady and chaotic flow regime, which occurs for Re_p >300 and qualitatively resembles turbulent flow, is categorized as a fourth flow regime based on flow visualization techniques [38]. Design of packing materials to achieve uniform distribution of the fluid across the cross-section throughout the column is an important subject as well. Here, the calculation of the Reynolds number and the pressure drop issue is discussed as well. The Ergun equation that is commonly employed is given below:

$$f_p = \frac{150}{Re_p} + 1.75 \tag{3-39}$$

Here, the friction factor f_p for the packed bed, and the Reynolds number Re_p , are defined as follow [42-43].

$$f_p = \frac{\Delta p}{L} \cdot \frac{d_p}{\rho V^2} \cdot \frac{\phi^3}{(1-\phi)} \quad , \qquad\qquad Re_p = \frac{d_p}{1-\varphi \cdot \mu} U \cdot \rho \tag{3-40}$$

The various symbols appearing in the above equations are defined as follows:

Δp: Pressure drop, L: Length of the bed, d_p Equivalent spherical diameter, ρ: Density of the fluid

μ: Dynamic viscosity of the fluid, U: Superficial velocity, ϕ: porosity of the packed bed

Two simpler results, each obtained by ignoring either of the two terms in the Ergun equation also are in use. One is the Kozeny-Carmen equation, used for flow under very viscous conditions

$$f_p = \frac{150}{Re_p} \qquad\qquad \text{When} \qquad\qquad Re_p < 1 \qquad\qquad (3.41)$$

The other is the Burke-Plummer equation, used when viscous effects are not as important as inertia.

$$f_p = 1.75 \qquad\qquad \text{When} \qquad Re_p > 1000 \qquad\qquad (3.42)$$

Table 3.18 shows calculation of Reynolds number for air main flow.

Table 3.18: Calculation of the Reynolds number and pressure drop.

$U = 0.3\frac{m}{s}$ $T_{air} = 30\dot{c}$ $\rho = 1.164\frac{Kg}{m^3}$ $\mu = 1.8680 * 10^{-5}\frac{Kg}{m.\,s}$	Reynolds number
$\phi = 0.32$	$Re_p = 2741$
$\phi = 0.4$	$Re_p = 3107$
$\phi = 0.48$	$Re_p = 3586$

Composition of Combustion Gas

In this work, methane is used as fuel to provide the heat for calcinations. The methane is injected through fuel burners in to the burning shaft. The gas combustion is described in the model with a standard two-step methane/air combustion model. The combustion gas contains CO_2 and H_2O, and ,from the air, O_2 and N_2. These first four components can be calculated from the molecular balances. The unburnt components CO and H_2 are the second step of the combustion of methane[49].

$$CH4 + \frac{3}{2}O_2 \rightarrow CO + 2H_2O , \qquad CO + \frac{1}{2}.O_2 \rightarrow CO_2 . \qquad\qquad (3\text{-}43)$$
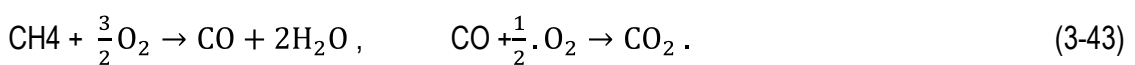
4.1 Experimental Set up

4.1.1 Packed bed

Experimental measurements were done to validate the CFD simulation. A box with the dimensions of 600 mm in length, 364 mm in width and 600 mm in height was used as a shaft. Ceramic spheres with a diameter of 52 mm were filled in as a packed bed. Two different gases were injected into the packed bed. Nitrogen coming from bundles was injected into the packed bed using a nozzle. The nitrogen nozzle has a diameter of 20 mm and 104mm depth through the bed. In the case of parallel flow, the nitrogen was injected from the bottom; in the case of radial cross flow, the nitrogen was injected from the side, as shown in Figure 4.1.
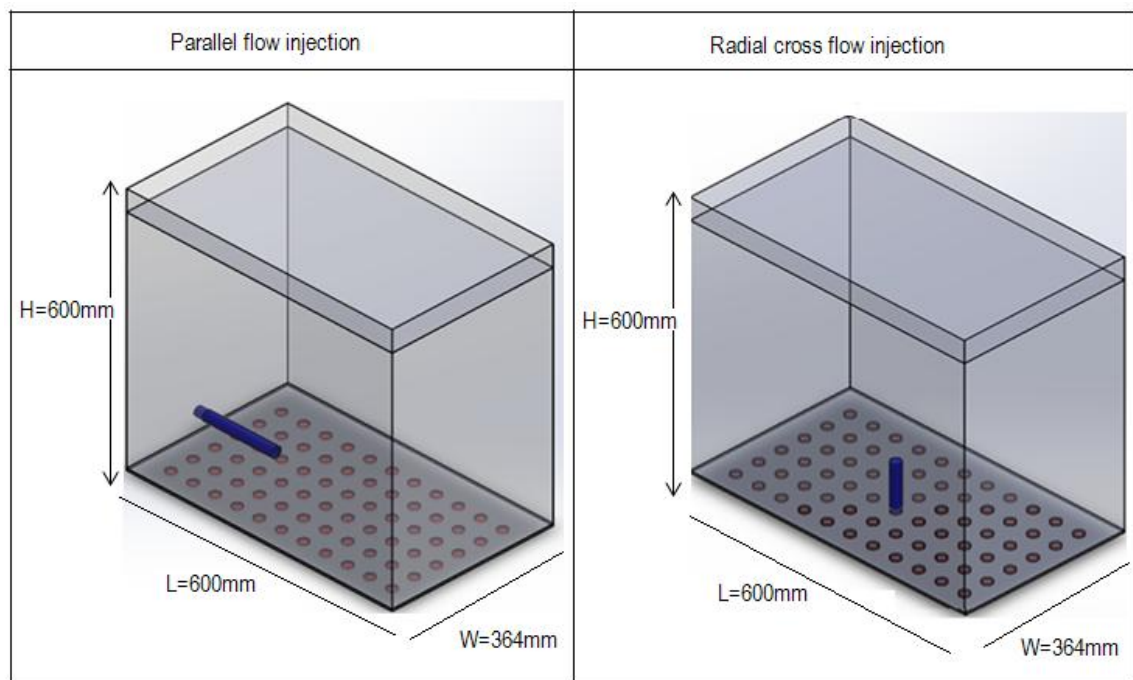
Figure 4.1: Dimensions and positions of injections.

Air was injected from a blower into the packed bed from the bottom through a perforated plate with 66 holes. The diameter of the air holes was 20 mm. This perforated plate cause even distribution of air in the packed bed. The schematic of the experimental setup shows in Figure 4.2.
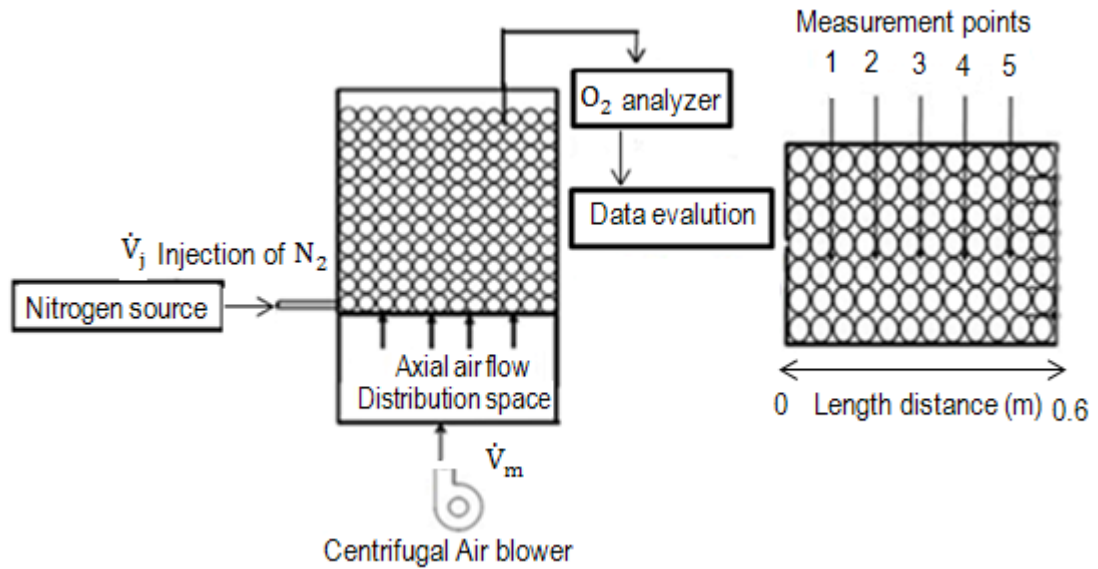
Figure 4.2: Schematic description of the experimental setup [19].

The experiment measurement was performed for two volumetric ratios ($\frac{V_j}{V_m}$ = 0.1, 0.6). The measurements were done at a distance of 104 mm, 208, 312, 416, and 524 mm from the wall, which is named the length distance (5 points). The nitrogen flow rate was fixed at $V_j = 25 \frac{m^3}{h}$ for all the cases. The pressure was adjusted by a ball valve, and the air volumetric flow rate was measured by using a flow meter. Firstly, the airflow rate was adjusted by the valve and was fixed at V_m=250 $\frac{m^3}{h}$ ($\frac{V_j}{V_m} = 0.1$). When the exact flow rate of air and nitrogen was supplied, the mole fraction of O2 was measured with the help of a gas analyzer with an accuracy of ±0.2 and a response time of 45 seconds (Figure 4.3). In the second measurement, the flow rate of air was changed to 40$\frac{m^3}{h}$, while the flow rate of nitrogen was kept at the same volume flow rate of 25 $\frac{m^3}{h}$ ($\frac{V_j}{V_m} = 0.6$).

Figure 4.3: Conducting experimental packed bed measurement.

4.1.2 Particle arrangement

The Simple Cubic (S.C) arrangement (Hexa-based) is formed by eight spheres with the centers at the apexes of the cube, as shown in Figure 4.4. This arrangement has a simple structure and can be easily created. Four particles are always in contact with each other in the first and second layers, and a channel-like space is formed, which can lead to a non-representative flow pattern [15]. The porosity of this arrangement is about $\varphi=0.48$. The Body-Centered Cubic (B.C.C) arrangement (Octa-based) included six spheres with the centers at the apexes of an octahedron. The porosity of the B.C.C arrangement is about $\varphi=0.32$. The Two particle arrangements in the packed bed show in Figure 4.4.

Porosity	Particles arrangement	Particles schematic
B.C.C $\phi=0.32$		
S.C $\phi=0.48$		

Figure 4.4 : S.C and B.C.C arrangments of particles.

In BCC, the particles were arranged according to a specific arrangement. In the first layer, 12x7=84 particles were arranged, and in the second layer, particles were placed within the gaps

of the first layer so that the second layer would consist of 11x6=66 particles. They were filled up to a specific height following the same pattern so that 984 particles were adjusted. In SC arrangement, again, 12x7=84 particles were placed in the first layer, but in the second layer, they were placed exactly above each other, so there would be again 12x7=84 particles in all other rows. The packed bed included 924 particles filled according to the SC arrangement. In the SC arrangement, the experimental measurements were repeated for the two volumetric flow rates, the same as what was done in case of BCC arrangement. In BCC arrangement, the air was injected from 65 holes with a diameter of 20 mm. Nitrogen was fixed in the center of the packed bed. While there were 66 holes for air injections in the SC arrangement. In the BCC arrangement, the nitrogen nozzle was fixed at 286 mm away from the wall and was not located in the center of the packed bed [50-53].

4.1.3 Injection velocity

The nitrogen velocity u_j was calculated with Eq 4-1, Where d is the diameter of nozzle.

$$V_J = \frac{\pi \cdot d^2}{4} u_j \tag{4-1}$$

The air velocity u_m was calculated with Eq 4-2, where D is the diameter of the holes in the perforated plate and n is the number of the holes.

$$V_m = n. \frac{\pi \cdot D^2}{4} u_m \tag{4-2}$$

The velocity of injections for the two volumetric ratios of 0.1 and 0.6 are shown in Table 4.1. It can be seen the velocity of nitrogen is much higher than the velocity of air [54-55].

Table 4.1: Calculation of volumetric ratios and velocities.

$\dfrac{\dot{V}_j}{\dot{V}_m}$	0.1	0.6
Nitrogen velocity $u_j\left(\frac{m}{s}\right)$	22.1	22.1
Air velocity(B.C.C) $u_m\left(\frac{m}{s}\right)$	3.38	0.54
Air velocity(S.C) $u_m\left(\frac{m}{s}\right)$	3.34	0.53

4.2 Validation of Parallel Flow Injection

4.2.1 Estimating the turbulence intensity

As setting boundary conditions for a CFD simulation is necessary to estimate the turbulence intensity on the inlets. To do this accurately, here are a few examples of common estimations of the incoming turbulence intensity.

1. **High-Turbulence case:**

High-speed inside complex geometries like heat-exchangers and flow inside rotating machinery (turbines and compressors). Typically, the turbulence intensity is between T.I=5%-20%.

2. **Medium-Turbulence case:**

Flow in not-so-complex devices like large pipes, ventilation flow, etc., or low-speed flows (low Reynolds number). Typically, the turbulence intensity is between T.I=1%-5%.

3. **Low-Turbulence case:**

Flows originating from a fluid that stands still, like external flow across cars, submarines and aircrafts. Very high-quality wind-tunnels can also reach really low turbulence levels. Typically, the turbulence intensity is very low, well below T.I=1%. The turbulence intensity for fully developed pipe flow is estimated using Eq 4-3:

$$I = 0.16 \mathrm{Re}_{\mathrm{Dh}}^{\frac{-1}{8}}.$$
(4-3)

Where Re is the Reynolds number based on the hydraulic pipe diameter D_h . The turbulence intensity is chosen based on the experimental results because two gases injected into the packed-bed. The CFD simulation will reply to two main questions:

1. Which turbulence models show reasonable matching with experiment results (k-ε Standard-ω, etc.) and

2. Which turbulence intensity at the inlets gives results closer to experimental results.

The mixing of two gases in a packed bed causes a high turbulence case. The flow changes the direction by 90 degrees during the overflow of every particle. The range of turbulence intensity is between 5% and 20%. This led to high turbulence intensity [38], [56-58].

4.2.2 Body center cubic (BCC) arrangement

The CFD simulation using PMM model was applied for the two volume ratios ($\frac{V_j}{V_m} = 0.1, 0.6$) and various porosities (ϕ=0.32-0.8). The oxygen contours of various porosities and volumetric ratio of injections are shown in Figure 4.5. The packed bed is arranged in from of B.C.C. The higher the porosity is, the higher the velocity becomes.
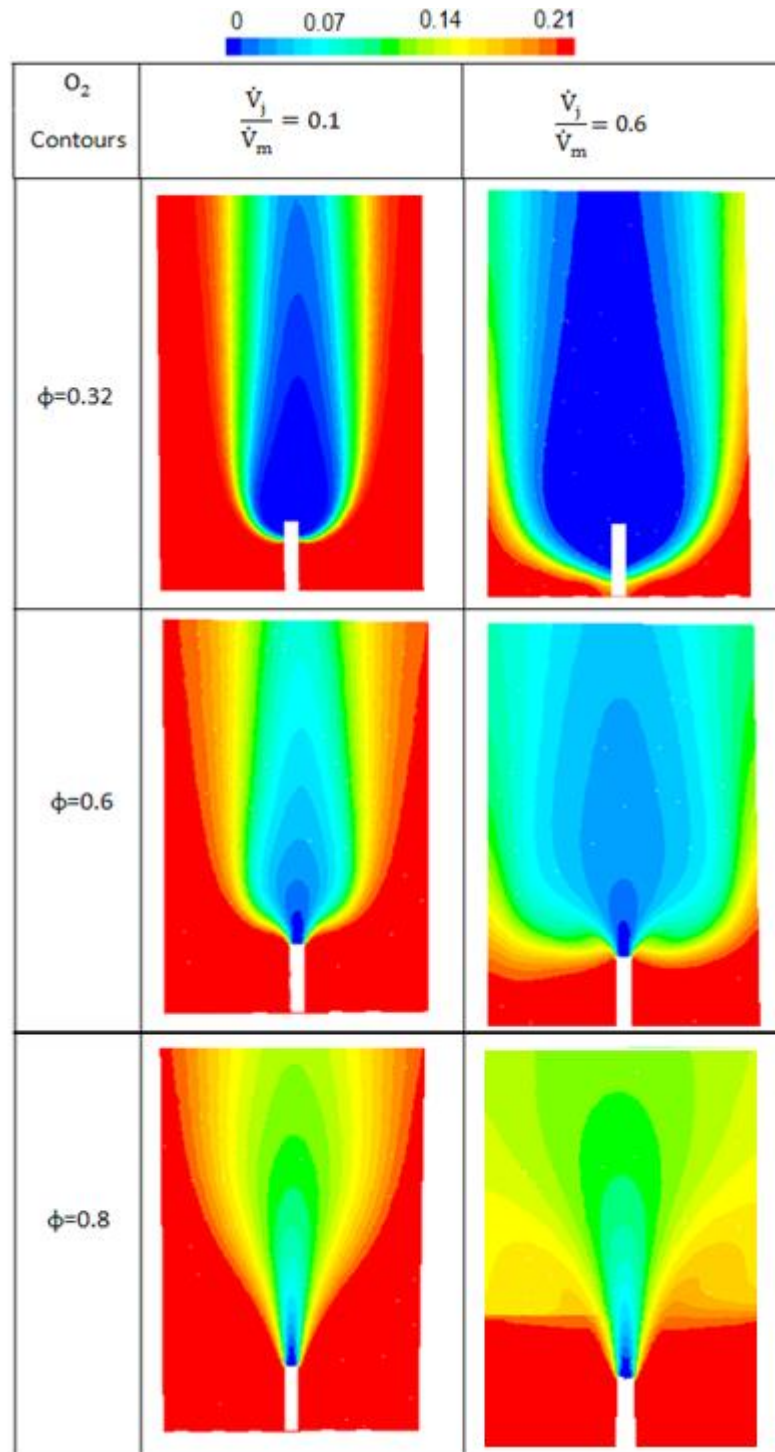
Figure 4.5: Oxygen contours in radial and axial directions (parallel flow injection).

Theoretically, the porosity is calculated to be φ=0.32 when the arrangement is in the form of B.C.C. The test was conducted at five different points. The minimum amount of oxygen concentration was always found to be a 0.3-meter distance from the wall (length distance). The nitrogen nozzle was located at z=0.3m (center of packed bed). Figure 4.6 shows the simulation done for various porosities and the results compared with the measurements. The simulation of porosity φ=0.32 showed better agreement with the experimental values. In this case, the k-ε standard model with TI=5% was applied.
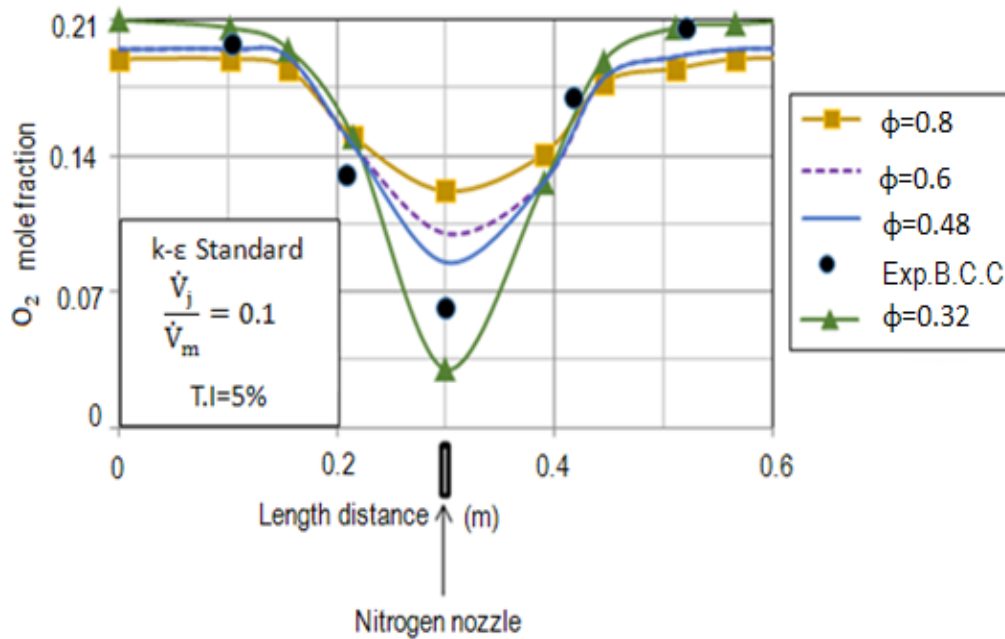
Figure 4.6: Oxygen profile in the case of a low volumetric ratio (B.C.C arrangement).

In the second step, different types of turbulence models were employed when the porosity is φ=0.32. As can be seen from Figure 4.7, the k-ε standard turbulence model shows the best accuracy for B.C.C arrangement.

In section 4.2.1, the higher TI case was chosen for the simulations. The reason is that the packed bed was completely filled with particles, and the two gases were injected close to the particles. Therefore, in order to estimate the exact value of TI, the CFD program was simulated for the TI in the range of 5-20 %. In Figure 4.8 the TI of 7.8% shows more accuracy with the validation results.
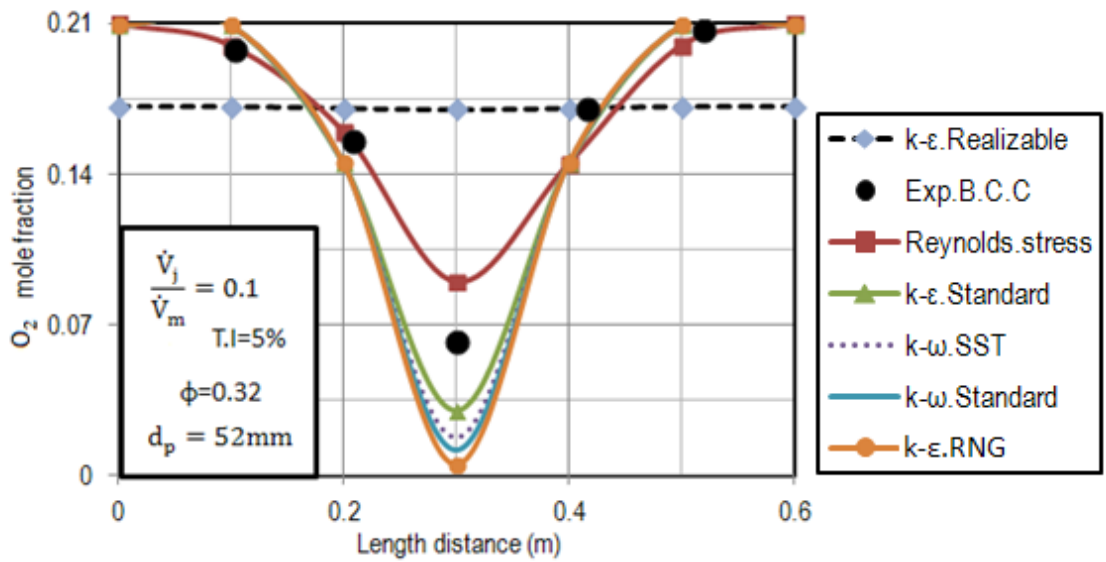
Figure 4.7: Oxygen profile for comparison for different turbulence models and validation (B.C.C arrangement) for the lower volumetric ratio when d_p=52 mm.
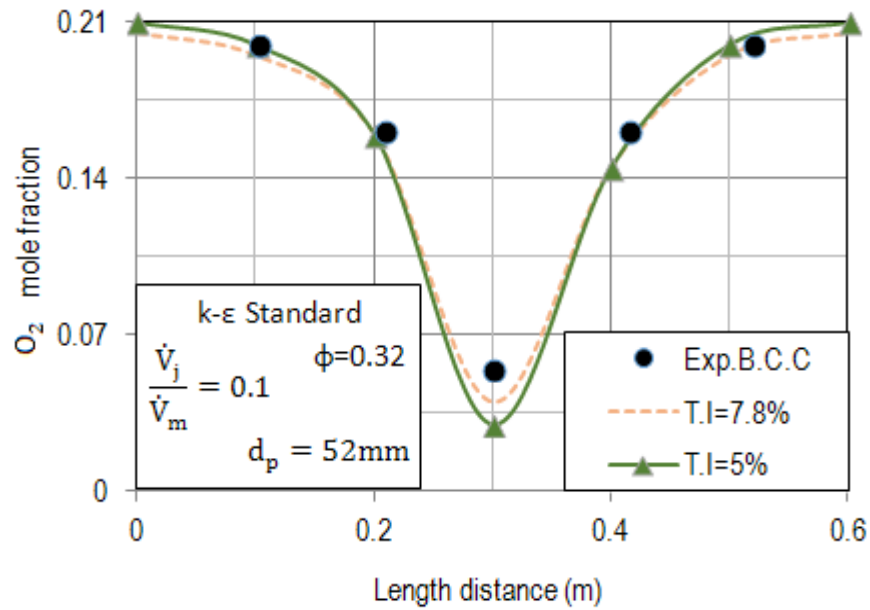
Figure 4.8: Influence of different turbulent intensities and validation (B.C.C arrangement).

Next, the experimental measurements and simulations were repeated for the higher volumetric ratio of 0.6. As shown in Figure 4.9, the results were independent on the volumetric rates and matched with the same porosity, the same turbulence model, and turbulence intensity.
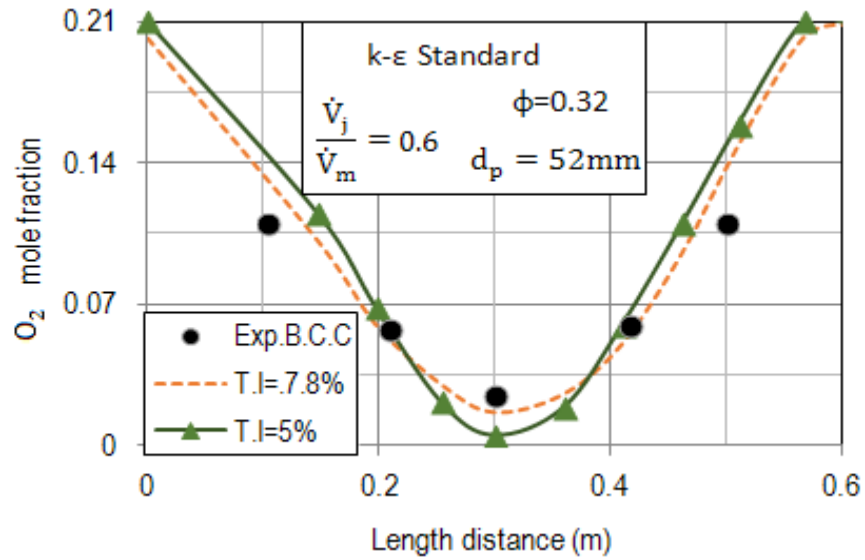
Figure 4.9: Oxygen profile in case of high volumetric ratio (B.C.C arrangement).

4.2.3 Simple cubic (SC) arrangement

The porosity ϕ=0.48 was calculated for SC arrangement. The distribution of O2 mole fraction for the volume ratio is 0.1 shows in Figure 4.10. In this case, the results of the turbulence model with a TI of 12% show better agreement when compared with experimental results. This was obtained through several simulations conducted for different turbulence models and different turbulence intensities (at about 60 other simulations by trial and error on the turbulence model and percentage of turbulence intensity). The reason is that the nitrogen nozzle in SC arrangement was not located in the center of the packed bed. Also, it is surrounded by four air injection holes at various distances from each other and the wall. Therefore, it causes more turbulence distribution between air and nitrogen on mixing points. To this end, the turbulence intensity (TI) increases up to 12%. Also, Figure 4.10 shows that the k-ε standard model does not match the experimental validation results for the SC arrangement (ϕ=0.48)
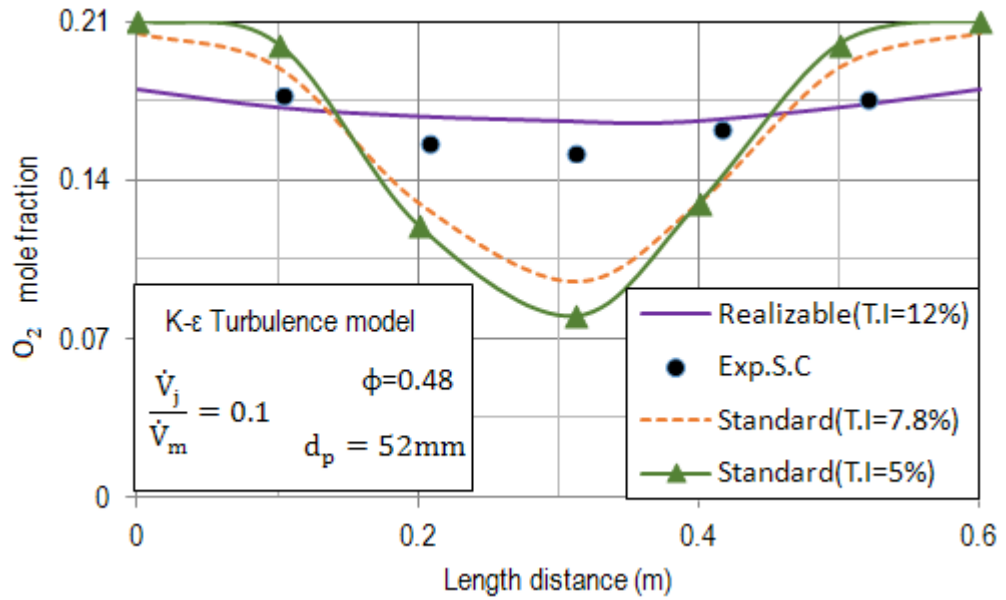
Figure 4.10: Oxygen profile in the case of low volumetric ratio (S.C arrangement).

The same experimental measurements and simulations were repeated for the high volumetric ratio of 0.6. The volumetric rate was increased from 0.1 to 0.6. The PMM was applied for various turbulence models and turbulence intensities. As shown in Figure 4.11, there is no influence on turbulence models when the volumetric ratio six times increased. The k-ε realizable with T.I=12% showed a better agreement with the experimental measurements.
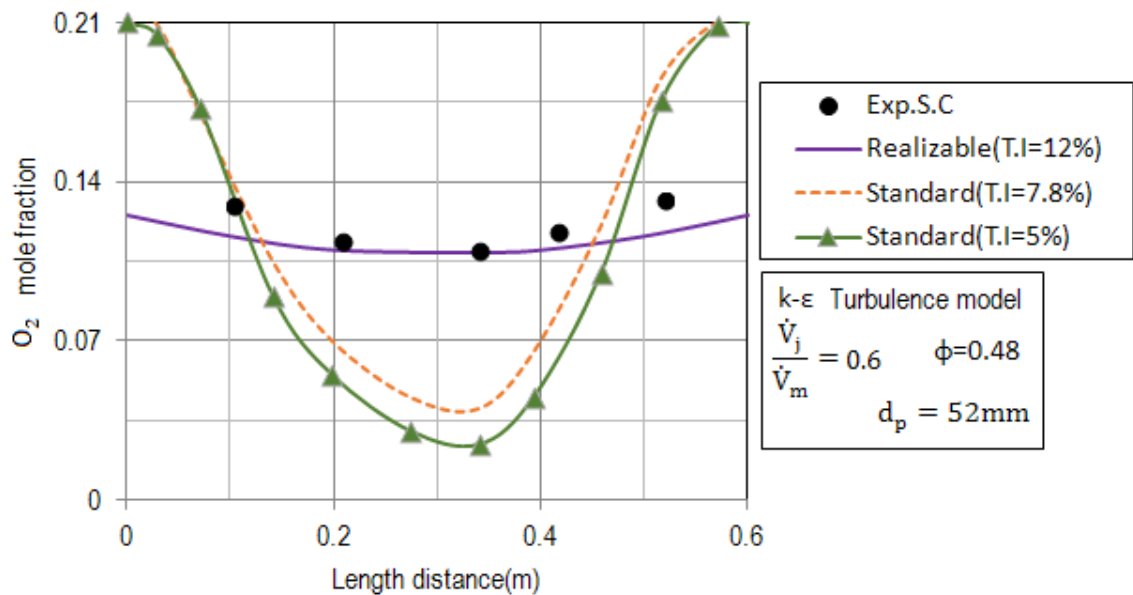
Figure 4.11: Oxygen profile in the case of a high volumetric ratio (S.C arrangement).

4.2.4 Influence of particle diameter

To check the particle diameter has influence, glass beads were used to form an unstructured packed bed where the particle diameter was approximately 4 mm. The CFD simulations were performed for a porosity of φ=0.4, which is typical for a packed bed of spheres with uniform size. Figure 4.12 show that the result of the k-ε standard model with a TI of 5% has more proximity to the experimental measurements for an unstructured packed bed.
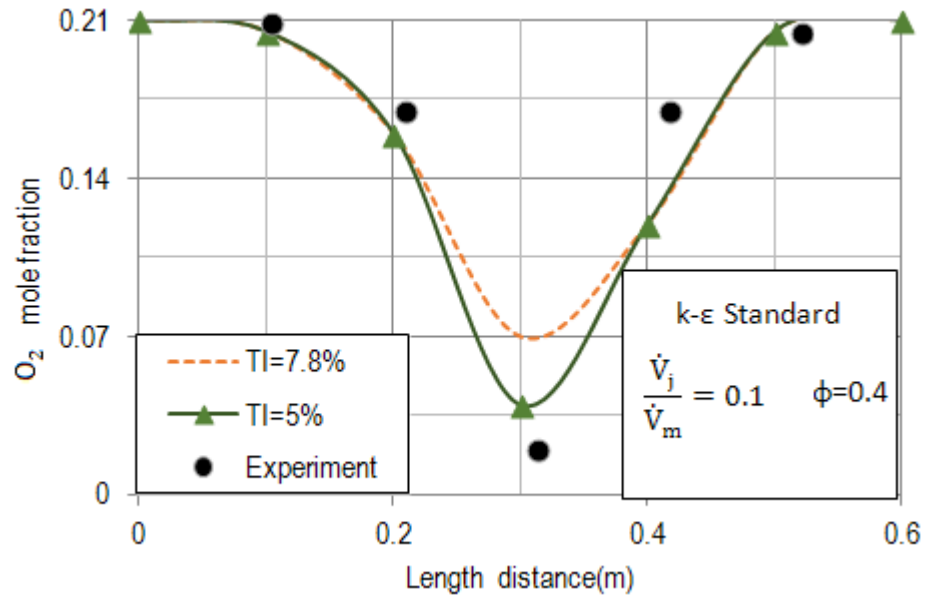
Figure 4.12: Validation of simulation results (unstructured packed bed).

4.3 Validation of Radial Cross Flow Injection

Here, the radial cross-flow injection in the packed bed is studied. The nitrogen nozzle is fixed on the wall in a radial direction.

4.3.1 Body center cubic (BCC) arrangement

The contours of oxygen for various porosities are as shown in Figure 4.15. The packed bed was arranged in the form of B.C.C. The nitrogen was injected radially through the packed bed. The jet immediately is diverted into the vertical direction. The nitrogen nozzle has always a diameter of 20 mm and 104mm depth through the bed. The higher the porosity is, the faster the velocity is, and the more the jet penetrates the packed bed.
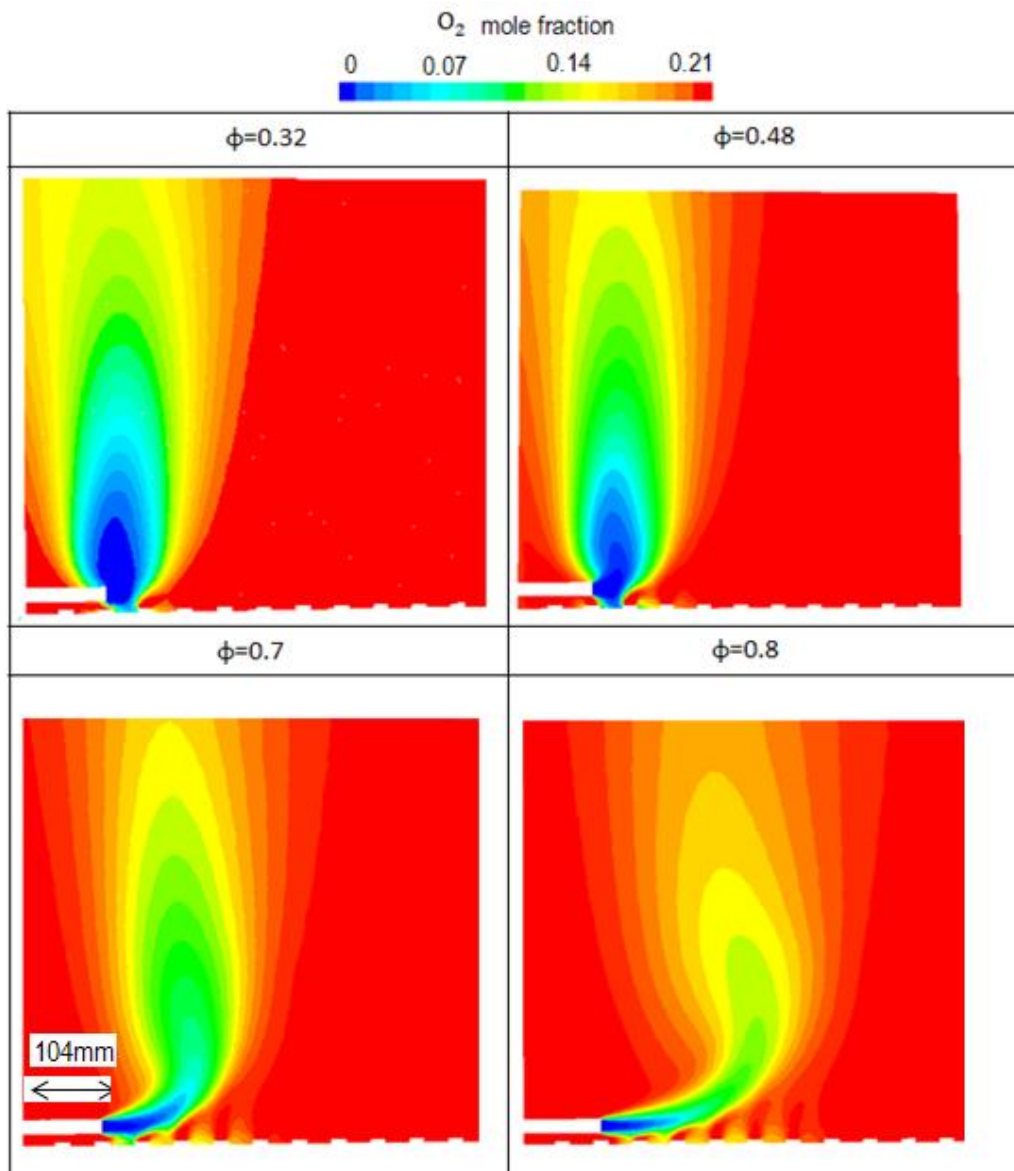
Figure 4.15: Oxygen contours of radial cross flow mixing.

Figure 4.16 shows the comparison between different porosities and experiment results. Theoretically, the porosity was calculated to be ɸ=0.32 when the arrangement is in the form of B.C.C. The results of the porosity of ɸ=0.32 show more accuracy with experiment results. In this case, the k-ε standard model with 5% turbulence intensity was applied.
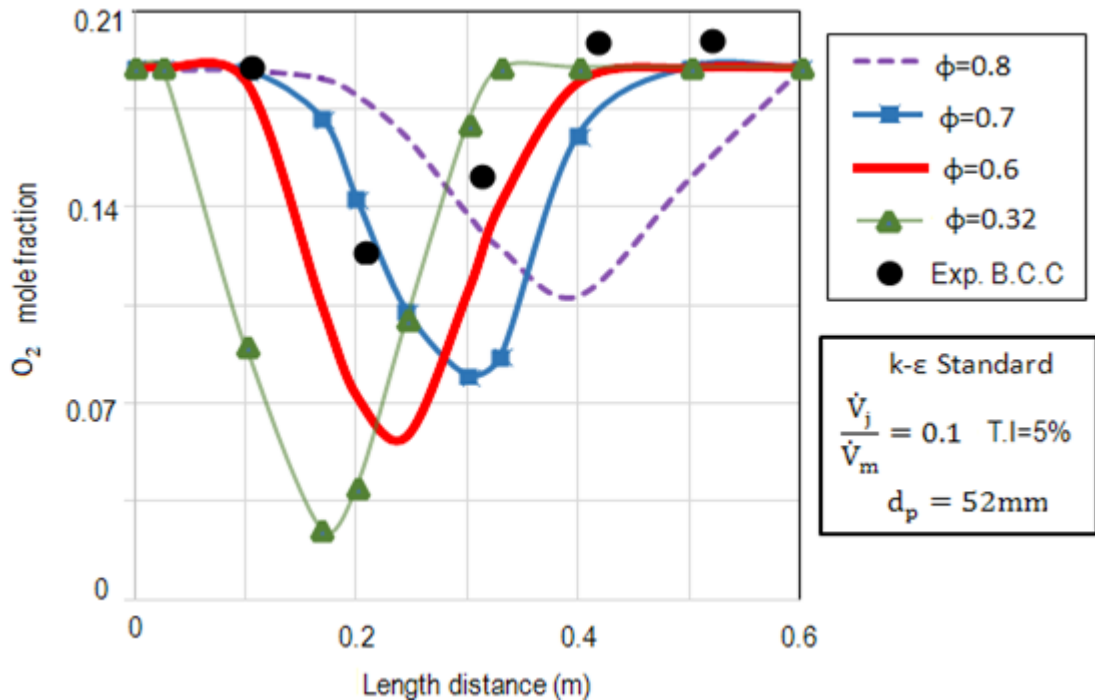
Figure 4.16: Comparison for different porosities and experimental results.

In Figure 4.17(a), different types of turbulence models were simulated at a porosity of ɸ=0.32. The PMM does not match with the experimental measurements when TI= 5%. However, the k-ω SST has more proximity to the experimental results in the case of a BCC arrangement. Figure 4.17 (b) shows that the k-ω SST with a T.I= 20% in more accuracy with the experiment results.
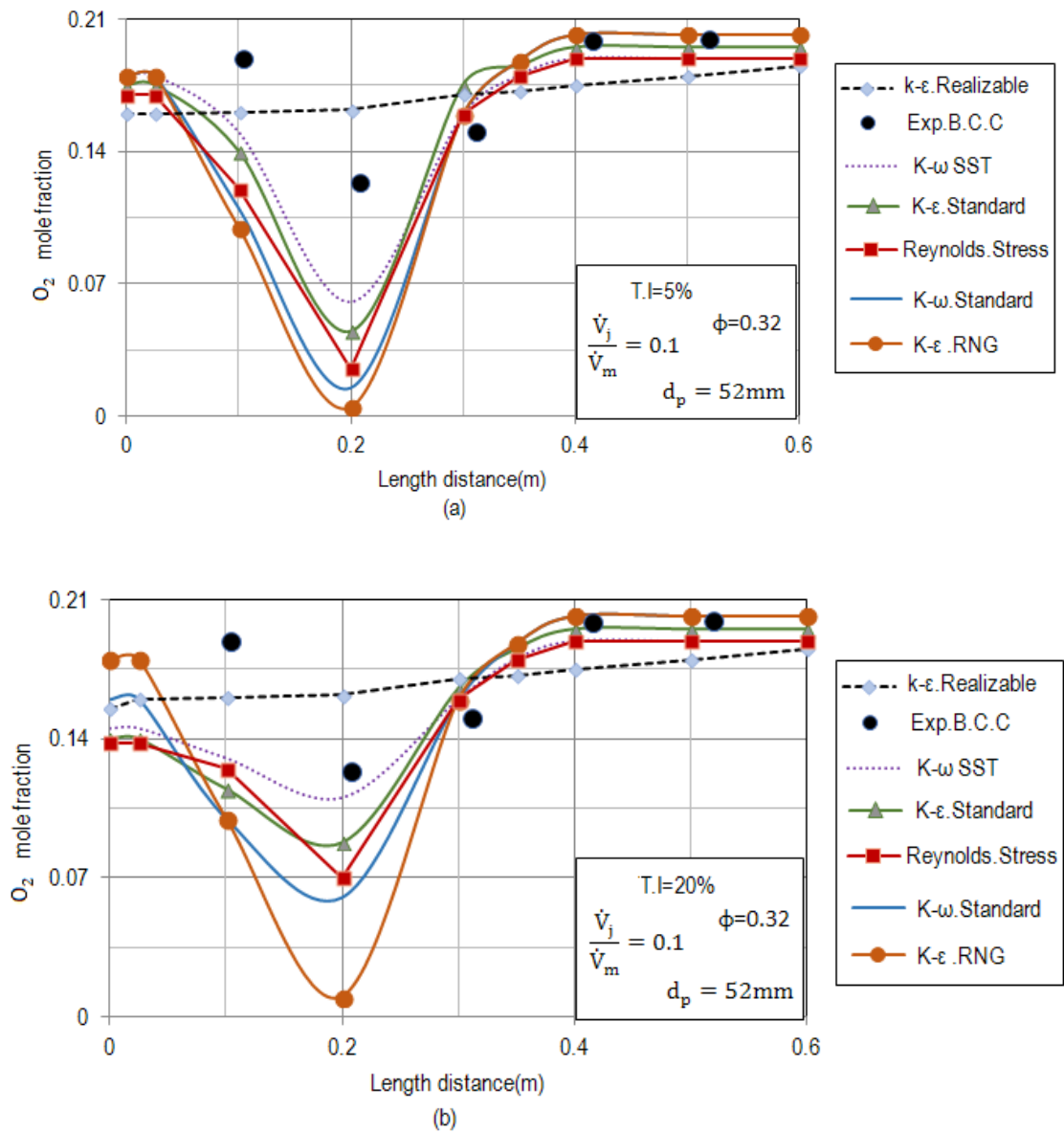
Figure 4.17: Comparison for different turbulence models and validation (B.C.C arrangement) for lower volumetric ratio when d_p=52 mm.

Figure 4.18 shows the maximum percentage of turbulence intensity in more accuracy with the experiment results.
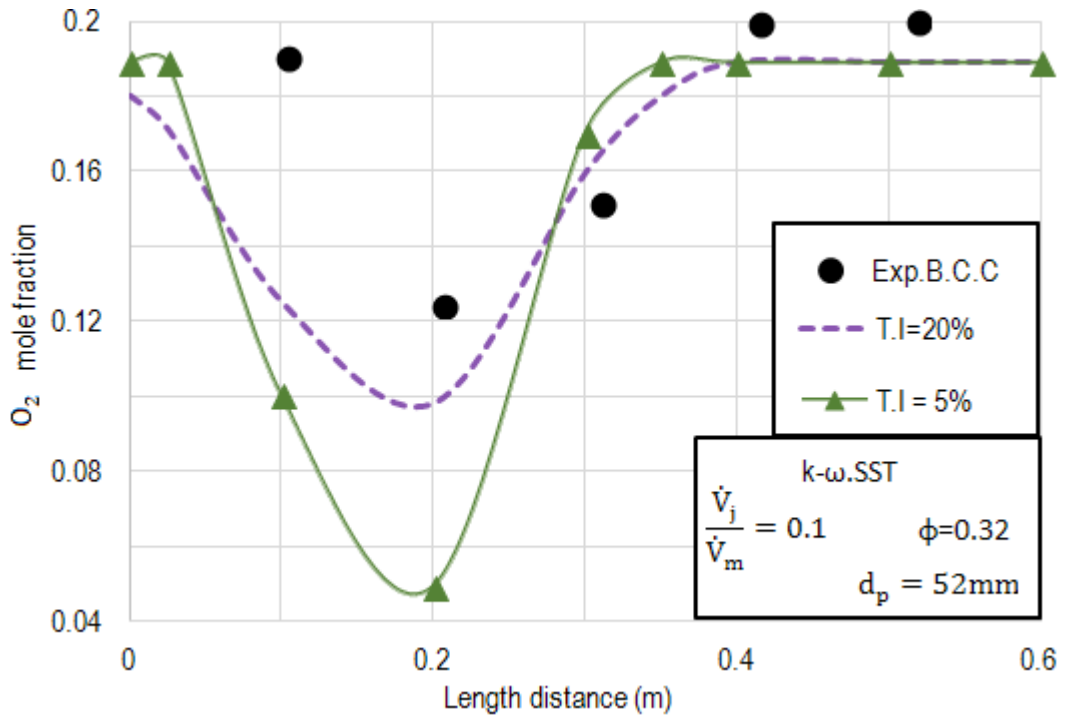
Figure 4.18: Influence of different turbulent intensities and validation (B.C.C arrangement).

The experimental measurements and simulations were now repeated for the high volumetric ratio of 0.6 once more. Figure 4.19 shows that the same turbulence model and the same turbulence intensity were used for the simulations. Therefore, the results are independent of increasing the volumetric ratio from a value of 0.1 to 0.6.
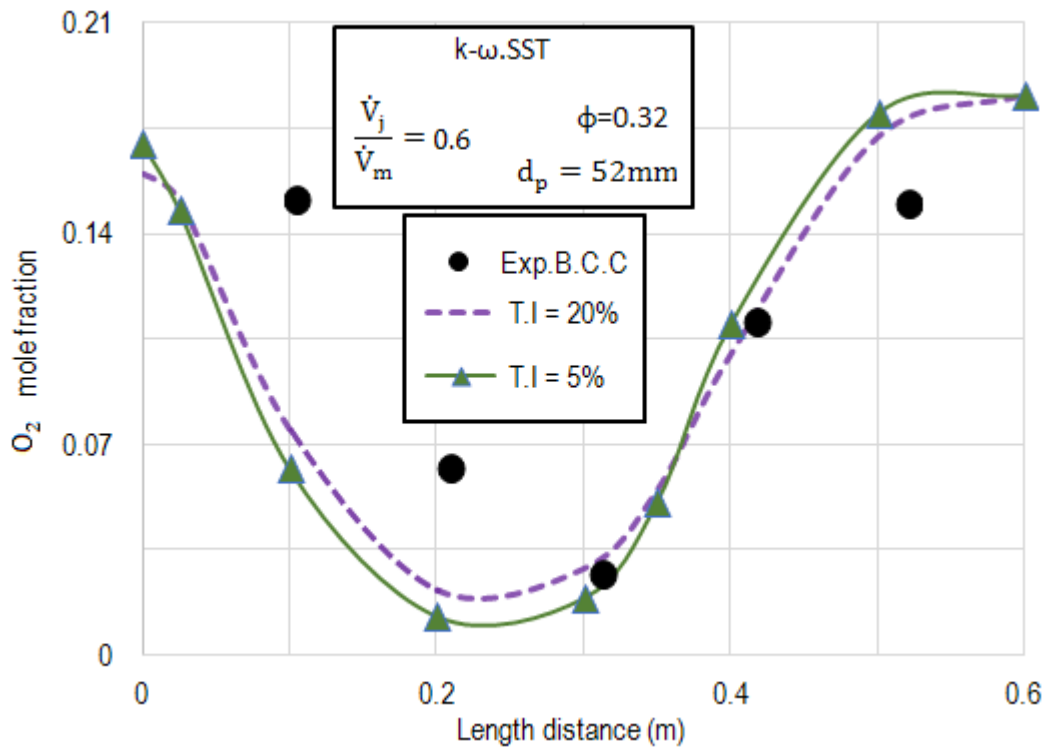
Figure 4.19: Oxygen profile in the case of high volumetric ratio (B.C.C arrangement).

Figure 4.20 shows Oxygen concentrations when the volumetric ratio is increased from 0.1 to 0.6.
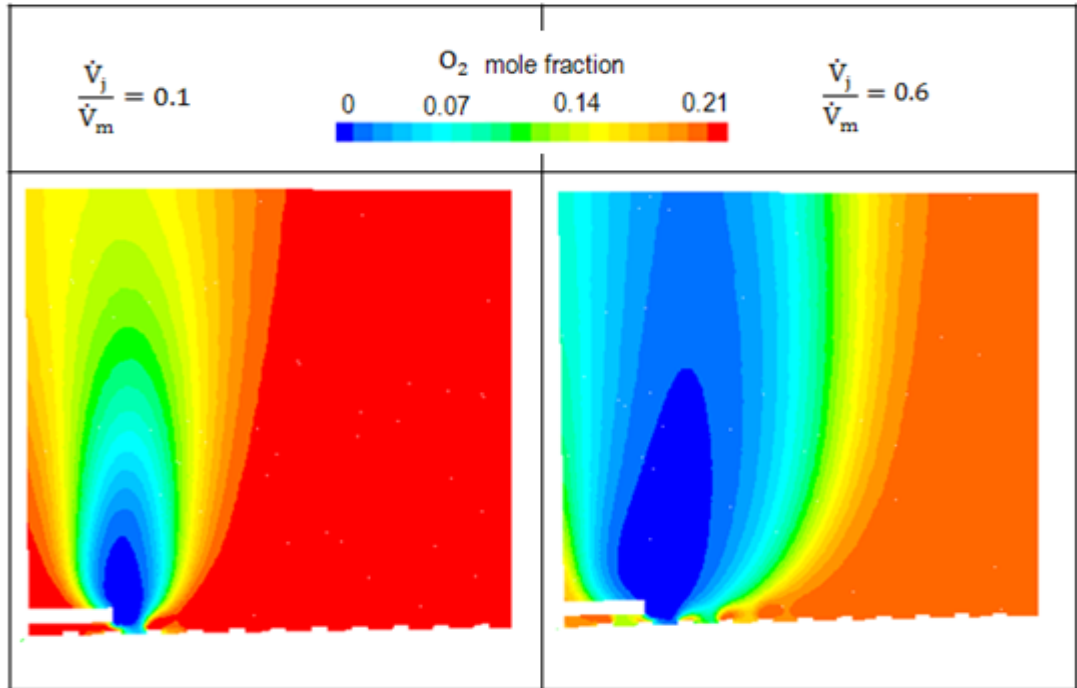
Figure 4.20: Oxygen contours of two volume ratios.

4.3.2 Simple cubic (SC) arrangement

The O2 profile for a volumetric ratio of 0.1 is shown in Figure 4.21, when the volume ratio is 0.1. The maximum percentage of turbulence intensity (20%) shows a better agreement with the experimental results.
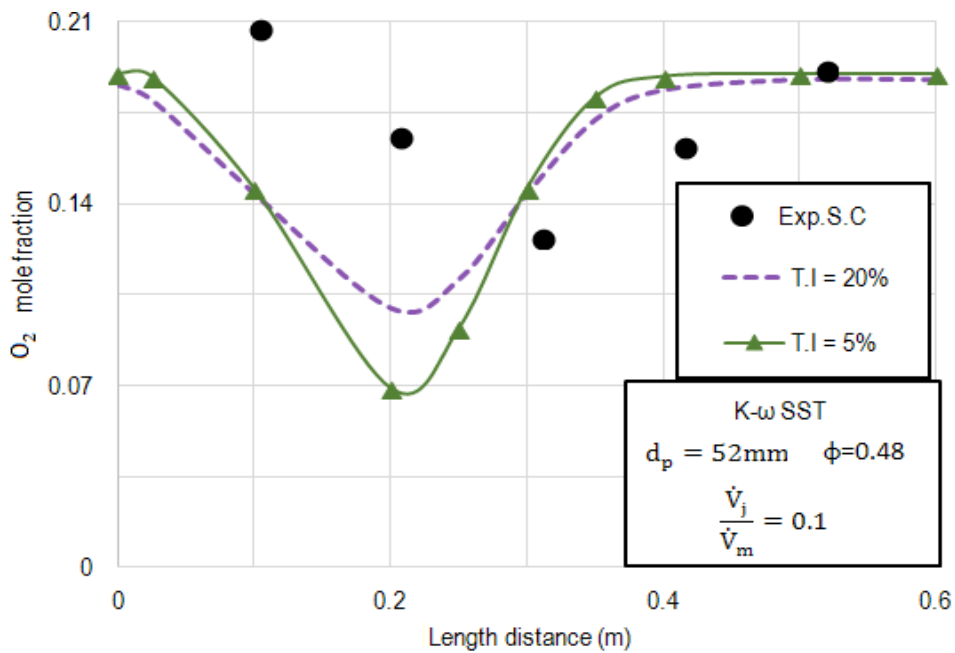
Figure 4.21: Distribution of O_2 mole fractions for volumetric ratio of 0.1 (S.C arrangement).
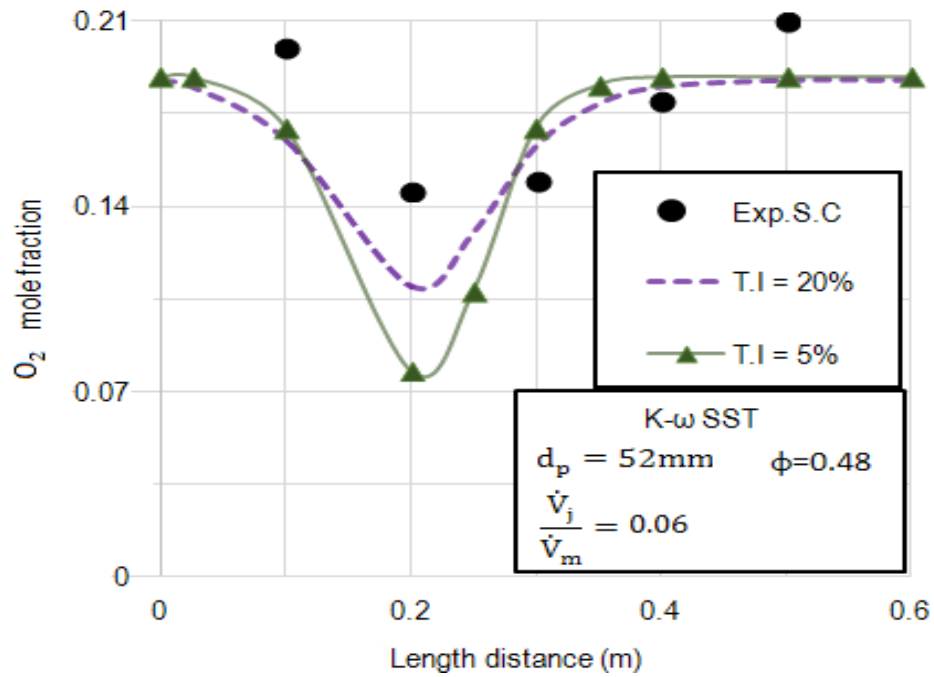
Figure 4.22: Distribution of O_2 mole fractions for volumetric ratio of 0.06 (S.C arrangement).

Figure 4.22 is showed the O_2 profile for the low volumetric ratio 0.06. Again, the higher percentage of turbulence intensity has more accurate results with the experiment results. When particles were arranged in the form of S.C, the k-ω turbulence model with higher TI is showed the best agreement with experimental measurements. The influence of increasing turbulence intensity is shown in Figure 4.23.
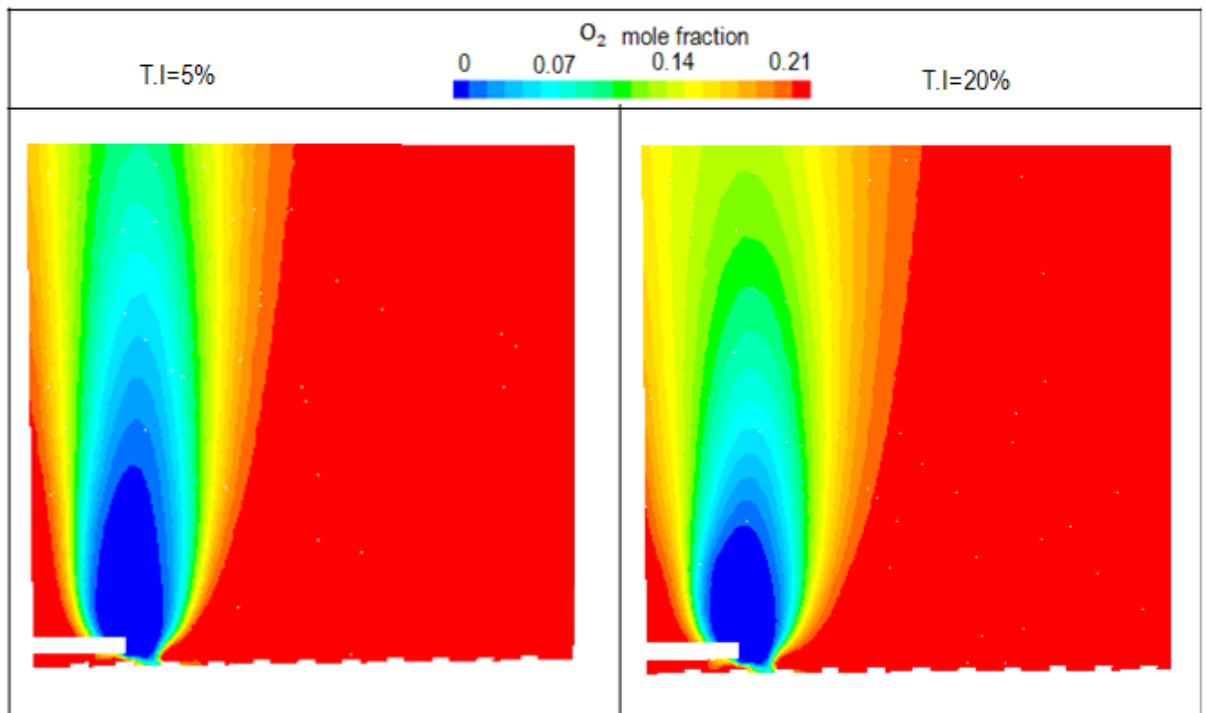
Figure 4.23: Influence of turbulence intensity on O_2 profile.

4.4 Conclusions

4.4.1 Parallel flow injection

To obtain more accurate results, the different turbulent models and different turbulence intensities were applied. The conclusions of parallel flow injection are listed below and presented in Table 4.2.

1. The porosity of ϕ=0.32 was used for the BCC arrangement, and ϕ=0.48 was used for the SC arrangement. In the case of the unstructured packed bed, the ϕ=0.4 was used (d_p =4 mm).

2. There is no influence on the turbulence model and percent of turbulence intensity when the volumetric ratio is increased from 0.1 to 0.6.

3. The turbulence models did not show the same profiles for those two arrangements. This should be considered for the simulation program related to the particle arrangements.

4. The k-ε standard turbulence model with T.I=7.8% will be used for simulation of reactive flow in lime PFR kilns when ϕ=0.32.

5. The k-ε Realizable with T.I=12% will be used for simulation of reactive flow in PFR kilns

When ϕ=0.48

Table 4.2: Summary of simulation results.

Particle arrangement	Particle diameter	porosity	Turbulence model	Turbulence intensity
Body Center Cubic (B.C.C)	$d_p = 52mm$	ϕ=0.32	k-ε Standard	T.I=7.8%
Simple Cubic (S.C)	$d_p = 52mm$	ϕ =0.48	k-ε Realizable	T.I=12%
Unstructured Packed bed	$d_p = 4mm$	ϕ= 0.4	k-ε Standard	T.I=5%

4.4.2 Radial cross flow injection

To obtain more accurate results, the different turbulent models and different turbulence intensities were applied. The conclusions of radial flow injection are listed below and presented in Table 4.3.

1. The porosity of ф=0.32 was used for the BCC arrangement, and ф=0.48 was used for the SC arrangement.

2. There is no influence on the turbulence model and percent of turbulence intensity when, the volumetric ratio is increased from 0.1 to 0.6.

3. The K-ω SST turbulence model with T.I=20% will be used for simulation of reactive flow in CFS kilns.

Table 4.3: Summary of simulation results.

Particle arrangement	Particle diameter	porosity	Turbulence model	Turbulence intensity
Body Center Cubic (B.C.C)	$d_p = 52mm$	Φ=0.32	k-ω SST	T.I=20%
Simple Cubic (S.C)	$d_p = 52mm$	Φ =0.48	k-ω SST	T.I=20%

The mean velocity and turbulence intensity are the two main inputs to investigate the flow mixing through a packed bed. More accurate data, including the turbulence intensity, is now available by using the experimental measurements and CFD porous media model approach.

Thus, the PMM method can be used as a CFD simulation model for reactive flow in lime shaft kilns with real a dimension of about 10 m in height without limitation in the number of nodes and computational times.

Parallel Flow Regenerative Lime Shaft Kilns (PFR)

5.1 Introduction

As shown in Figure 5.1, in the PFR kilns, the fuel and combustion air are injected separately from the top parallel with the movement of the packed bed. To achieve an even fuel distribution in the cross-section, a various number of burners were used
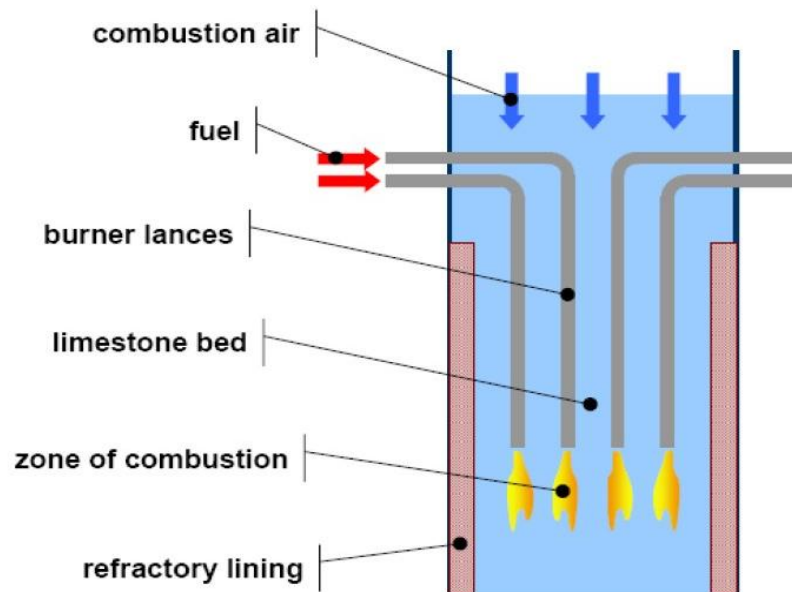
Figure 5.1: Schematic of burner system in PFR shaft kilns.

The non-premixed combustion simulated with the Porous Media Model (PMM) method. Here, the following parameters are studied:

- Fuel velocity, U_f (burner diameter, d_f),
- Particle diameter,
- Type of fuel (natural gas, lignite and coal dust, liquid type),
- Number of burners n and different arrangements,
- Porosity, ϕ,
- Excess air number, λ, and
- Type of PFR kilns (circular and rectangular).

Two cases considered for a better understanding of the influencing parameters. The first one is when air and fuel do not react with each other (non-reactive flow), and the second one is when fuel and air react with each other (reactive flow).

5.2 One Burner Non-reactive Flow

5.2.1 Velocity profile (when n=1)

For a better understanding of the mixing behavior, only one burner studied in the first step. Table 5.1 shows dimensions and specification details of one burner parallel flow injection.

Table 5.1 Schematic of parallel flow injection when n=1.

Fuel volume flow	CH4 Fuel Velocity	Air volume flow	Air velocity	Burner diameter
$\dot{V}_f$ $\dfrac{m^3}{s}$	U_f $\dfrac{m}{s}$	$\dot{V}_m$ $\dfrac{m^3}{s}$	U_m $\dfrac{m}{s}$	d_f mm
0.1	50	1	0.3	50
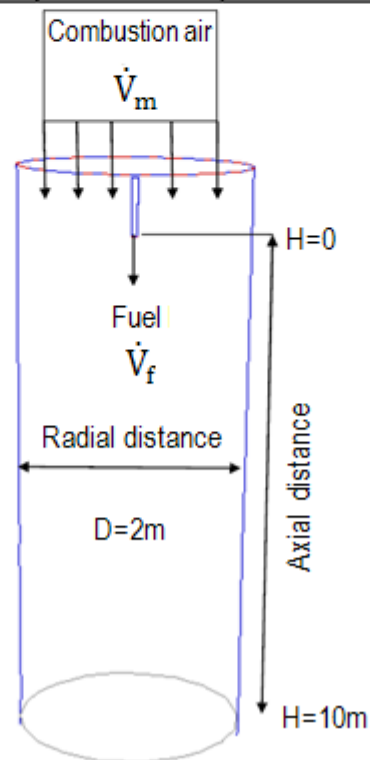
The superficial velocity U_o is the total flow divided by the cross-sectional area. The value of 0.3 $\frac{m}{s}$ is typical for airflow in PFR kilns. The interstitial velocity is the superficial velocity divided by porosity:

$$U = \frac{U_0}{\phi}.$$ (5-1)

The porosity is one present empty shaft. So the interstitial velocity will be the same as the superficial velocity. Figure 5.2 shows the radial profile of the local velocity in the bed at the burner position for different porosities. In the center, the velocity is always the burner outlet velocity. The lower porosity results in a wider profile. For φ=0.32, the width is 400 mm, which is eight times more than the burner diameter. Because of the high flow resistance in the axial direction, the flow extends to the radial direction. For a low porosity, the profiles nearly become rectangular.
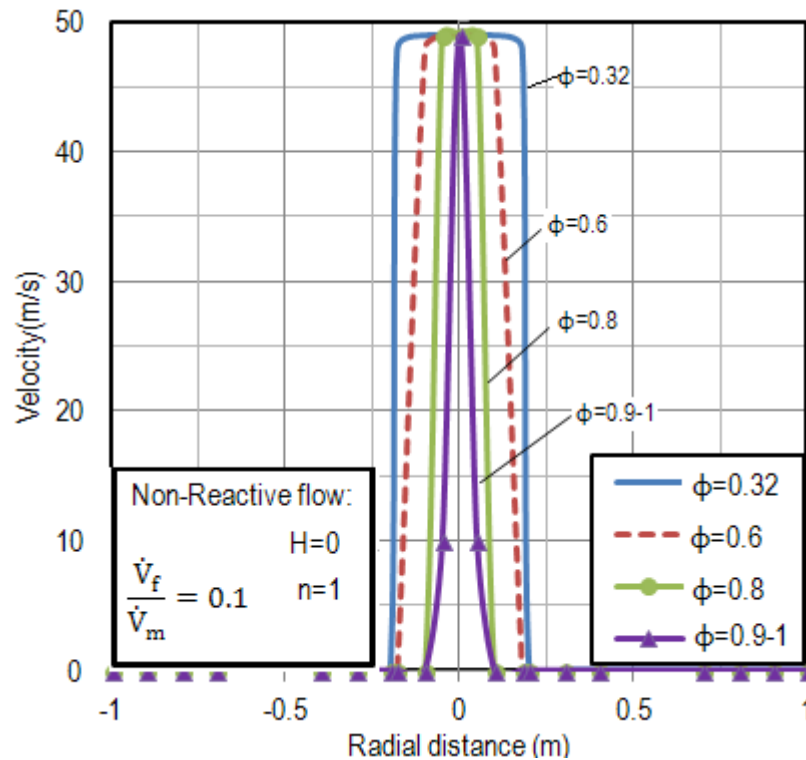
Figure 5.2: Influence of different porosities on the velocity profile at burner level (Φ=0.32-1).

Figure 5.3 shows the radial profile of the local velocity after a height of 2 m, which is one kiln diameter in height. The lower the porosity is, the more even the profile becomes.
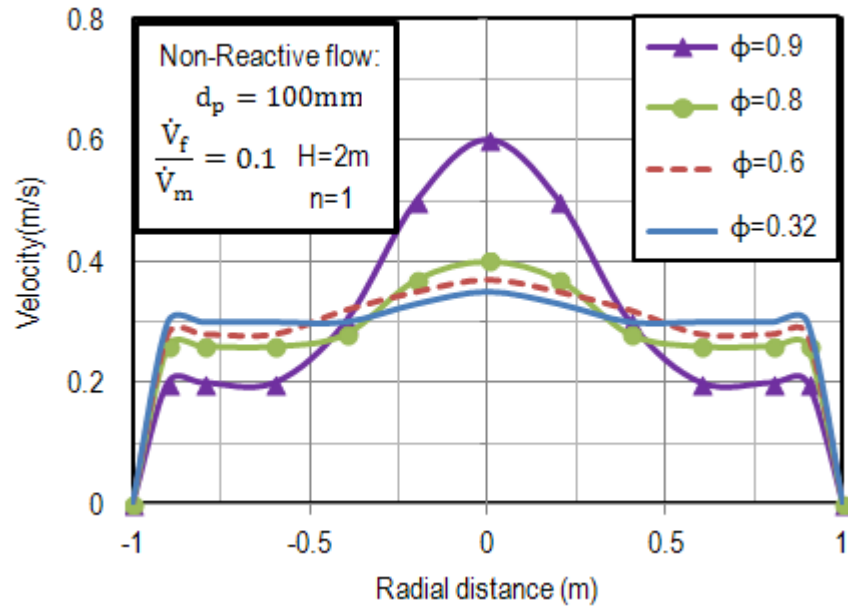
Figure 5.3: Influence of different porosities on the velocity profile at H=2 m (φ=0.32-0.9).

Figure 5.4 shows the velocity profile at different heights. The maximum velocity is always in the center. The higher the distance from the burner is, the more homogeneous the velocity profile becomes.
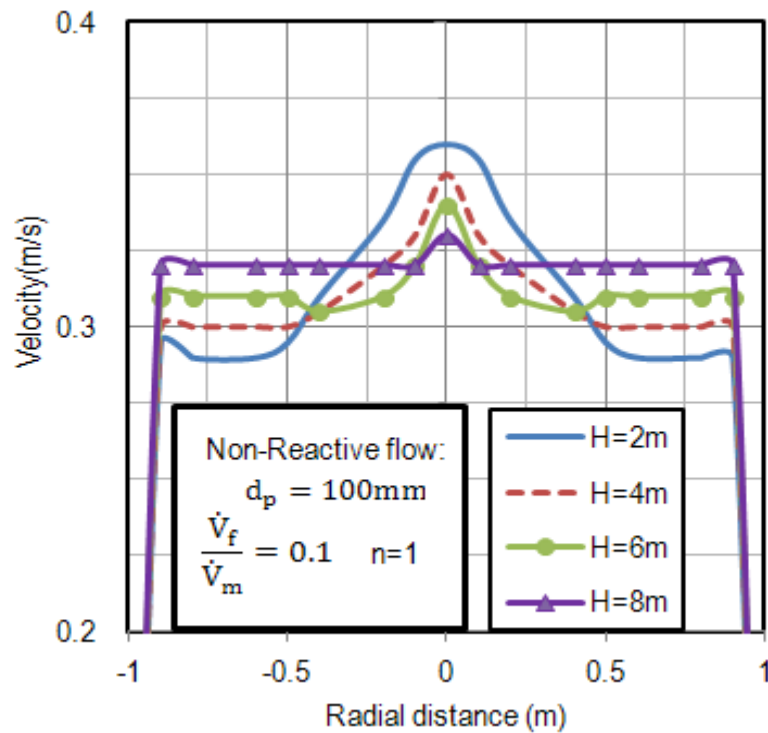
Figure 5.4: Velocity profile at different heights at φ=0.32.

Figure 5.5 shows the wall effect for different particle diameters (d_p =10-200 mm). For a particle diameter of 10 mm, the velocity profile decreases very sharply at the wall. The decrease to the wall is in the range of one particle diameter.
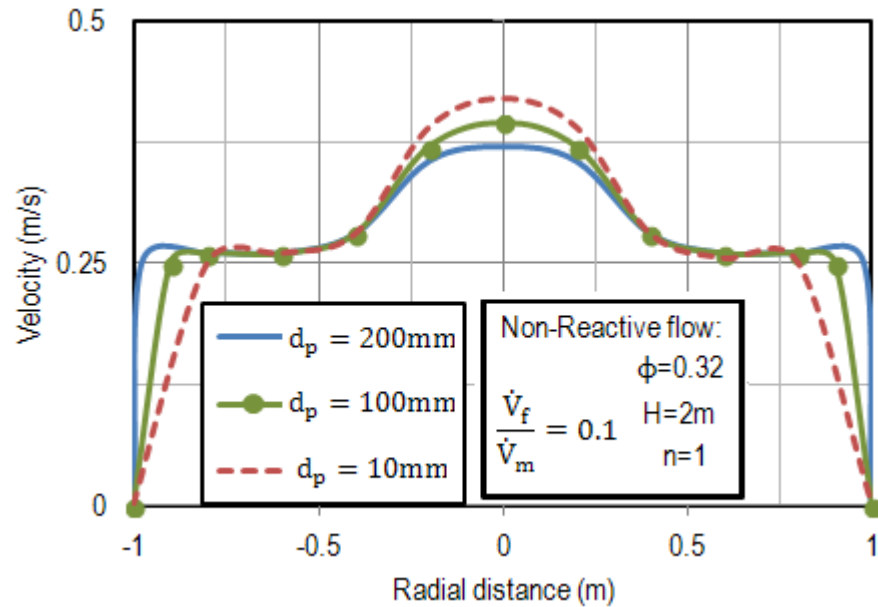
Figure 5.5: Influence of particle size on the velocity profile in radial directions.

Figure 5.6 shows the radial profile for an empty shaft (φ=1) for comparison. In this case, we have the typical Gaussian profile.
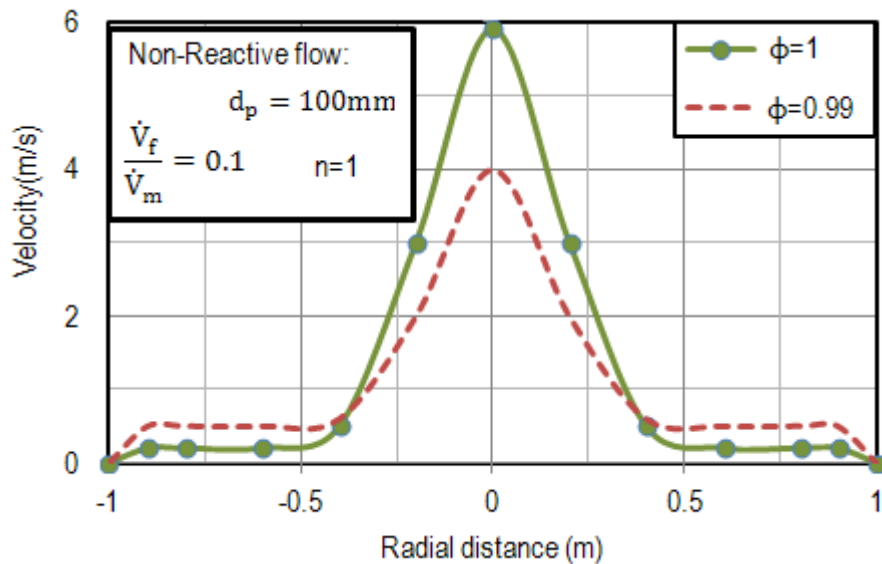
Figure 5.6: Influence of different porosities on the velocity profile at H=2 m (φ=0.99-0.1)

for an empty shaft.

Figure 5.7 shows the axial velocity (in the center of the packed bed) as a function of the injection distance. After approximately 2 m, the velocity decreases to one-tenth of the outlet velocity.
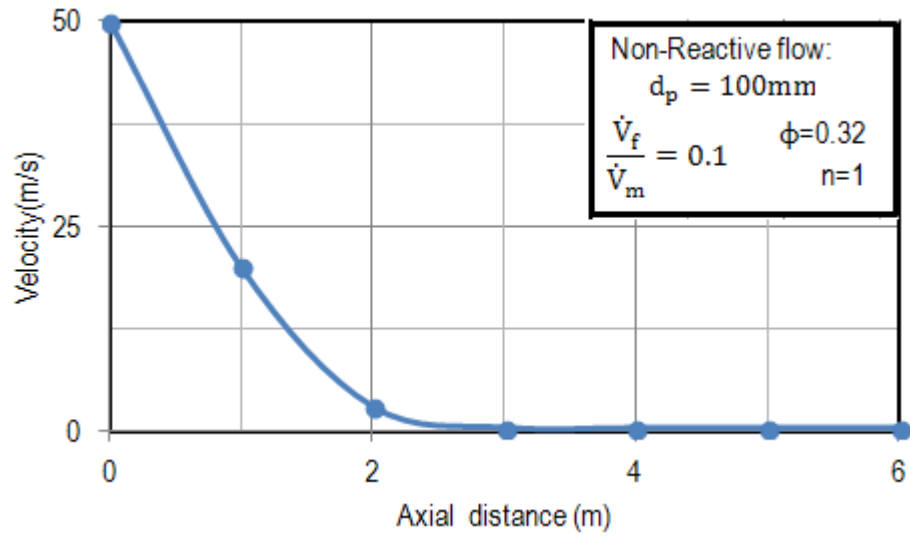
Figure 5.7: Velocity profiles in axial direction.

Figure 5.8 shows the decrease in the distance for different porosities. Lower porosities caused a higher drop of the axial velocity.
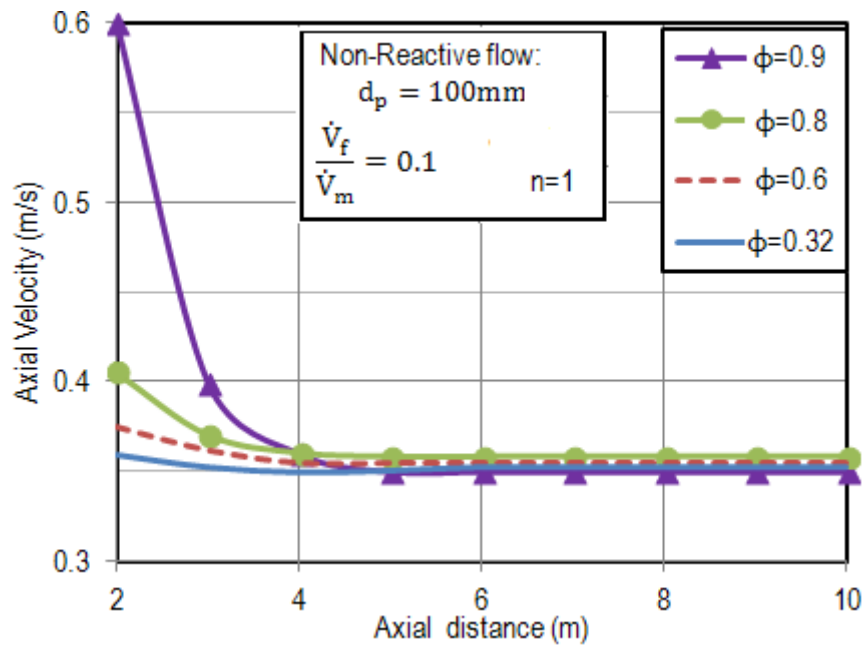
Figure 5.8: Influence of different porosities on axial velocity profile (ϕ=0.32-0.9).

Figure 5.9 shows the axial velocity profile for an empty shaft (ϕ=1) for comparison. After a 6 m distance from the burner, the velocity reaches the mean flow velocity of $0.3\ \frac{m}{s}$.
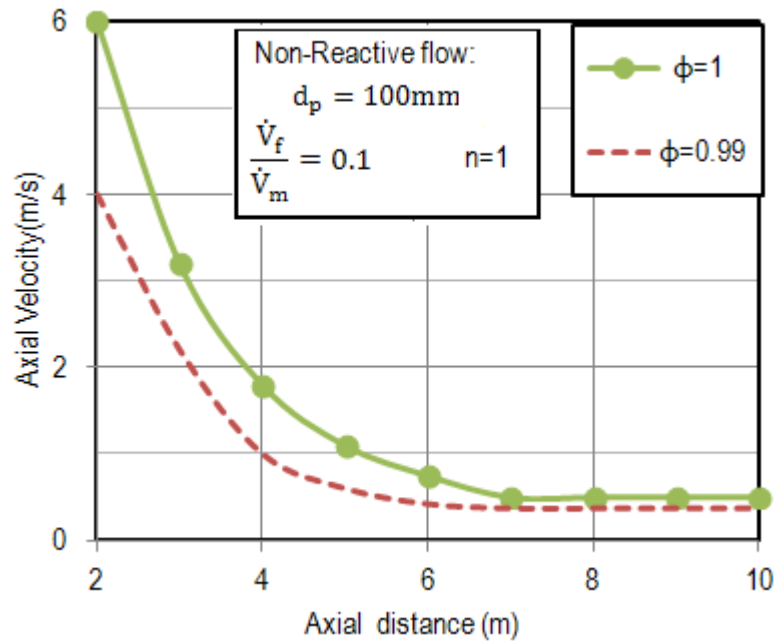
Figure 5.9: Influence of different porosities on the axial velocity profile for an empty shaft.

5.2.2 Fuel profile

Figure 5.10 shows the influence of the radial fuel profile in the bed on the burner position for different porosities. The lower porosity results in a wider profile. For ϕ=0.32, the width is 400 mm (8 times more than the burner diameter). When compared with Figure 5.2, it can be seen that for a porosity of 0.32, the profiles for fuel and velocity are similar.
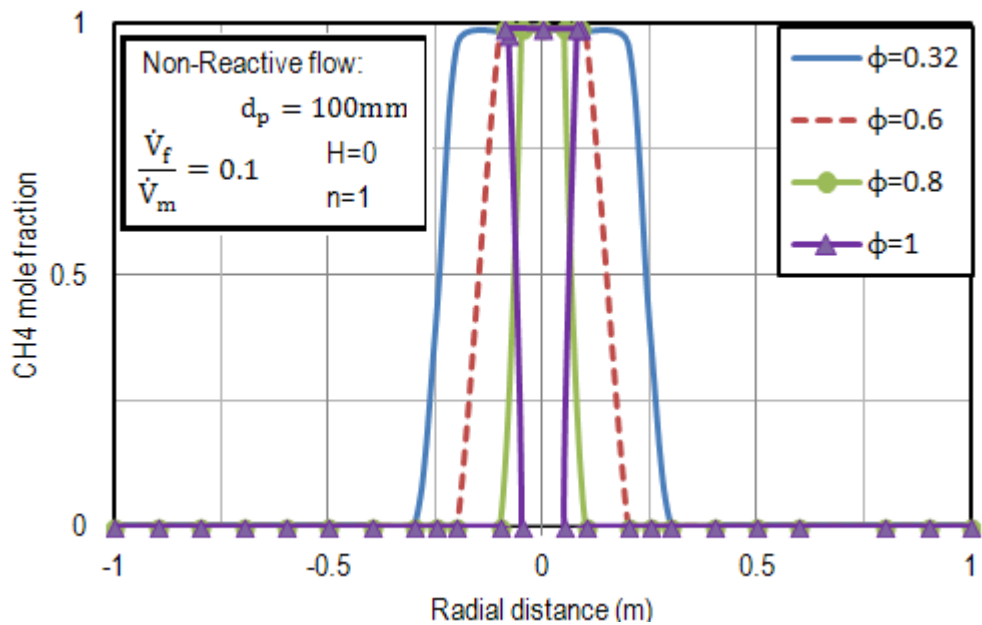
Figure 5.10: Influence of different porosities on the fuel distribution at burner level (ϕ=0.32-1).

Figure 5.11 shows the radial profile after 2 m. In contrast to velocity on the axis, the concentration increases with lower porosity. The lower the porosity is, the higher is the concentration in the center becomes. Also, the smaller is the fuel in the radial direction.
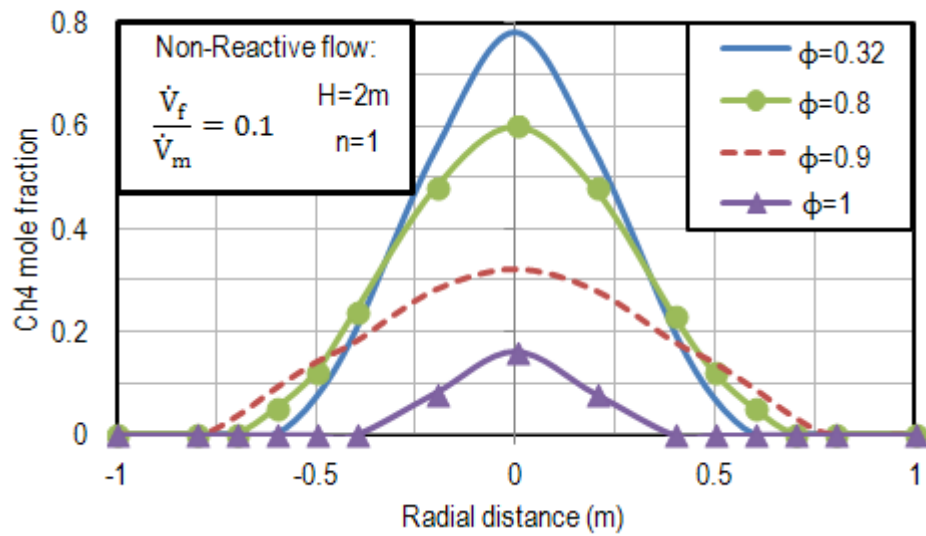
Figure 5.11: Influence of different porosities on the radial fuel profile at H=2 m.

Figure 5.12 shows the axial profile. The concentration becomes approximately zero after 10 m. From Figure 5.7, it can be seen that the velocity becomes zero at a distance of only 2 m.
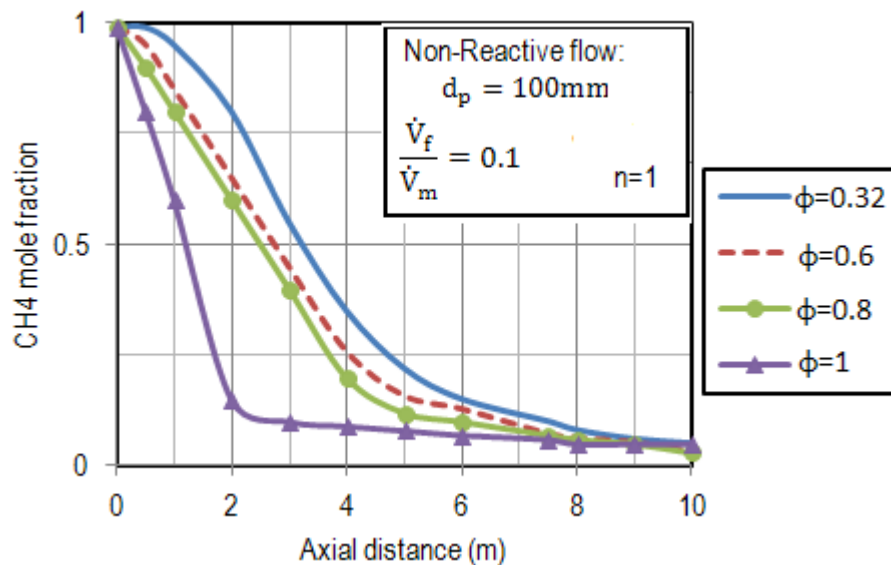
Figure 5.12: Influence of different porosities on fuel profile in axial direction.

In diffusion flames, the profiles of velocity and concentration are similar. However, in a packed bed, both have different behaviors. Figure 5.13 shows the contours of concentration. In the empty shaft ($\phi=1$), only a small range of CH4 exists. The lower the porosity is, the longer the mixing range becomes.
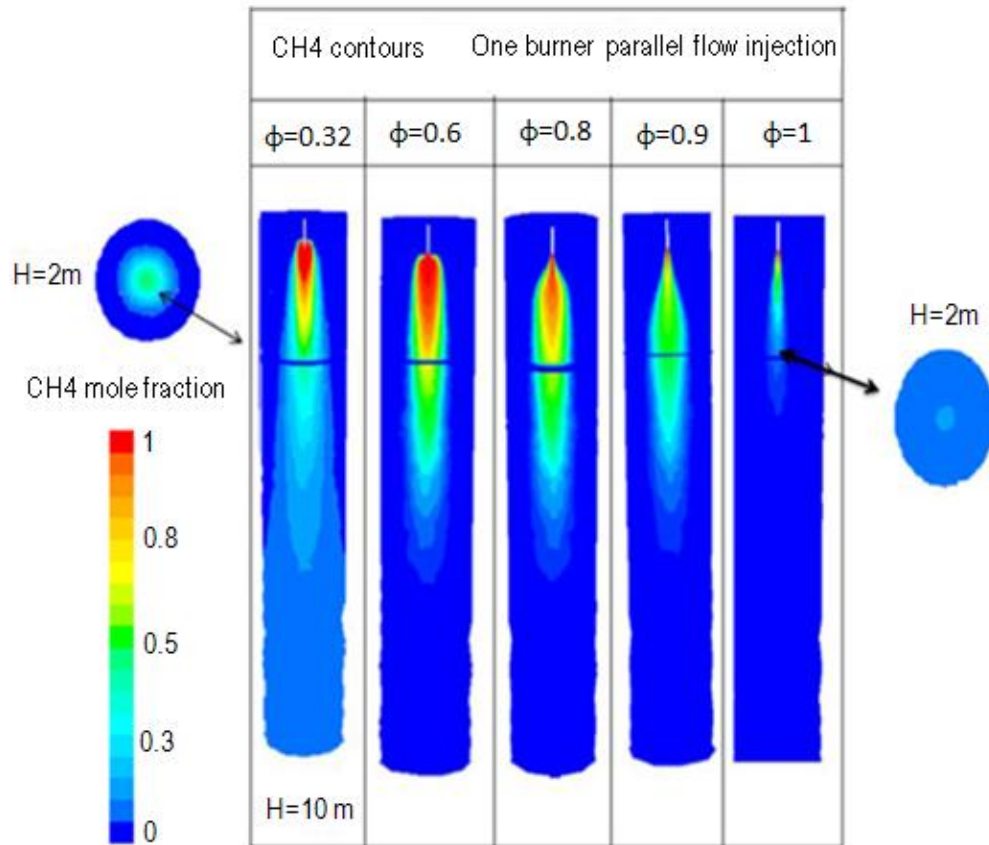
Figure 5.13: Contours of fuel in parallel flow injection when n=1.

The length of mixing can be estimated from the axial profile. The mixing length is the position where the fuel fraction has fallen to the stoichiometric value. Due to the very small amount, the reverse fraction versus the injection distance shows in Figure 5.14. This stoichiometric value marked with a dashed line. The flame expected to be between 7 to 7.5 m for the packed bed.
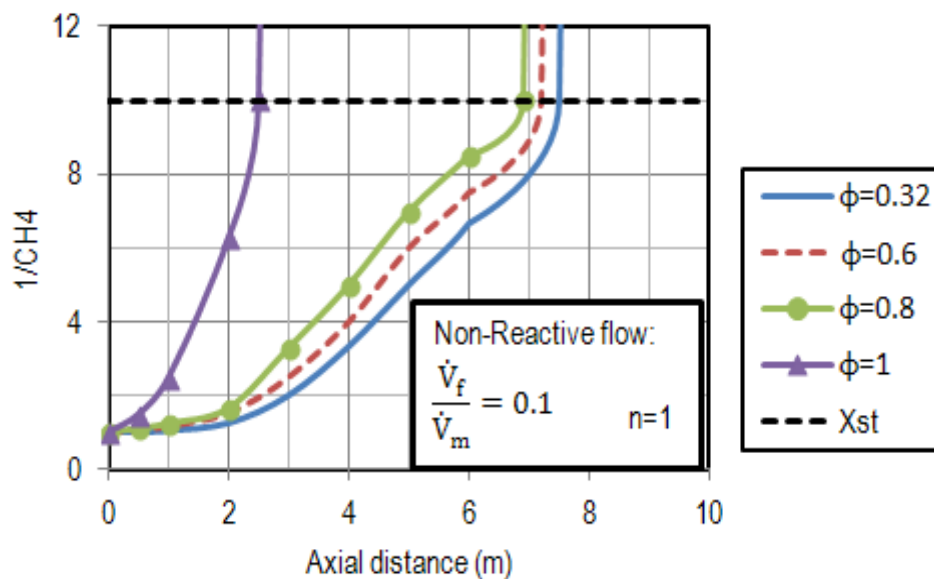
Figure 5.14: Influence of porosity on length of mixing when $d_P = 100mm$.

Figure 5.15 shows the distribution of the fuel in the radial direction. The fuel concentration reached to the stoichiometric value of approximately 7 m.
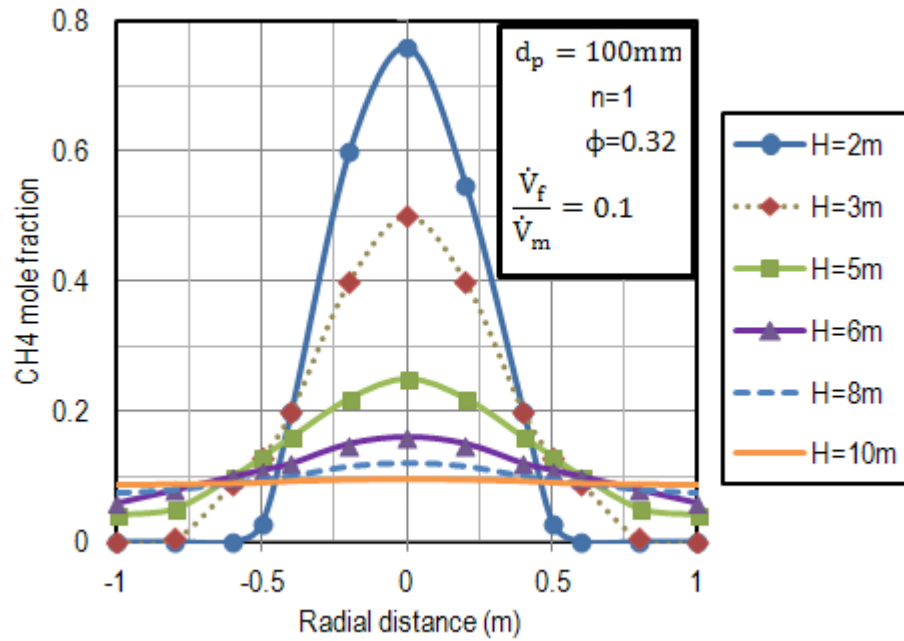
Figure 5.15: Fuel distribution at different heights.

Figure 5.16 shows the reverse fraction for an empty shaft for comparison. The axial profile is similar to a free jet. Hence, the length of mixing is 55 times more than the burner diameter.
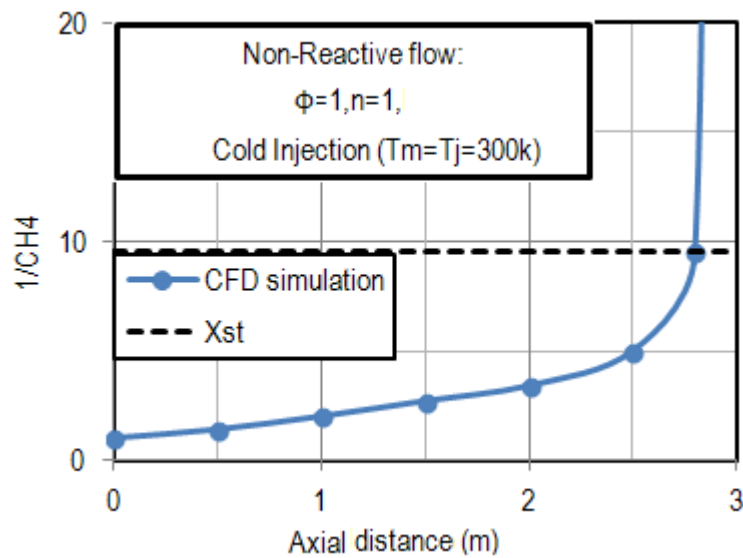
Figure 5.16: CFD simulation for parallel injection in an empty shaft.

In a free jet, the decrease of concentration, X and the mean velocity, u is :

$$\frac{X}{X_o} = \frac{1}{\frac{Z}{d_f} \cdot tg_\varphi + \frac{1}{2}} \cdot \frac{\overline{\rho_o}}{\rho} \qquad , \qquad \frac{u}{u_o} = \frac{1}{tg_\varphi \cdot \frac{Z}{d_f} + 1} \cdot \frac{\overline{\rho_o}}{\rho} . \qquad (5\text{-}2)$$

Where Z is the length coordinate, d_f is the nozzle diameter, is the density of fuel, is the density of the air, and is the angle of the jet. The length of the flame can be defined with respect to the position where the concentration of the fuel has reached its stoichiometric value. Therefore, the length of the flame becomes with $X_{st} = \frac{1}{1+L}$ (L is the stoichiometric air demand). The length of mixing calculated for a parallel flow free jet by Eq. (5-3) below [49].

$$z = \frac{1}{0.32} \quad 1 + L \quad \frac{\overline{\rho_o}}{\rho} - 1 \ . d_o \tag{5-3}$$

The mixing length is proportional to the burner diameter. The length is independent of the fuel velocity. Table 5.2 shows a comparison between the analytic calculation of the mixing length and the CFD simulation. For a free jet, the length of mixing, which calculated from the equation, is 2.7 m. For an empty shaft when the diameter of fuel injection is 50 mm, the length of mixing, which obtained from CFD simulation is about 2.8 m. Therefore, there is good agreement between the analytic calculation and CFD simulation of free jet injection.

Table 5.2: Calculation of the length of mixing.

Cold Injection $T_m = T_j = 330 \ k$ CH4	$\frac{\rho_o}{\rho} \approx 1, L=15$ $n=1, \phi=1$ $\frac{\dot{v}_j}{v_m} = 0.1$
Mixing length $L_f(m)$ Equation (5-3) Calculation	2.7
CFD simulation	2.8

5.2.3 Influence of fuel velocity

In this section, the influence of fuel velocity on the length of mixing studied. For this aim, nozzles with a diameter range of d_f=20 to 50 mm used. The main air volume flow was kept constant. Figure 5.17 shows the influence of the fuel velocity and nozzle diameter on the length of mixing for ϕ=0.32. When the fuel velocity increased from 25 $\frac{m}{s}$ to 100$\frac{m}{s}$, the mixing length linearly increased. The length of mixing in the case of d_f=50 mm is higher than the one in the case of d_f=20 mm. The length of mixing increases with the nozzle diameter when the fuel velocity is constant. Therefore, the mixing length increases with the fuel volume flow [49].
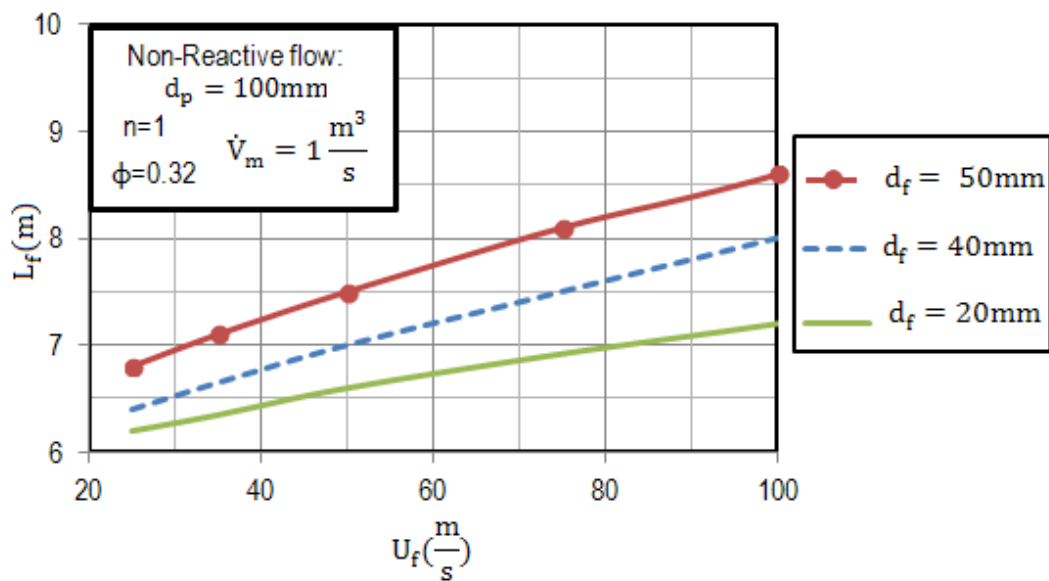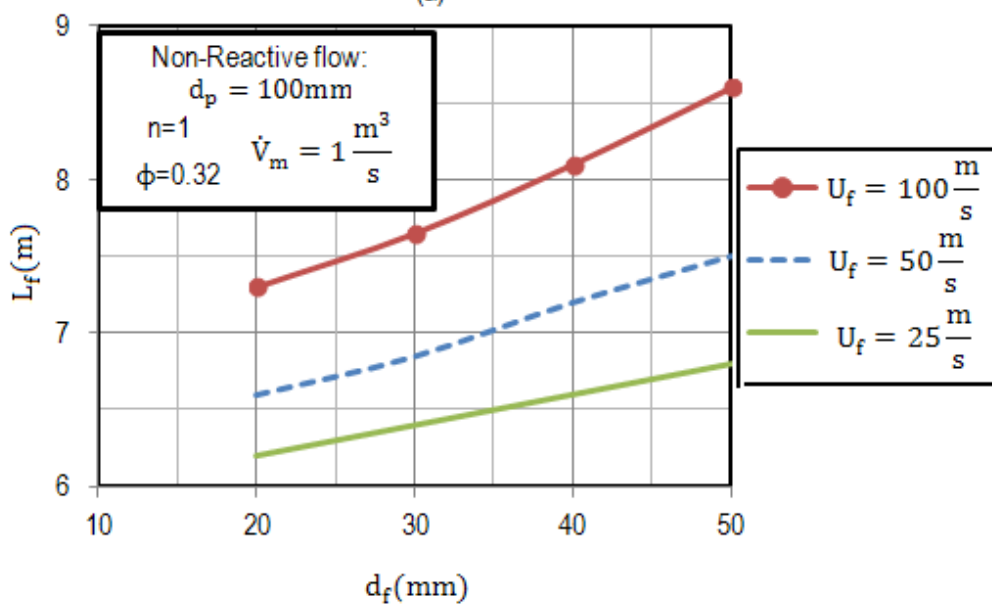
Figure 5.17 Influence of fuel velocity (a), nozzle diameter (b) on mixing length when $U_m = 0.3\ \frac{m}{s}$.

Figure 5.18 shows the influence of fuel volume flow on the length of mixing. When the nozzle diameter was kept constant, the length of mixing increased by increasing the fuel volume flow. It can be seen that the mixing length is not proportional to the volume flow.
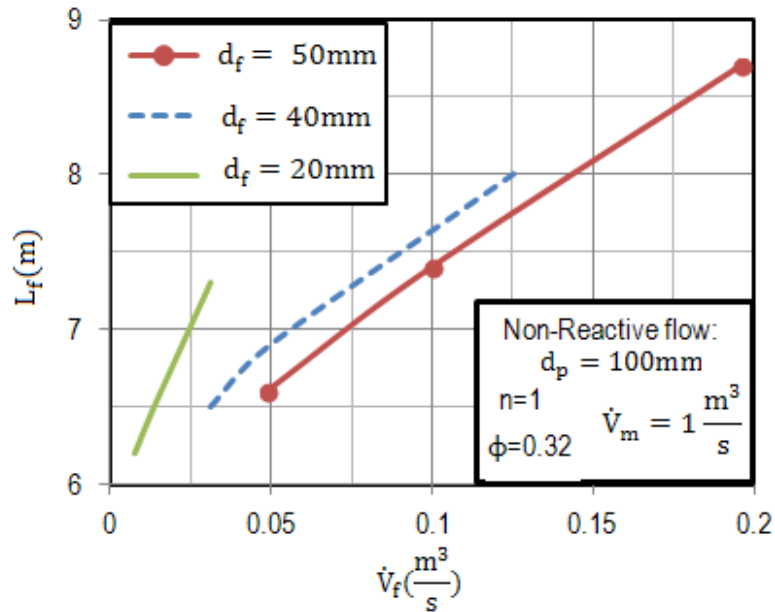
Figure 5.18: Influence of fuel volume flow when $U_m = 0.3 \frac{m}{s}$.

Figure 5.19 shows the influence of the product of the burner diameter and fuel velocity on the mixing length. The three fuel velocities, U_f=25, 50, and 100$\frac{m}{s}$, are injected from the three typical nozzle diameters, d_f= 20, 40, and 50 mm. It can be concluded that the mixing length increases approximately linearly with the product of fuel velocity and burner diameter.
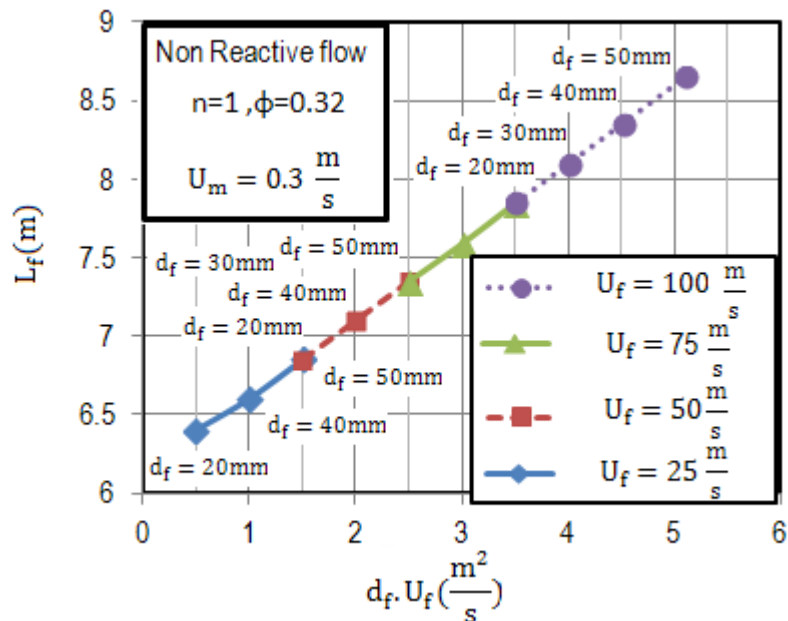
Figure 5.19: Influence of product of burner diameter and fuel velocity.

Figure 5.20 shows the Influence of air velocity (a) and the ratio of air to fuel (b). In this case, the fuel volume flow was kept constant($V_f = 0.1 \frac{m^3}{s}$).The air volume flow is proportional to the velocity. Therefore, the higher the airflow is, the higher the excess air number is, and the shorter the length of mixing becomes. When fuel-injected with a constant velocity from a smaller burner diameter, the length of mixing is always shorter.

(a)

(b)
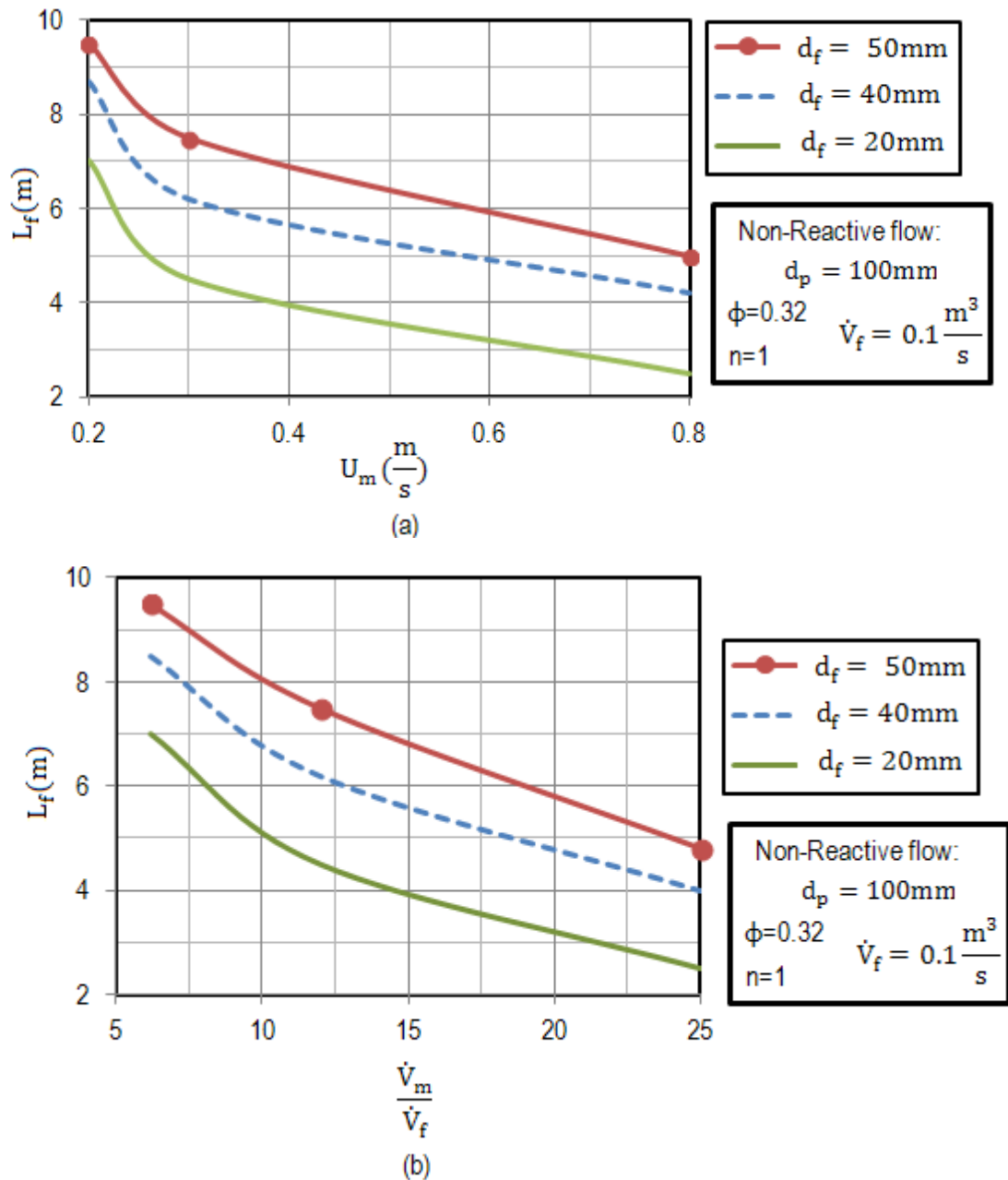
Figure 5.20: Influence of (a) air flow velocity and (b) ratio of air to fuel.

5.3 One Burner Reactive Flow

5.3.1 Temperature profile (when n=1)

In the following case, methane and combustion air react with each other. The volume flow of the fuel is increased by about 30% to $V_f = 0.13 \frac{m^3}{s}$, which is a typical value for a kiln with a diameter of 2 m. The amount of air is fixed at an excess air number of 1.3 to ensure complete combustion of the fuel. The radial temperature profiles and the contour for $\lambda=1.3$ is shown in Figure 5.21. The longer the distance from the burner is, the higher the temperature becomes (both near walls and in the center). That means combustion is not completed until the 10 m. The position of maximum temperature reached in the radial cross-section at different heights is always $\frac{1}{4}$ of the kiln diameter distance of the walls (0.5 m). This is also visible from the temperature contour.
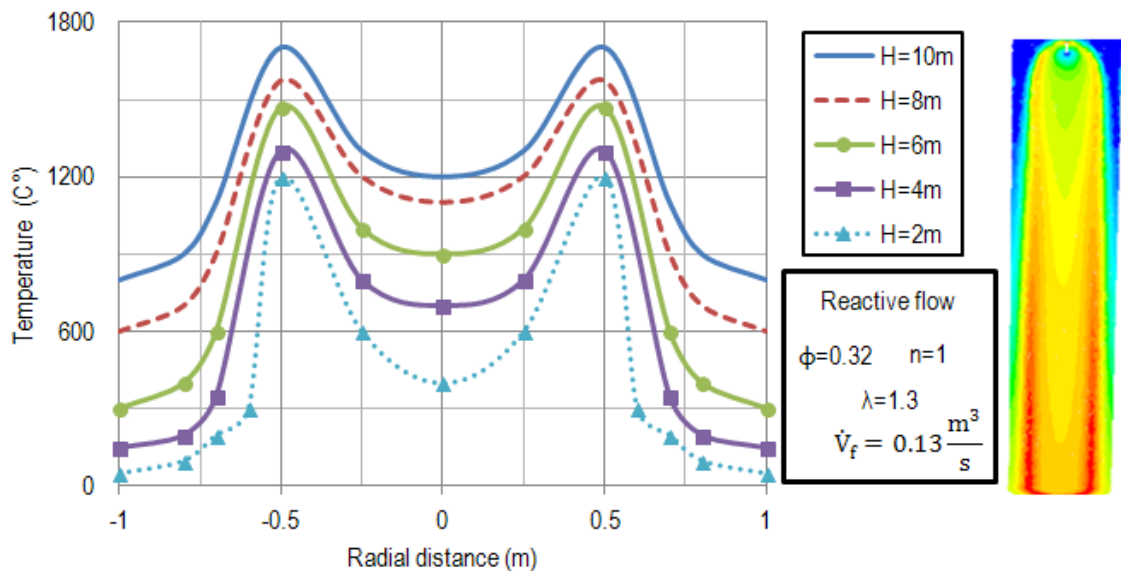
Figure 5.21: Temperature profile at different heights.

Next, the influence of the excess air number discussed. Figure 5.22 shows the core temperature versus the axial distance for three excess air numbers. The injected fuel flow is kept constant, and the airflow is varied. The higher the air volume flow is, the higher the temperature becomes. That is surprising because, in other firings, the temperature is lower, when the excess air number is higher.
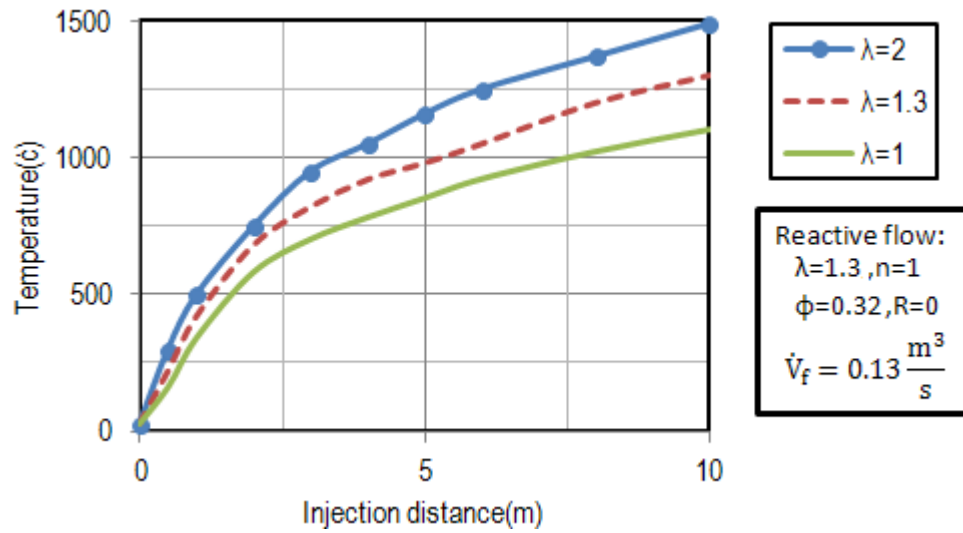
Figure 5.22: Profile of temperature in axial direction

Figure 5.23 shows the radial temperature profile. It can be seen that the higher the excess air number is, the higher the temperature in the core and peak becomes. However, in the outer annular ring (for a radial distance of about 0.5 m), the temperature for λ=1 is higher.
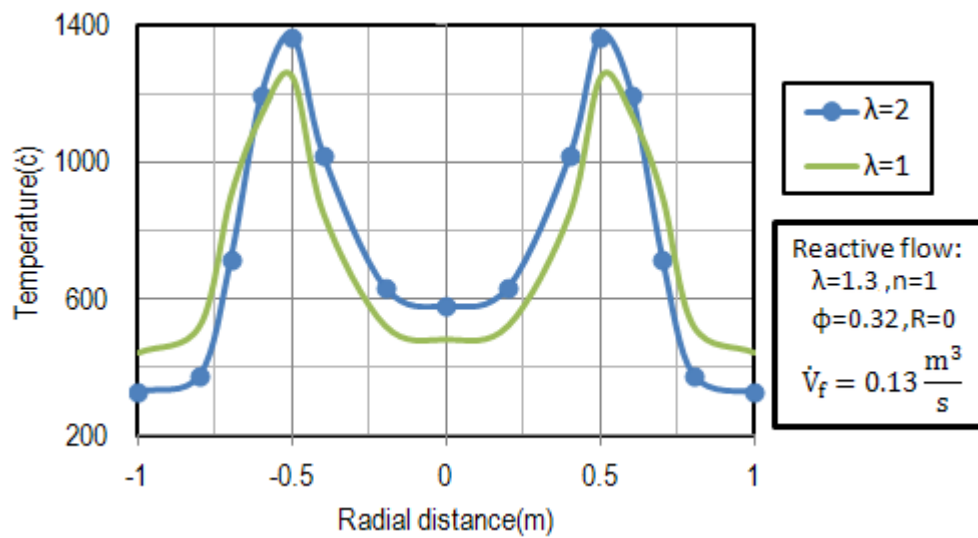
Figure 5.23: Influence of excess air number on radial temperature profile at H=2m.

This can also be seen in Figure 5.24, which shows the temperature contours.
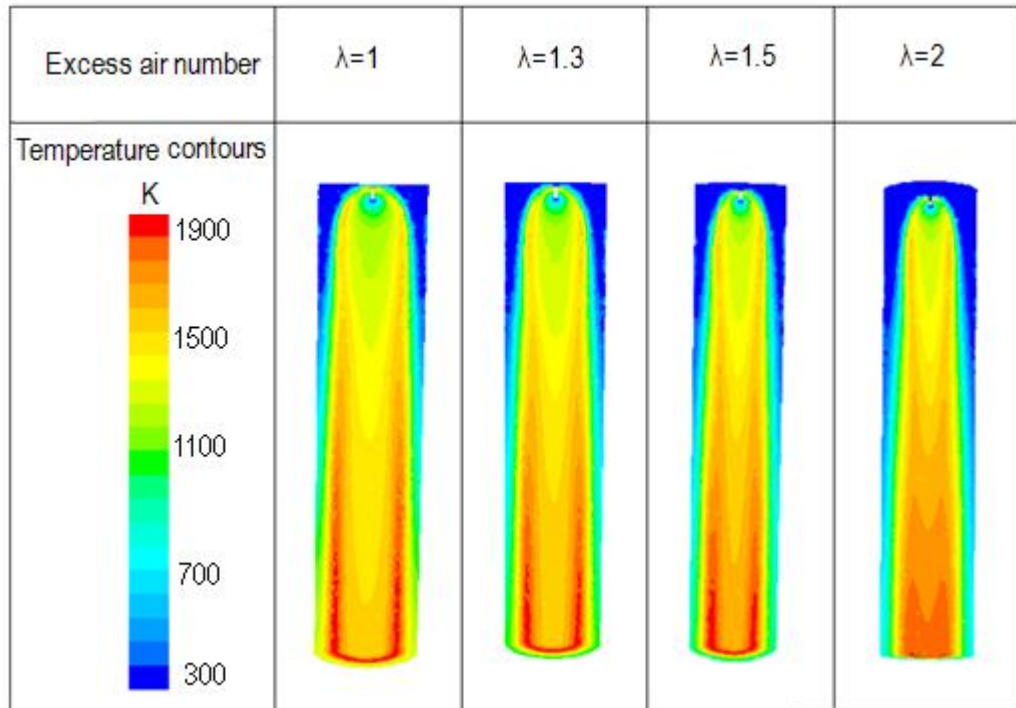
Figure 5.24: Influence of excess air number on temperature profile.

5.3.2 Velocity profile

Figure 5.25 shows the radial velocity profile at the burner level for different porosities. In the center, the velocity is always the burner outlet velocity. The lower porosity results in a wider profile. For ɸ=0.32, the width is 400 mm, which is eight times more than the burner diameter. Due to the high flow resistance in the axial direction, the flow extends to the radial direction. The profiles are similar to those of the non-reactive case in Figure 5.2.
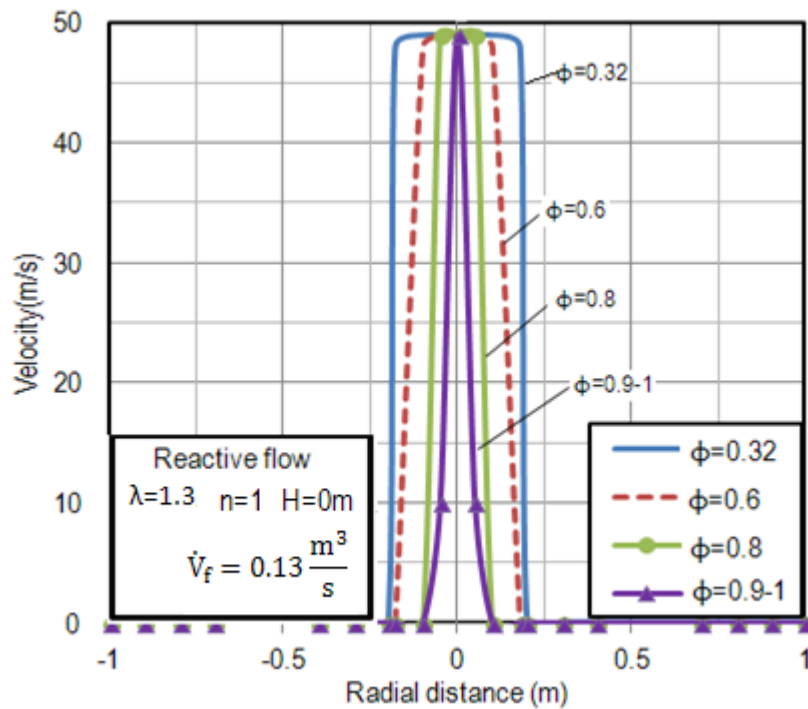
Figure 5.25: Influence of different porosities on velocity profile at burner level (ɸ=0.32-1).

Figure 5.26 shows the radial profile of the local velocity after the height of 2 m. The lower the porosity is, the more even the profile becomes after one kiln diameter in height. Also, at the position of the maximum temperature, the velocity has the highest value. The reason is because of the lowest density. After the radius of 0.5 m, the velocity drops continuously to zero at the walls. In a reactive flow, the radial profile is not as even as in a non-reactive flow, as shown in Figure 5.3.
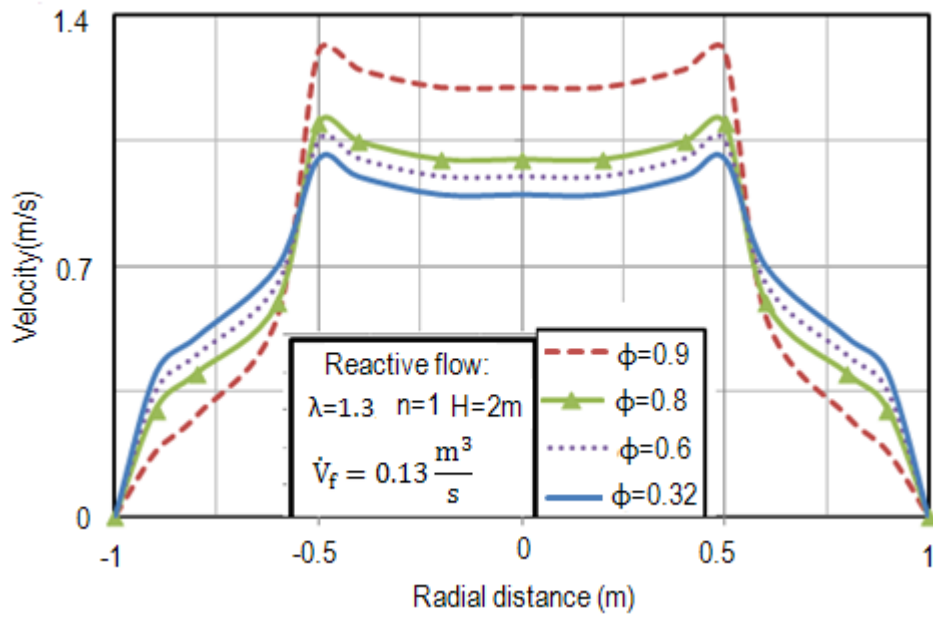
Figure 5.26: Influence of different porosities on velocity profile when H=2 m (ϕ=0.32-0.9).

The product ρ.u which represents the mean flux is shown in Figure 5.27. As it can be seen in this Figure, the radial mass flux distribution is relatively even after 2 m.
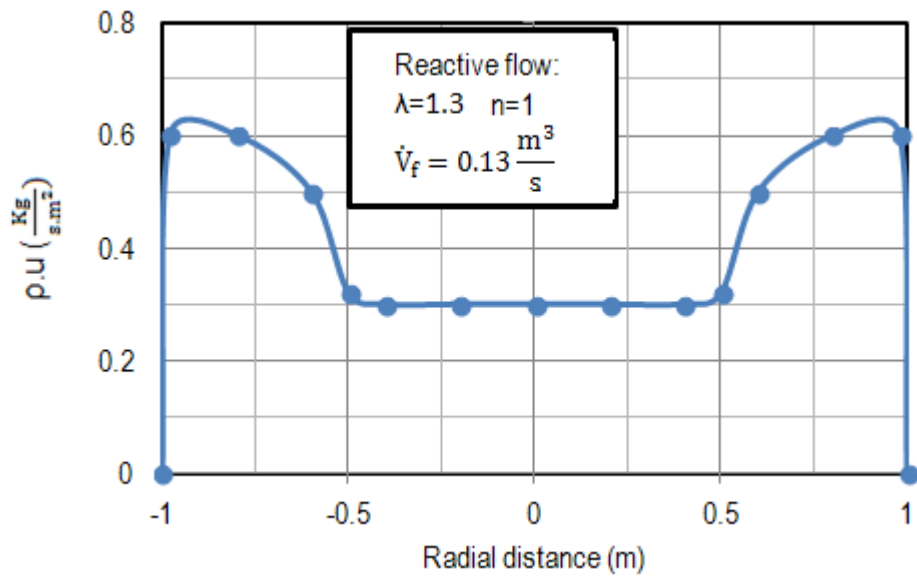
Figure 5.27 : Radial mass flux profile when H=2 m.

5.3.3 Fuel distribution

Figure 5.28 shows the radial fuel distribution profile in the bed at the burner position for different porosities. A lower porosity gives a wider profile. For ϕ=0.32, the width is 400 mm (8 times more than burner diameter). This is again, similar to the non-reactive case of Figure 5.10.
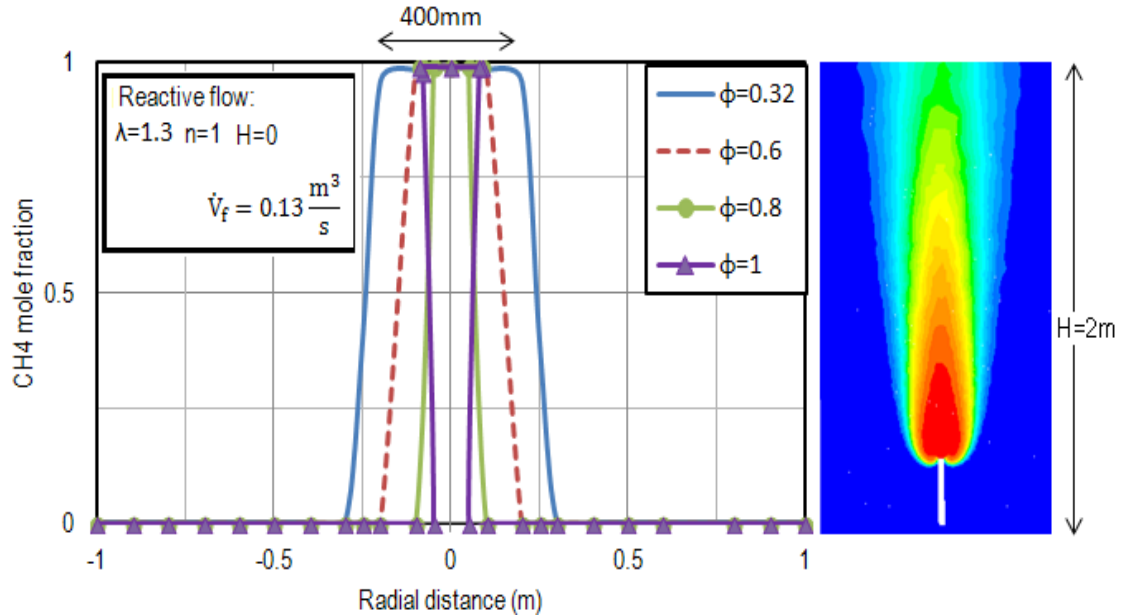
Figure 5.28: Influence of different porosities on fuel distribution at burner level (ϕ=0.32-1).

Figure 5.29 shows the radial profile after 2 m. In contrast to the velocity on the axis, still, a height concentration exists. The lower porosity results in a higher velocity. In comparison with the non-reactive case (Figure 5.11), the concentration in the middle is a little more significant, and the width of the profile is smaller. The reason is that the velocities are higher in the reactive case.
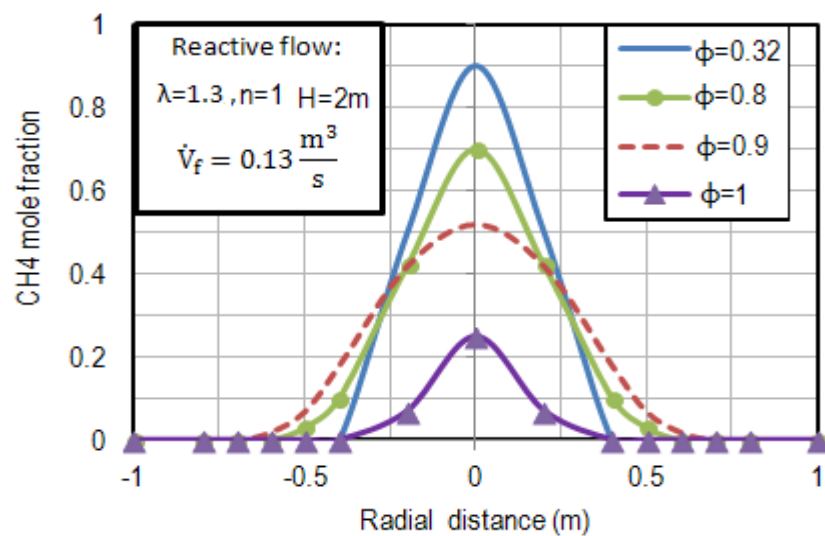
Figure 5.29: Influence of different porosities on radial fuel distribution at H=2 m.

As already considered in Figure 5.30, carbon-monoxide still exists where the methane completely burned. Therefore, the complete combustion range (flame length) is longer. Figure 5.30 shows the contours of CH4, CO, and temperature. The concentration of CO is always the highest at the peak maximum temperature. The methane concentration has its highest value, still on the axis.
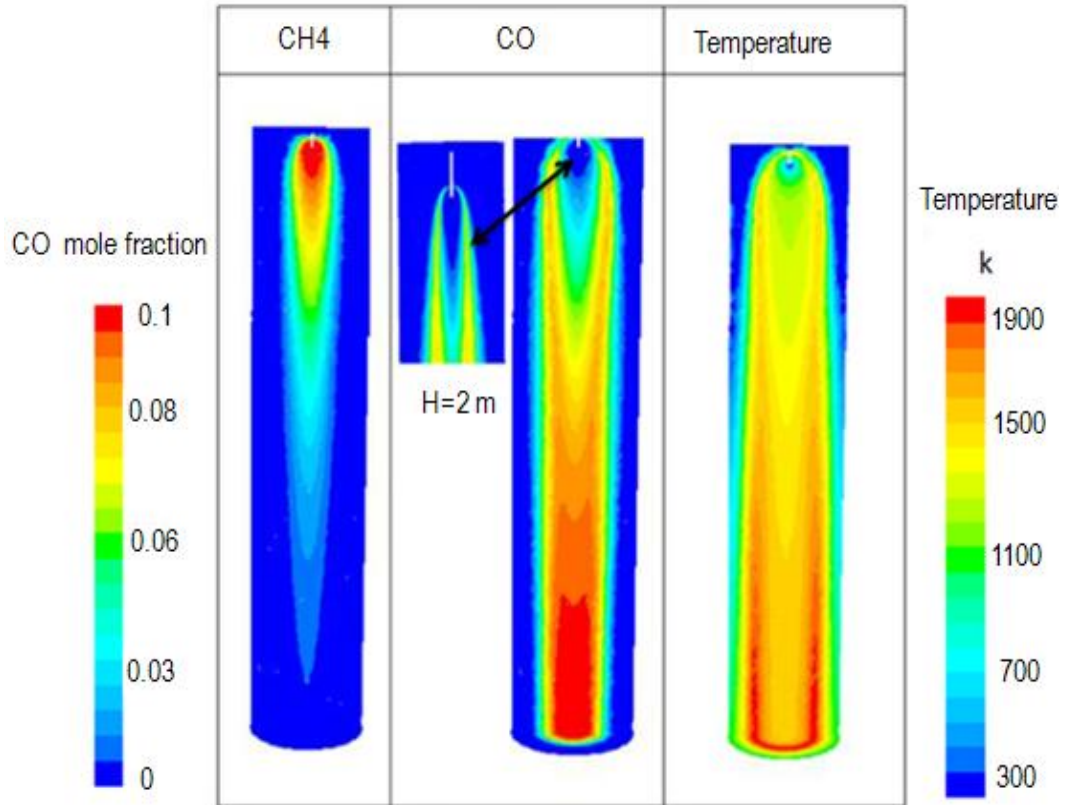
Figure 5.30: Contours of one burner reactive flow (n=1, λ=1.3 H=10 m).

Figure 5.31 shows the CH4 and CO concentrations after a 4 m distance from the burners. Both concentrations always have their lowest values near the walls. The maximum CH4 fraction is always in the center, while the concentration of CO has two peak values at the same radial distance as the temperature profile.
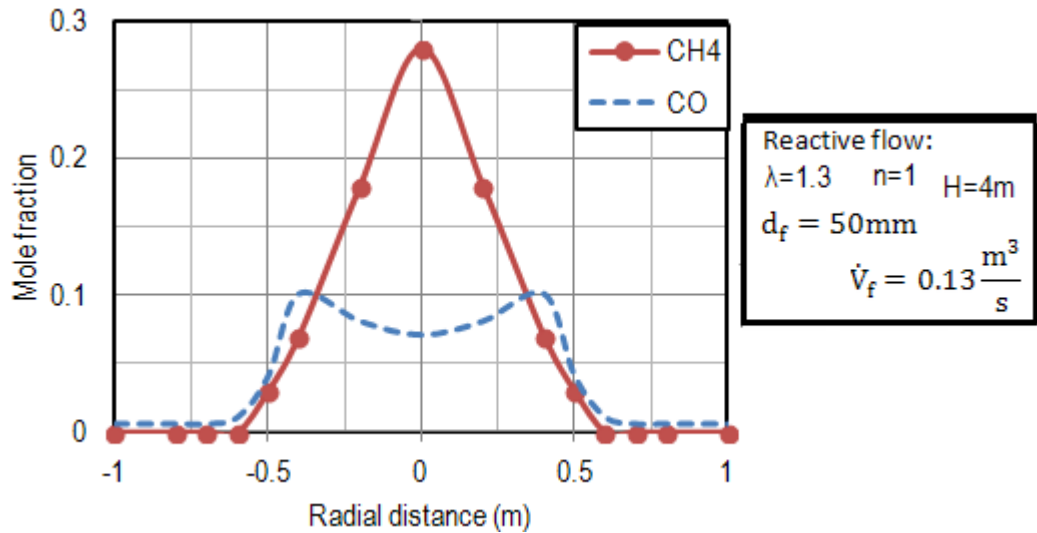
Figure 5.31 Fuel mole fractions in cross- section when H=4m.

Figure 5.32 shows the mole fraction axial profile. The methane mole fraction reaches zero after 8m. At this point, the CO has its maximum value on the axis. The CO concentration exists until a length of approximately 15 m.
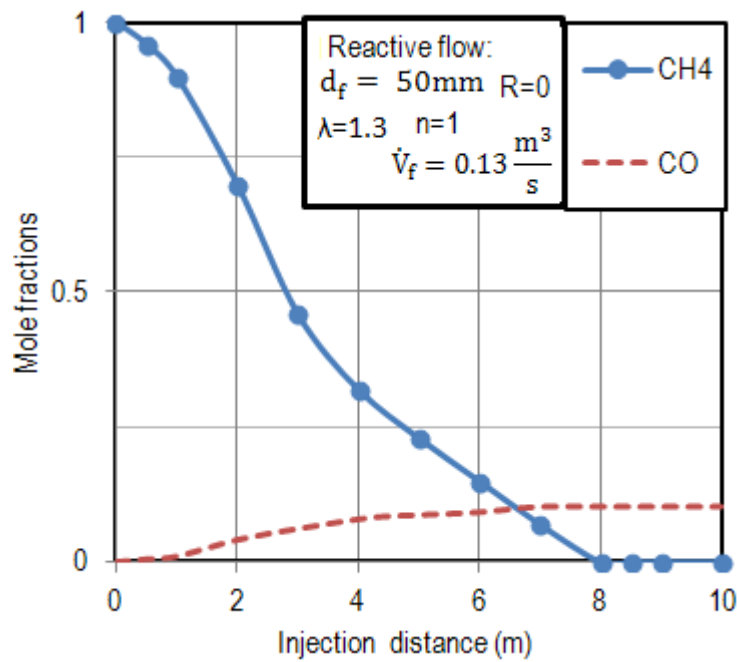
Figure 5.32: Axial mole fraction profiles.

The flame length can be estimated from the axial profile of the fuel fraction in the center. Figure 5.33 shows, the CH4 and CO reverse fractions versus the injection distance instead of the fuel fraction versus injection distance as it becomes very small. It can be seen that the methane concentration goes to zero after 8.5 m. In the non-reactive case (Figure 5.14), the flame length was estimated using the stoichiometric value. The mixing length was 7.5 m, which is near to 8.5 m. However, the

CO concentration reaches approximately zero after 15 m. There is no significant difference in flame length for porosities in the range of φ=0.32 to 0.6.
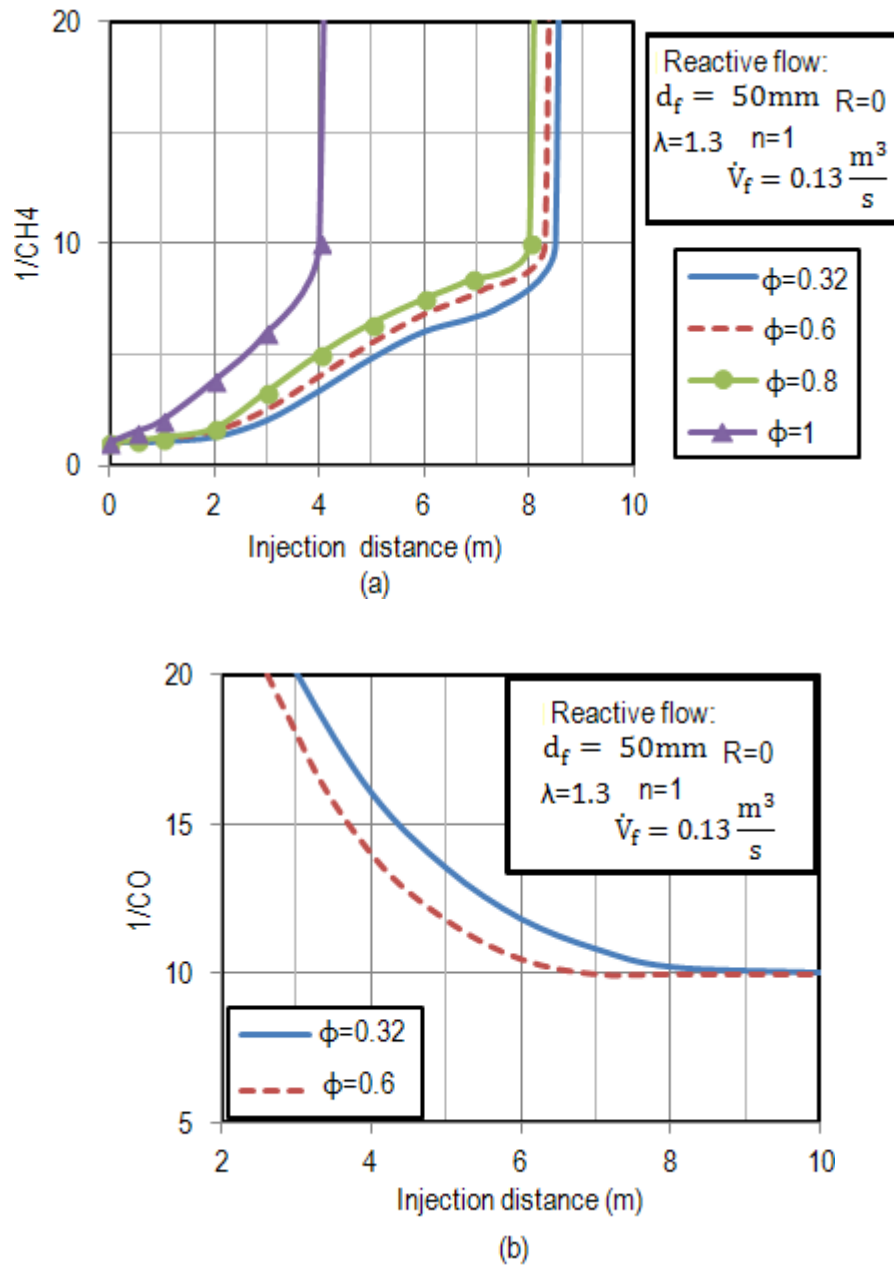
Figure 5.33: Influence of porosity on the (a) CH4 profile and (b) CO profile when n=1.

Figure 5.34 shows the influence of the excess air number for the CH4 contours presented. The higher the excess air number is, the shorter the combustion ranges. Especially for values lower than 1.1, the combustion length increases sharply.
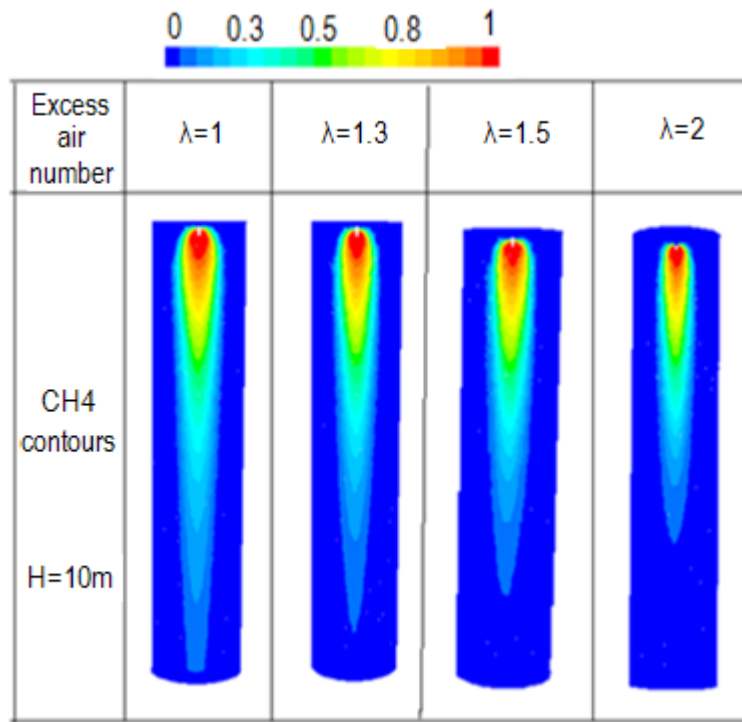
Figure 5.34: Influence of excess air number on the flame length.

The range of the flame length is between 6.2 and 9 m when λ=1.1 to 2. The CH4 mixing in non - reactive flow is always about 1 m shorter than reactive flow. It can be seen in Figure 5.35 that the mixing length starts to increase very sharply for values lower than 1.2.
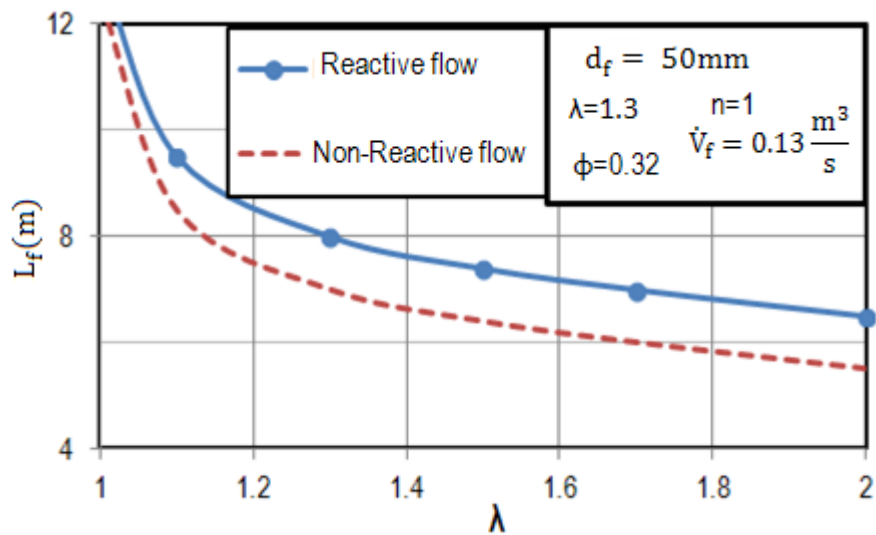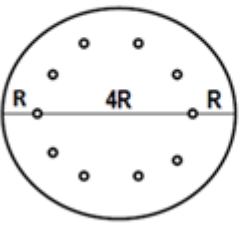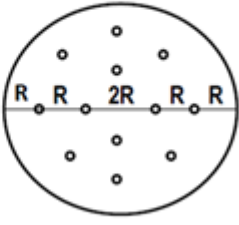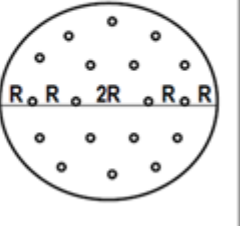
Figure 5.35: Influence of excess air number on the flame length.

5.4 Burner Fields

5.4.1 Principle burner arrangements

The previous section has shown that the fuel and temperature distribution in the cross-section is very inhomogeneous if only one burner used. Also, the flame length of 15 m is too long. To shorten the flame length, the fuel diameter or outlet velocity must be decreased, as explained in Figure 5.19. To insert the same amount of fuel, more burners must be used. With more burners, the fuel distribution in the cross-section can be improved. Various arrangements are possible for burners. To discuss the influence on the flame length, three principle arrangements were studied, as depicted in Table 5.3. The first arrangement includes ten burners placed only in an outer ring. In the second arrangement, the burners placed in two rings, eight burners in the outer ring, and four burners in the inner ring. In the third arrangement, again, two rings are used, but 12 burners placed in the outer ring and six burners in the inner ring. The distance between the burners is R=0.33 m, and the distance up to the cross-over channel is 6 m, which is a typical length for the burning zone in PFR kilns. The diameter of the shaft is 2 m, and the fuel amount is $0.13 \frac{m^3}{s}$ as before.

Table 5.3: Three types of burner arrangement.

Number of burners	n=10	n=12	n=18
Principle arrangement R=0.33m			

The burner diameter is kept constant at d_f =50 mm. The excess air number (air volume flow) is kept constant at λ=1.3. When the number of burners is increased from 10 to 18, only the fuel velocity is decreased from $6.6 \frac{m}{s}$ up to $3.7 \frac{m}{s}$.

Table 5.4: Used data of STP for n=10-18.

CH4 volume flow $\left(\frac{m^3}{s}\right)$	Burner diameter $d_f(mm)$	Fuel velocity $U_f\left(\frac{m}{s}\right)$ n=10	Fuel velocity $U_f\left(\frac{m}{s}\right)$ n=12
0.13	50	6.6	5.6
Combustion air volume flow $\left(\frac{m^3}{s}\right)$	Combustion air velocity $\left(\frac{m}{s}\right)$	Kiln diameter D(m)	Fuel velocity $U_f\left(\frac{m}{s}\right)$ n=18
1.6	0.5	2	3.7

5.4.2 Influence of burner arrangement on fuel profile

The fuel distribution in the core will be discussed in the next three Figures, which shows the contours in the cross-section for different heights. Figure 5.36 shows the contours for the arrangement with ten burners. It can be seen again that the fuel concentration at the wall and in the core is very less. However, the fuel mole fraction in the circumferential distance is relatively homogeneous.
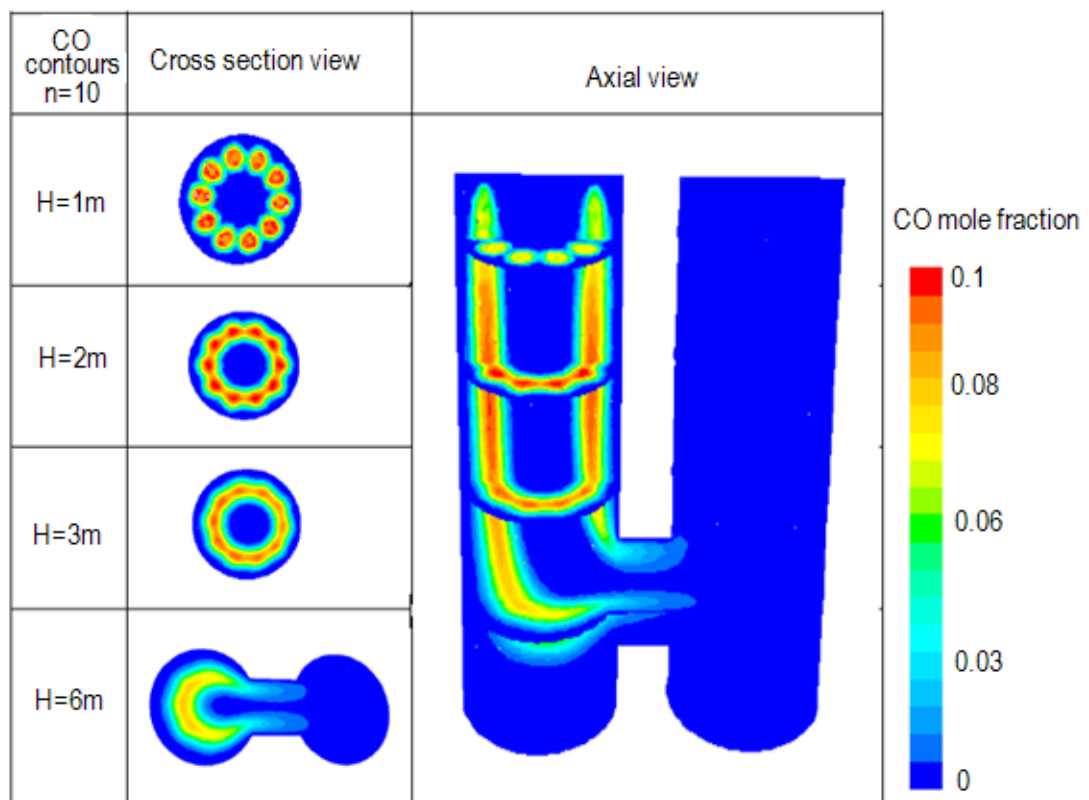
Figure 5.36 : Contours of carbon monoxide when n=10.

Therefore, in the second arrangement with 12 burners, the burners on the outer ring are reduced, and burners added to the inner ring. The contours are as shown in Figure 5.37. It can be seen that the burners are too close together. Therefore a staggered arrangement is preferable. Eight burners at the outer ring and four burners on the inner ring are also less for proper distribution in the circumferential direction.
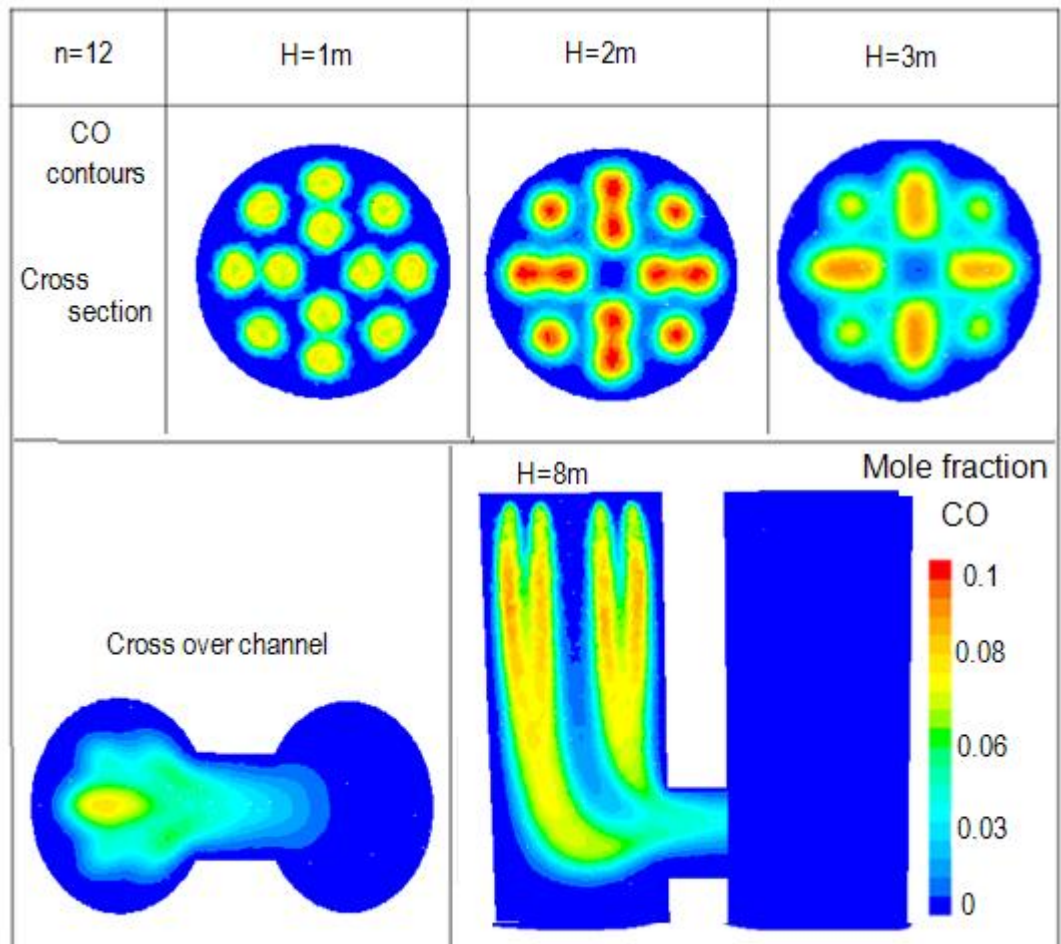
Figure 5.37: Contours of carbon monoxide when n=12.

The third arrangement depicted in Figure 5.38. The 12 burners placed on the outer ring and six burners on the inner ring. It can be seen that the distribution in the circumferential direction is relatively homogeneous.
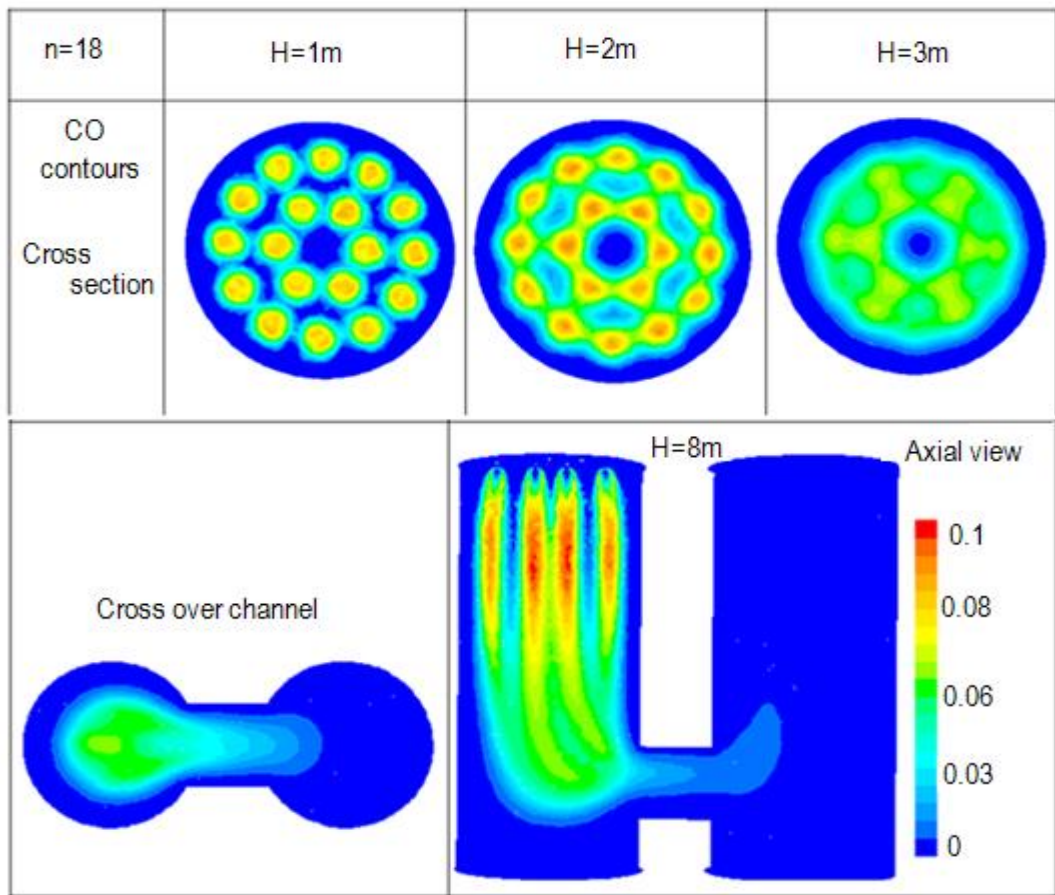
Figure 5.38: Contours of carbon monoxide when n=18.

Figure 5.39 shows the CO mole fraction of those three arrangements after a height of 3 m. It can be seen that no fuel reaches the wall and very less reaches the core. That is the reason for the low temperature at these positions.
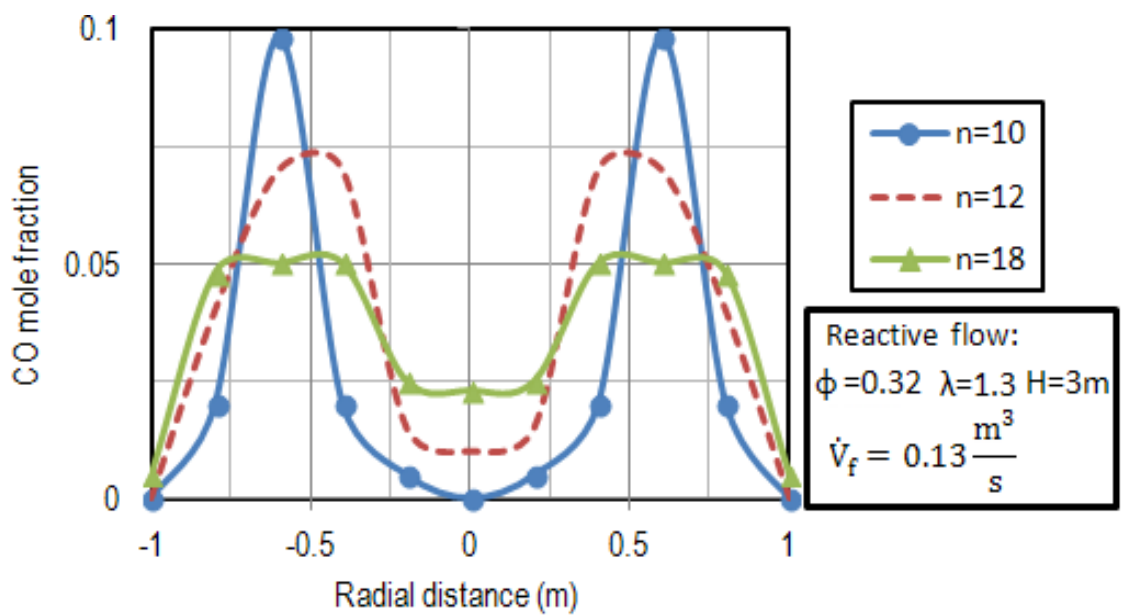
Figure 5.39: Fuel profiles in cross section at H=3 m.

As shown in Figure 5.40, arranging the burners on the outer radius (n=1-4) results in shorter flames, while the burners in the inner radius result in more widespread fuel distribution in the central area of the kiln (n=7-9). However, the range of fuel distribution is about 4.8 m to 5.2 m for various burners.
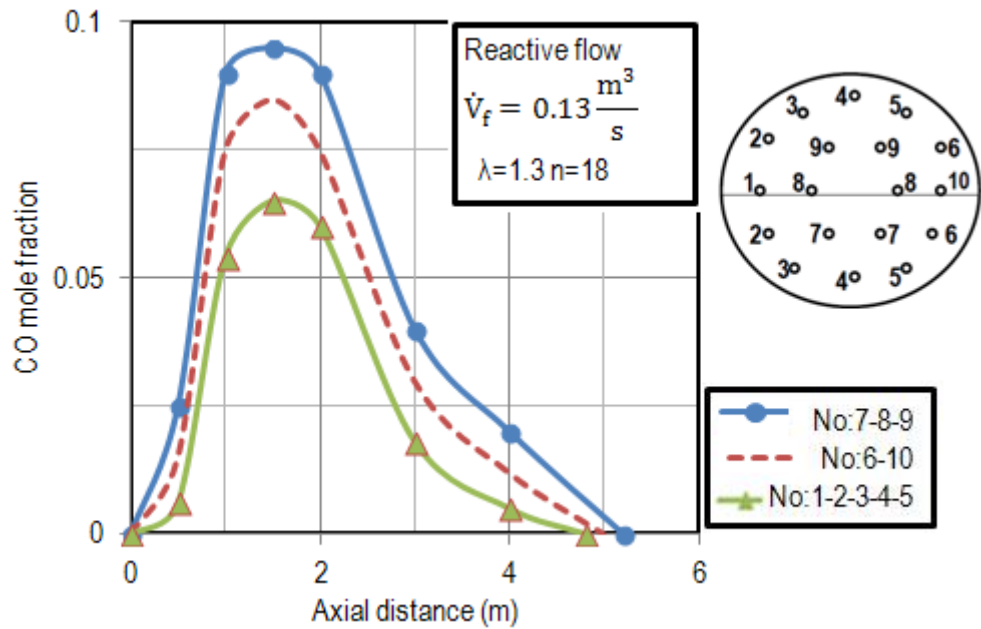
Figure 5.40: Fuel profiles in axial direction for various burners.

Figure 5.41 shows the axial profile of the CO mole fraction below a burner of the outer ring. After the end of the burning zone of 6m, all the fuel burnt. A burning zone of 6 m is enough for the complete burning of the fuel. The main problem is the distribution of fuel over the cross-section.
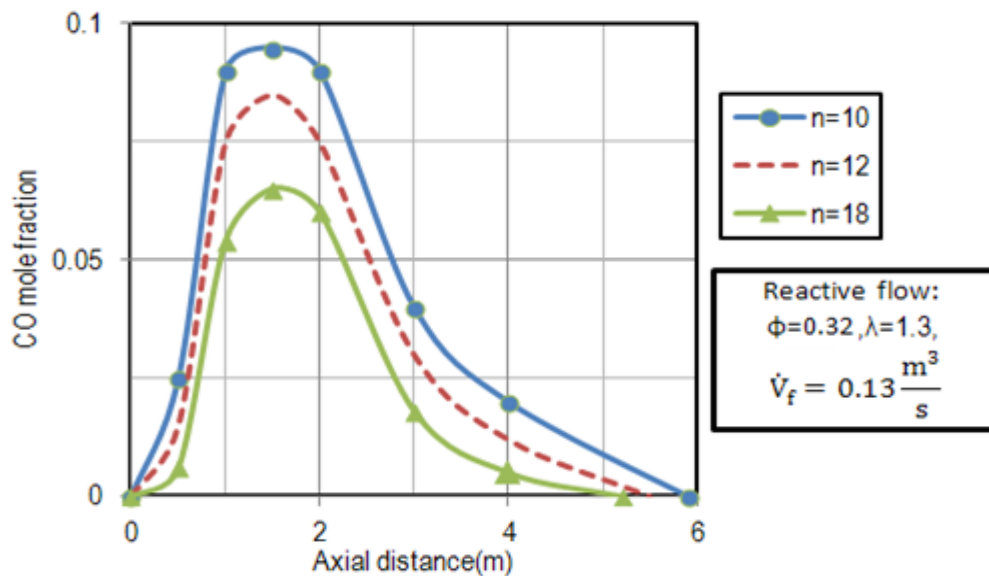
Figure 5.41: Influence of number of burners for various burner arrangements.

5.4.3 Influence of burner arrangement on temperature profile

Figure 5.42 shows the radial temperature profile for the three arrangements after a distance of H=2 m. For the profiles, the centerline shown in Table 5.3 is chosen, which hits the highest number of burners. The higher the number of burners is, the more homogeneous the temperature profile becomes. However, in all arrangements, a significantly low temperature exists in the core (center of packed bed) and at the walls. As a consequence, one burner should be placed in the core, and the burners of the outer ring should be shifted near to the wall.
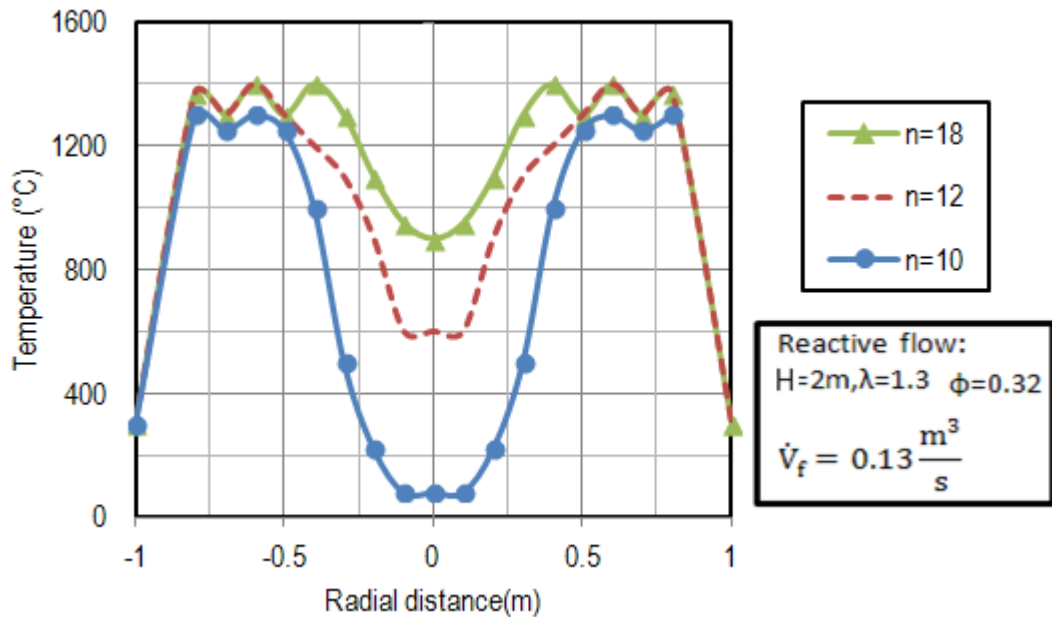
Figure 5.42: Temperature profile in radial direction for n=10-18.

Figure 5.43 shows the temperature profile at different heights. After 1 m distance from burners, there are still cold areas near the walls, and the minimum temperature located in the middle. After 2 m, the combustion gas temperature distributed more to the middle and near the walls. The temperature homogenization starts after a 2 m distance from the burners. The higher the distance from the burner is, the higher the temperature becomes.
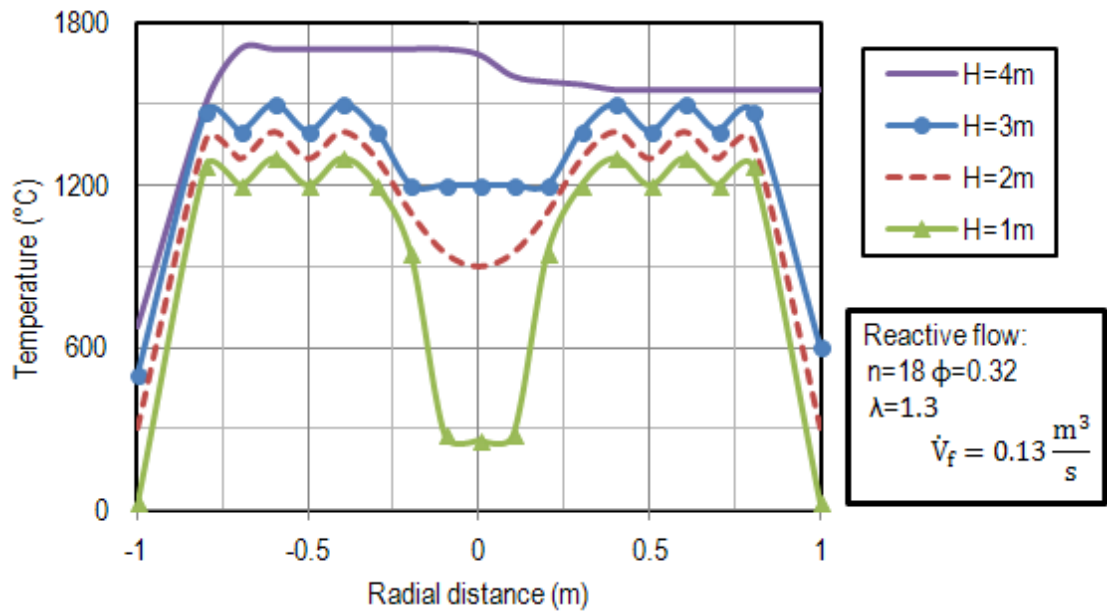
Figure 5.43: Temperature profile in radial direction at different heights.

The temperature profile dependent on axial distance is shown in Figure 5.44 for one burner as an example (No=7). The combustion gas temperature until 2 m height dramatically increases and reaches to the maximum value after 4 m distance from the burners.
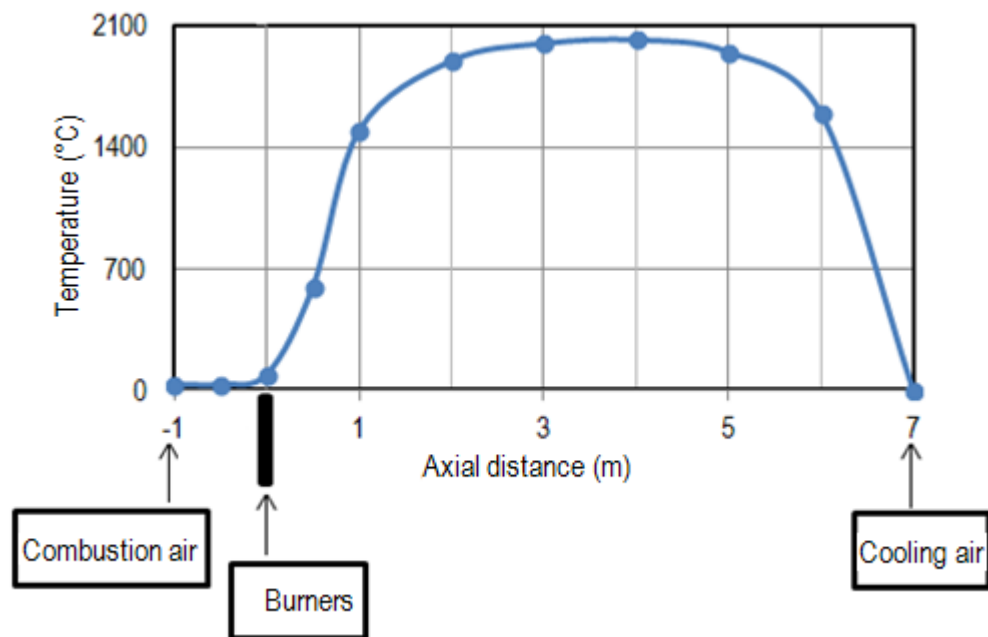
Figure 5.44: Temperature profile in height of the burning shaft kiln.

The temperature contours are shown in Figure 5.45. Even after a 2 m distance from the burners, low temperature still exists in the middle and near the walls. However, the temperature in the circumferential direction is relatively homogeneous after 2m.
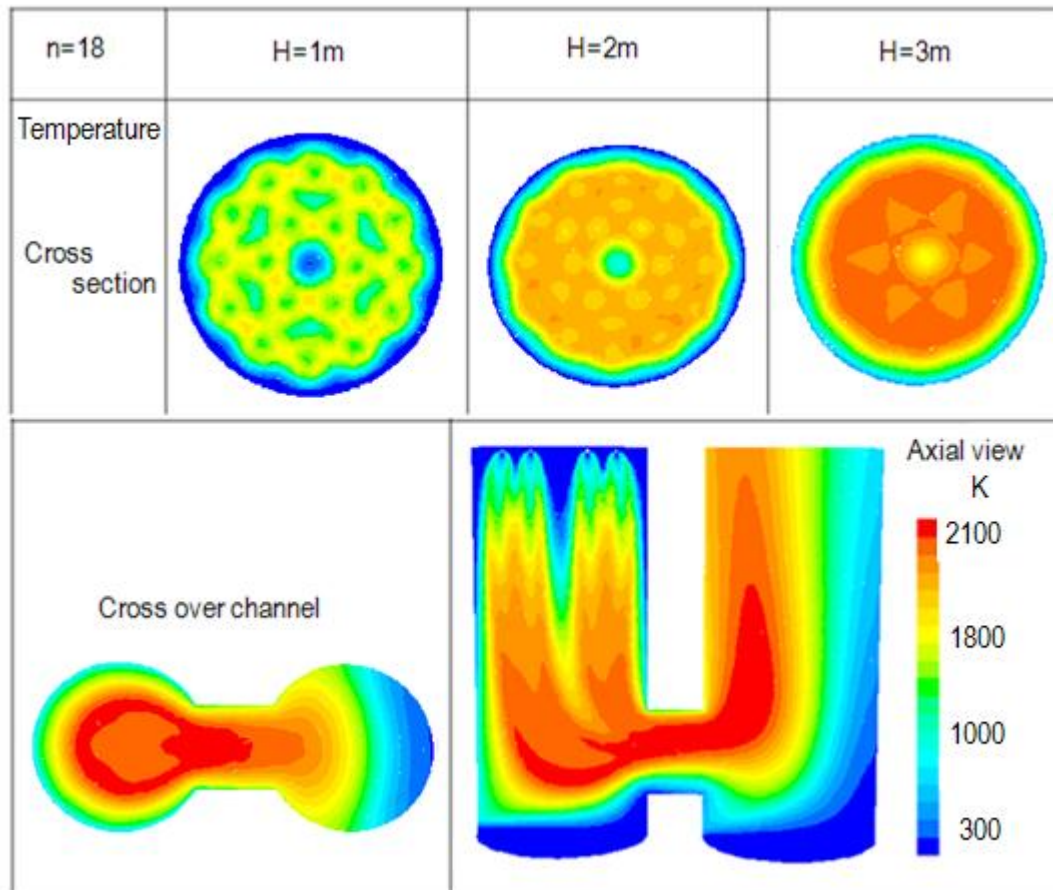
Figure 5.45: Temperature contour for n=18.

5.4.4 Extended arrangement

The extended arrangement includes 21 burners. Twelve burners placed in the outer ring, and eight burners set in the inner ring. One burner placed in the center. The distance to the wall decreased from 0.33 m (Principle arrangement) to 0.2 m. The same as before, the fuel diameter is kept constant at d_f =50 mm. In this case, the volume flow of combustion air and fuel is kept constant. When the extended arrangement used, the fuel velocity decreased from $3.7\frac{m}{s}$ to $3.17\frac{m}{s}$. The extended arrangement with 21 burners depicted in Table 5.5. The centerline below the burners in the radial direction showed for both arrangements.

Table 5.5: Schematic of extended arrangement.
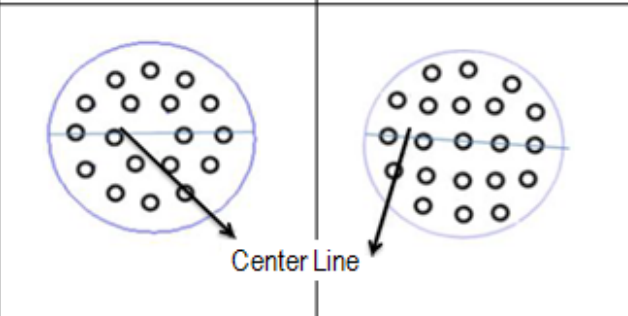
Φ=0.32 λ=1.3 $\dot{V}_f = 0.13\frac{m^3}{s}$ $d_f = 50mm$	Principle arrangement n=18 R=0.33 m $U_f = 3.7\frac{m}{s}$	Extended arrangement n=21 R=0.2 m $U_f = 3.17\frac{m}{s}$
Burner arrangements		Center Line

Figure 5.46 shows the CO concentrations after 2 m height from burners for both arrangements. The total amount of combustion air and fuel is kept constant. When the extended arrangement used, the CO profile is more homogeneous in the cross-section. In comparison with the 18 burners' arrangement, the fuel concentration near the walls and in the center significantly increased, and the peaks decreased. Figure 5.47 shows the CO contour. The fuel contour does not look as symmetric as before. The reason is that the flow converted in the other shaft with the cross-over channel. This cross flows mildly influences the flame length. However, this effect not considered in more detail because of the already existing designs of cross-over channels.
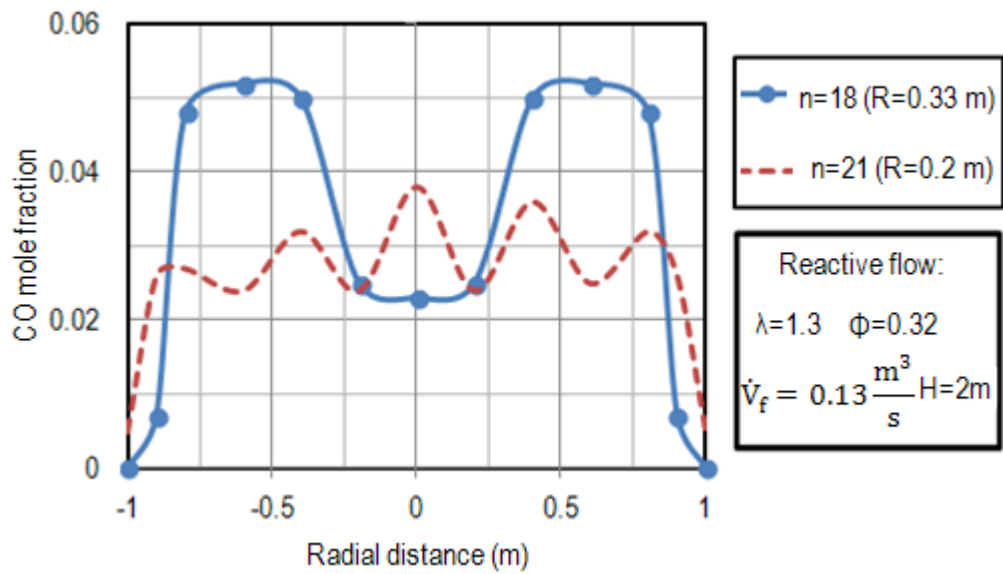
Figure 5.46: CO profile for n=18 and n=21 arrangements.
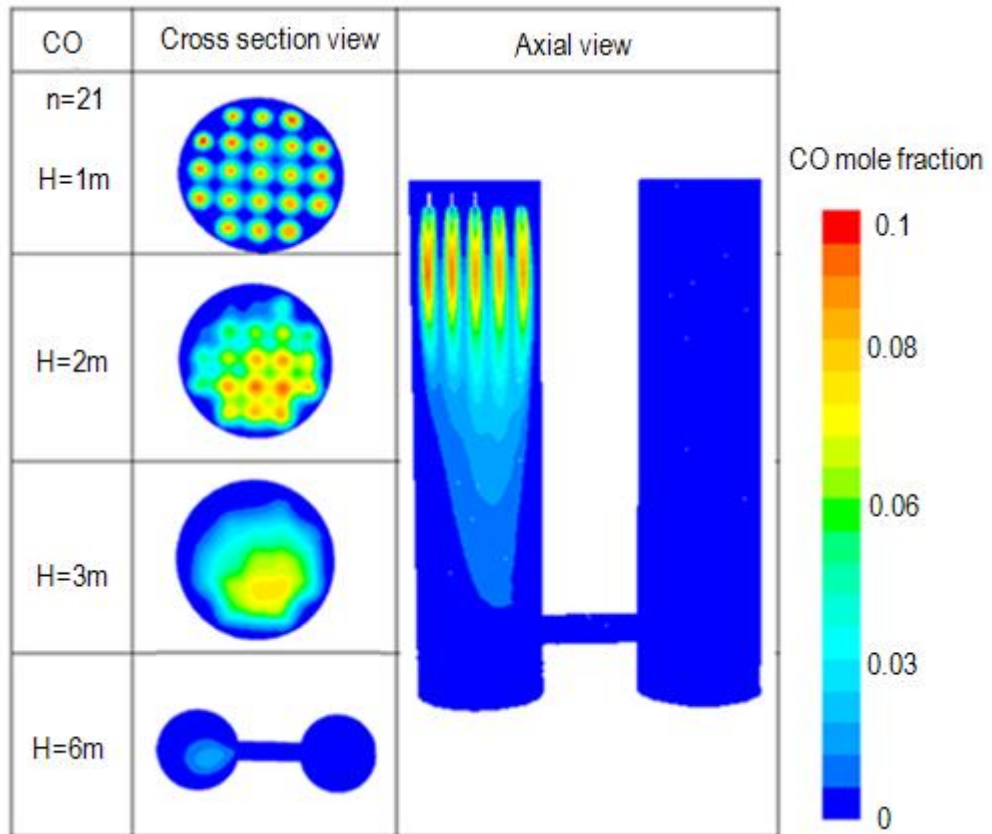
Figure 5.47: CO contours for extended arrangement (n=21).

Figure 5.48 shows CO concentrations at different heights when the extended arrangement used. After the 2 m distance from burners, the fuel profile is more homogeneous but not much more symmetric. The fuel concentration reached to near zero before the cross-over channel.
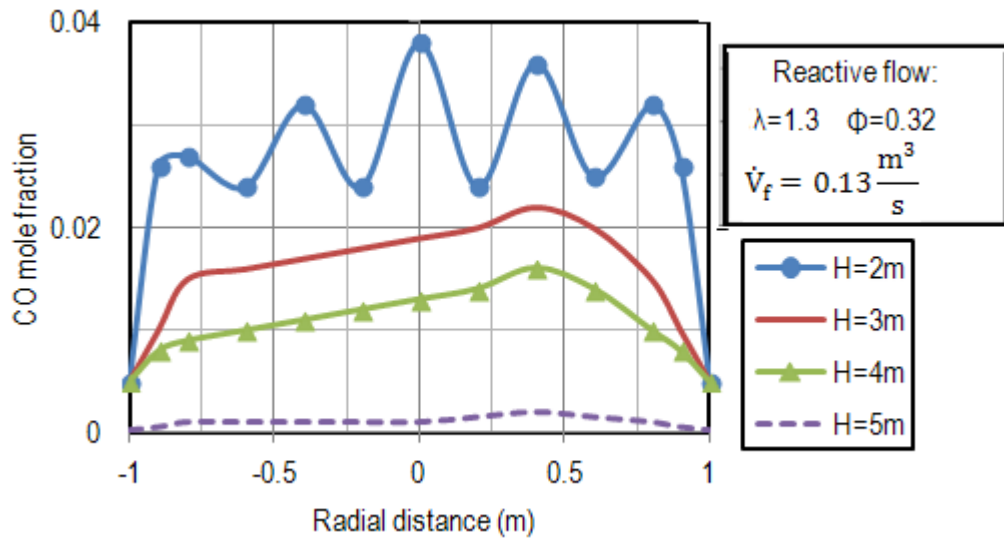
Figure 5.48: Fuel profile at different height when n=21.

Figure 5.49 shows the temperature profile for the two mentioned arrangements. The temperature near the walls and in the center increased when the extended arrangement used. The temperature is distributed more homogeneously in the cross-section after the 2 m height from burners when the extended arrangement used. Hot temperature covers more areas near the walls and in the center of the packed bed.
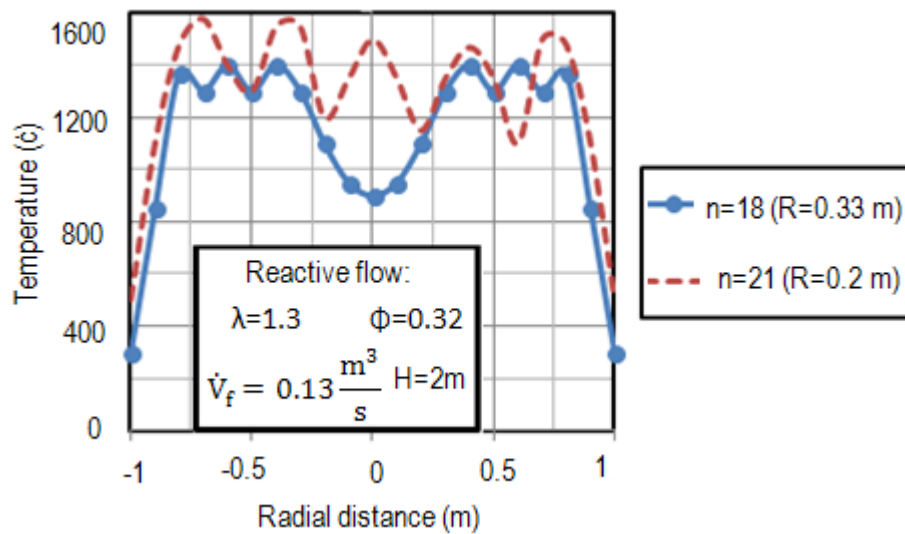
Figure 5.49: Temperature profile when n=18 and n=21.

Figure 5.50 shows the temperature profile at different heights. The higher the distance from the burner is, the higher the temperature becomes. In comparison with Figure 5.43, it can be seen that the temperature homogenization starts at a shorter distance from the burners. The homogenization distance decreased from 2 m (Principle arrangement n=18) to 1m (extended arrangement n=21). Five burners placed radially, as depicted in Figure 5.50. The positions can be seen with the profile at 1m height, where the relative minimum value of about 1000 °C exists.
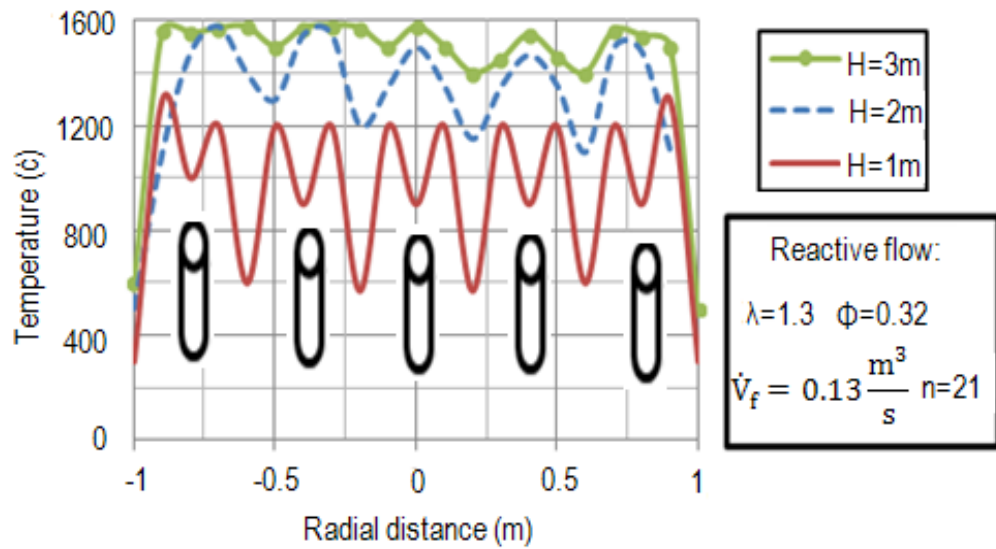
Figure 5.50 : Temperature profiles at different heights   when n=21.

Figure 5.51 shows the temperature contour. The contour is not perfectly symmetric because of the influence of the cross-over channel
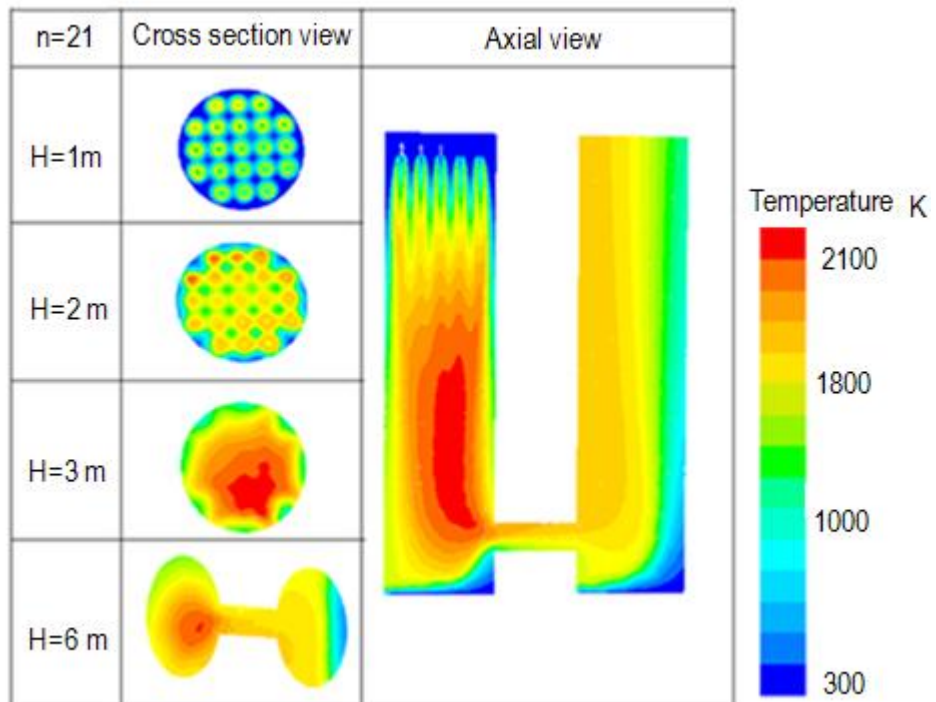
Figure 5.51: Temperature contour when n =21.

Hence, the fuel and temperature are distributed more homogeneously in the radial direction when the extended arrangement used.

1.4 Flame Length

5.5.1 Definition of flame length

The flame length of a single burner was already discussed in section 5.3.3. Now the definition of the flame length for more burners will be discussed. Figure 5.52 shows the CH4 and CO mole fraction contours. The Figure includes not only the burning shaft but also the cross-over channel and the non-burning shaft. In the case considered here, both shafts directly connected. In industrial applications, this exists only for rectangular shafts. For cylindrical shafts, the combustion gas is sucked off through holes in the walls. Then the gas is transported through a ring channel to the other shaft and blown in through these holes in the walls. This flow is difficult to calculate because of the complex geometry. In this study, the more natural direct connection closed, because only the principal influence of the cross-over channel should be shown. It can be seen from Figure 5.52 that the flow in the cross-over channel influences the flame length. Figure 5.40 shows the fuel concentration for different burners. The burners in the middle have a longer flame length. However, the differences are very small. In the following, only the burner with the longest flame considered.
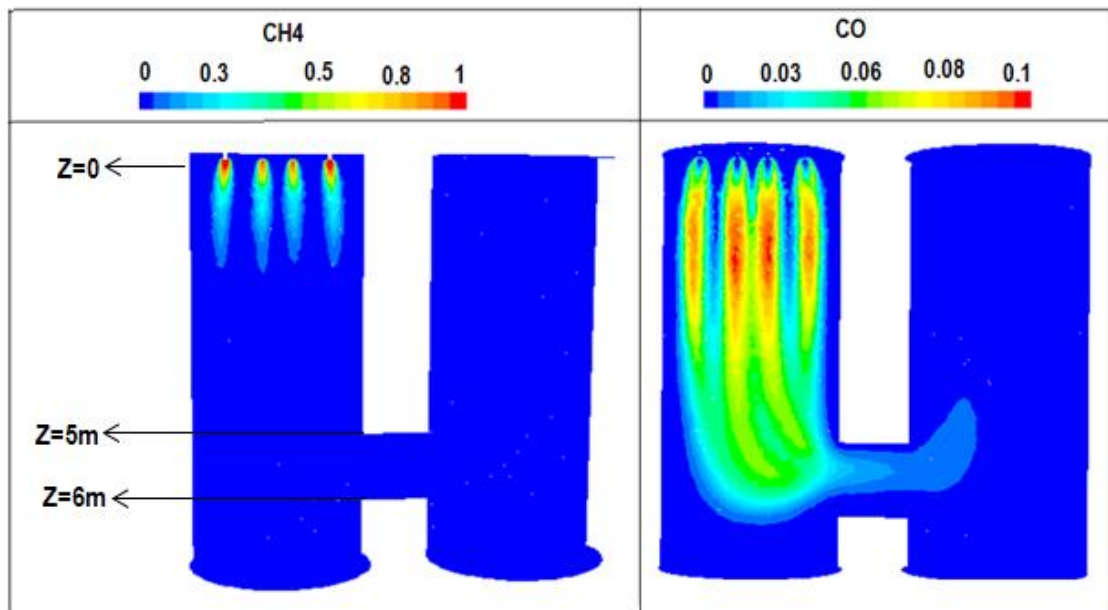
Figure 5.52: Fuel contours when n=18.

The flame length is one of the most important properties of non-premixed flames and a key factor for the design of a shaft kiln. So far, the flame length has been studied with different methods. The best performance is by those defined from the carbon monoxide ratio at $\frac{x_{CO}}{x_{CO_{max}}} = 0.01$. Therfore the flame length is the position where the CO concentration reaches to 1 percent of

maxium amount. It is also found that only the use of this definition exhibits the flame behavior and gains the height properly [59]. Figure 5.53 (a) shows the axial profile of CH4 and CO mole fractions. It can be seen methane has fallen to the near zero after approximately 4 m. While the CO has its maximum values after a 1 m distance from the burners and reaches to 1 percent of maximum amount after approximately 5 m. For better understanding, Figure 5.53 (b) shows the CO concentration after a height of 4 m up to 6 m. The flame length is defiend as the position where CO mole fraction has fallen to 1 percent of its maximum value ($\frac{X_{CO}}{X_{CO_{max}}} = 0.01$). As a consequence, the flame length in PFR shaft kilns is about 5.2 m, with the 18 burner arrangement.
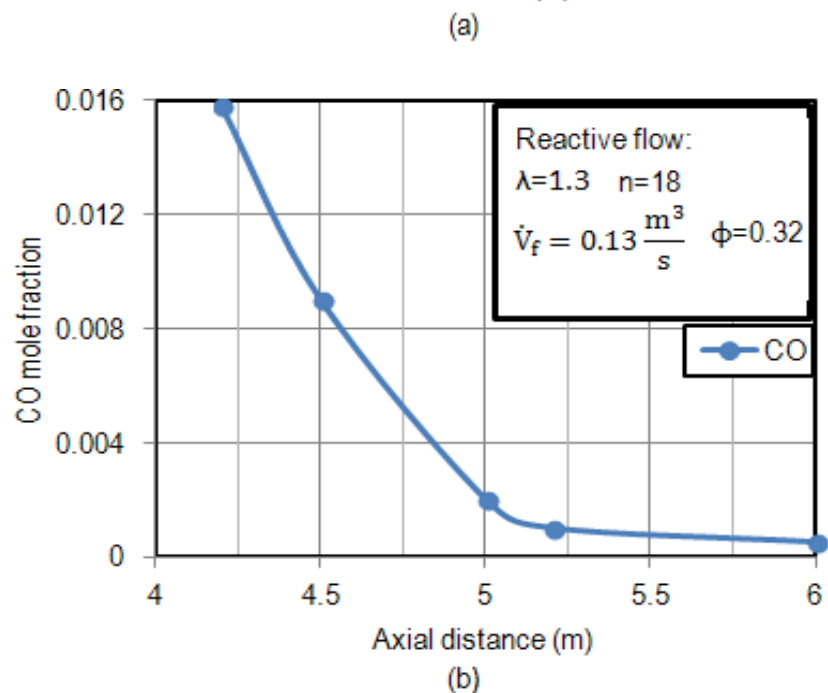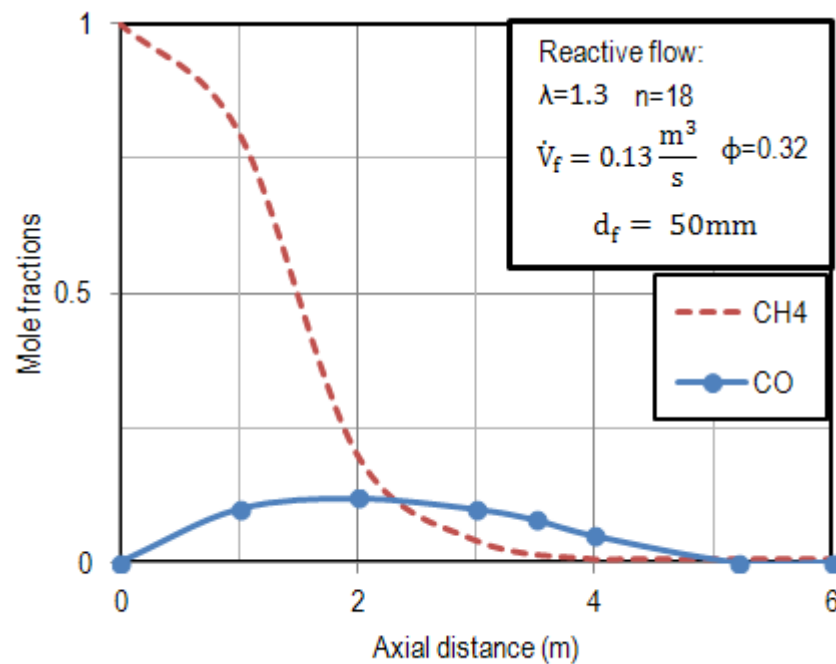
Figure 5.53: (a) Axial CH4 and CO profiles, (b) CO profile of H=4-6m.

In section 5.5.4, the extended arrangement with n=21 burners introduced. The fuel and temperature are distributed more homogeneously in the cross-section. In this case, the fuel burner diameter is kept constant at d_f =50 mm. Also, the volume flow of combustion air and fuel are kept constant. When the number of burners increased from 18 to 21, the fuel velocity decreased from $3.7\frac{m}{s}$ to $3.17\frac{m}{s}$. As a consequence, the higher the number of burners is, the shorter the flame length becomes. Table 5.6 shows the flame length.

Table 5.6: Influence of burner arrangements on the flame length.

$d_f = 50mm$ $\dot{V}_f = 0.13\frac{m^3}{s}$ λ=1.3	Principle arrangement n=18 $U_f = 3.7\frac{m}{s}$	Extended arrangement n=21 $U_f = 3.17\frac{m}{s}$
$L_f\,(m)$	5.2	4.7

5.5.2 Influence of porosity

Figure 4.4 shows two-particle arrangements in a packed bed mentioned. The minimum porosity is ɸ=0.32 when the particles arranged in the form of a B.C.C. Table 5.7 shows the influence of porosities in the range of ɸ= 0.32 up to ɸ =0.6 on the flame length. For this purpose, all parameters are kept constant. Only the porosity is changed. The flame length is decreased from 5.2 m up to 5 m. The porosity in lime shaft kilns is always in the range of ɸ=0.4 to 0.42. Therefore, there is no significant difference in the flame length when porosity changed from 0.32 to 0.6.

Table 5.7: Flame length for various porosities for $d_{p=}100mm$.

n=18 λ=1.3 $d_f = 50mm$ $\dot{V}_f = 0.13\frac{m^3}{s}$	ɸ=0.32	ɸ=0.6
$L_f\,(m)$	5.2	5

Figure 5.54 shows the CO contours for two porosities φ=0.32 and φ=0.6. The higher the porosity is, the shorter the flame length becomes. When the porosity is 0.6, a lesser amount of fuel concentration goes to the cross-over channel. As discussed in Figure 5.53, the flame length is in

the range of 5 to 5.2 m. Therefore the total height of 6 m is sufficient to research flame length in PFR lime shaft kilns.
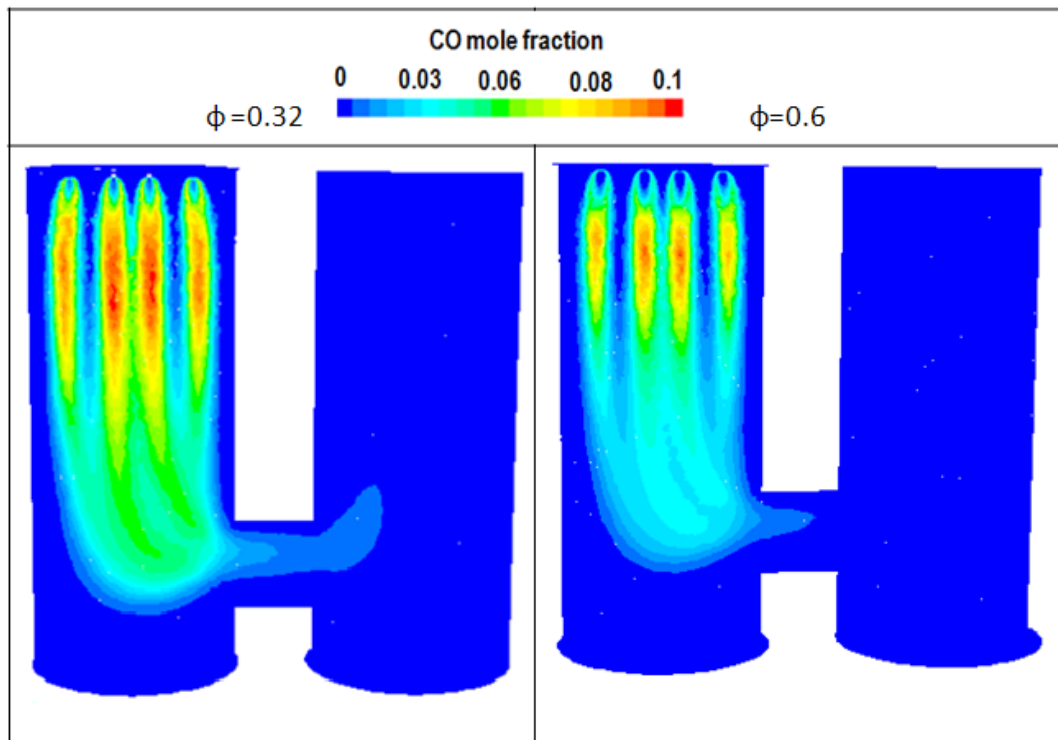
Figure 5.54: CO contours of packed bed arrangements.

5.5.3 Influence of excess air number

At first, the influence of the excess air number on the flame length will be discussed. When the excess air number changed from $\lambda=1$ up to $\lambda=2$, the combustion air volume flow increased. That means the velocity of combustion air increased from the value of $0.39\frac{m}{s}$ up to $0.78\frac{m}{s}$. Figure 5.55 shows the CO contours for different excess air numbers. The higher the excess air number is, the shorter the flame length becomes. For the higher value of two, the fuel completely burnt before the end of the burning shaft. For both values of 1.3 and 1.5, the combustion reaches the cross-over channel.

(a)
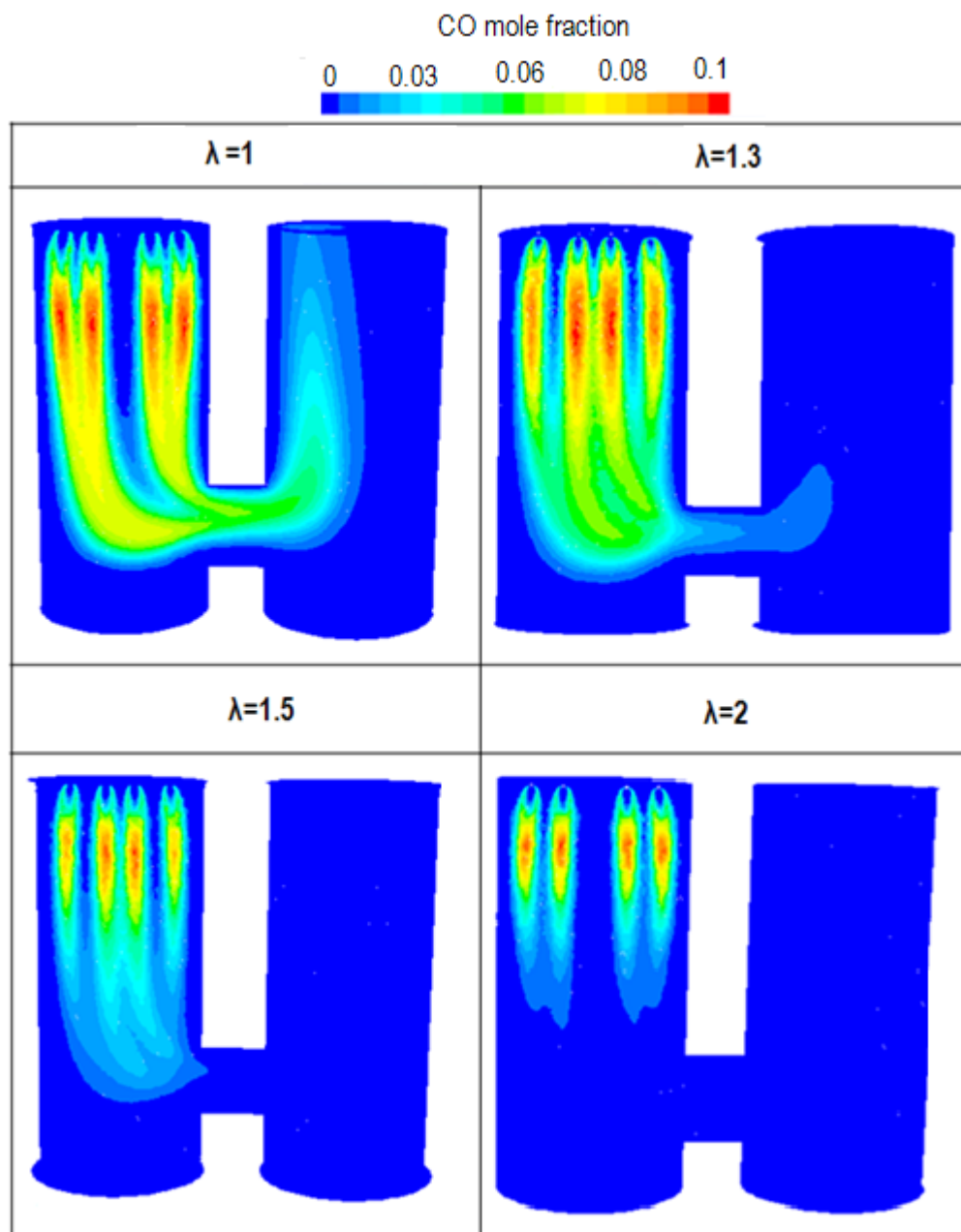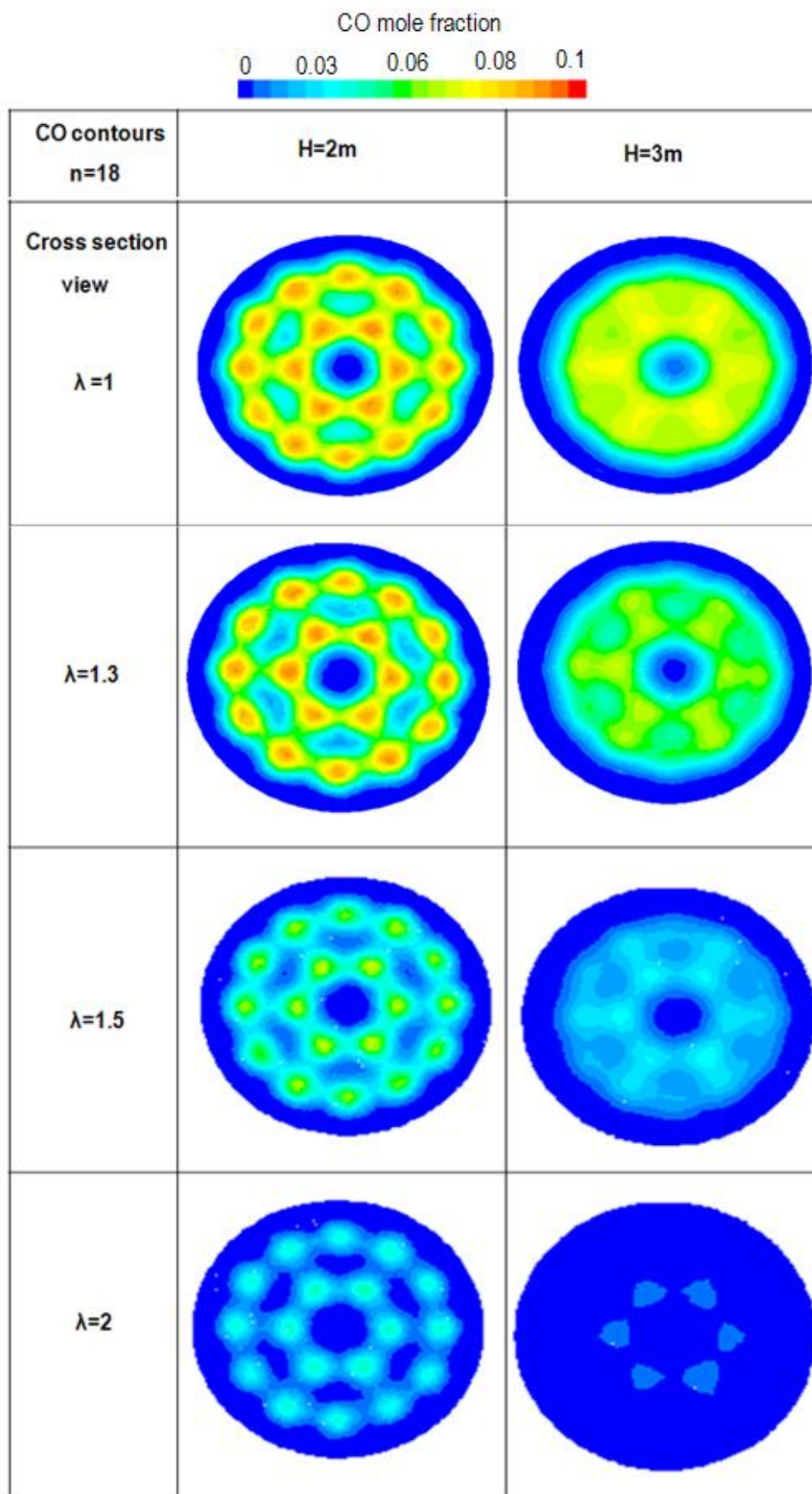
Figure 5.55: CO contours when λ=1-2: (a) Axial direction, (b) Radial direction.

A 5 m length of the burning shaft is too small for complete combustion. Therefore, the burning shaft should have a length of about 6 m. For an excess air number of one, the final combustion takes place in the non-burning shaft, but only on the left side. The preheated cooling air flows in the right part, in which no combustion can take place. As a consequence, the combustion should be completed in the left shaft. Figure 5.56 shows the dependence of flame length on the excess air number. It can be seen that the flame length starts to increase very sharply for values lower than 1.2. When the excess air number increased from λ=1.1 to λ=2, the flame length decreased from 9.5 m to 3 m.
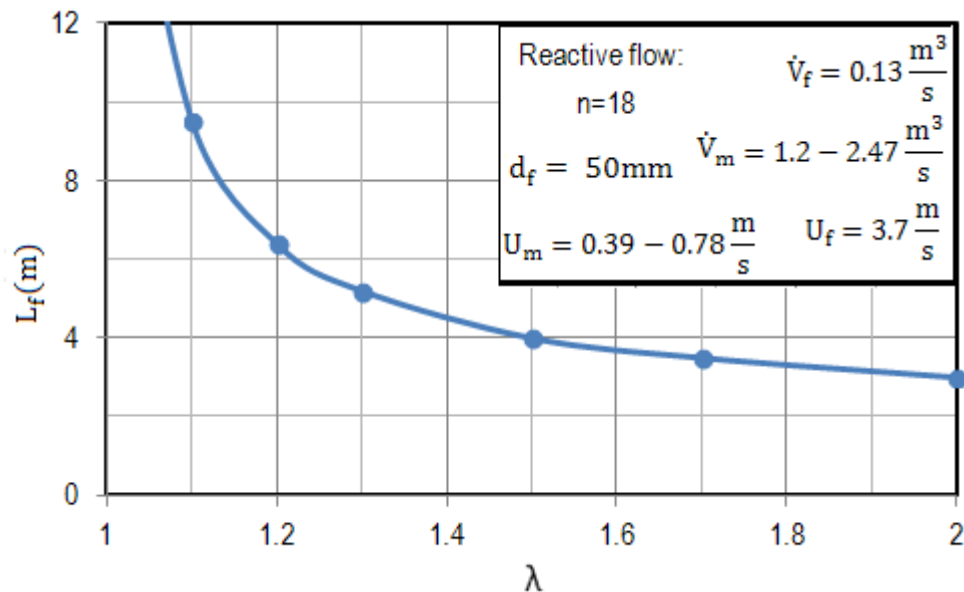
Figure 5.56: Influence of excess air number on flame length.

5.5.4 Influence of fuel velocity

Figure 5.57 shows the influence of fuel velocity (a) and burner diameter (b) when the fuel volume flow is kept constant. The number of burners and the excess air number are kept constant. Fuel velocity increased from $3.7\frac{m}{s}$ up to $92\frac{m}{s}$. For this aim, the burner diameter decreased from 50 mm to 10 mm. The higher the fuel velocity is, the longer the flame length becomes. When the fuel velocity is increased from $3.7\frac{m}{s}$ to $92\frac{m}{s}$ (by about 20 times), the flame length increased by 0.6 m. the various particle sizes (d_p =20 to 150 mm) studied. As a consequence, the bigger the particle diameter is, the longer the flame length becomes
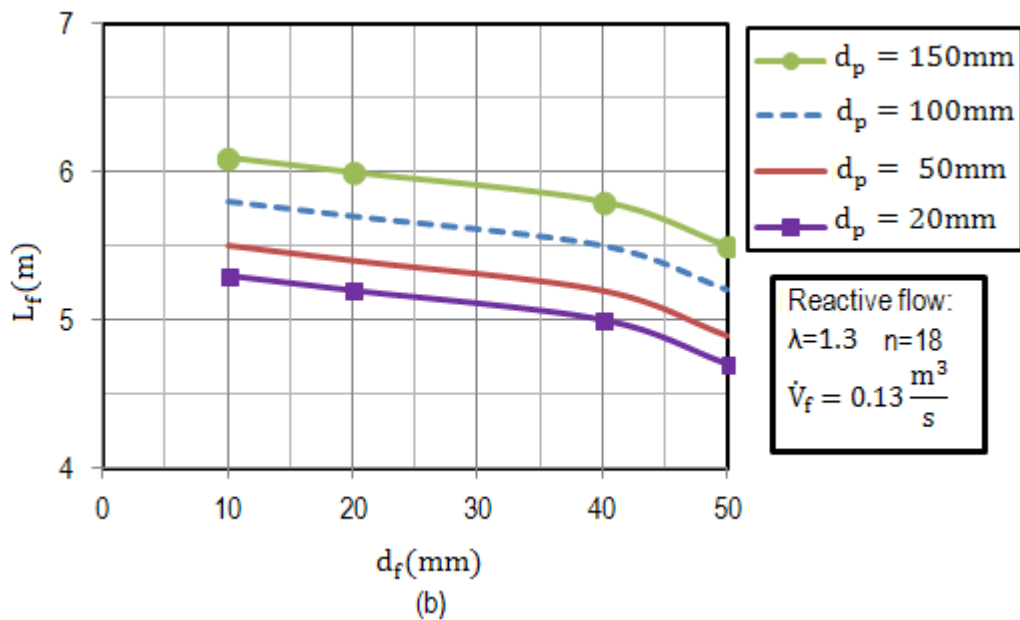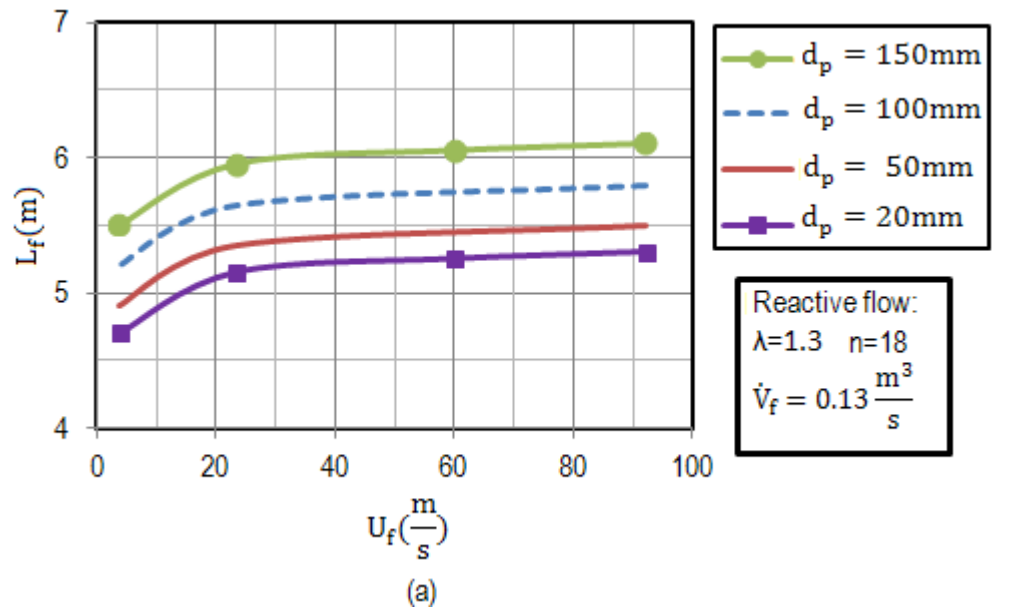
Figure 5.57: Influence of fuel velocity on flame length.

Figure 5.58 shows the influence of the product of the burner diameter and fuel velocity on the flame length. The three fuel velocities, U_f=3.7, 23.3 and 92$\frac{m}{s}$, are injected from the three typical burner diameters, d_f =10, 40, and 50 mm. It can be concluded that the flame length increases linearly with the product of fuel velocity and burner diameter. When the fuel volume flow is constant, the product of burner diameter and fuel velocity was calculated with the Eq (5-4) below:

$$V_f = \frac{n.\pi}{4}.d_f^2.U_f \rightarrow U_f.d_f = \frac{4.V_f}{n.\pi}.\frac{1}{d_f} \rightarrow U_f.d_f \sim \frac{1}{d_f} \qquad (5\text{-}4)$$

As a consequence, the product of burner diameter and fuel velocity is inversely proportional to the burner diameter.
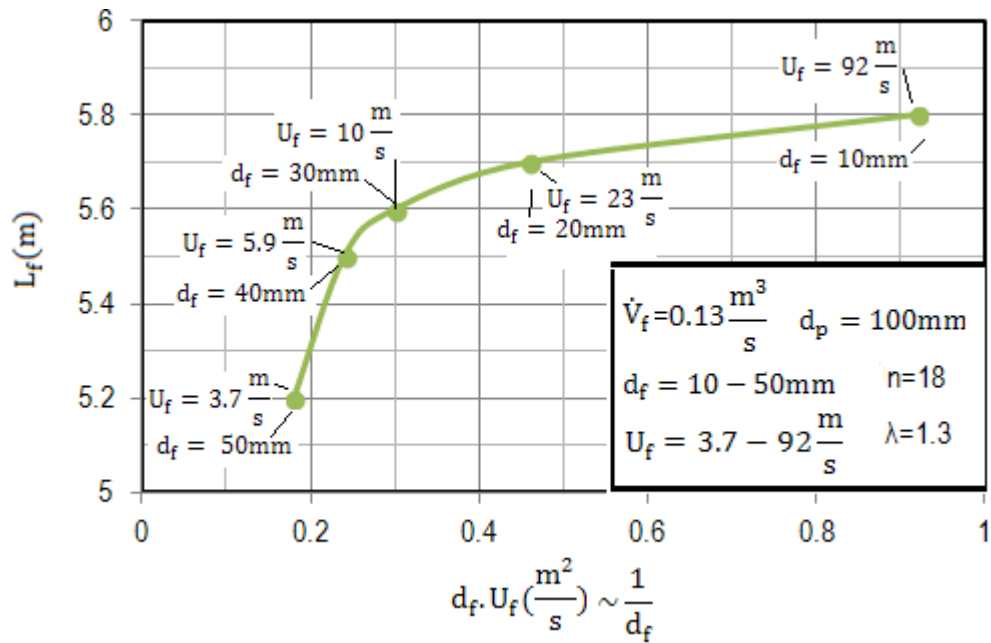
Figure 5.58: Influence of product of burner diameter and fuel velocity.

5.5.5 Influence of particle diameter

Figure 5.59 shows the influence of particle size. Bigger particle diameters lead to longer flame length. When the particle diameter increased from 20mm up to 150mm (about seven times), the flame length increased about 0.8 m.

The flame length depends on the particle diameter. This was studied for various fuel velocities $U_f = 3.7 - 92\frac{m}{s}$. The higher the fuel velocity always injected from a smaller burner. As a consequence, when methane used as a fuel, the flame length in PFR lime shaft kilns is varied in the range of 4.8 m up to 6.2 m. Particle size and fuel velocity (Burner diameter) are the main influencing parameters on the flame length. In this case, the fuel volume flow and air excess number are kept constant.

.
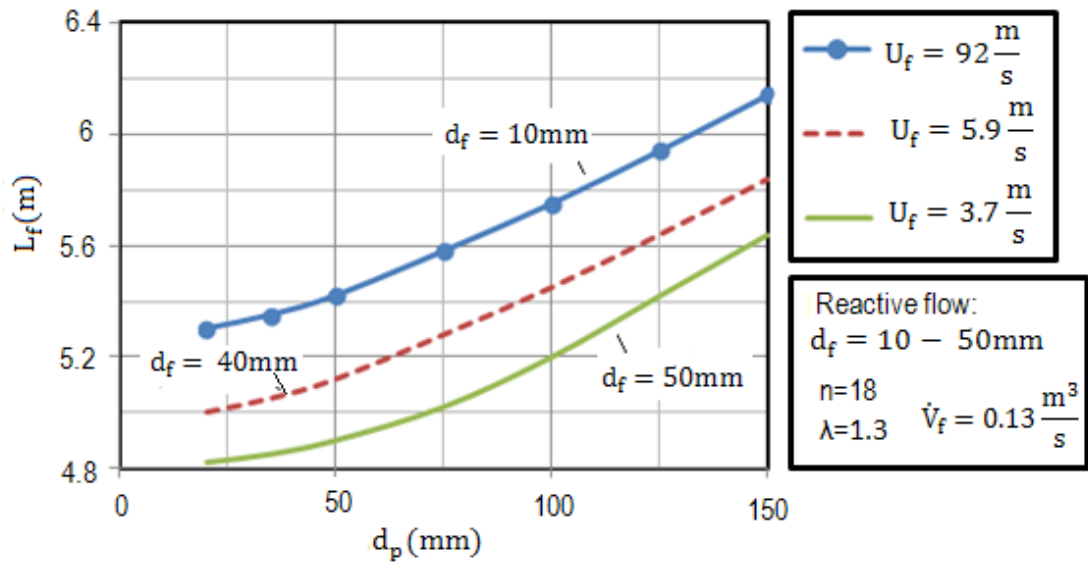
Figure 5.59: Influence of particle size on flame length.

5.5.6 Influence of different types of fuel

Fuels are characterized by their physical state (gaseous, liquid, and solid) and by their chemical composition. The material specifications of the fuels provided in Table 5.8. The excess air number and energy input are kept constant for all types of fuels. The fuel volume flow was changed while the burner diameter is kept constant (d_f= =50 mm).

Table 5.8: Material specification of different types of fuel.

Phase	Fuels	Molecular Formula	Molecular weight	Lower Heating value LHV MJ/kg
Gas	Methane	CH_4	16	50
Liquid	Methanol	CH_3OH	32	20
Liquid	Ethanol	C_2H_5OH	46	26
Liquid	Benzene	C_6H_6	78	41
Liquid	Gasoline	C_8H_{18}	114	44
Liquid	Diesel	$C_{12}H_{22}$	166	43
Liquid	Fuel Oil	$C_{19}H_{30}$	258	41
Solid	Anthracite	C= 92%	-	27
Solid	Coal lv	C =86%	-	19
Solid	Lignite	C=70%	-	15

The non-premixed combustion model calculates the flame length with high accuracy and less computational times because the program does not require a solution for a large number of species transport equations. Therefore, this model gives enough information about flame length behavior when gaseous fuel used.

In the case of liquid and solid fuels, Ansys Fluent introduced to deal with the mixture species transport model. The advantage of this model is that the liquid and solid fuels are assumed to be in the mixture with air. This simplification allows users to research the influence of different types of fuels on the flame length in a single-phase flow. The multiphase flow models need a high computational time, and the results do not show significant differences with the mixture model. Therefore for comparison between various types of fuels, the mixture species transport model is used.

Gaseous fuels

Methane is used in the simulation program as an example for gaseous fuel (natural gas), and the results were compared with those of biogas in two cases: first when the energy input is equal, and second when the fuels flow rate is constant. The CO concentration in the axial direction is shown in Figure 5.60.
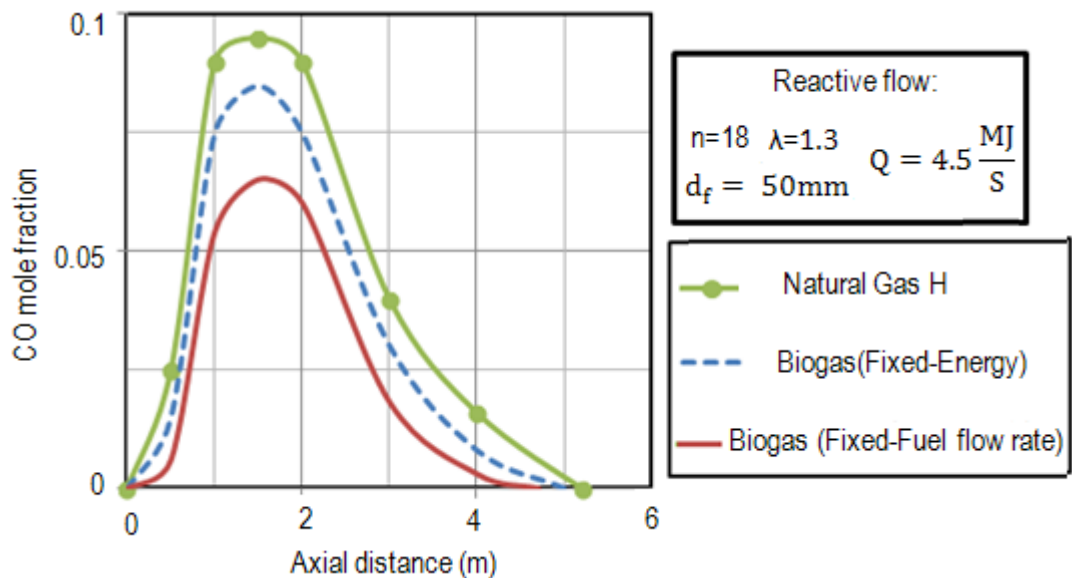
Figure 5.60: Influence of gaseous fuels on the flame length.

Using methane results in longer flames than the biogas when the energy for the two gases is kept constant.

Liquid fuels

The main difference between liquid fuels is their percentage of carbon and hydrocarbon content. For example, the fuel oils exhibit carbon content between 84 and 87% and hydrocarbon contents between 11 and 14%. The fuel oil results in longer flames in comparison to gasoline when the energy supplied is kept constant. The higher the percentage of carbon content is, the longer the flame length becomes. Table 5.9 shows the flame length of the different fuels.

Solid fuels

In many areas, coal, lignite, or pet coke are less expensive and more readily available than gaseous and liquid fuels. Here, three types of solid fuels simulated. The coal LV results in a longer flame. The influence of different kinds of fuels listed in Table 5.9. The gaseous fuels give the longest flames.

Table 5.9 Calculation of flame length for various types of fuels when λ=1.3

Type of Fuel	Constant in Energy Input	Flame Length $L_f(m)$
Gaseous	Natural Gas H	5.2
	Biogas	5
Solid	Coal LV	4.6
	Anthracite	4.3
	Lignite	3.8
Liquid	Fuel Oil (C19H30)	4.6
	Benzen (C6H6)	4.3
	Ethanol (C2H5-OH)	4.1
	Methanol (CH3-OH)	3.9
	Gasoline (Petrol-C8H18)	3.7

5.5.7 Influence of different types of PFR kilns

The circular and rectangular PFR shaft kilns have been used in a large number of industrial processes for the production of lime. Here, these two types of kilns investigated. All operation parameters such as fuel flow rate, number of burners, excess air number, and burner diameter were kept constant. As can be seen in Figure 5.61, the flame length for rectangular PFR kilns is about 0.3 m shorter than for the circular kilns. The fuel distributed to the edges of a rectangular kiln causing the fuel to collapse in the corners. Thus the fuel is not transported to the bottom of the kiln completely.
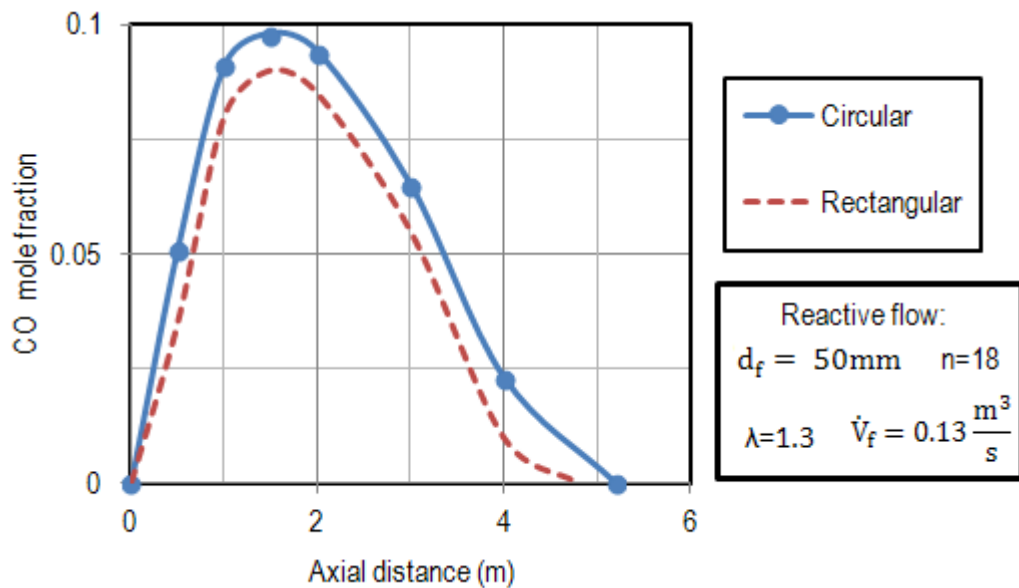
Figure 5.61: Axial CO concentration for circular and rectangular PFR lime kilns.

As it can be seen in Figure 5.62, the CO concentration has reached a zero value before the cross-over channel in the case of a rectangular PFR kiln because of the shorter flame length.
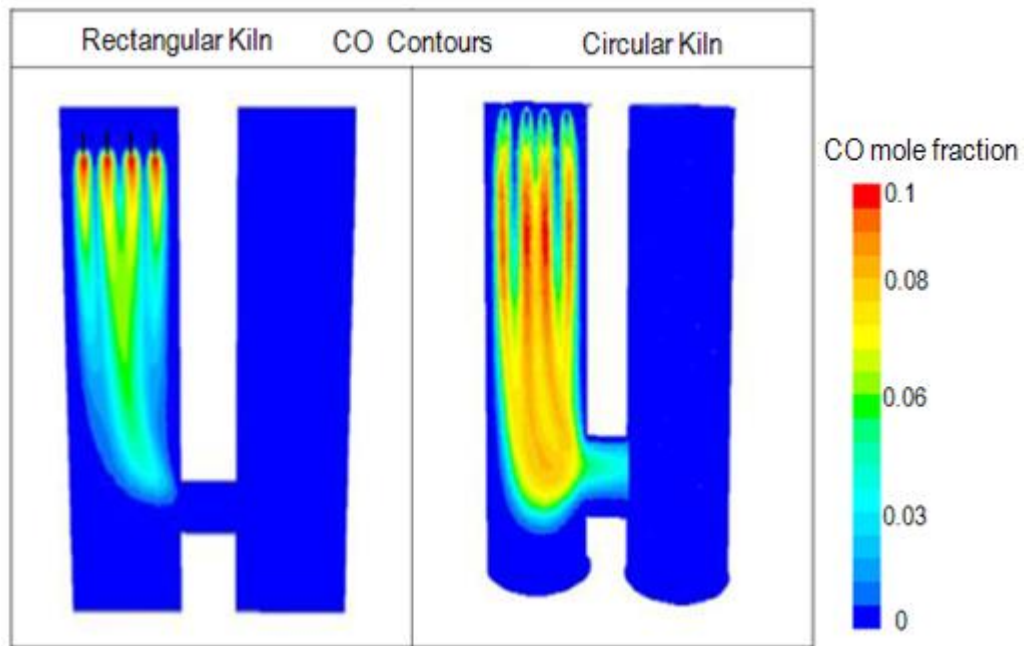
Figure 5.62: CO contours for circular and rectangular PFR Kilns.

5.5.8 Influence of fuel volume flow when λ=1.3

Here, the influence of various specific kiln throughputs is researched (from 50 to $400\frac{t}{day}$). For this aim, the fuel volume flow changed from $0.06\frac{m^3}{s}$ to $0.46\frac{m^3}{s}$. When the excess air number is kept constant the combustion air volume flow is changed from $0.7\frac{m^3}{s}$ to $5.7\frac{m^3}{s}$. Therefore, the air velocity increased from $0.23\frac{m}{s}$ to $1.8\frac{m}{s}$. The particle size and the burner diameters are kept constant. Table 5.10 shows the calculation of fuel and combustion air volume flows.

Increasing the fuel volume flow by about seven times increases the flame length by about 20 cm. The overall influence of the fuel volume flow on the flame length is very small. As a consequence, all results in this section for the chosen fuel volume flow of $0.13\frac{m^3}{s}$ can be generalized to all other fuel volume flows and also kiln throughputs

Table 5.10: Calculation of fuel and combustion air volume flows and flame length for D=2m.

CH4 PFR kiln n=18	Lime mass flow $\dot{M}_{lime}(\frac{t}{day})$	Fuel flow rate	Combustion air flow rate λ=1.3	Flame length $L_f(m)$
φ=0.32 $d_f = 50mm$ $d_p = 100mm$	$50 - 400$	$\dot{V}_f = 0.06 - 0.46\frac{m^3}{s}$ $U_f = 1.7 - 13.4\frac{m}{s}$	$\dot{V}_m = 0.7 - 5.7\frac{m^3}{s}$ $U_m = 0.23 - 1.8\frac{m}{s}$	$L_f=5.1\text{-}5.3\ m$

Chapter 6

Counter Flow Single Shaft Kiln (CFS)

6.1 Introduction

In CFS shaft kilns, the fuel is injected horizontally and not vertically, as before. Therefore, the fuel jet must be burned in a vertical direction. As a consequence, the penetration depth of fuel jets must be researched. To influence the penetration depth, a part of the combustion air was not pressed through the cooling zone but was injected horizontally with the fuel. Now additional parameters have to be investigated:

- Ratio of combustion air/cooling air ($\frac{V_j}{V_m} < 2$)

The influence of pervious parameters on the penetration depth and flame length is again listed below:

- Number and arrangement of burners (n=8-24)

- Fuel velocity (Burner diameter d_f=20-50 mm)

- Burner depth and two rows arrangements in the packed bed

- Kind of fuel (NG, coal, liquid fuel, etc.)

- Excess air number (λ=1-2)

- Particle size (d_p=20-150 mm).

Figure 6.1 shows the burners system in CFS lime shaft kilns with radial injection. The required thermal energy introduced through radially-arranged burners situated at one or more burner levels. Fuel and combustion air was distributed evenly throughout the CFS kiln using a defined number of burners arranged at the burner level. The burners protrude into the hotbed of material at different depths to enable an optimal fuel distribution over the whole cross-section of the kiln.

Some simplifications were made for the CFD simulation of reactive flow in a lime shaft kilns. They are as summarized below:

- The limestone is moving down the kiln. However, considering that the packed bed velocity is extremely low, the bed is defined to be fixed.

- The limestone varies in size and shape and is randomly packed in the kiln, even though the lime stones are assumed to be uniform spheres and having a uniform arrangement. In this research, the packed bed is modeled as a porous medium.

- The porosity distributions are presumed constant. However, the porosity in the packed bed changed in all directions.

- The bed is presumed to be stationary (steady-state) and the decomposition of limestone (solid phase) is not considered.

- The calcinations process does not influence the reactive flow. Therefore, it is not necessary to consider the process of heat transfer.
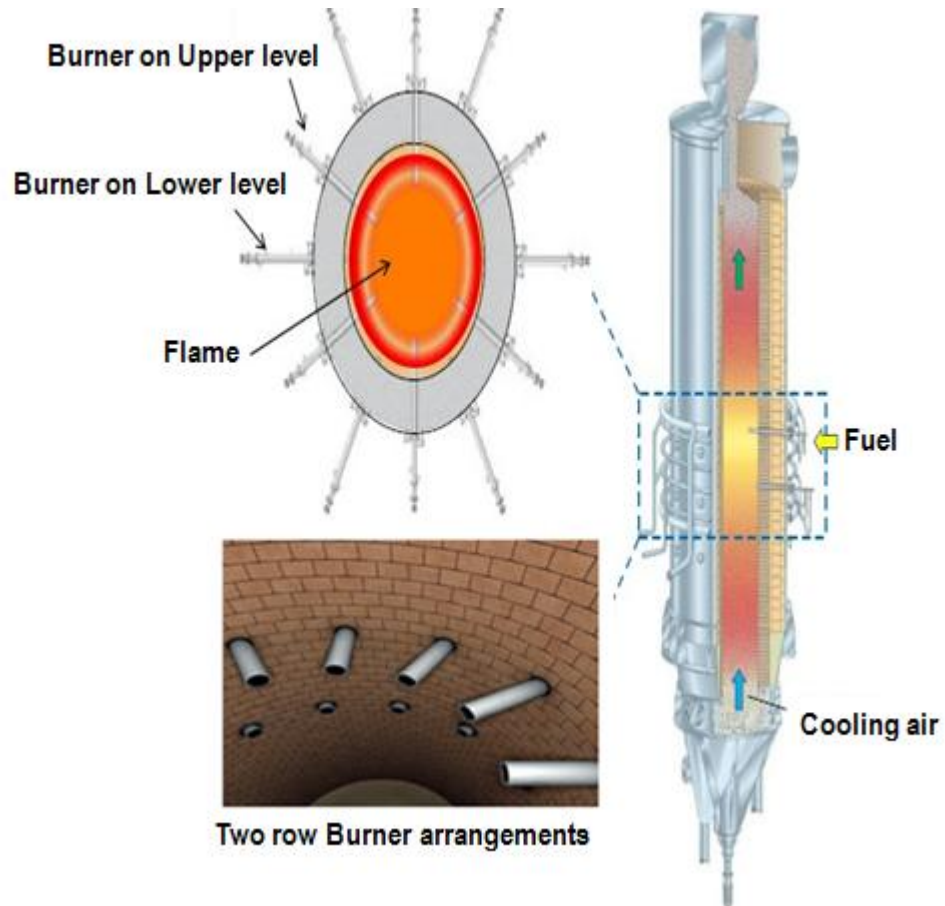
Figure 6.1: Burner arrangements in CFS lime shaft kiln.

The CFS kiln considered in Figure 6.2 has a total height of 10m and a diameter of 2m. The fuel used is natural gas. The fuel and combustion air radially injected from the burners, and the cooling air axially injected from the bottom. The burners' depth can be varied from the wall position, $L_b = 0$ up to $L_b = 0.3\text{m}$, depth through the packed bed.
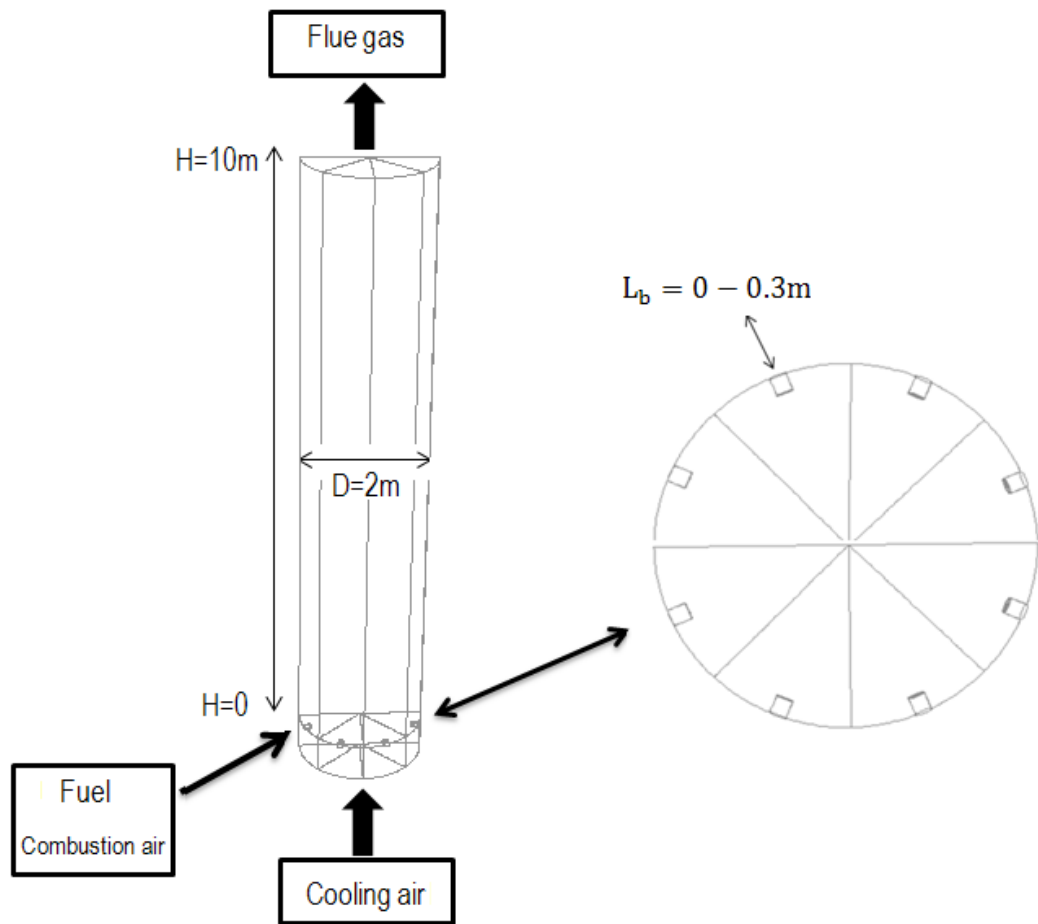
Figure 6.2: Schematic of radial flow injection.

The specific energy consumption is E=3.8$\frac{MJ}{Kg_{Lime}}$. The specific kiln throughput is 200$\frac{t}{day}$. The fuel lower heating value is 37000$\frac{KJ}{m^3}$. The kiln's specific fuel input is calculated by the Eq. (6-1).

$$E_{CFS} = \frac{\text{Heat Consumption}}{\text{Lower Heating value}} = 3800 \frac{KJ}{Kg_{Lime}} \cdot \frac{1}{37000\frac{Kj}{m^3_{Fuel}}} = 0.1 \frac{m^3_{Fuel}}{Kg_{Lime}} \tag{6-1}$$

In Table 5.11 it was concluded that, when the excess air number is constant, the influence of the fuel volume flow on the flame length is very small. The fuel flow rate is calculated using Eq. (6-2) below:

$$V_{Fuel} = E_{CFS}.M_{Lime} = 0.1 * 200 \frac{t}{d} = 0.24 \frac{m^3_{Fuel}}{s}. \tag{6-2}$$

The fuel velocity is calculated using Eq. (6-3).

$$U_f = \frac{4.V_{Fuel}}{n.\pi.d_f^2} \tag{6-3}$$

Where, n is the number of burners and d_f is the burner diameter. The amount of air is calculated using Eq. (6-4) as shown below:

$$V_{air} = \lambda. L. V_{Fuel} = 1.3 * 9.5 * 0.24 = 2.964 \frac{m^3}{s} \tag{6-4}$$

The methane air demand is $L = 9.5 \frac{m^3_{air}}{m^3_{CH4}}$. The amount of cooling air depends on the mass flow of lime, and is calculated using Eq. (6.5) as shown below:

$$M_{Cooling.air} \cdot C_{p.air} = M_{Lime} \cdot C_{p.lime} \rightarrow M_{Cooling.air} = M_{Lime} \frac{C_{p.lime}}{C_{p.air}} = 1.8 \cdot \frac{0.9}{1.15} = 1.4 \frac{m^3}{s} \qquad (6\text{-}5)$$

Therefore, the minimum value of cooling air is always equal to $1.4 \frac{m^3}{s}$ and the rest value from 3 $\frac{m^3}{s}$ is the combustion air of $1.6 \frac{m^3}{s}$. This amount of air was injected from combustion air burners. Table 6.1 shows the values of the fuel and air volume flow and velocities when n=8.

Table 6.1: Fuel and air volumes flow calculations.

Fuel volume flow $\dot{V}_{Fuel}(\frac{m^3_{Fuel}}{s})$	Fuel velocity $U_f(\frac{m}{s})$	Total air volume flow $\dot{V}_{air}(\frac{m^3}{s})$	Maximum Combustion air volume flow $\dot{V}_j(\frac{m^3}{s})$	Minimum Cooling air volume flow $\dot{V}_m(\frac{m^3}{s})$
0.24	15.2	3.0	1.6	1.4

6.2 Definition of Penetration Depth ($\frac{h}{r}$)

In CFS kilns, the fuel and combustion air radially injected from the burners, and the cooling air axially injected from the bottom. Therefore, the two gas streams of different flow rates have to be contacted at the burner level. Here, the jet diverted into the vertical (axial) direction. In this section, the fuel penetration in the radial direction and the influencing parameters investigated. Figure 6.3 shows the penetration depth defined as the ratio of the distance between the wall and maximum fuel position (h) to the radius of the kiln (R).
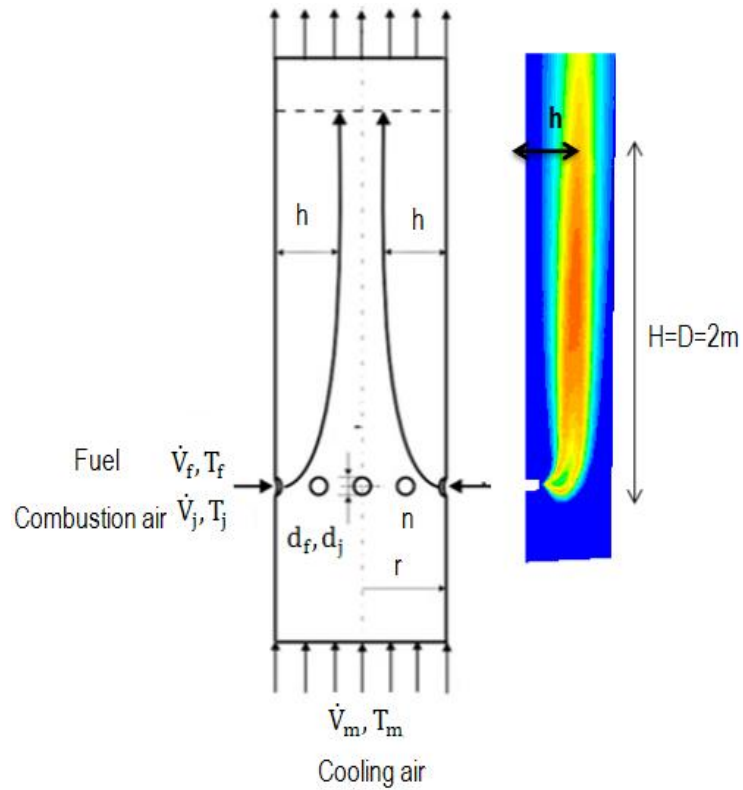
Figure 6.3: Schematic of flame profile in axial direction.

Figure 6.4 shows the CO concentration at different heights. For this aim, the burners arranged at the walls (($L_b = 0$). The air volumetric ratio is kept constant $\frac{V_j}{V_m} = 0.6$. It can be seen that the position of maximum fuel amount after 2m distance from the burners is constant. As a consequence, one kiln diameter distance from the burners is sufficient to estimate the penetration depth.
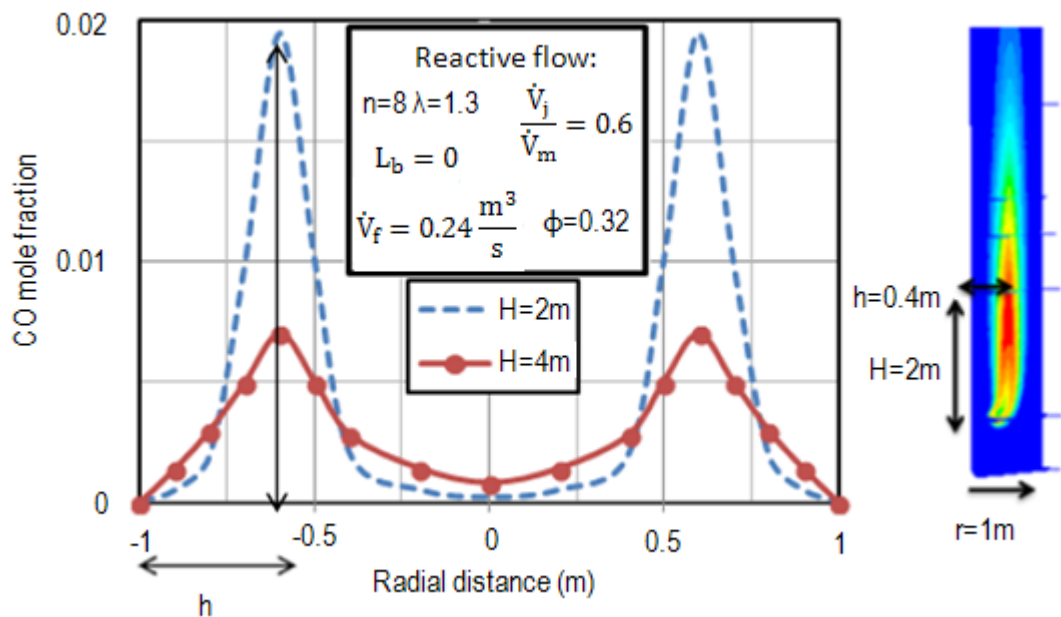
Figure 6.4: Definition of penetration depth (CO profile).

Figure 6.5 shows the CH4 profile to estimate the penetration depth. It can be seen that the position of penetration depth for CH4 concentration is the same as CO concentration. The amount of CO is approximately ten times less than CH4.
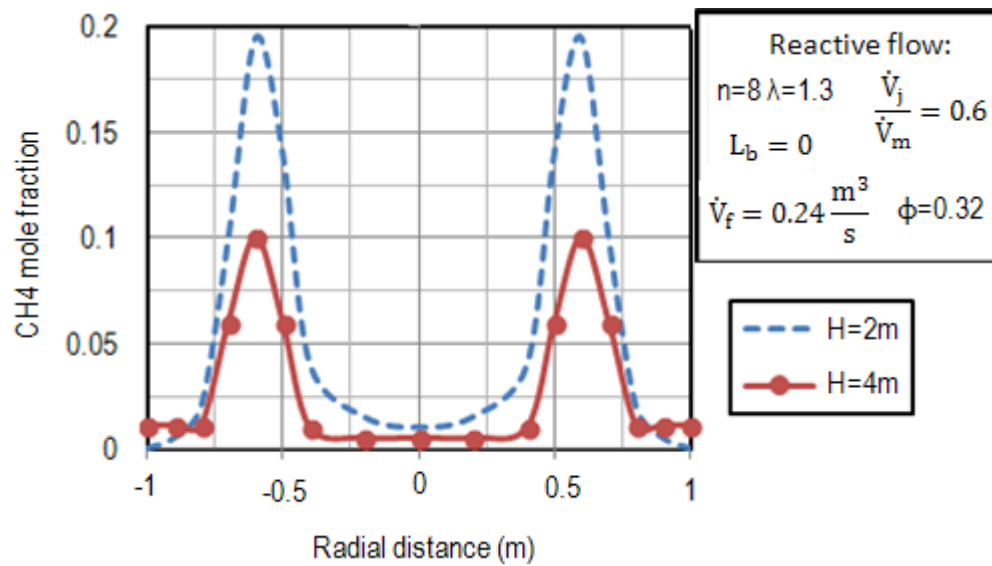
Figure 6.5: Definition of penetration depth (CH4 profile).

Non-reactive flow is a constant temperature process when the air and fuel mix. For comparison with the reactive flow, the CH4 concentration shows in Figure 6.6. The penetration depth in the case of non-reactive flow is always 5cm shorter than that of reactive flow keeping the air volumetric ratio is constant.
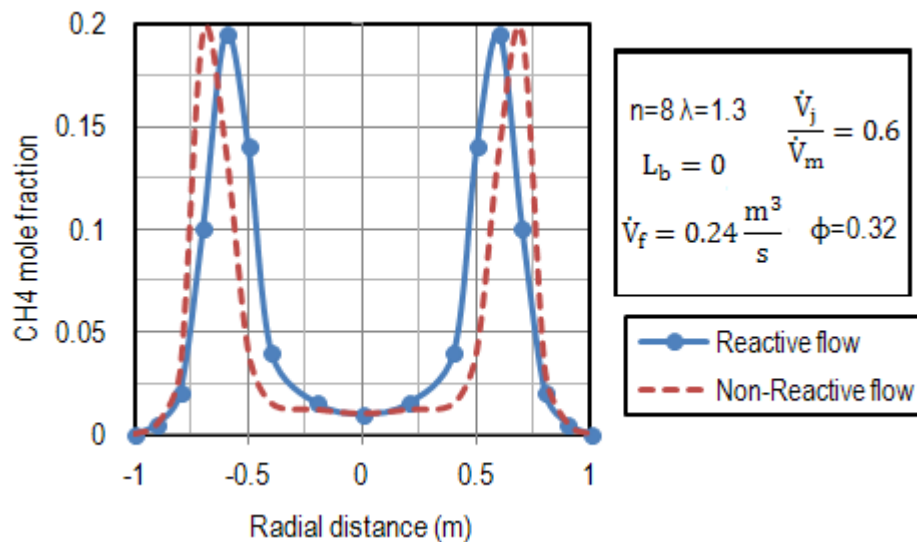
Figure 6.6: Comparison between reactive flow and non-reactive flow ($\frac{V_j}{V_m} = 0.6$).

Here, the air volumetric ratio increased from 0.6 to 1. Again, for comparison with the reactive flow, the CH4 concentration is shown in Figure 6.7. The higher the air ratio is, the deeper the penetration depth becomes. When the air ratio increased from 0.6 to 1, the penetration depth is increased from 0.4 up to 0.48. In this case, the burners arranged at the walls ($L_b = 0$).
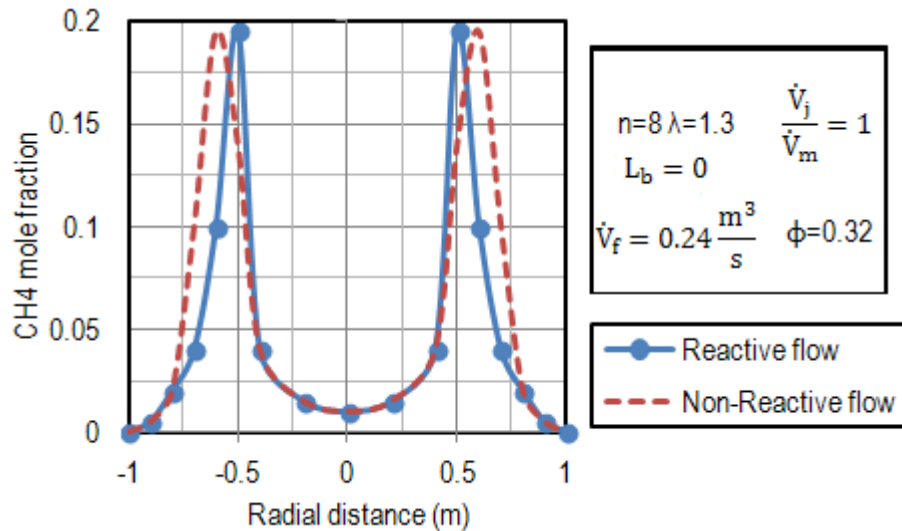
Figure 6.7: Comparison between reactive flow and non-reactive flow ($\frac{V_j}{V_m} = 1$).

The same as before, the penetration depth in the case of non-reactive flow is always 5 cm shorter than reactive flow when the air volumetric ratio is constant. It can be seen that still no fuel reaches to the walls and only less reaches to the core after 2m distance from the burners. Therefore, for deeper penetration depth, the influencing parameters such as a number of burners, depth of burners, and fuel velocity should be discussed.

6.3 Definition of Flame Length (L_f)

The length of the flame determines the temperature profile and that, thus, also the quality of the burnt lime. Methane is used as fuel where injected from 8 burners. Figure 6.8 shows methane reduced to approximately zero at a distance of about 4m from burners. In this case, the ratio of combustion air to cooling air is 0.6.
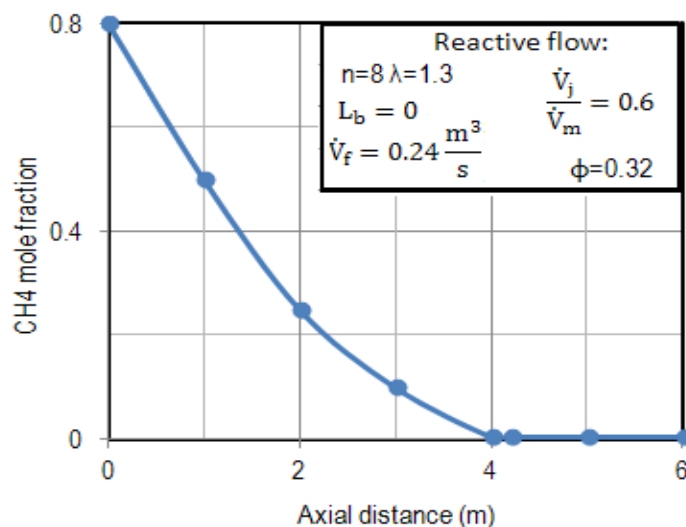
Figure 6.8: CH4 distribution in axial direction.

Figure 6.9 (a) shows the CO contour in the axial direction. The jet is diverted into the vertical (axial) direction.

Figure 6.9 (b) shows the CO mole fraction varying in the axial direction. The burners start at the zero levels. It can be seen that the CO concentration reaches a maximum value of about 0.5m from the burners. However, the CO concentration decreased sharply after 2m and reached 1% of the maximum amount at approximately a 6m distance from the burners.

(a)

(b)
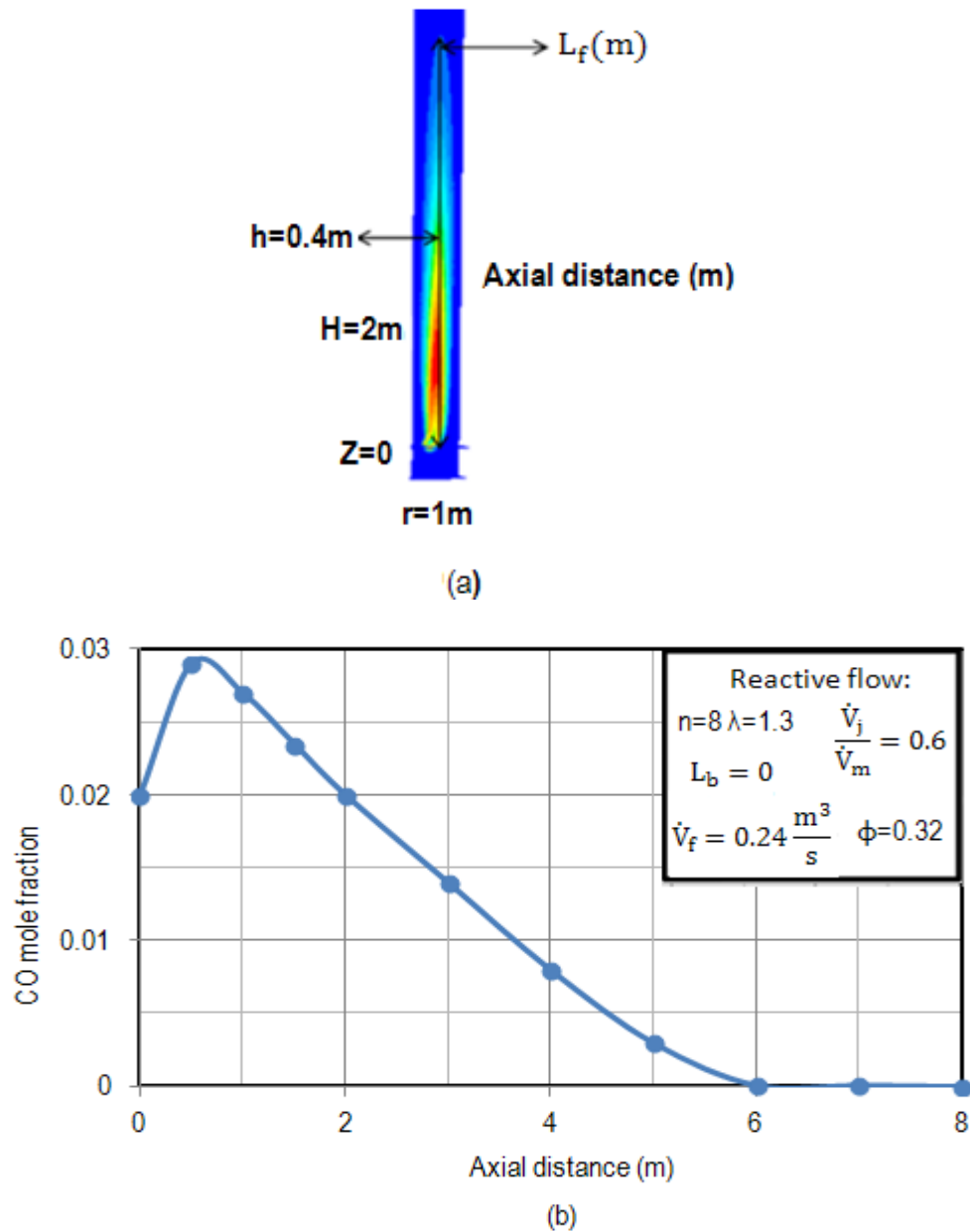
Figure 6.9: (a) Schematic of flame length, (b) Axial CO profile.

6.4 Non-Reactive Flow

6.4.1 Radial velocity profile (when n=8, L_b=0, d_L=50mm)

Figure 6.10 (a) shows the radial profile of interstitial (local) velocity at the burner position. The burner outlet velocity was kept constant (50 $\frac{m}{s}$)and the porosity (ϕ = 0.32-1) was varied. As can be seen, the lower the porosity is, the wider the velocity profile becomes. However, no significant difference in the velocity profiles between the range of ϕ=0.32 up to ϕ=0.6 could be observed. In Figure 6.10 (b), the velocity profiles for values, $U_f = 50\frac{m}{s}$ and 15.2 $\frac{m}{s}$ compared. The velocity reaches a minimum amount at a distance of 0.2 m from the burners, after which it becomes homogeneous.
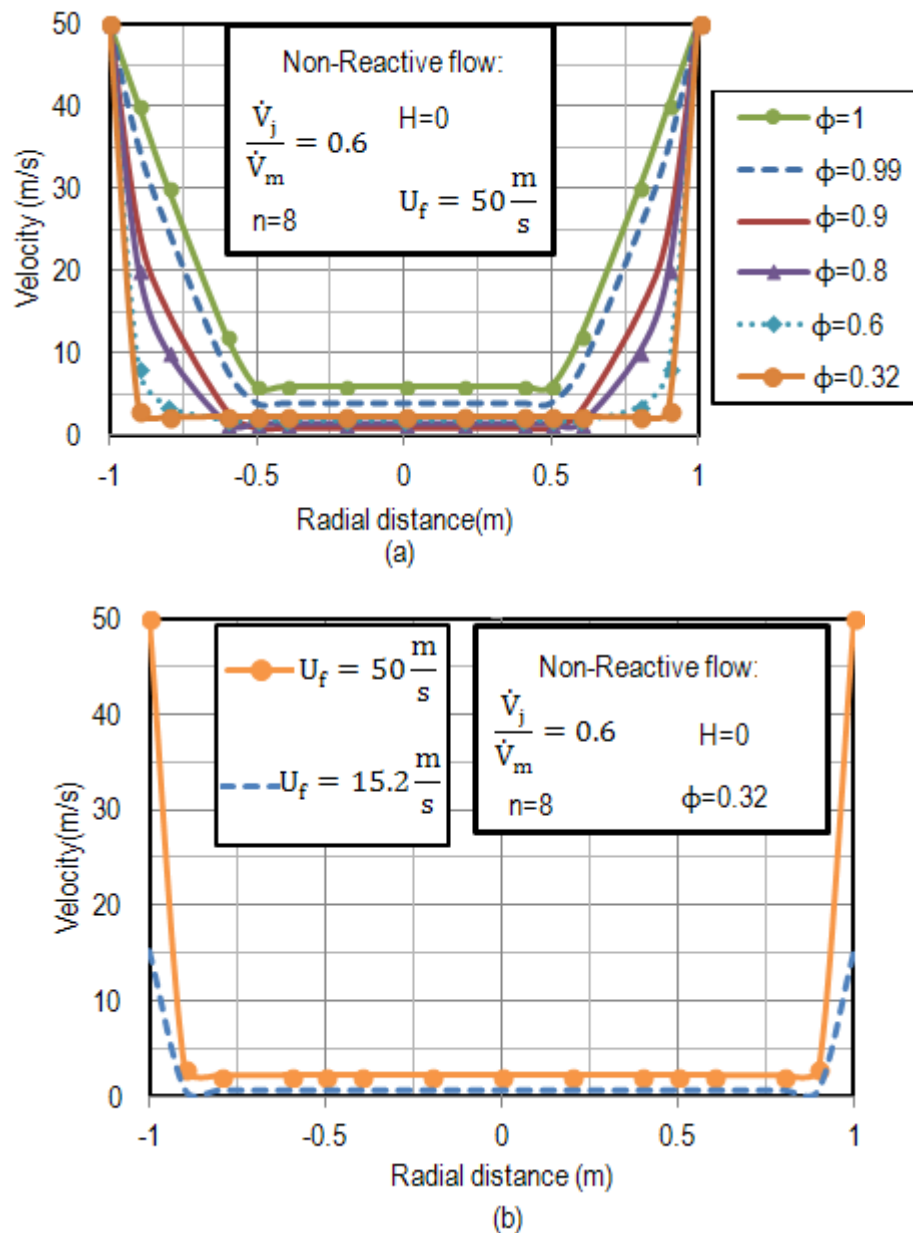
Figure 6.10: Velocity profiles at burner level H=0 for various porosities ϕ=0.32-1

Figure 6.11 (a) shows the velocity profile for values less than $10\ \frac{m}{s}$. The velocity is always the lowest at the center of the packed bed.

Figure 6.11 (b) shows the velocity profiles for the values $U_f = 50\ \frac{m}{s}$ and $15.2\frac{m}{s}$. As can be seen, the minimum amount for the velocity profile achieved by 0.2 m from the wall. The shape of the velocity profile is independent of the burner outlet velocity.
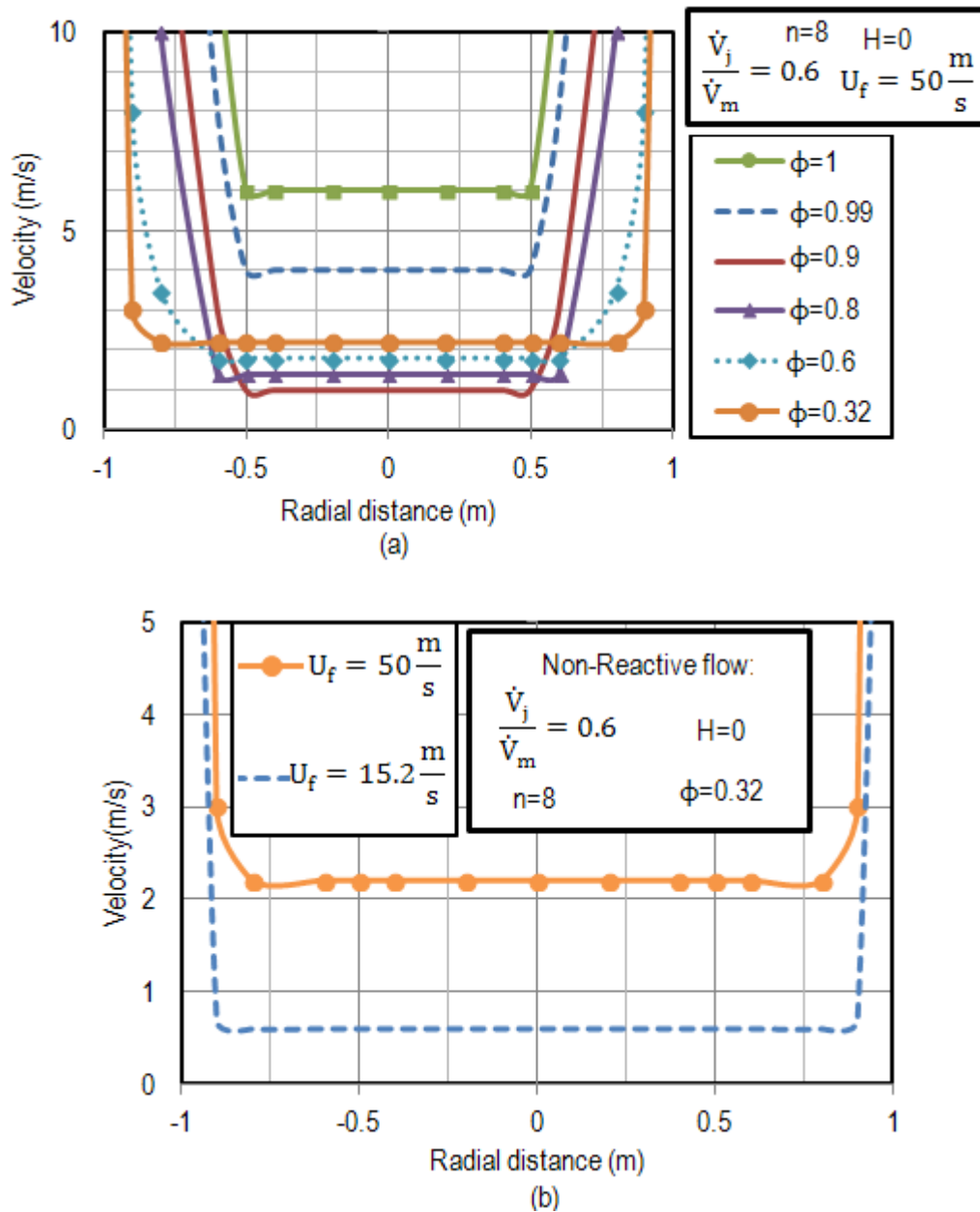
Figure 6.11: Velocity profiles at burner level H=0 for various porosities ɸ=0.32-1.

Figure 6.12 (a) shows the radial velocity profile after a height of 2m. It can be seen that the profile is very homogeneous. A small peak in the center can be observed for porosities higher than 0.6. However, the porosity has almost no influence for values lower than ɸ=0.9

Figure 6.12 (b) shows the velocity profile for two fuel outlet velocities $U_f = 50\frac{m}{s}$ and $15.2\frac{m}{s}$. The velocity profile has the same trend near the walls and in the center of the packed bed. The outlet velocity has almost no influence on the shape of the velocity profile.
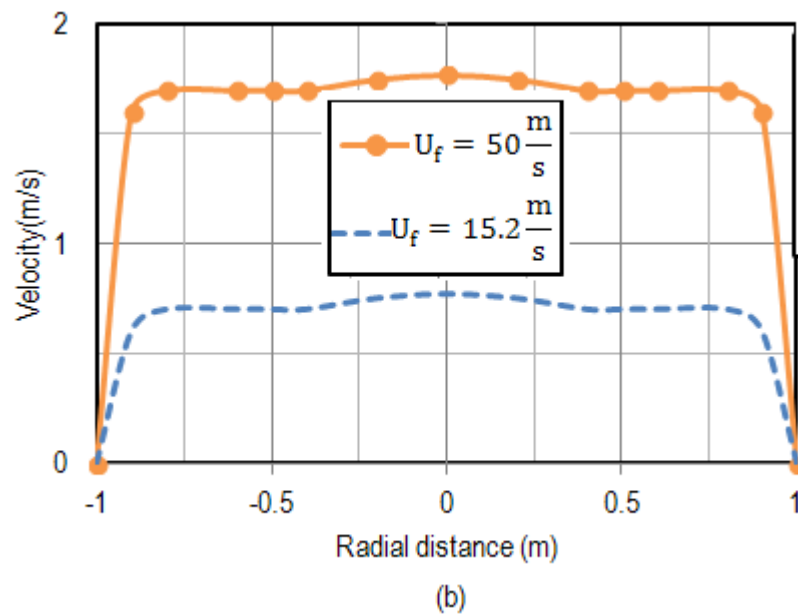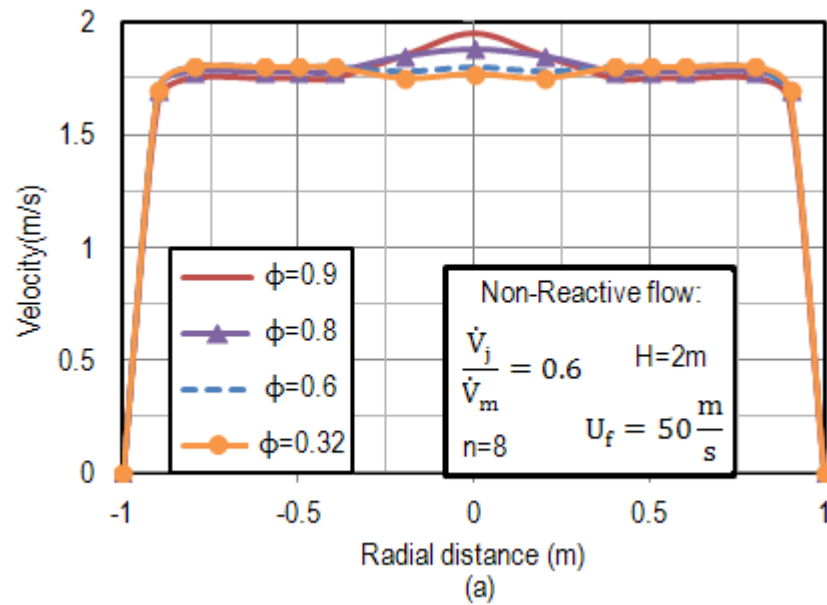
Figure 6.12 Velocity profiles at H=2m for various porosities ϕ=0.32-0.9.

When no solids are present, the porosity is equal to 1. Therefore the interstitial velocity will be the same as the superficial velocity. Figure 6.13 shows the superficial velocity profile for an empty kiln (ϕ=1). The velocity profile after 2m distance from burners is not homogeneous. The maximum peak is in the center. The velocity profile in the packed bed is always more homogeneous than an empty shaft.
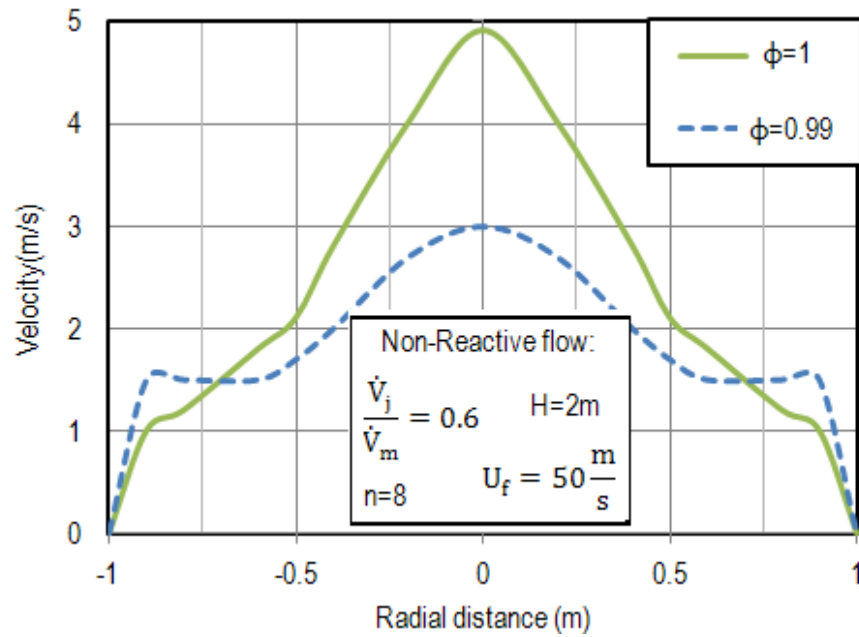
Figure 6.13: Velocity profile at H=2m (φ=0.99-1).

Figure 6.14 shows the velocity profile in the radial direction at a 2m distance from the burners. Three particle diameters, d_p=10, 100 and 200mm, are used. For the particles of diameter =d_p 10 mm, the velocity profile decreases very sharply near the walls. The decrease of velocities is in the range of one particle diameter.
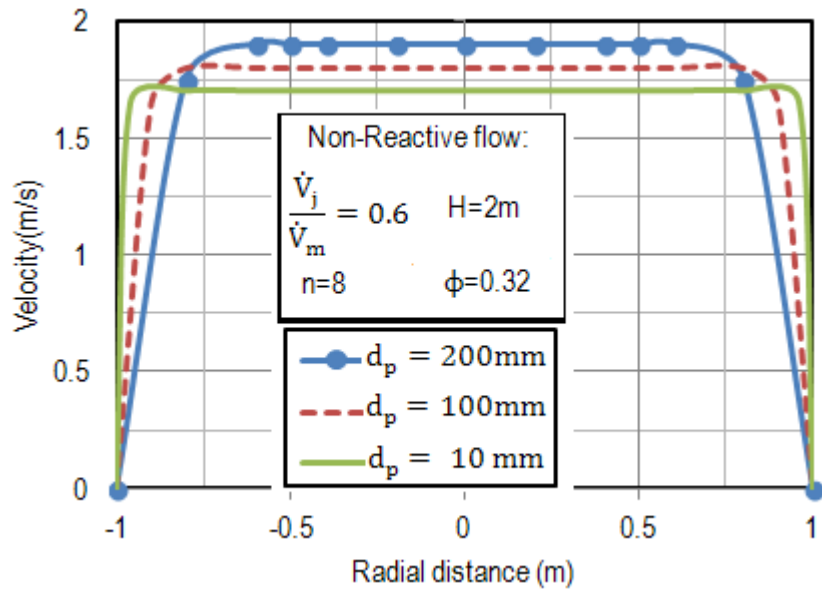
Figure 6.14: Velocity profile for various particle diameters.

Figure 6.15 shows the velocity profile at different heights keeping the particle diameter constant at d_p=100 mm. There is no big difference between the velocity profiles after the heights of 0.5m up to 2m.
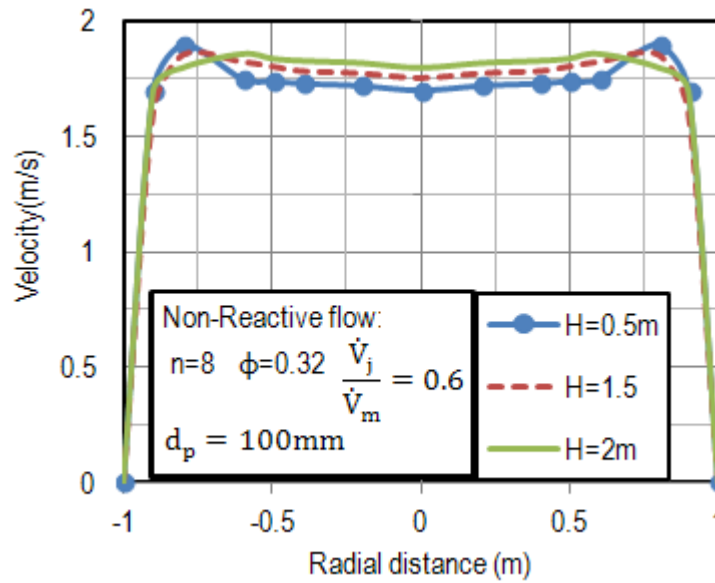
Figure 6.15: Radial velocity profile at different heights.

6.4.2 Fuel profile

Figure 6.16 shows the fuel profile at the burner level for different porosities. The porosity researched in the range of ϕ=0.32-0.8. It can be seen that the lower the porosity is, the wider the fuel profile becomes. However, there is no significant difference in the CH4 profiles for porosities in the range of ϕ=0.32 up to ϕ=0.6.

Figure 6.16: Fuel profile for various porosities (ϕ=0.32-1) at burner level.

Figure 6.17 shows the fuel profile at different heights. The higher the distance from the burner is, the more even the fuel profile becomes. In this case, the fuel and air do not react with each other (Non-Reactive flow).
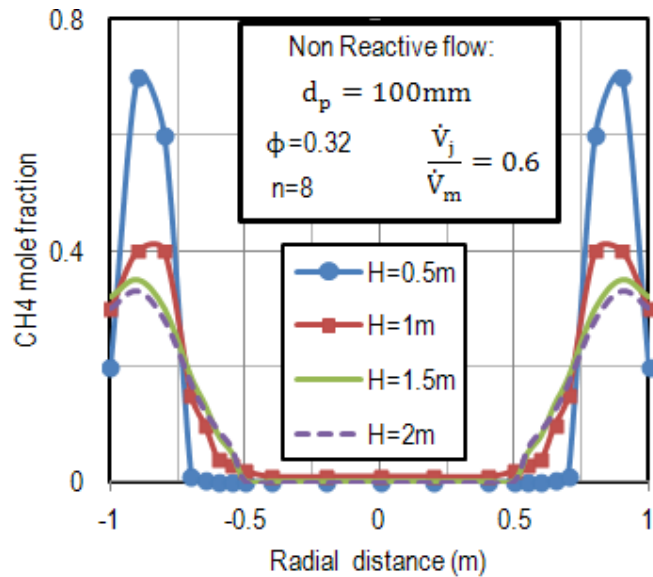
Figure 6.17: Fuel profile at different heights (non-reactive flow).

6.5 Reactive Flow

In the previous section, the mechanism of mixing was considered for a constant temperature. Here, the mixing is discussed for the reactive flow to see the influence of temperature distribution. The particle diameter is kept constant in all the cases at $d_p = 100mm$.

6.5.1 Fuel profile

Figure 6.18 shows the fuel profile at the burner level for different porosities ranging between $\phi = 0.32\text{-}0.8$. It can be seen that the lower the porosity is, the wider the fuel profile becomes. However, there is no significant difference in the CH4 profiles for porosities in the range of $\phi=0.32$ up to $\phi=0.6$. The fuel is completely combusted about 0.4 m after the burner outlet when the porosity is $\phi=0.32$.
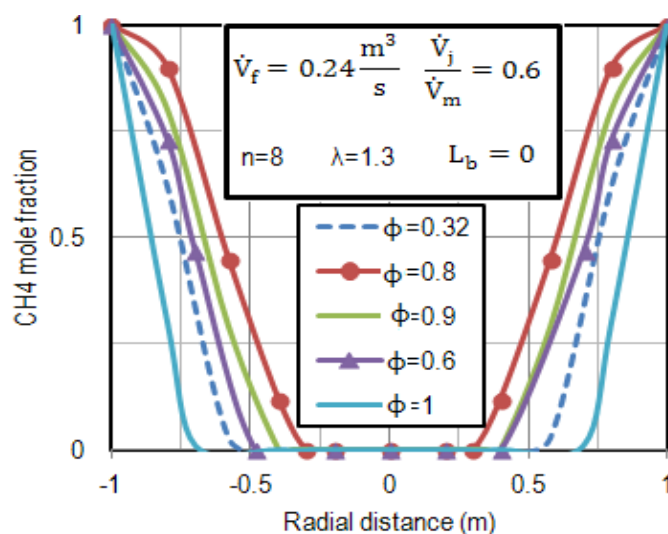
Figure 6.18: Fuel profile for various porosities (ϕ=0.32-1).

Figure 6.19 shows the CO concentration in a radial direction. After a distance of 0.6m from the burners, the CO mole fraction is zero. Therefore, the depth of burners in the packed bed must be increased to inject more fuel to the core.
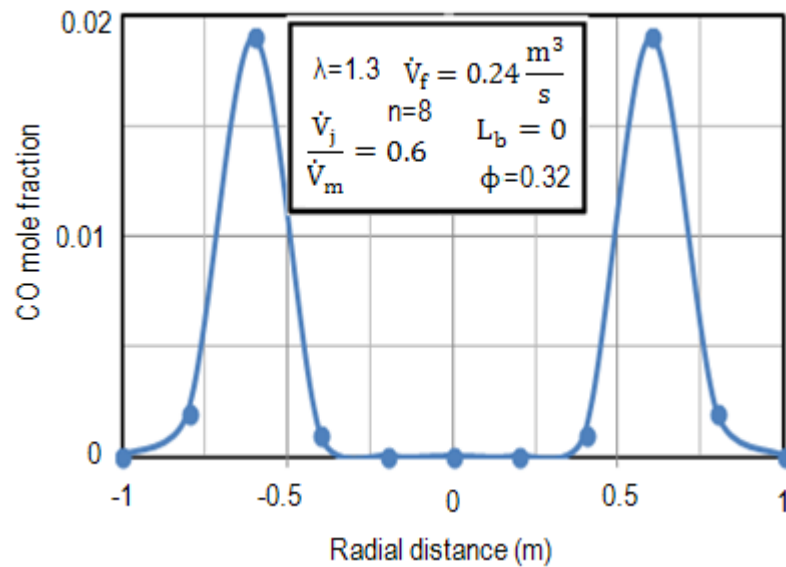

Figure 6.19: Radial CO profile at burner level for ɸ=0.32.

Figure 6.20 shows the fuel profile at different heights. As can be seen, the maximum value of the fuel is always at a distance of 0.4m from the walls. The higher the distance from the burners is, the lower the concentration of fuel becomes. However, even fewer amounts reach the core after a 2m distance from the burner level. Therefore, to enhance deeper fuel penetration, more burners with varying depths will need to be used.
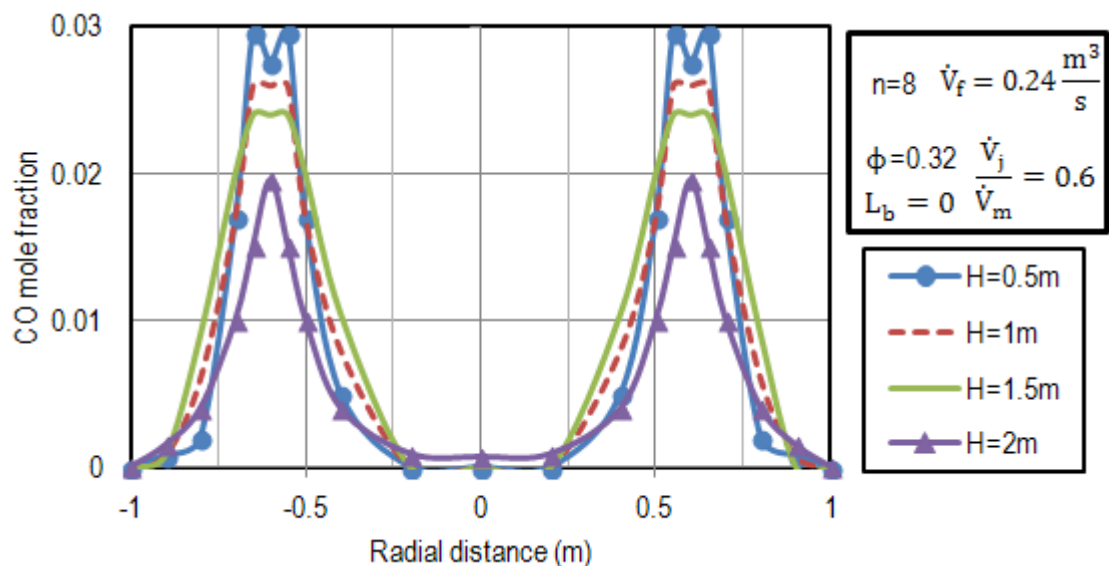
Figure 6.20: Fuel profile in different heights for ɸ=0.32.

Figure 6.21 shows the CO contours in the radial direction for various heights. As can be seen, the fuel concentration is minimum at the core. However, the fuel in the circumferential distance is relatively homogeneous.
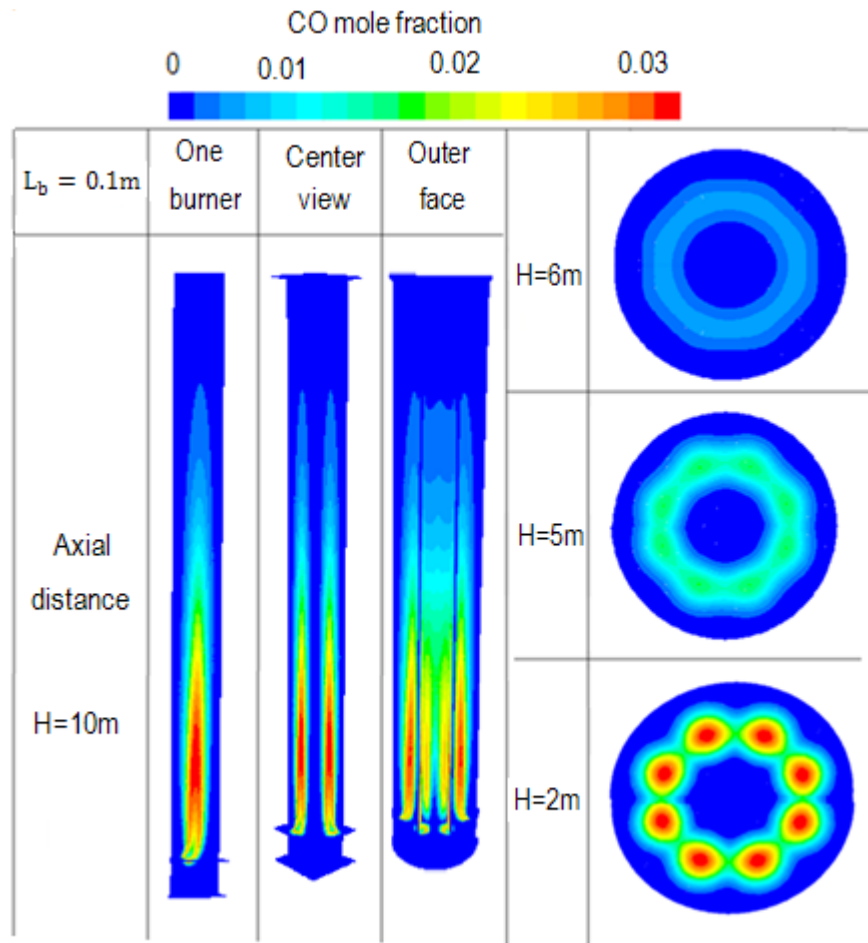

Figure 6.21: CO contours in different directions ($\frac{V_j}{V_m}$=0.6).

6.5.2 Temperature profile

Figure 6.22 shows the radial temperature profile at different heights. As can be seen, the penetration depth is always at a 0.4m distance from the walls ($L_b = 0$). After a vertical height of 3m from burners, the temperature reaches to the maximum values and then steadily decreases. Homogenization starts after a height of 3m from the burners. Therefore, the temperature profile at H=7m is more homogeneous in the core and near the walls.
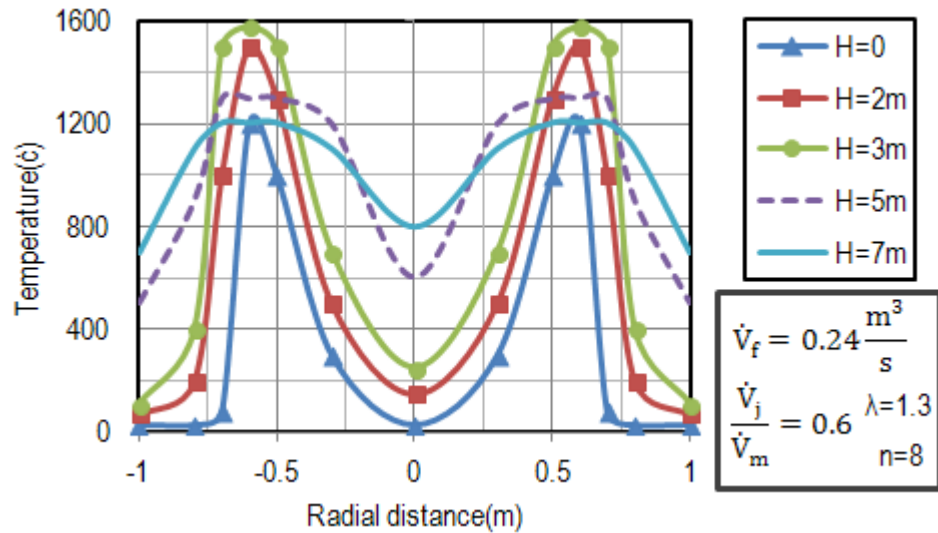
Figure 6.22: Temperature profile at different heights ($L_b = 0$).

It can be seen in Figure 6.23 that the temperature in the core and near the walls are much lower than the peak temperature. However, the temperature in the circumferential distance is relatively homogeneous.
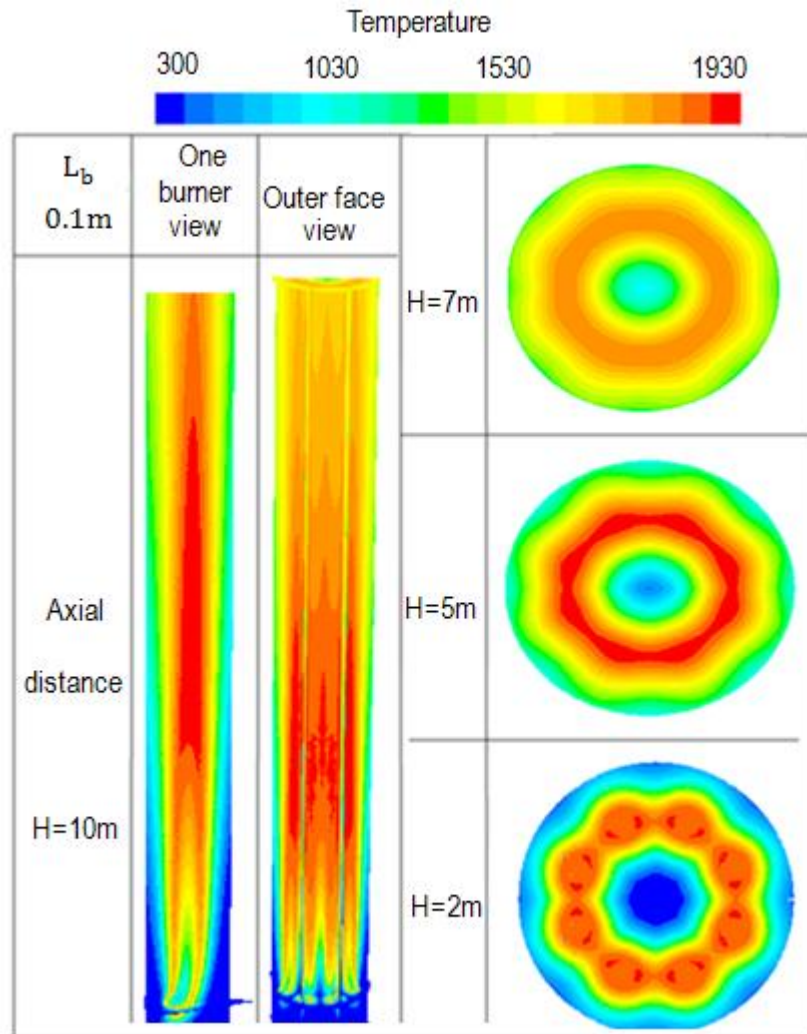
Figure 6.23: Temperature contour in radial and axial directions.

6.5.3 Velocity profile

Figure 6.24 shows the radial velocity profile at different heights. Where the temperature is maximum, the velocity is maximum as well. The higher the distance from the burners is, the higher the velocity becomes.

It can be seen that at a radial distance of 0.25m from the walls, the velocity drops continuously to the value of zero. In reactive flow, the radial profile is not as even as in non-reactive flow, as shown in Figure 6.12. The velocity profile after a distance of 2m from the burners shows the same trend. However, there is no significant change in the velocity profile after the 2m distance from the burners.
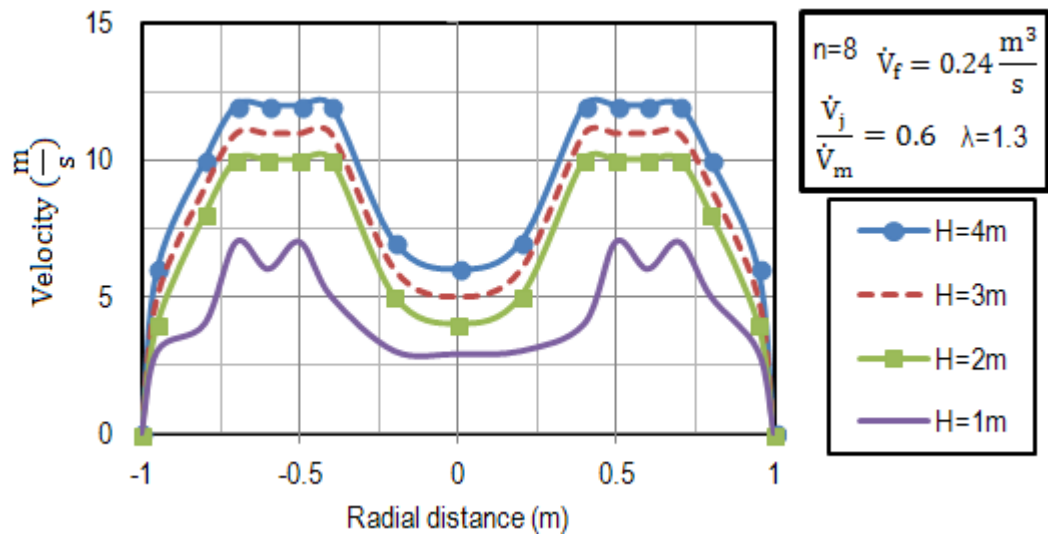
Figure 6.24: Velocity profile at different heights.

Figure 6.25 shows the density profile in the radial direction at H=2m from the burners. As a consequence, the higher the density is, the lower the velocity becomes.
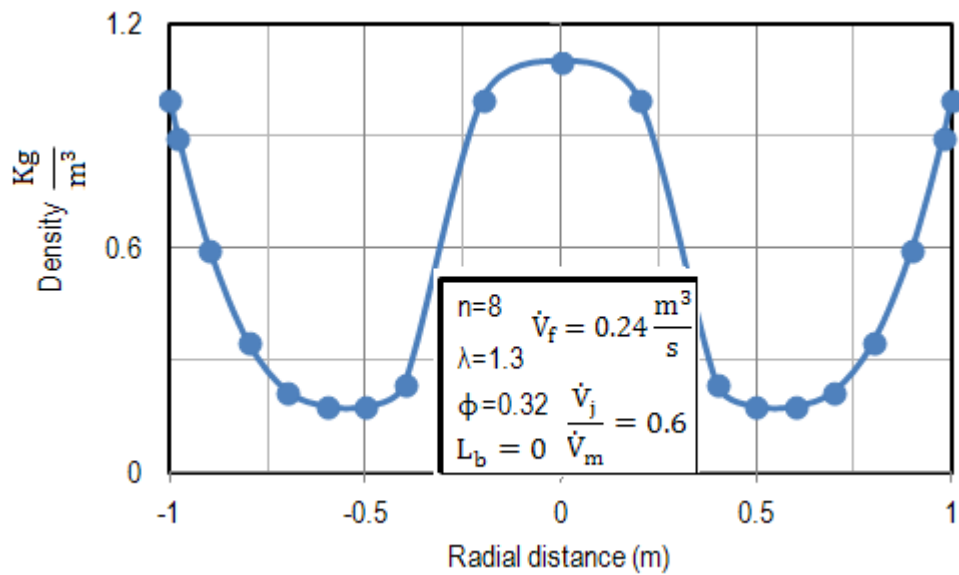

Figure 6.25: Density profile in radial direction at H=2m.

The mass flow rate is the product of velocity and density. Figure 6.26 shows that the mass flow rate after 2m is more even.
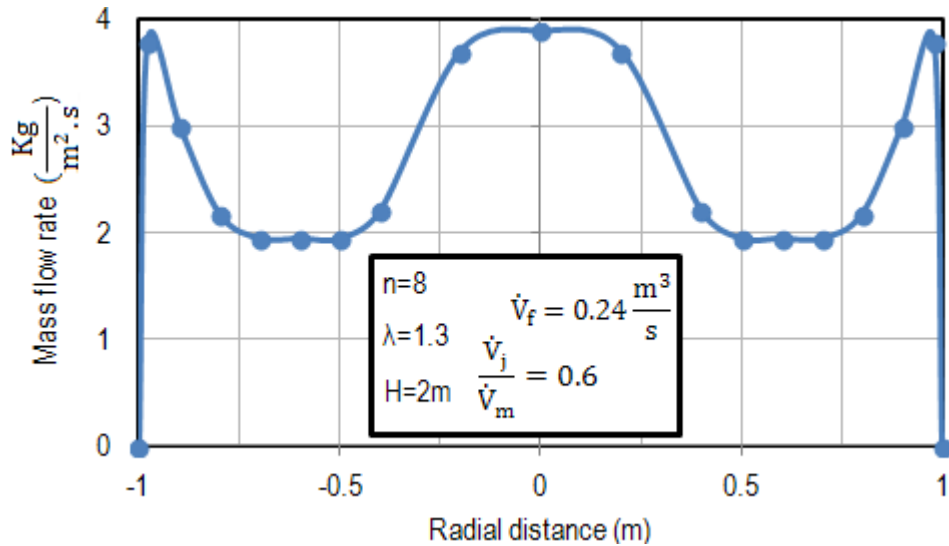
Figure 6.26: Mass flow rate profile in radial direction at H=2 m.

6.6 Penetration Depth

6.6.1 Reactive flow

In this section, the penetration depth compared to reactive and non-reactive flows. Figure 6.27 shows the influence of the number of burners on the penetration depth. The fuel and combustion air volume flows were kept constant. Also, the ratio of combustion air to cooling air and the fuel burner diameter was kept constant. When the number of burners increased from 8 to 32, the fuel velocity decreased from $15.3 \frac{m}{s}$ up to $3.8\frac{m}{s}$. As can be seen in Figure 6.27, when the number of burners increased from n=8 up to n=32 (about four times), the penetration depth is increased by about 4cm. In reactive flow, the penetration depth is always 5cm deeper than in non-reactive flow.
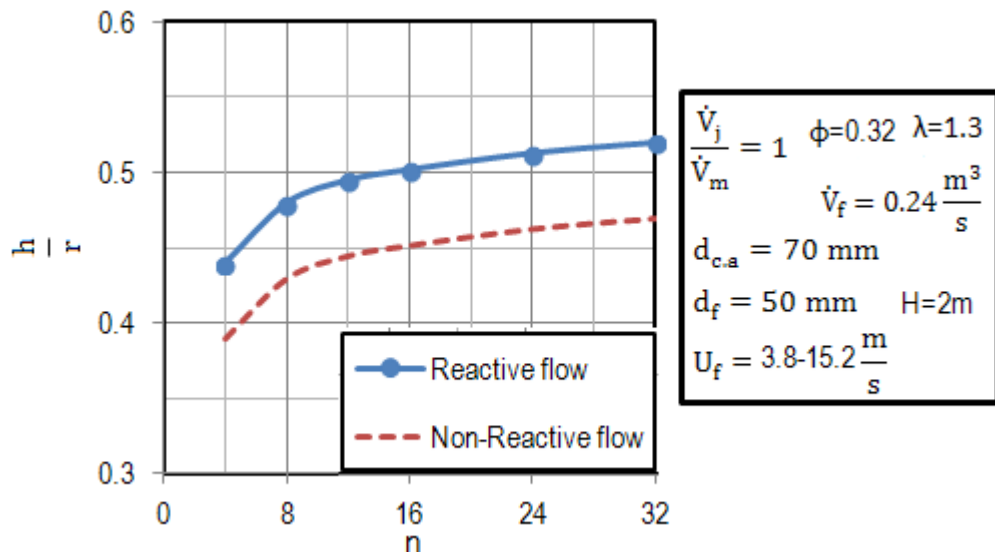

Figure 6.27: Influence of number of burners on the penetration depth.

Figure 6.28 shows the influence of the particle diameter on the penetration depth. In this case, all the operation parameters were kept constant. As can be seen, the bigger the particle diameter is, the deeper the penetration depth becomes. The penetration depth increase is sharper for the small range (d_p= 20-50mm) of particles compared to the more significant range (d_p =50-150 mm). Again the penetration depth in non-reactive flow is 5cm shorter than that in reactive flow. The more the air volumetric ratio is, the deeper the penetration depth becomes.
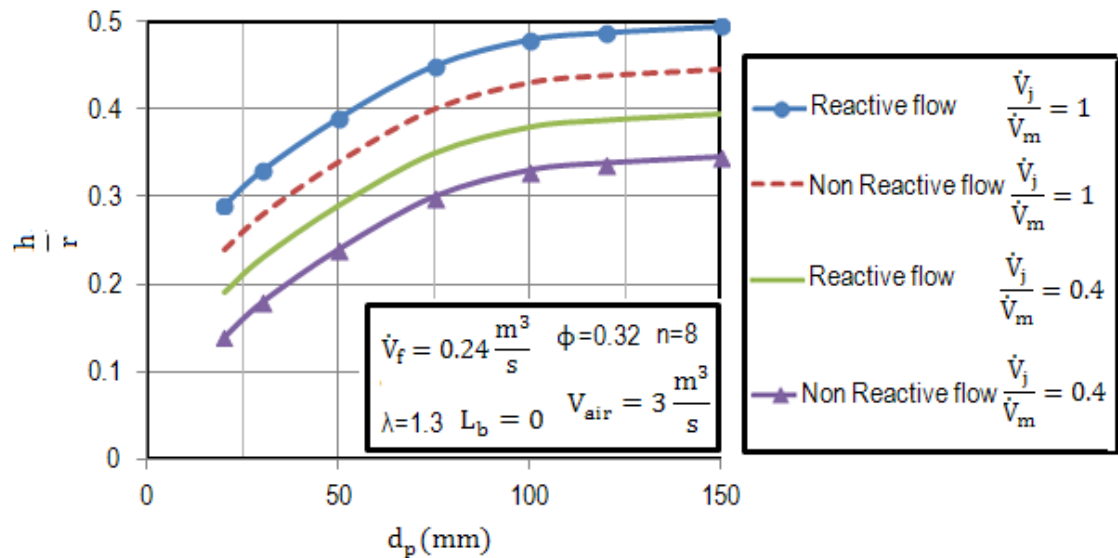

Figure 6.28: Influence of particle size on penetration depth.

6.6.2 Influence of burners depth on penetration depth

Burners can have different depths (L_b) in the CFS shaft kiln. Figure 6.29 presents the contour of CH4 mole fraction for various burner depths. In this case, the number of burners was kept constant (n=8). As can be seen, the deeper the burners are, the deeper the penetration depth becomes.
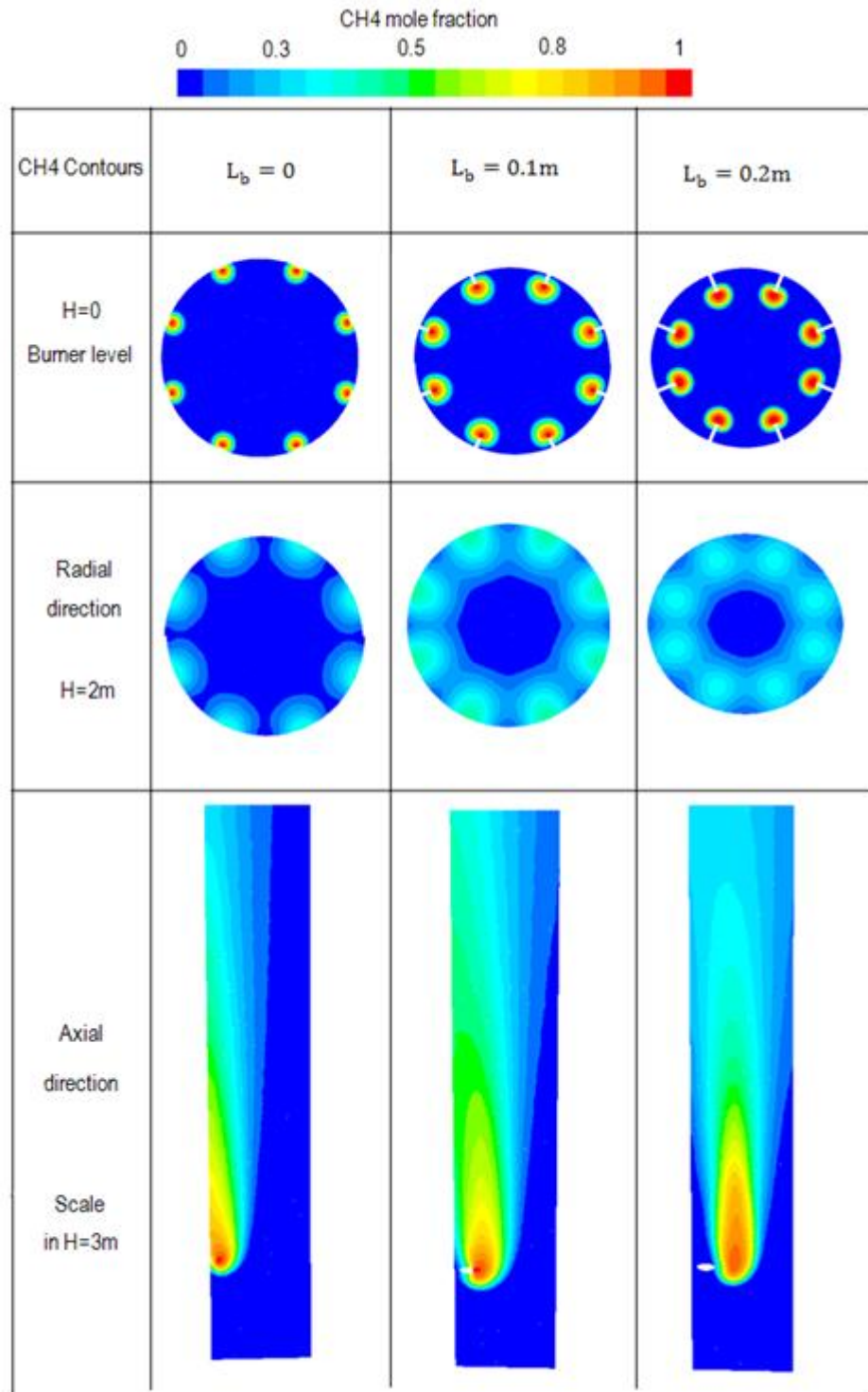
Figure 6.29: CH4 contours for various burner depths.

Figure 6.30 shows the CO concentration and temperature profiles after a 2m distance from the burners. When the burner depth from the wall position ($L_b = 0$) is increased up to 0.2m through the packed bed, the CO concentration and also temperature shifted to the middle.
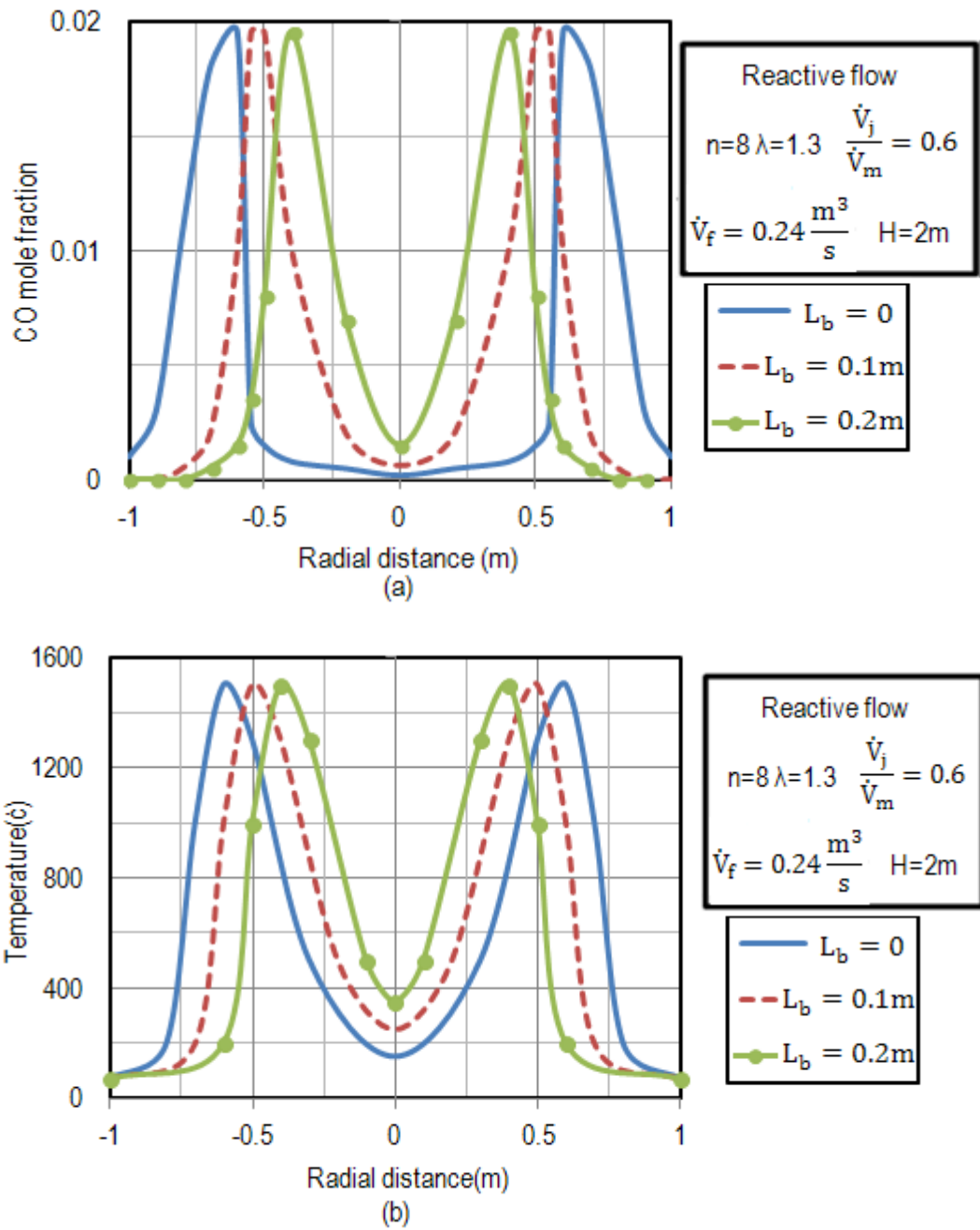
Figure 6.30: (a) CO profile (b) Temperature profile for various burner depths.

Figure 6.31 shows the penetration depth independence to the burner depth. The number of burners, fuel, and air volume flows was kept constant. The volumetric air ratio varied between $\frac{V_j}{V_m}$ =0.6 and 1. As a consequence, the penetration depth is directly proportional to the burner depth.
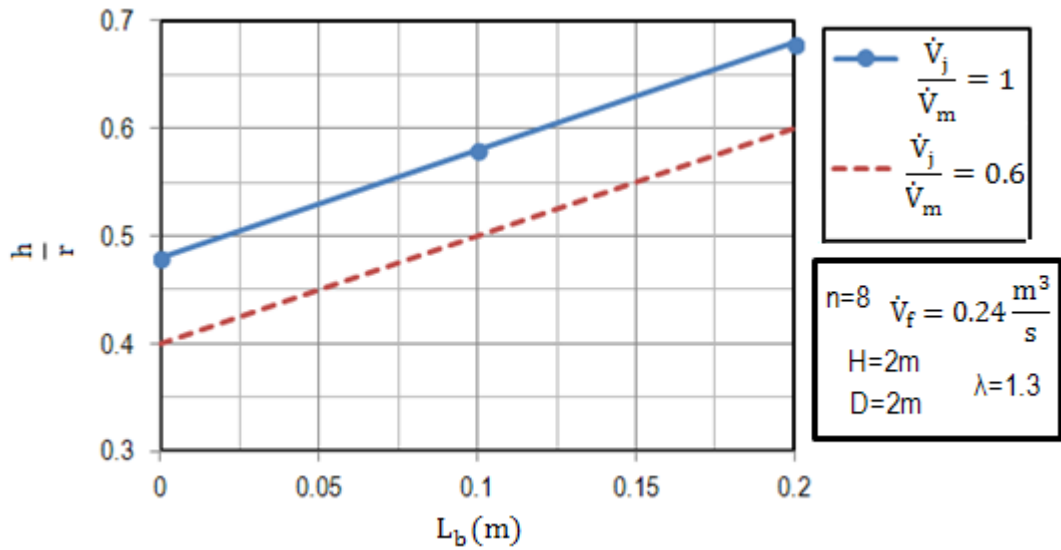
Figure 6.31: Influence of the burner depth on penetration depth $\left(\frac{h}{r}\right)$.

6.6.3 Influence of ratio of combustion air to cooling air $\frac{\dot{V}_j}{\dot{V}_m}$

The ratio of combustion air to cooling air has a significant influence on the penetration depth. Figure 6.32 shows the influence of this ratio when the eight burners arranged. The minimum value for the ratio occurs when all the air used as cooling air, and none used for combustion. When the value for the ratio exceeds 1.0, the lime cannot be completely cooled anymore. The more significant amounts are presented in the figure below to show the influence in more detail.
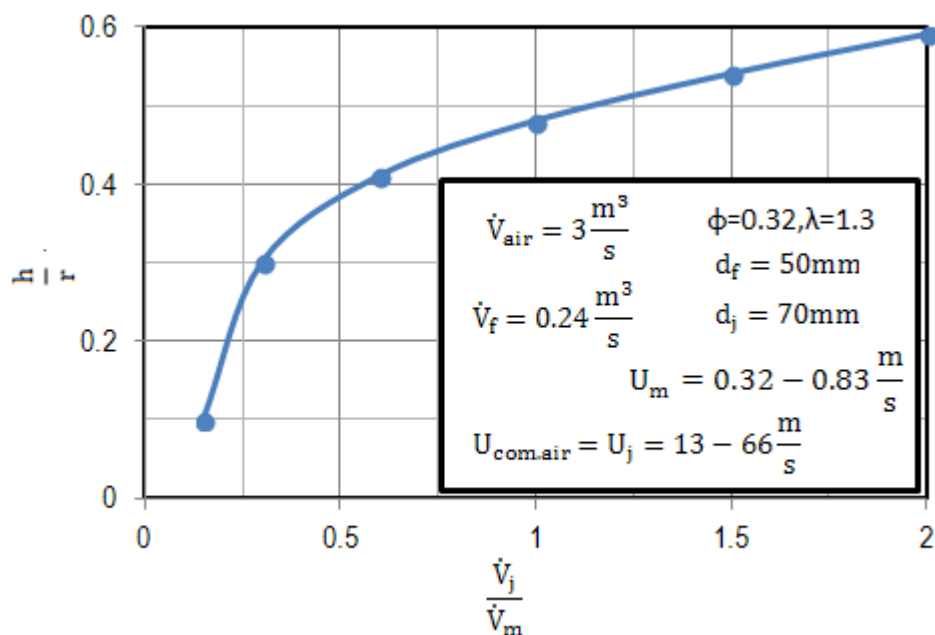

Figure 6.32: Influence of air ratio on the penetration depth when $L_b = 0.$

6.6.4 Influence of fuel velocity on penetration depth

Here, the influence of fuel velocity (burner diameter) researched. For this aim, the diameter of the combustion air nozzle is kept constant($d_{com.air} = 70mm$). The fuel burner diameter is changed from $d_f = 60mm$ down to 20mm. Therefore, the respective change in fuel velocity is from $U_f = 10.9\frac{m}{s}$ to $96\frac{m}{s}$.

Figure 6.33 shows the influence of fuel velocity on the penetration depth. When the fuel velocity increased by about nine times, the penetration depth is increased by about 0.18m. Due to more significant turbulent mixing and entrainment, the higher the fuel velocity is, the deeper the penetration depth becomes. When the air volumetric ratio increased from 0.4 to 1, the penetration depth is increased by 0.1m.
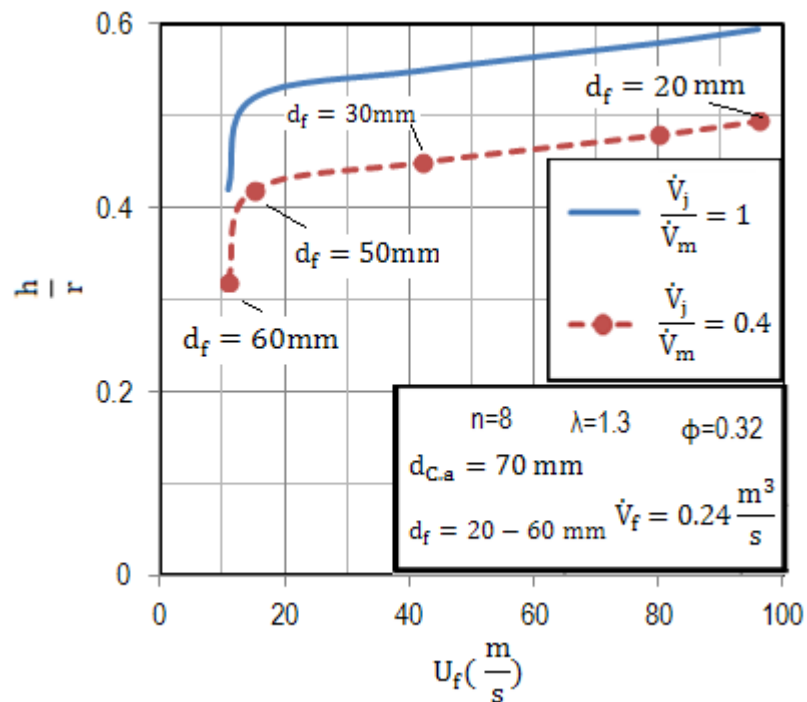

Figure 6.33: Influence of fuel velocity on penetration depth.

In conclusion, when the air volumetric ratio is one ($\frac{\dot{V}_j}{\dot{V}_m} = 1$), there are two possible ways to improve the penetration depth so that it reaches 0.6m. Firstly, increasing the fuel velocity from $10\frac{m}{s}$ up to $96\frac{m}{s}$ increases the penetration depth from 0.42m up to 0.6m. Secondly, increasing the burner depth from the wall position ($L_b = 0$ up to $L_b = 0.12m$) causes the penetration depth to increase from 0.48m up to 0.6m.

6.6.5 Influence of combustion air velocity on penetration depth

Here, the combustion air nozzle diameter changed from 70mm to 150mm. For this aim, the fuel burner diameter was kept constant d_f =50 mm. As can be seen in Figure 6.34, when the combustion air increased by about five times, the penetration depth is increased by 3cm. As a consequence, the combustion air velocity has a small influence on the penetration depth. The influence of the combustion air velocity researched for the air ratios of 0.6 and 1.
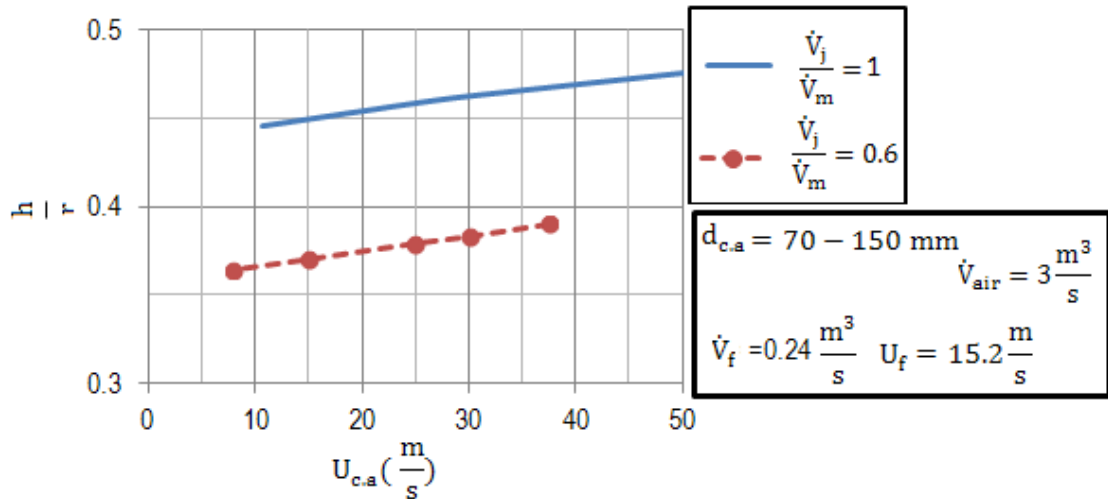

Figure 6.34: Influence of combustion air velocity on penetration depth n=8.

6.6.6 Influence of number of burners on penetration depth

Here, the influence of the number of burners (n=4 to 32) is studied. In this case, the fuel and air volume flow, as well as the air excess number, were kept constant. Also, the fuel burner and combustion air nozzle diameters were kept constant. Only the fuel velocity is changed when the number of burners is changed.

When the number of burners increased from 8 to 32, the penetration depth is increased by about 5cm. However, the influence of increasing the number of burners would be very small. As can be seen in Figure 6.35, the influence of the number of burners on penetration depth is more prominent when the number of burners is lesser than 8.
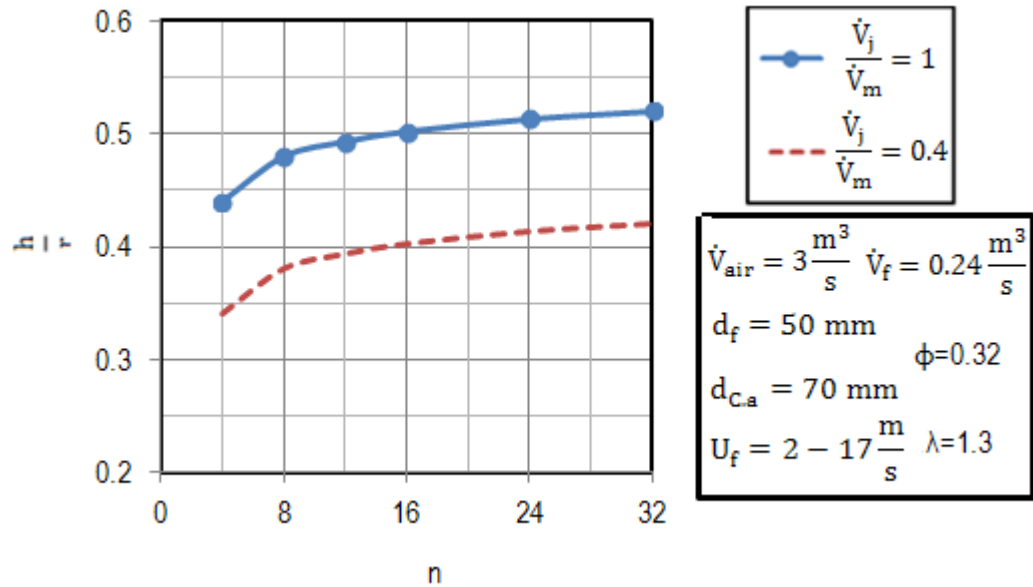
Figure 6.35: Influence of the number of burners on penetration depth.

Figure 6.36 shows the influence of air ratios on the penetration depth for various numbers of burners. The more the air injected from the burner is, the deeper the penetration depth becomes. However, the typical air volumetric ratio for CFS shaft kilns is $\frac{\dot{V}_j}{\dot{V}_m}$ =1. In this case, when the number of burners increased by three times, the penetration depth increased by 5 cm.
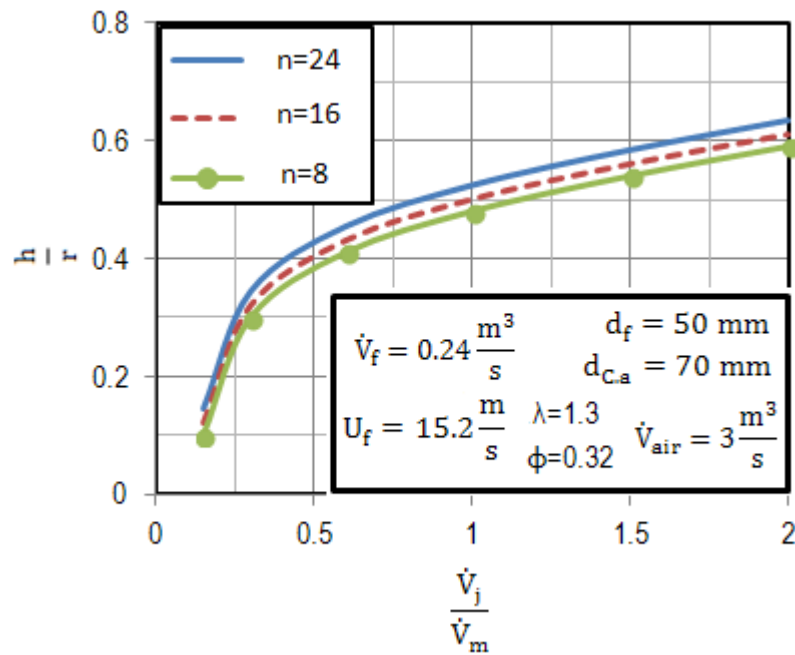

Figure 6.36: Influence of ratio of combustion air to cooling air for n=8-24.

6.6.7 Influence of kiln diameter on penetration depth

Here, the influence of various kiln diameters researched. The mass flow of limestone is 200 $\frac{ton}{day}$. The fuel flow rate was kept constant ($V_f = 0.24 \frac{m^3}{s}$). In this case, only the cooling air velocity changed. Figure 6.37 shows that increasing the kiln diameter from 1m up to 4m increase the penetration depth by 7cm.

Overall, the influence of the kiln diameter is very small. As a consequence, all results in this section for the chosen diameter of 2m can be generalized to all other kiln diameters and kiln throughputs.
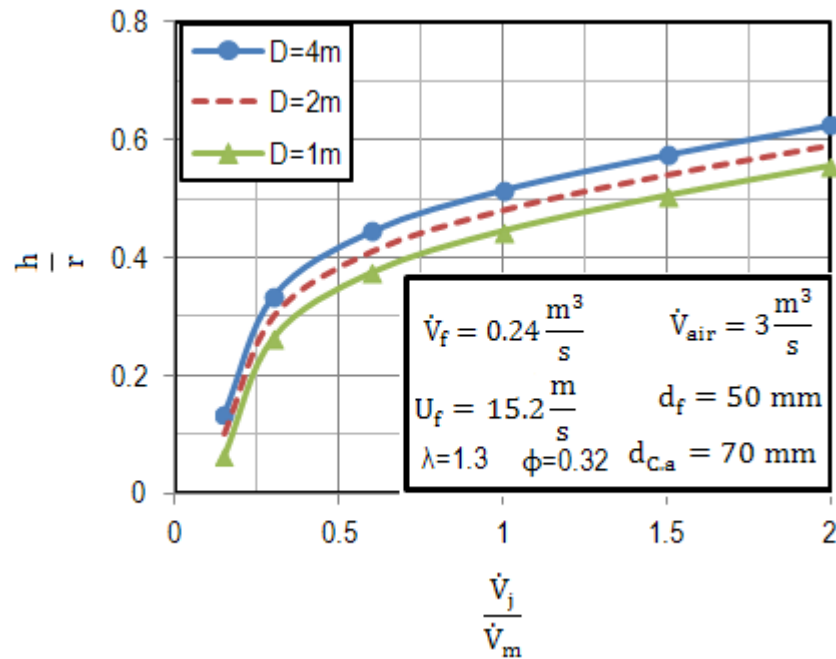

Figure 6.37: Influence of kiln diameter on the penetration depth.

6.6.8 Influence of particle diameter on penetration depth

In this section, the influence of various particle diameters on the penetration depth researched. The porosity and other operation parameters were kept constant.

Figure 6.38 shows the influence of particle diameters on the penetration depth. For this aim, the fuel and air volume flow, as well as the excess air number, were kept constant.

The bigger the particle diameter is, the higher the penetration depth becomes. The smaller range of particle diameters ($d_p = 20 - 50mm$) has a more significant influence on the penetration depth.

When the particle diameter increased from 20mm up to 150mm (by about seven times), the penetration depth improved from 0.29m to 0.5m. Here, the air volumetric ratios of $\frac{V_j}{V_m}$ 0.4, 0.6, and 1 considered. The air ratio $\frac{V_j}{V_m}$ =1 is the typical ratio of the combustion air to the cooling air for CFS shaft kilns. In this case, the excess air number is always kept constant at λ=1.3. Again, it can be seen that the higher the air ratio is, the deeper the penetration depth becomes.
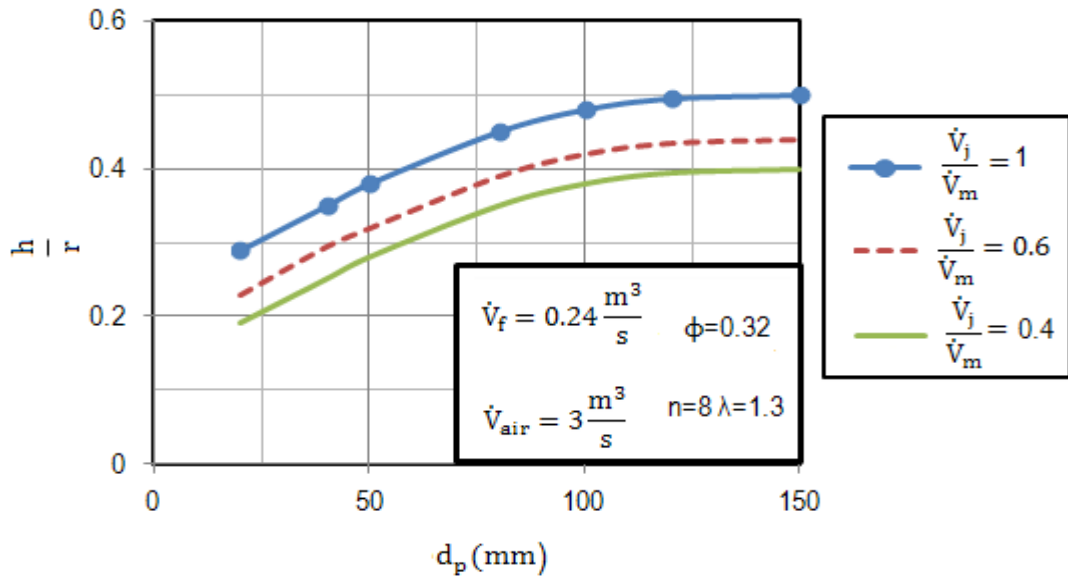

Figure 6.38: Influence of particle diameter on penetration depth $L_b = 0$.

6.7 Flame Length

6.7.1 Influence of fuel velocity on the flame length

It can be seen in Figure 6.39 that the higher the outlet fuel velocity is, the longer the flame length becomes. When the fuel velocity increased from $5\frac{m}{s}$ up to $96\frac{m}{s}$, the flame length is increased by approximately two times (when n = 8). The velocities ranging from smaller than $5\frac{m}{s}$ and up to 10 $\frac{m}{s}$ have a very strong influence on the flame length. Therefore, the fuel velocity should be more significant than these values.
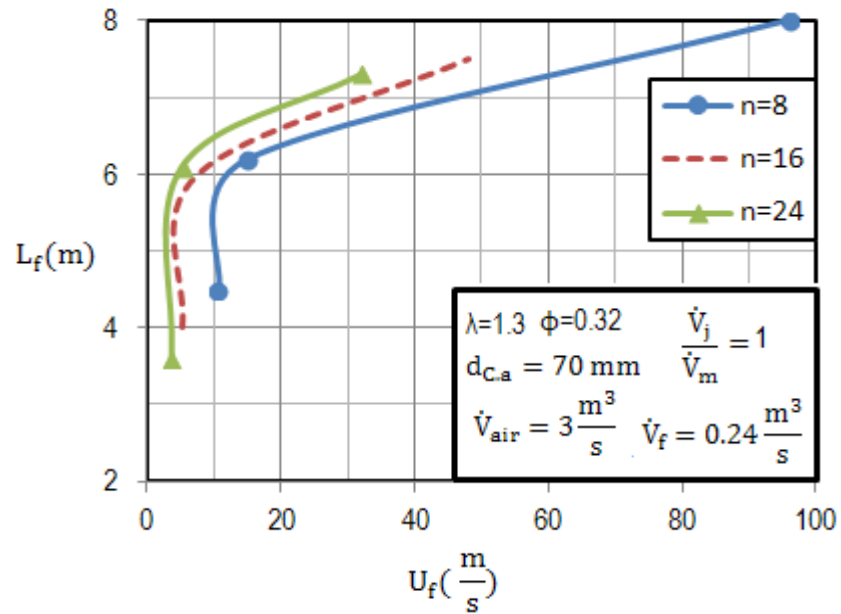
Figure 6.39: Influence of fuel velocity on flame length.

Figure 6.40 shows the CO contours for fuel velocities in the range $10\frac{m}{s}$ to $96\frac{m}{s}$. It can be seen that the higher the fuel velocity is, the higher the flame length becomes. The higher fuel velocity results in a more homogeneous concentration in the radial direction after a 2m distance from the burners. However, the fuel in the circumferential distance is relatively homogeneous.
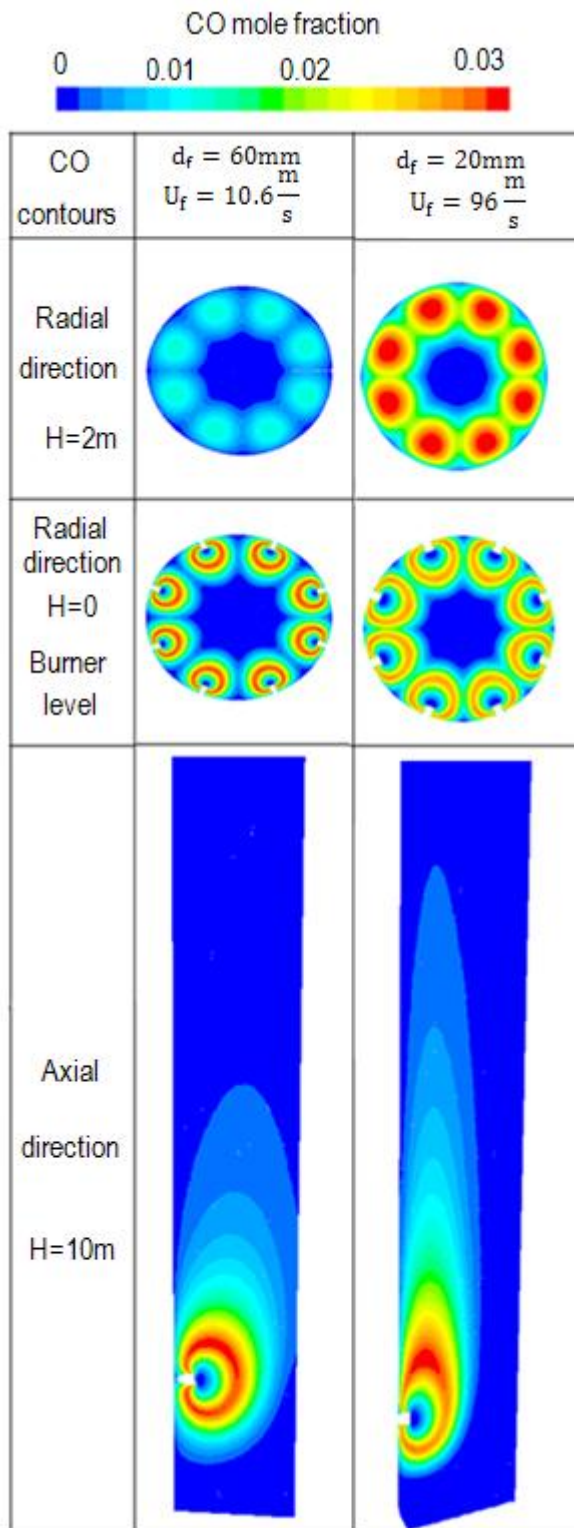
Figure 6.40: CO contours for various fuel velocities ($\frac{V_j}{V_m} = 1$).

6.7.2 Influence of combustion air velocity on the flame length

Here, the influence of combustion air velocity researched for volumetric air ratios of $\frac{\dot{V}_j}{\dot{V}_m} = 0.6$ and 1. For this aim, the diameter of the combustion air nozzle changed from 70mm to 150mm, and the fuel burner diameter was kept constant (d_f =50 mm).

The higher combustion air velocity injected from, the smaller nozzle diameter. As can be seen in Figure 6.41, the higher the combustion air velocity is, the longer the flame length becomes. When the combustion air increased by about five times, the flame length is increased by about half-a-meter.
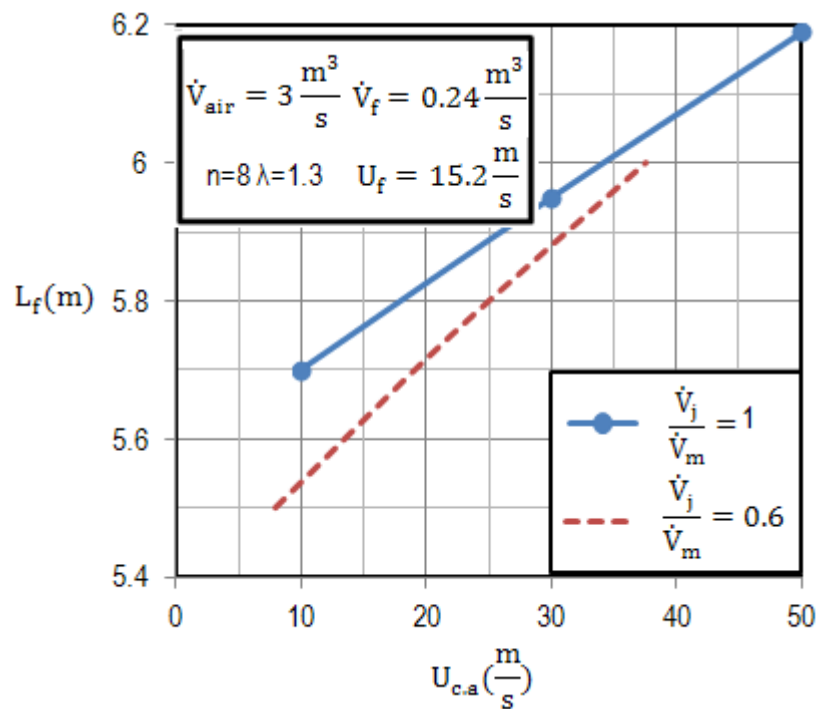

Figure 6.41: Influence of combustion air velocity.

6.7.3 Influence of porosity on flame length

In this section, the influence of porosity in the range of φ=0.32-1 researched. For this aim, all the operating parameters were kept constant. Only the porosity is changed. Figure 6.42 shows the CO mole fraction in the axial direction. As mentioned in section 6.3, the flame length is the position at which the CO fraction has fallen to 1% of the maximum concentration.

When the porosity increased from φ=0.32 to φ=0.6, there is no significant difference in the flame length (20cm). The flame length is increased only from 6.2m up to 6.4m.

The higher the porosity is, the longer the flame becomes (φ=0.32 - 0.8). A porosity of φ=0.8 gives the maximum length of the flame. When the porosity is higher than φ=0.8, the flame length is decreased down to 2m.

On the other hand, the flame length is a minimum at a porosity of φ=0.32. In reality, the packed bed porosity is always ϕ=0.4.
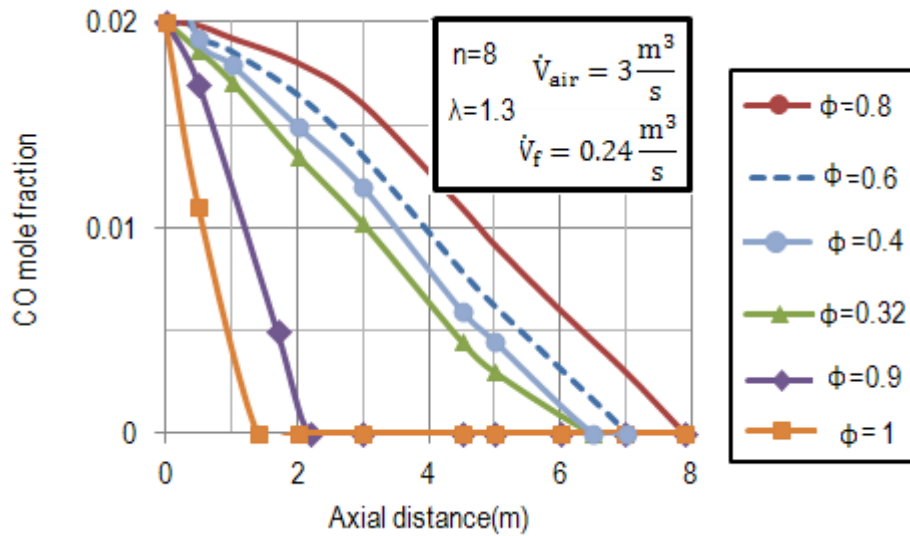

Figure 6.42: Influence of porosity on flame length (ϕ=0.32-1).

Table 6.3 shows the flame length for various porosities. The flame length for a porosity of ϕ=0.4 is about 6.3m. Overall, the influence of the porosity in the range ϕ=0.32 - 0.6 is very small. As a consequence, the results for ϕ=0.32 can also be generalized to ϕ=0.4 and ϕ=0.6.

Table 6.3: Influence of porosities on length of flame.

D=2m n=8 $d_f = 50mm$ $L_b = 0.1m$	ϕ	0.32	0.4	0.6	0.8	0.9-1
$\dfrac{\dot{V}_j}{\dot{V}_m} = 1$	$L_f(m)$	6.2	6.3	6.4	8	1.5-2

Figure 6.43 shows the CO contours for porosities ϕ=0.32, 0.4, and 0.6. It can be seen that there is no significant change in the CO concentration both in axial and radial directions. For better understanding, the axial direction is shown only up to H=6.5m.
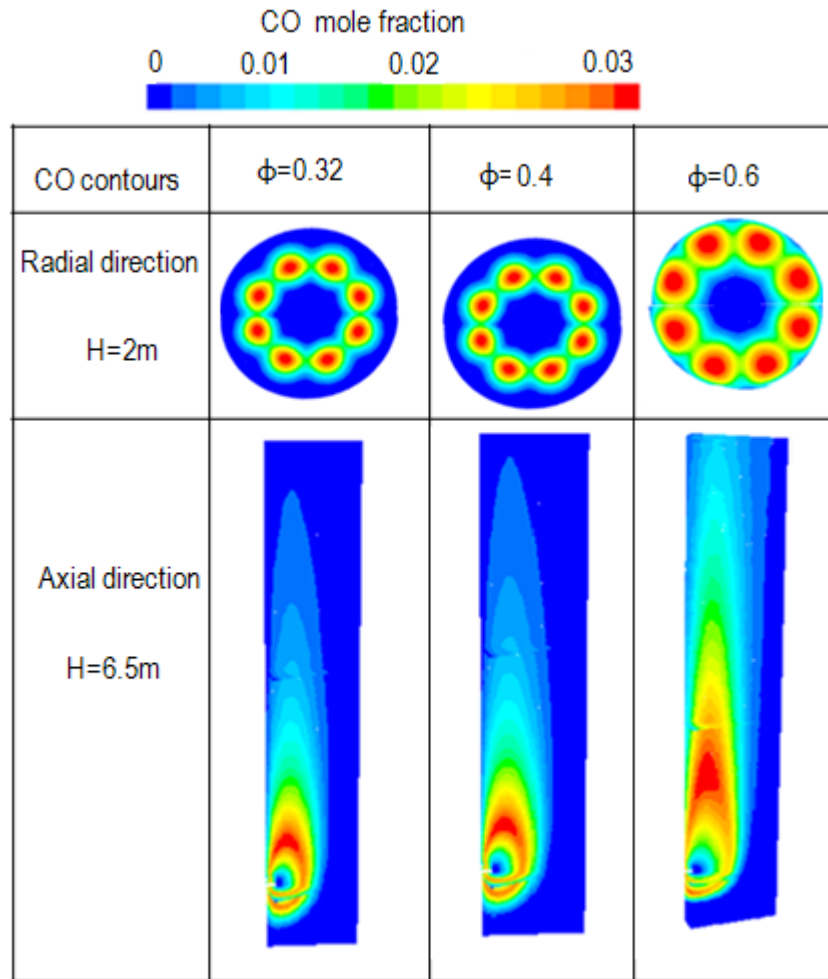
Figure 6.43: CO contours for various porosities (ϕ=0.32-0.6).

Figure 6.44 shows the CO contours for the porosity range ϕ>0.8. When the porosity is 0.8, the fuel reaches the center of the packed bed. For porosities larger than ϕ=0.8, the flame length is very short, and the CO completely consumed at about a 2m distance from the burners. The empty shaft (ϕ=1) has the minimum flame length.
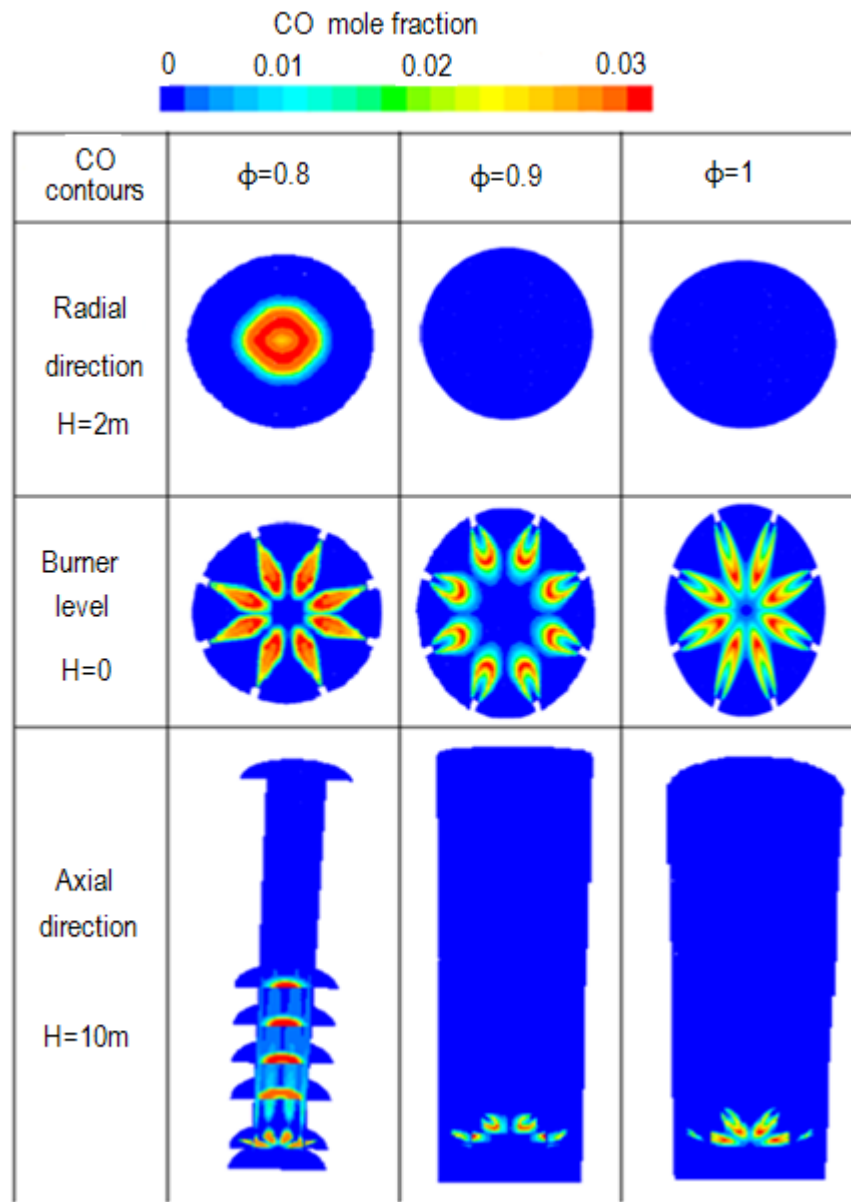
Figure 6.44: CO contours for various porosities (φ=0.8-1).

6.7.4 Influence of number of burners on the flame length

Figure 6.45 shows the influence of volumetric air ratios on the flame length and also penetration depth. For this aim, the number of burners is kept constant (n=8).

When the air volumetric ratio increased from 0.6 to 2, both penetration depth and flame lengths are increased (n=8). When the air volumetric ratio is $\frac{V_j}{V_m} = 1$, the typical value of cooling air $(1.4\frac{m^3}{s})$ injected from the bottom, and the rest $(1.6 \frac{m^3}{s})$ injected from the combustion air nozzles. To end this, when the eight burners used, the penetration depth, $\frac{h}{r}$ = 0.48, and the flame length, L_f =6.2m, are calculated.
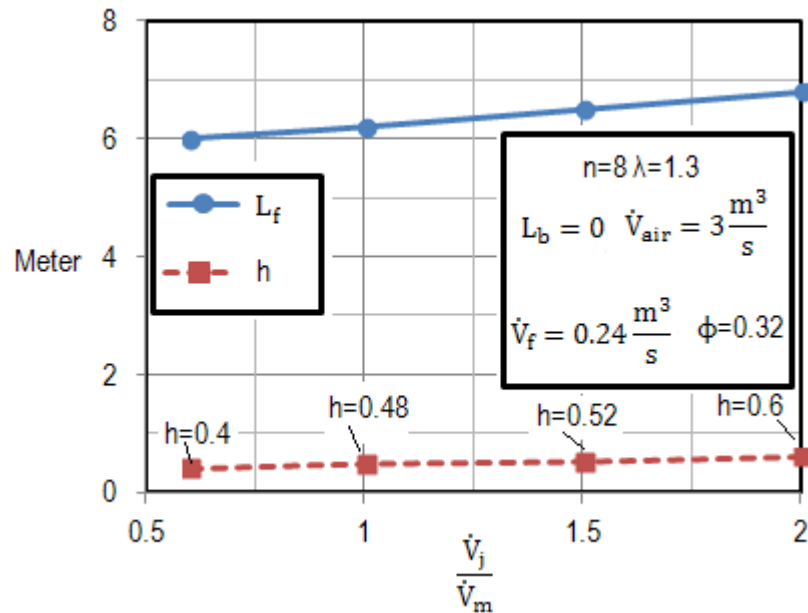
Figure 6.45: Influence of ratio of combustion air to cooling air for n=8.

Next, the influence of several burners on the flame length will be discussed. For this aim, the fuel and air volume flow and burner diameter were kept constant. The less amount of fuel injected from the more number of burners. Figure 6.46 shows the influence of the number of burners on the flame length. It can be seen that the more the number of burners is, the shorter the flame length becomes.

As a consequence, when the number of burners is increased by three times, the flame length is decreased by about 0.8m. The influence of the number of burners researched for various air volumetric ratios. Again, the higher the air volumetric ratio is, the longer the flame length becomes.
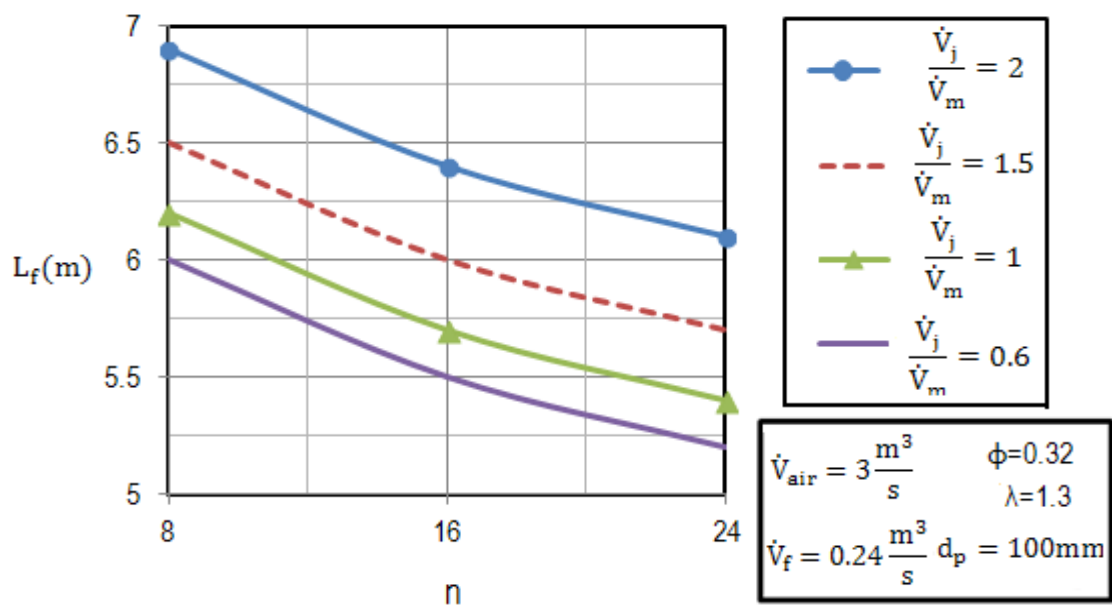
Figure 6.46: Influence of number of burners on flame length $L_b = 0$.

Figure 6.47 shows the CO contours for a scale of H=5m. The flame is shorter when 24 burners are used compared to 8 burners. However, the more the number of burners is, the deeper the penetration depth becomes. It can be seen that the CO distribution in the circumferential direction is relatively homogeneous after a 2m distance from the burners.

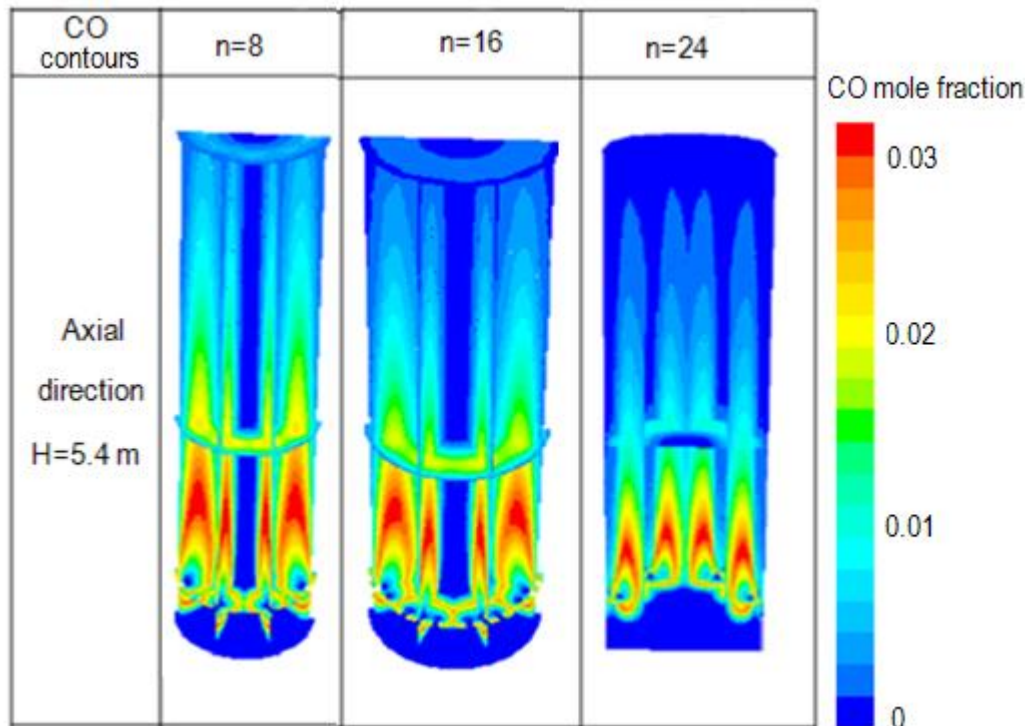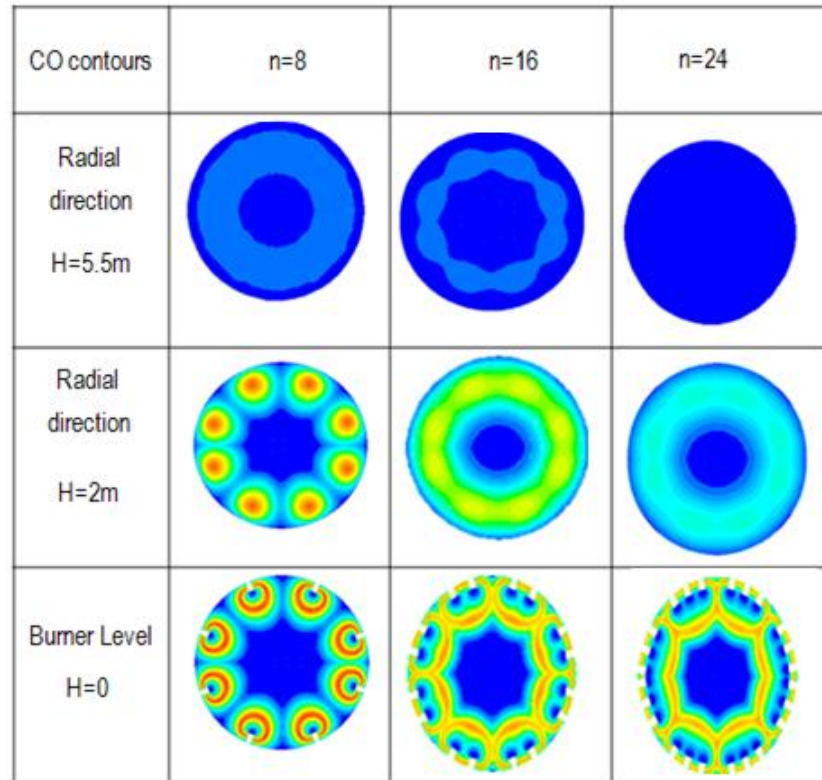

Figure 6.47: Influence of number of burners on the flame length.

Figure 6.48 shows the temperature contours for various numbers of the burners. As can be seen, the more the number of burners is, the more the temperature distribution in the radial direction becomes. The temperature is relatively homogeneous in the circumferential direction. However, the temperature in the middle of a packed bed is still at a minimum. Therefore, for deeper penetration in the cross-section, various burner depths, and a two-level burner arrangement can be discussed.
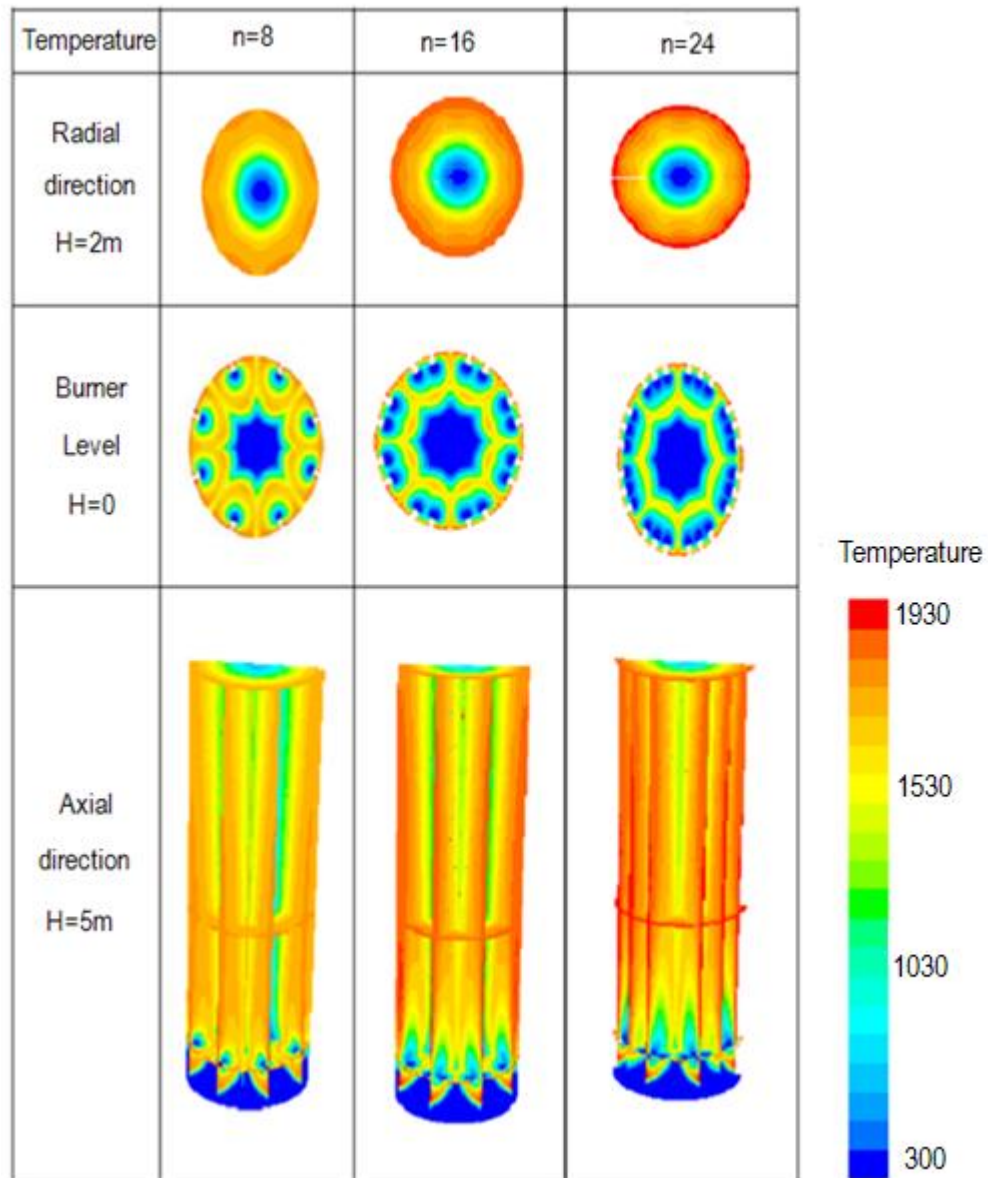
Figure 6.48: Influence of number of burners on temperature profile.

6.7.5 Influence of particle diameter on flame length

Figure 6.49 shows the influence of particle diameters on the flame length. For this aim, all the other operating parameters were kept constant. It can be seen that bigger particle diameters lead to a longer flame length. When the particle diameter increased from 20mm up to 150mm (by approximately seven times), the flame length increased by about 0.8m. The influence of the

particle diameter researched for various numbers of burners. Again, it can be seen that the more the number of burners is, the shorter the flame length becomes. In this case, the typical air volumetric ratio $\frac{V_j}{V_m}=1$ used for the CFS lime shaft kilns.

Figure 6.49: Influence of particle diameter on the flame length.

Figure 6.50 shows CO contours for the three-particle diameters (d_p=20, 50, and 100 mm). The bigger the particle is, the deeper the penetration depth and also the longer the flame length becomes.

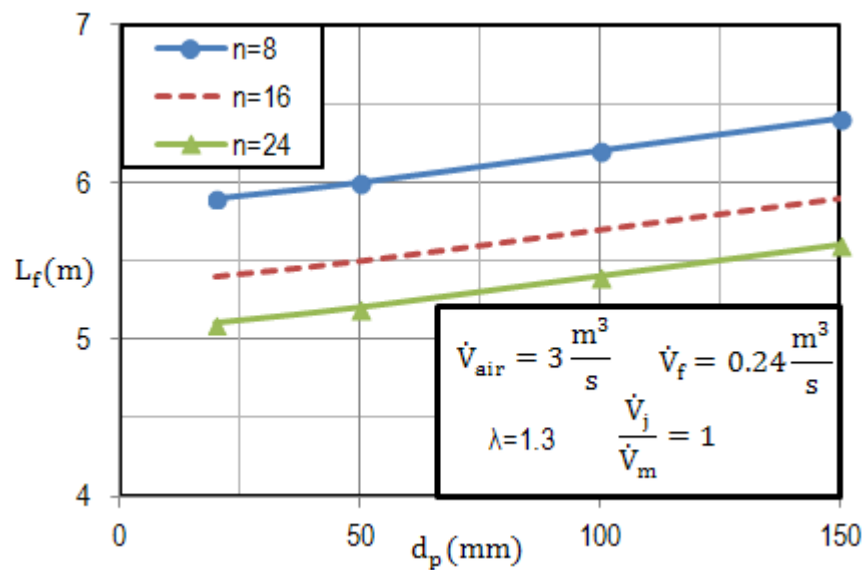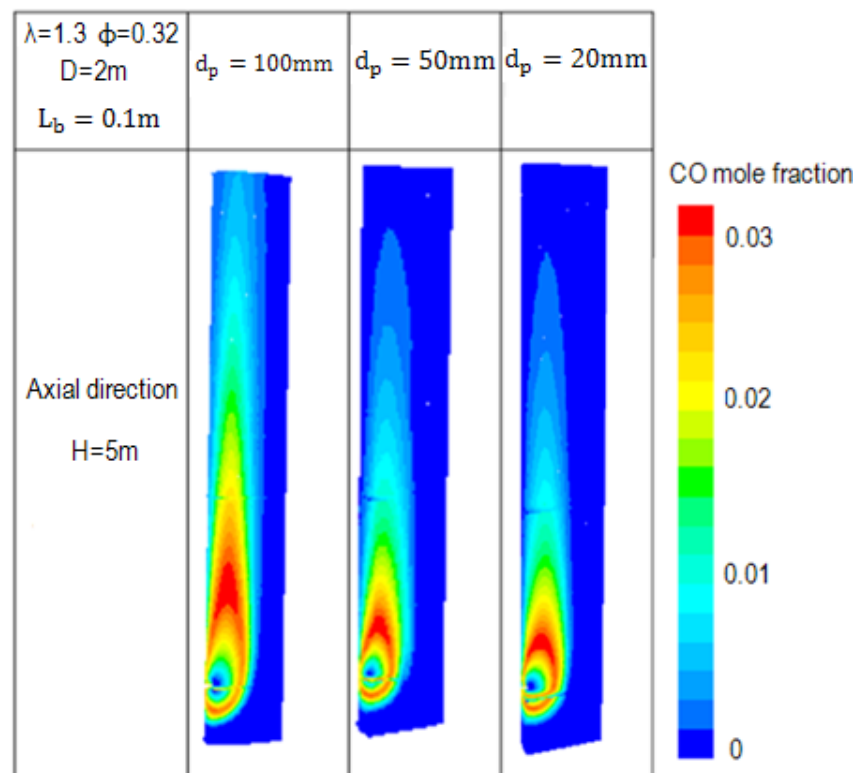

Figure 6.50: CO contours when d_p=20-100 mm.

6.7.6 Influence of kiln diameter on the flame length

Figure 6.51 shows the influence of the various kiln diameters (D=1- 4m) on the flame length. The mass flow of limestone fixed at $200\frac{ton}{day}$. For this aim, the fuel and air volume flows were kept constant. When the kiln diameter increased from 1m up to 4m, the flame length is decreased by about 0.8m. In this case, various numbers of burners used. As can be seen, the more the number of burners is, the shorter the flame becomes.
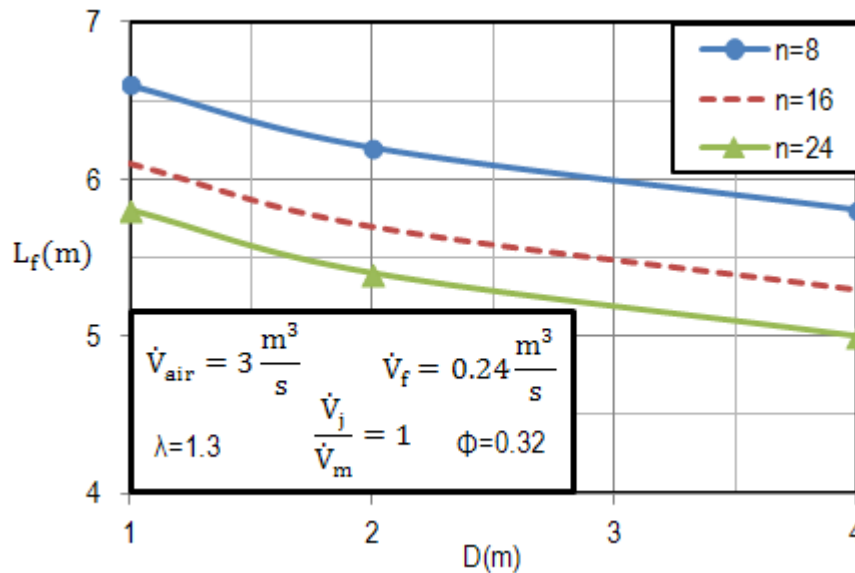
Figure 6.51: Influence of kin diameter on the flame length.

6.8 Influence of Burners Arrangement on Flame Length

6.8.1 Various burner depth arrangements

The burners can be arranged at the walls ($L_b = 0$) or the depth is increased up to $L_b = 0.3\text{m}$. In this case, the burner depth was constant for all the burners.

As it concluded in Figure 6.48, the temperature profile is minimum in the middle. Therefore, for deeper penetration in the cross-section, various burner depths should be used. Figure 6.52 shows the schematic of burners with various depths. Twenty-four burners were chosen. First, all the 24 burners are adjusted to reach a depth of 0.1m through the packed bed.
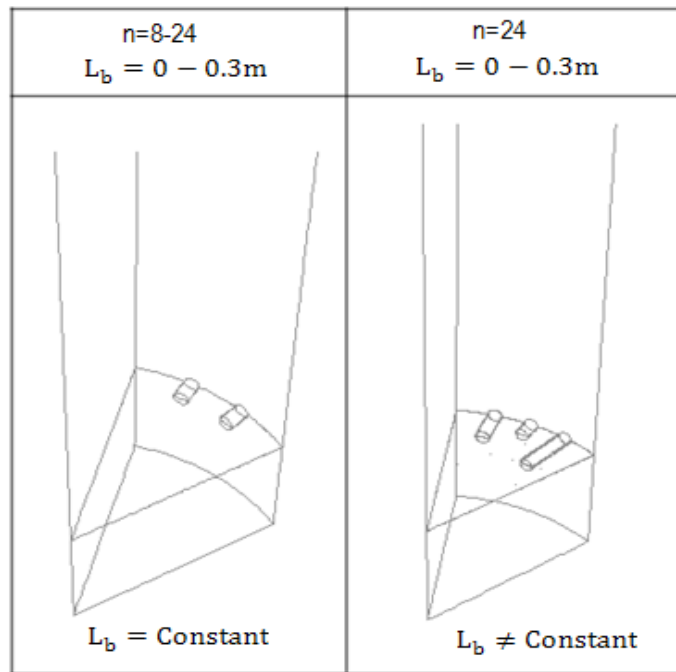
Figure 6.52: 1/8 symmetry section of burner arrangements.

Second, eight burners are retained at a depth of 0.1m, while 16 burners have 0.2m depth. Third, the 24 burners are divided equally at depths of 0.1m, 0.2m, and 0.3m, i.e., eight burners at each depth. The CH4 contours for the three different depth arrangements show in Figure 6.53.The volume flows of air and fuel were kept constant. Also, the air and fuel velocities, as well as the air volumetric ratio, were kept constant. Only the depth of burners is varied. As can be seen from the contours, the fuel distribution in the circumferential direction is relatively homogeneous after a 2m distance from the burners.
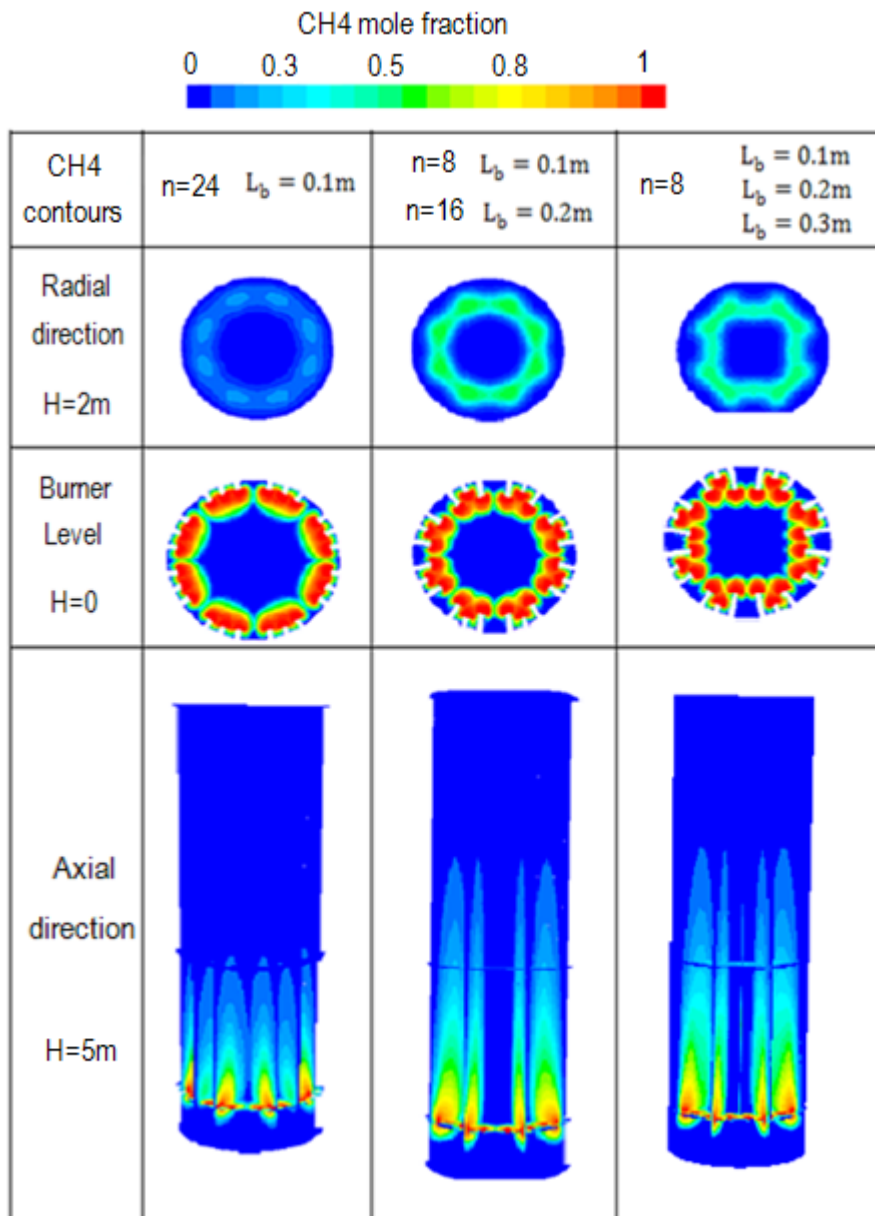
Figure 6.53: CH4 contours for different burner depth arrangements.

In this case, the typical air volumetric ratio of $\frac{V_j}{V_m} = 1$ used. When the 24 burners arranged at the walls (L_b=0), the penetration depth calculated about $\frac{h}{r}$ =0.52 (Figure 6.36).

For the deeper penetration depth, the burner depth is increased up to L_b=0.1m. Therefore, the penetration depth increased to $\frac{h}{r}$ =0.62.

Here, the influence of this burner depth arrangement compared with two other burner depth arrangements. Figure 6.54 shows the CO contours in the radial direction. Using the three different burner depths increases the penetration depth. Various burner depth arrangements lead to better mixing at the burner level (H=0). Therefore, this leads to more areas being covered by fuel.

Consequently, to a better homogenization in the cross-section. The fuel concentration in the circumferential direction is relatively homogeneous after a 2m distance from the burners. The fuel penetrates far from the walls and deeper into the center of the packed bed. However, still, no fuel reaches the core.
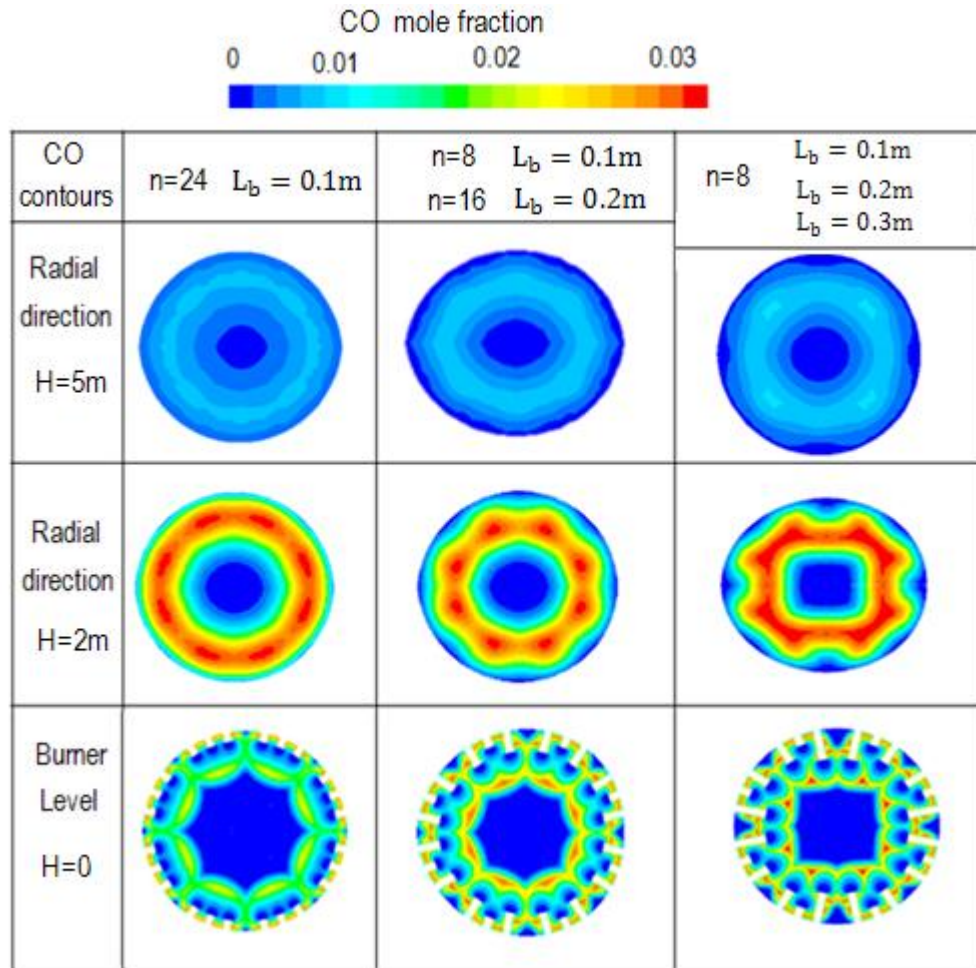

Figure 6.54: Cross section view of CO contours at various heights.

As can be seen in Figure 6.55, when the three different burner depth arrangements are employed, the fuel concentration is higher in the axial direction. Therefore, the penetration depth and the flame length are higher. Table 6.4 shows the values of L_f and $\frac{h}{r}$ for various burner depth arrangements.
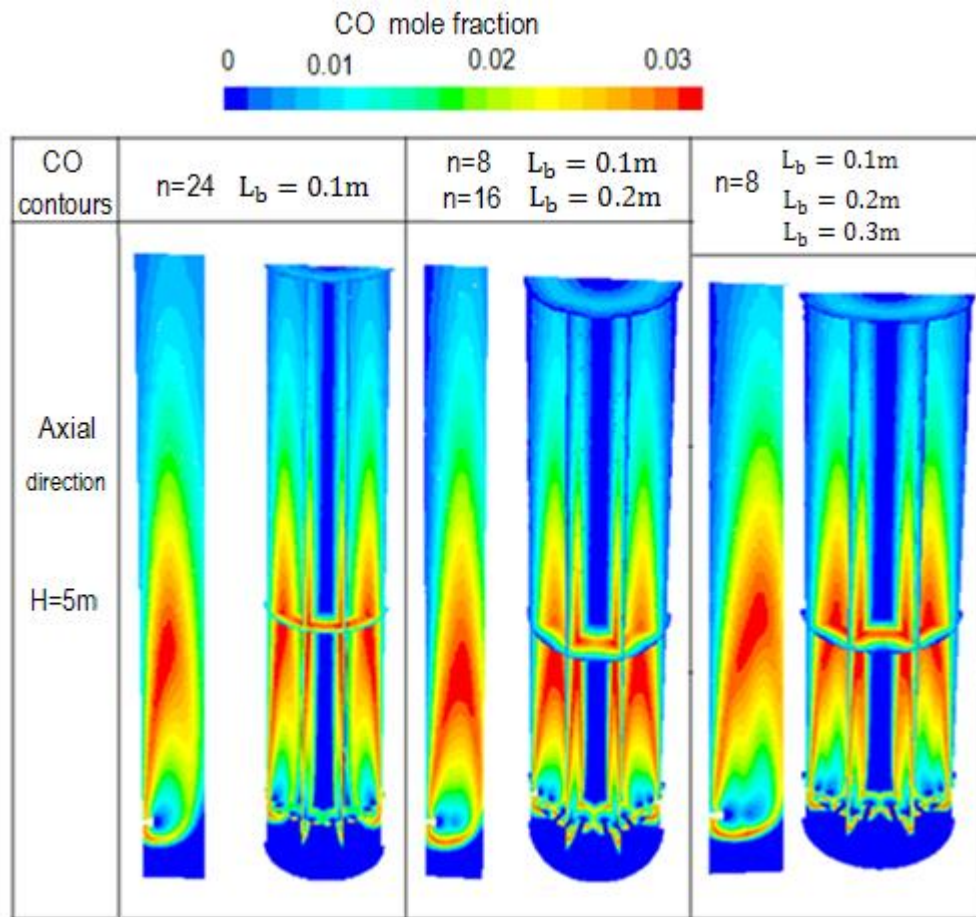
Figure 6.55 : Axial direction view of CO contours for various burner depth arrangements.

Table 6.4: Flame length and penetration depth for various burner depth arrangements.

n=24 λ=1.3 ϕ=0.32 D=2m	$d_{c.a} = 70$ mm $d_f = 50$ mm $\dot{V}_{air} = 3\frac{m^3}{s}$	$L_b = 0.1m$	$L_b = 0.1m$ $L_b = 0.2m$	$L_b = 0.1m$ $L_b = 0.2m$ $L_b = 0.3m$
$\dfrac{\dot{V}_j}{\dot{V}_m} = 1$	$L_f(m)$	5.4	5.7	5.9
$\dot{V}_f = 0.24\dfrac{m^3}{s}$	$\dfrac{h}{r}$	0.62	0.64	0.66

As a consequence, when the 24 burners adjusted in the form of the three various burner depth arrangements, the penetration depth is increased up to 0.66, which is the highest that has been reached so far. However, the penetration depth is not even in the cross-section, and the fuel has not reached the center of the packed bed. Therefore, the influence of the two-row arrangement on the penetration depth will be discussed in the next section.

6.8.2 Two- row burner arrangements

Here, to reach a deeper penetration depth, a two-row burner arrangement is studied. The burners adjusted in two rows. The depths of the lower row (first row) burners are 0.1m. The upper row (second row) burners adjusted with a 0.3m depth through the packed bed. The height between the two-rows is 0.3 m. Figure 6.56 shows the schematic of the two-row arrangements.
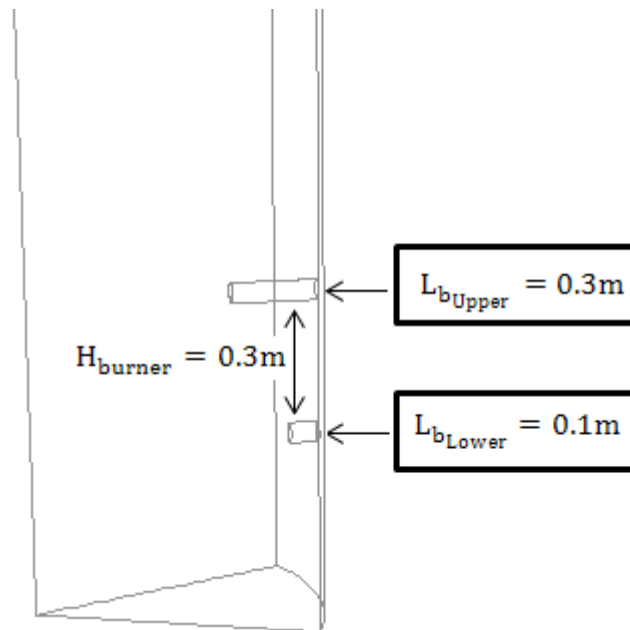
Figure 6.56: Schematic position of two row arrangements.

For this aim, the fuel and air volume flows were kept constant. The typical air volumetric ratio of $\frac{V_j}{V_m} = 1$ used. The combustion air and fuel volume flow injected in three ways.

First, the same fuel volume flow injected from all the burners. Second, 20% of the fuel volume flow injected from the upper row (second row) and 80% from the lower row (first row). Third, 80% of the fuel volume flow injected from the upper row and 20% from the lower row.

Figure 6.57 shows the CO contours for the three cases. The n=16 burners arranged in two rows with eight burners on each row. As can be seen, when the same fuel volume flow injected from all the burners, the flame length is the shortest. When the percentage of fuel volume flow injected from the upper row (second row- case three) is higher, the flame length is the longest. Therefore, the percentage of fuel volume flow influences the penetration depth and the flame length.

As a consequence, when 80 % percent of the fuel injected from the upper row, and the remaining injected from the lower row, the penetration depth and flame length decreased.
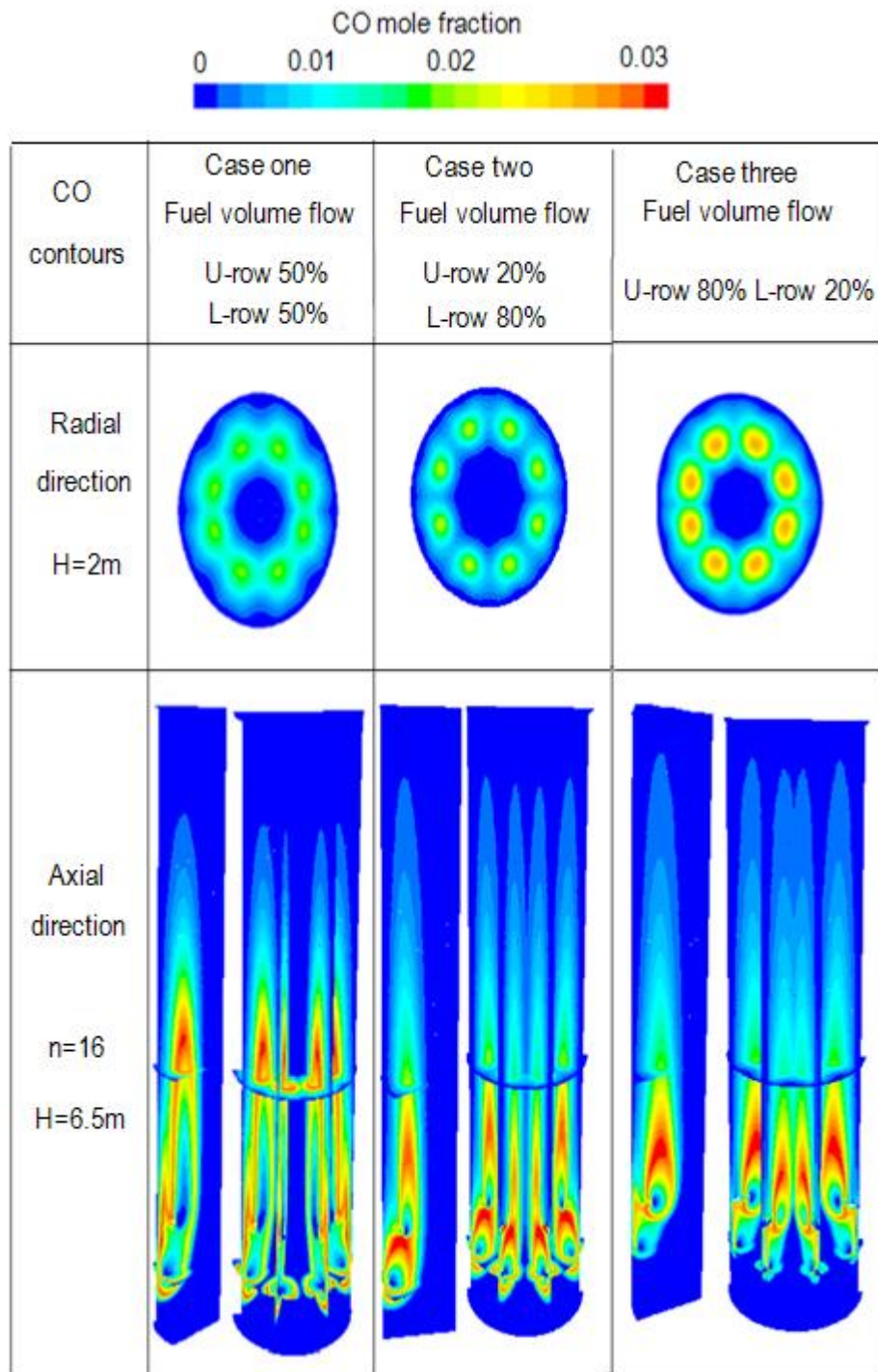
Figure 6.57: Influence of two-row arrangements for n=16.

Figure 6.58 shows the CO contours for the case of the n=16 burner, where they are arranged both in one and in two levels. As can be seen, when the burners arranged in two rows, the fuel penetrates deeper in the cross-sectional direction, and the flame is also longer.
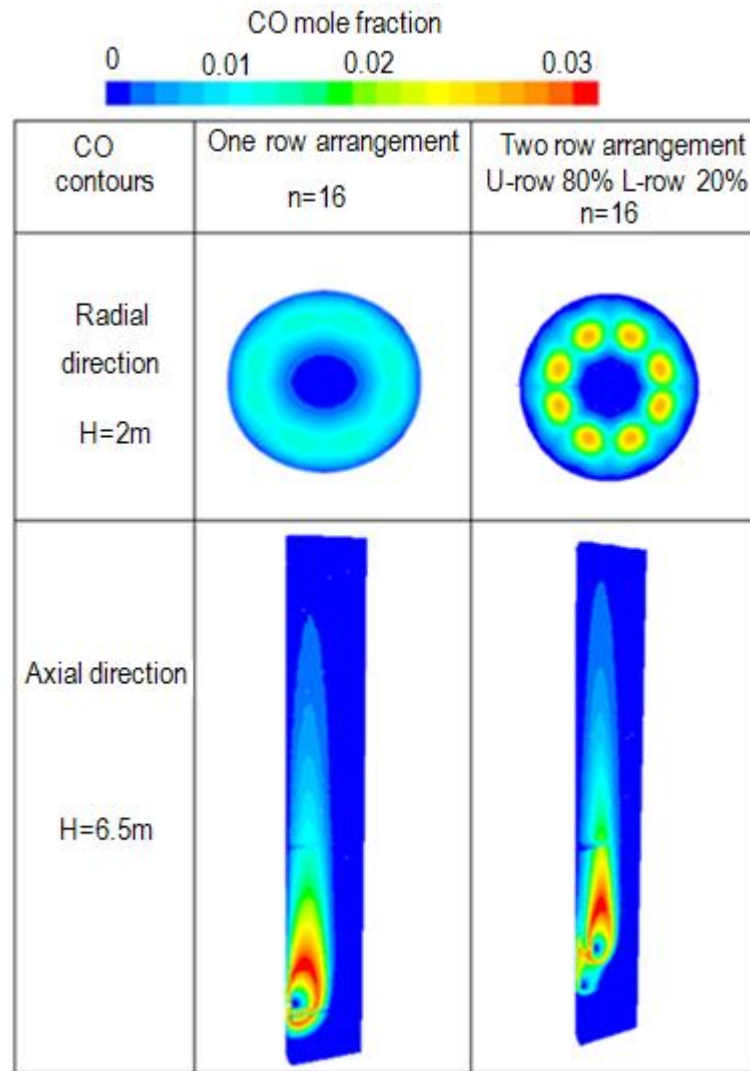
Figure 6.58: CO contours for both one- and two-row burner arrangements when n=16.

Table 6.5 shows the calculations for one- and two-row arrangements. Arranging the burners in two rows, while keeping the number of burners constant, increasing the penetration depth by 3 cm. Also, the flame length is increased by half-a-meter.

Table 6.5: Details of one- and two-row arrangements.

$\lambda=1.3$ $\phi=0.32$ $D=2m$ $L_b = 0.1m$	$d_{C.a} = 70mm$ $d_f = 50mm$ $\dot{V}_{air} = 3\frac{m^3}{s}$	One row arrangements n=16	Two row arrangements n=16	One row arrangements n=24	Two row arrangements n=24
$\frac{\dot{V}_j}{\dot{V}_m} = 1$	$L_f(m)$	5.6	6.1	5.9	6.4
$\dot{V}_f = 0.24\frac{m^3}{s}$	$\frac{h}{r}$	0.6	0.63	0.66	0.69

The deepest penetration depth of $\frac{h}{r} = 0.69$ obtained when the 24 burners arranged in various depths in the two rows.

6.8.3 Extended two-row burner arrangement

In the previous section, the two-row burners arranged with various depths. The deepest penetration depth of $\frac{h}{r} = 0.69$ was obtained.

Accordingly, a burner depth of 0.3m is not sufficiently high enough for obtaining a satisfactory penetration depth. Therefore, the upper burner depth is increased from 0.3m to 0.6m, while the lower burners' depth is kept constant at 0.1m. The angle between the two rows is between 10° to 15°. Figure 6.59 shows the schematic of the extended two-row burner arrangement.
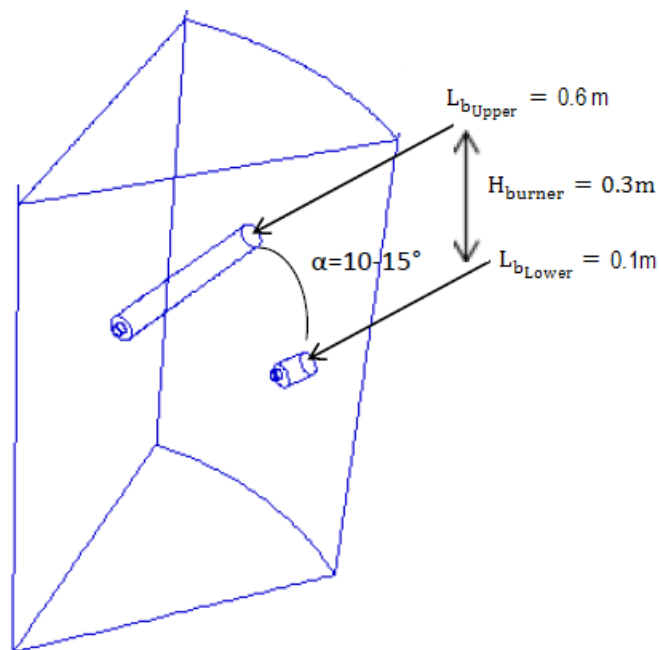
Figure 6.59: Schematic of the extended two-row arrangement.

Figure 6.60 shows the CO and temperature contours in the radial direction. When the burner of 0.6m depth used, the fuel reaches the core and covers more areas. The temperature is relatively homogeneous at 2m. The temperature is always low near the walls and maximum at the center.

Figure 6.61 shows the CO and temperature profiles in the axial direction. As can be seen, the CO concentration reaches the maximum value. It then becomes relatively even in the center of the packed bed. Also, the temperature distribution is the highest in the center of the packed bed.
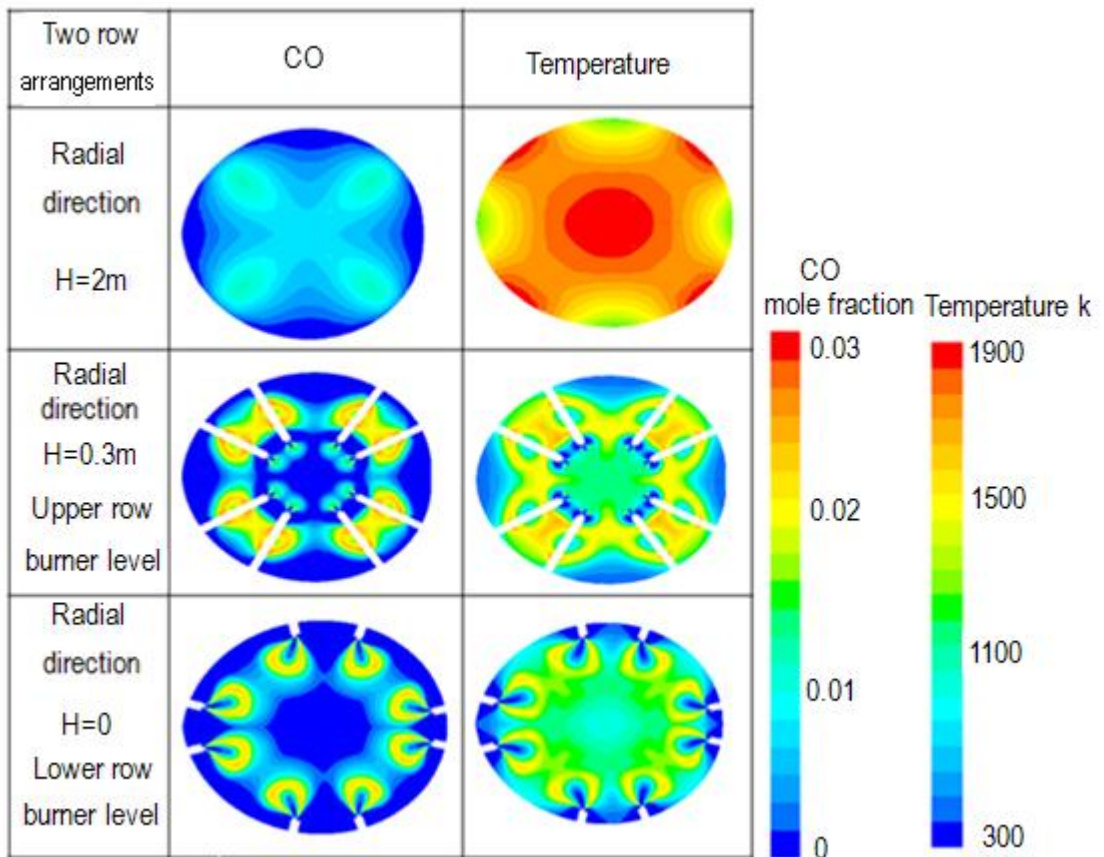
Figure 6.60: Radial temperature and CO contours for extended two-row arrangements.
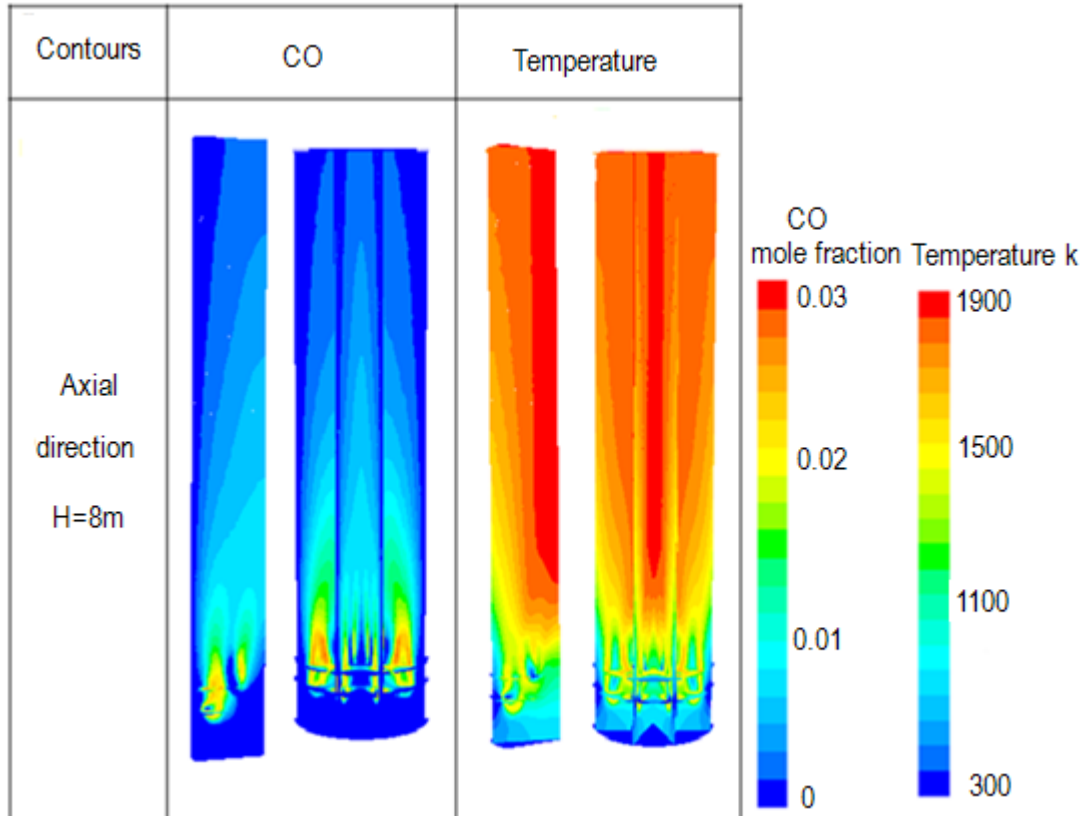
Figure 6.61: Axial temperature and CO contours for extended two-row arrangements.

164

Figure 6.62 shows the CO profile after a 2m distance from the upper burners. As can be seen, the fuel profile is more homogeneous in the center of the packed bed. Also, the CO concentration covered more areas near the walls.
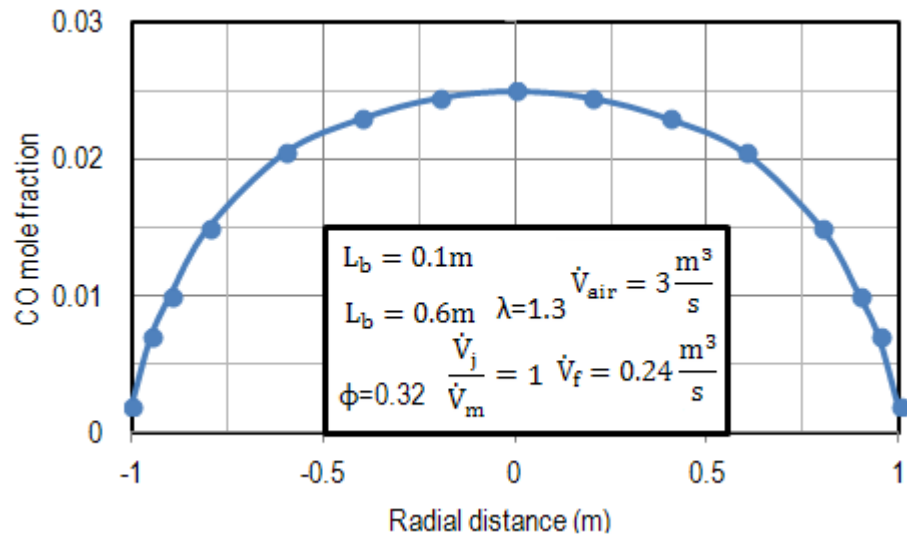
Figure 6.62: CO profile for extended two-row arrangement after H=2m.

Figure 6.63 shows the temperature profile after a 2m distance from the upper burners. It can be seen that the temperature at H=2m is completely homogeneous.
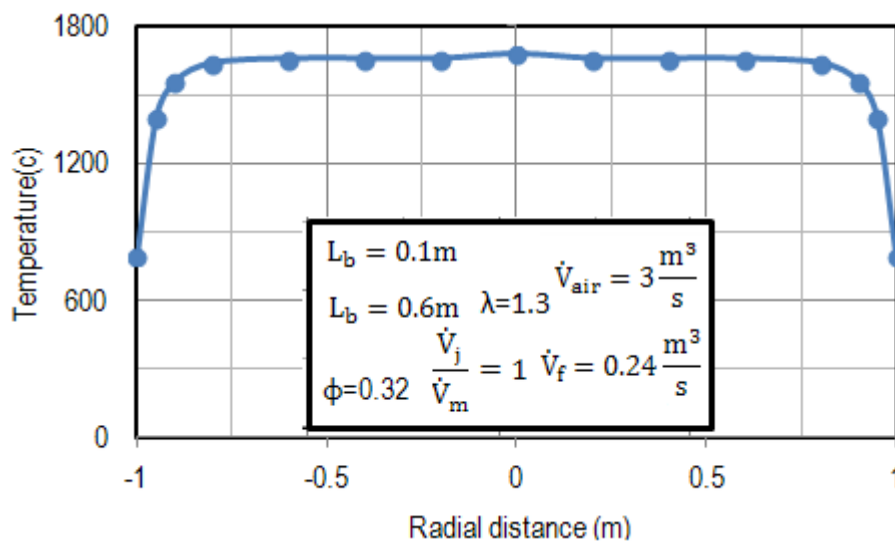
Figure 6.63: Temperature profile for extended two-row arrangement after H=2m.

As a consequence, when the extended two-row arrangement used, the CO concentrations are reached to the center of the packed bed. Therefore, the longest flame length is $L_f = 8m.$

6.9 Influence of Excess Air on Flame Length

The combustion air injected from the radial nozzles, and the cooling air injected from the bottom of the kiln. Here, the influence of excess air number on the flame length is studied.

For this aim, the fuel volume flow $(V_f = 0.24 \frac{m^3}{s})$ and cooling air volume flow $(V_{cooling.air} = 1.4 \frac{m^3}{s})$ were kept constant. The extra air is injected from the combustion air nozzles. The typical air ratio is also kept constant $((\frac{V_j}{V_m} = 1$. The excess air number is studied for three different numbers of burners: n=8, 16 and 24. Figure 6.64 shows the influence of excess air number on the flame length. When the excess air number is increased from λ=1.3 to λ=2, the flame length is decreased from 6.2m to 4.2m (by about 2m). It can be seen that the flame length starts to increase very strongly for λ values lower than 1.2. Overall, the higher the excess air number is, the shorter the flame length becomes.

Figure 6.64: Influence of excess air number on the flame length.

Figure 6.65 shows the CO and temperature contours in the radial direction at H=2m. It can be seen that when the excess air number increased to λ=2, the CO concentration at H=2m is lower than the other scenarios. Therefore, the higher the excess air number is, the lower the penetration depth becomes.
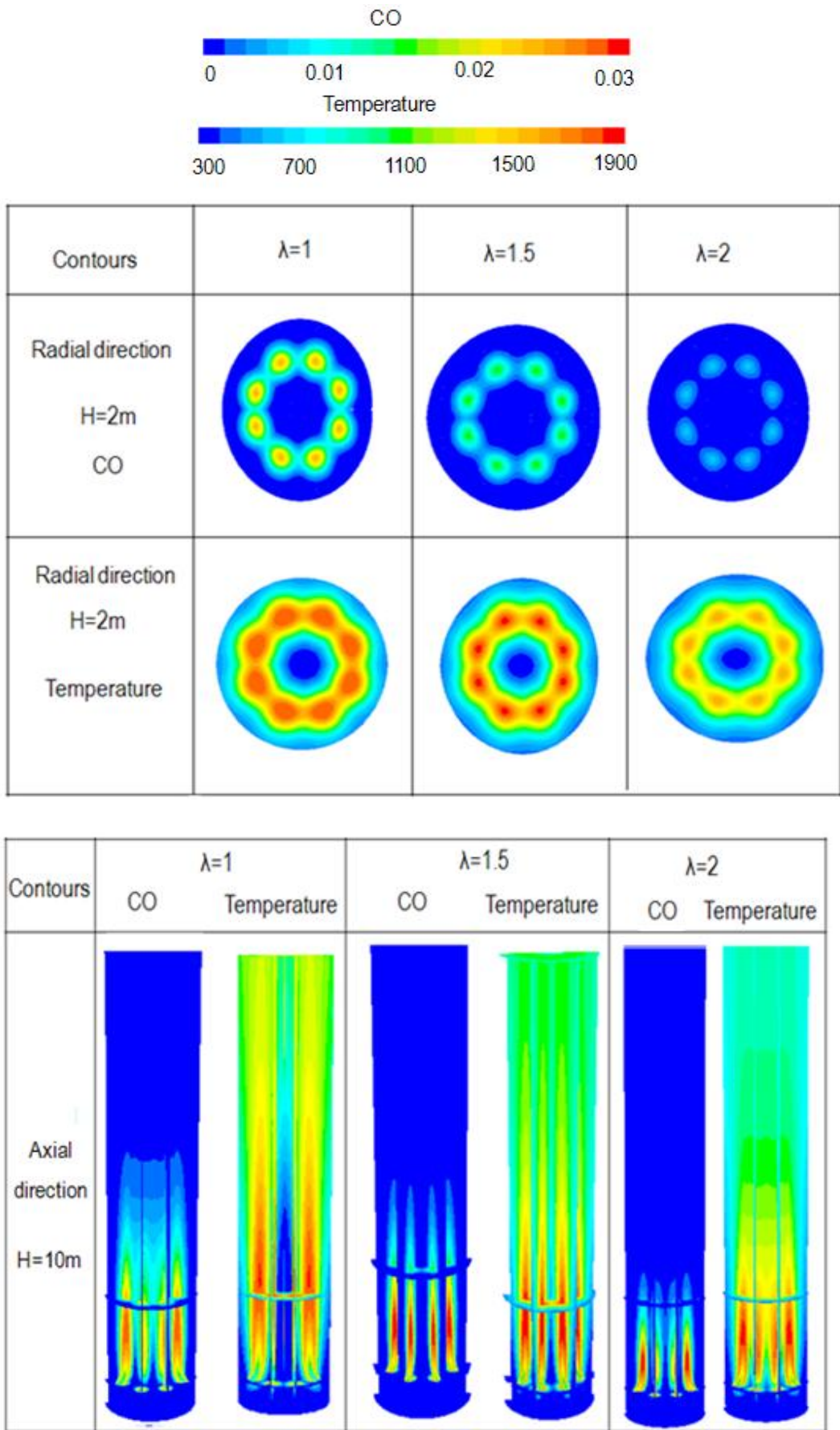
Figure 6.65: Contours of temperature and CO for λ=1 to 2.

6.10 Influence of Fuel Types on the Flame Length

Methane used as an example of gaseous fuel (natural gas) and the results compared to other types of fuels keeping the energy input and the excess air number constant.

Table 6.6 shows the flame lengths for various fuel types. For this aim, the air volumetric ratio and the fuel volume flow are kept constant. When methane used as a combustion fuel, the longest flame lengths obtained.

Usage of fuel oil as a fuel source results in longer flames in comparison to gasoline, when the energy was kept constant. The higher the percentage of carbon content in fuel is, the longer seems to be the flame length.

In many areas, coal, lignite, or pet coke are less expensive and more readily available compared to gaseous and liquid fuels. Here, the three types of solid fuels are studied. The coal LV results in the longest flame. Table 6.6: Influence of fuel types on flame length for n=24.

Type of Fuel	Constant in Energy Input	Flame Length $L_f(m)$
Gaseous	Natural Gas H	5.4
	Biogas	5
Solid	Coal LV	4.8
	Anthracite	4.5
	Lignite	4
Liquid	Fuel Oil ($C_{19}H_{30}$)	4.7
	Benzen (C_6H_6)	4.4
	Ethanol ($C_2H_5\text{-}OH$)	4.2
	Methanol ($CH_3\text{-}OH$)	4
	Gasoline (Petrol-C_8H_{18})	3.7

Chapter 7

Conclusion

Current research studies focus on the influence of mixing parameters on the flame length in PFR and CFS shaft kilns. Validation of simulations with experimental results done by injecting two different gases into a sample of packed bed from an experiment.

This research study demonstrates that PMM is a proper approach to simulate the reactive flow in the packed bed of a shaft kiln. The k-ε standard and k-ω SST turbulence models showed the best accuracy with the experimental measurements.

The non-premixed combustion of methane and flame length has been investigated. In reality, the packed bed porosity is always φ=0.4. The flame length reaches its minimum value at a porosity of ϕ=0.32. Overall, the influence of the porosity in the range ϕ=0.32 - 0.6 is very small. As a consequence, the results for φ=0.32 can also be generalized for porosities from ϕ=0.4 up to ϕ=0.6.

When the excess air number was kept constant at $\lambda = 1.3$, increasing the fuel volume flow by about seven times, it increased the flame length by about 20 cm. The overall influence of the fuel volume flow on the flame length is very small. As a consequence, all results for the chosen fuel volume flow of $0.13\frac{m^3}{s}$ can be generalized to all other fuel volume flows, kiln throughputs, and also different types of kilns.

The flame length simulated for a large number of burners for both PFR and CFS shaft kilns. It was found that the flame length decreased with an increasing number of burners, while the fuel and temperature became better distributed in the radial direction. Therefore, more burners must be used.

When the particle diameter increased from 20mm to 150mm (by approximately seven times), the flame length was increased by about 0.8m.

Fuel velocities approximately in the range of $5\frac{m}{s}$ to $96\frac{m}{s}$ were researched. The higher the outlet fuel velocity is, the longer the flame length becomes. In CFS kilns, the flame length increased by approximately two times. While in PFR kilns, the flame length is increased only by 0.6m.

When the excess air number increased from λ=1.3 to λ=2, the flame length observed to decrease. The flame length starts to rise very sharply for λ values lower than 1.2. Overall, the higher the excess air number is, the shorter the flame length becomes.
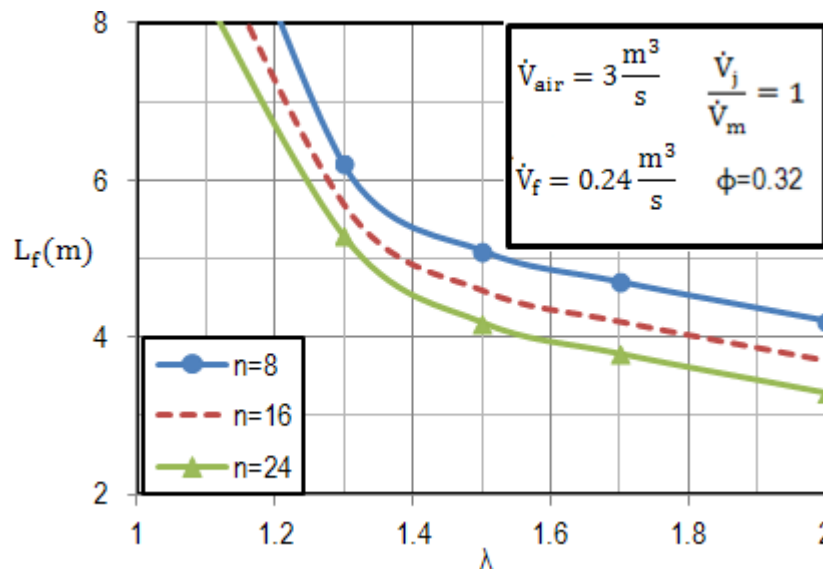
Methane used as an example of gaseous fuel (natural gas), and the results were compared to other types of fuels while keeping the energy input and the excess air number constant. The most extended flame lengths obtained when methane used as the combustion fuel.

In CFS kilns, the fuel and combustion air radially injected from the burners, and the cooling air axially injected from the bottom. Therefore, the fuel penetration in the radial direction and the influencing parameters investigated. The more the air injected from the burners, the deeper the penetration depth. However, the typical air volumetric ratio for CFS shaft kilns is 1. When the number of burners increased three times, the penetration depth increased by 5 cm.

When the 24 burners arranged at the walls (L_b= 0), the penetration depth calculated as about $\frac{h}{r}$=0.52 .Increasing the burner depth to L_b=0.1m increases the penetration depth to about $\frac{h}{r}$ =0.62. Therefore, for deeper penetration in the cross-section, various burner depths should be used. When only the depth of the burners is varied, the penetration depth observed to increase.

To reach a deeper penetration depth, a two-row burner arrangement was studied. Arranging the burners in two rows while keeping the total number of burners constant, increasing the penetration depth by 3 cm. Also, the flame length is increased by half-a-meter.

The deepest penetration of $\frac{h}{r} = 0.69$ obtained when the 24 burners arranged in various depths in two rows. Accordingly, a burner depth of 0.3m is not sufficiently high enough for getting a satisfactory penetration depth. Therefore, the upper burner depth is increased from 0.3m to 0.6m, while the lower burners' depth is kept constant at $L_{b.Lower} = 0.1m$.

As a consequence, when the extended two-row arrangement used, the CO concentrations reach the center of the packed bed. Therefore, the longest flame is $L_f = 8m$ long.

Measurements cannot provide these parameters. These results may help to optimize the kiln design, performance, and operational modes in terms of high-temperature distribution and energy efficiency.

References

[1] J. Oates, "Lime and limestone chemistry and technology, production and uses", *Wiley VCH, 1 edition*, 1998.

[2] The Maerz, "Lime Shaft kilns", /www.maerz.com/#up"

[3] D. HaiDo, "Simulation of lime calcinations in normal shaft kilns and PFR kilns", *Otto von Guericke University Magdeburg, Ph.D. thesis*, 2011.

[4] Agnieszka Bes, "Dynamic process simulation of lime stone calcinations in normal shaft kiln", *Ph.D. Thesis, Magdeburg, Otto von Guericke University Magdeburg, Ph.D. thesis*, 2006.

[5] V. Shagapov and M. Burkin, "Theoretical modeling of simultaneous processes of coke burning and lime stone decomposition in furnace", *Combustion, Explosion, and Shock Waves*, vol. 44, pp. 55–63, 2008.

[6] F. Marias and B. Bruyres, "Modeling of a biomass fired furnace for production of lime", *Chemical Engineering Science*, vol. 64, pp. 3417–3426, 2009.

[7] A. Senegacnik and J. Oman, "Annular shaft kiln for lime burning with kiln gas recirculation", vol. 28, 2008.

[8] T. Bluhm-Drenhaus and E. Simsek, "A coupled fluid dynamic-discrete element simulation of heat and mass transfer in a lime shaft kiln", *Chemical Engineering Science*, vol. 65, pp. 2821–2834, 2010.

[9] Y. Gordon and V. Shvidkiy, "Optimization of the design and operating parameters of shaft furnaces", *3rd International Conference Science and Technology of Iron making*, pp. 311–316, 2006.

[10] A. F. Reshetnyak and V. Konev, "Improvement of shaft furnace construction for roasting limestone", *Refractories and Industrial Ceramics,* vol. 49, pp. 25–27, 2008.

[11] A. Senegacnik and J. Oman, "Analysis of calcinations parameters and the temperature profile in an annular shaft kiln. Part 1: Theoretical survey," *Applied Thermal Engineering*, vol. 27, pp. 1467–1472, 2007.

[12] V. T. Ryazanov and V. V. Madison, "Improving the heating system and structure of shaft furnaces for roasting limestone", *Steel in Translation*, vol. 40, pp. 298–304, 2010.

[13] P. Accinelli, "New life for old lime kilns", *World Cement,* vol. 37, 2006.

[14] Y. Zhengming and Z. Jiemin, "Numerical simulation of thermal process and energy saving of lime furnace", *Journal of Central South University of Technology*, vol.12, pp. 295–299, 2005.

[15] Zhiguo Xu, "Reduced Model for simulation in the burner region of lime shaft kilns", *Otto Von Guericke-University Magdeburg, Ph.D. thesis*, 2010.

[16] H. Mikulcica and E. V. Bergb, "Numerical modeling of calcinations reaction mechanism for cement production"*, Chemical Engineering Science*, vol. 69, pp. 607–615, 2012.

[17] M. Rasul and D. Saotayanan, "Modeling and simulation of thermodynamic processes of vertical shaft kiln used for producing dead burned magnesia," *International journal of energy and environment*, vol. 1, pp. 37–44, 2007.

[18] B. Eisfeld and K. Schnitzlein , "A new pseudo continuous model for the fluid flow in packed beds", *Chemical Engineering Science*, vol. 60, pp. 4105–4117, 2005.

[19] Ali Al-Khalaf, "Experimental and Numerical Analysis for flow mixing in packed bed", *Otto Von Guericke-University Magdeburg, Ph.D. thesis*, 2016.

[20] W. Guo and A. Ying, "Influence of 2d and 3d convection diffusion flow on tritium permeation in helium cooled solid breeder blanket units", *Fusion Engineering and Design*, vol. 81, pp. 1465–1470, 2006.

[21] C. Wu and Y. Ferng, "Investigating the advantages and disadvantages of realistic approach and porous approach for closely packed pebbles in CFD simulation", *Nuclear Engineering and Design*, vol. 240, pp. 1151–1159, 2010.

[22] M. Nijemeisland and A. Dixon, "CFD study of fluid flow and wall heat transfer in a fixed bed of spheres", *American Institute of Chemical Engineers*, vol. 50, pp. 906–921, 2004.

[23] W. Van-Rooyen and D. Krueger, "Simulation and optimization of gas storage tanks filled with heat sink", *Nuclear Engineering and Design*, vol. 236, pp. 156–163, 2006.

[24] H. A. Jakobsen and H. lindborg, "A numerical study of the interactions between viscous flow, transport and kinetics in fixed bed reactors", *Computers and Chemical Engineering*, vol. 26, pp. 333–357, 2002.

[25] K. Vafai and C. Tien, "Boundary and inertia effects on flow and heat transfer in porous media", *Int. J. Heat Mass Transfer*, vol. 24, pp. 195–203, 1981.

[26] Y. Demirel and R. Kahraman, "Thermodynamic analysis of convective heat transfer in annular packed bed," *Int. J. Heat Mass Transfer*, vol. 21, pp. 442–448, 2000.

[27] MacDonald and M. S. El-Sayed, "Flow through porous media the ergun equation revised", *Ind Eng Chem. Fund.*, vol. 18, pp. 199–208, 1979.

[28] R. Hicks, "Pressure drop in packed beds of spheres", *Ind .Eng. Chem. Fund.* vol. 9, pp. 500–502, 1970.

[29] R. D. Bradsha and J. E. Myers, "Heat and mass transfer in fixed and fluidized beds of large particles", *AIChe*, vol. 9, pp. 590–598, 1963.

[30] D. Handly and P. Heggs, "Momentum and heat transfer mechanisms in regular shaped packings", *Trans. Inst. Chem. Eng.* vol. 46, pp. 251–259, 1968.

[31] D. Nemec and J. Levec, "Flow through packed bed reactors: 1.single-phase flow", *Chemical Engineering Science, vol. 60, pp. 6947–6957, 2005.*

[32] J .Wu and B. Yu, "A resistance model for flow through porous media", *Transp Porous Med*, vol. 71, pp. 331–343, 2008.

[33] J. Hellström and T.Lundström, "Flow through porous media at moderate Reynolds number", *International Scientific Colloquium, Modeling for Material Processing*, June 8–9, 2006.

[34] Masaki, "Masaki okuyama, turbulent combustion characteristics of pre mixed gases in a packed pebble bed at high pressure", *Proceeding of the combustion Institute*, vol. 33, pp. 1639–1646, 2011.

[35] C. Johansen and G. Ciccarelli, "Combustion in a horizontal channel partially filled with a porous media", *International symposium on shock waves*, pp. 97–106, 2008.

[36] K. Kamiuto and S. Miyamoto, "Diffusion flames in plane-parallel packed beds", *International Journal of Heat and Mass Transfer, vol*. 47, pp. 4593–4599, 2004.

[37] H. Liu and S.Dong, "Parametric investigations of premixed methane air combustion in two-section porous media by numerical simulation", *Fuel*, vol. 89, pp. 1736–1742, 2010.

[38] ANSYS, "Ansys Fluent 12.0, user's guide", April 2009.

[39] Patankar, "Numerical heat transfer and fluid flow", Mc Graw–Hill Book Company, 1980.

[40] Adnan Al-Hasnawi, "Mixing behavior of side injection of air jets and gaseous fuel jet in to the axial flow of tunnel kilns*", Otto Von Guericke-University Magdeburg, Ph.D. thesis*, 2016.

[41] M. Salim and S. C. Cheah, "Wall y+ strategy for dealing with wall bounded flows", in *Proceeding of International conference of engineers and computer scientists*, Hong Kong, 2009.

[42] Lars Davidson, "An introduction to turbulance models", http://www.tfd.chalmers.se/~lada, 2015.

[43] A. Bakker, "Turbulence models", 2006. [Online]. Available: www.bakker.org.

[44] H.F.Elattar,Rayko Stanev,Eckehard Specht ,A.Fouda ," CFDsimulation of confined non-premixed jet flame in rotary kilns for gaseous fuel" Computers &Fluids,http://dx.doi.org/10.1016/j.compfluid.2014.05.0330045-7930.

[45] A. G. Dixon and M. Nijemeisland, "CFD as a design tool for fixed-bed reactors", *Ind .Eng. Chem. Res.*, vol. 40, pp. 5246–5254, 2001.

[46] Richard W. Johnson, Handbook of Fluid Dynamics, ISBN 0-8493-2509-9(1998), Chapter 21, P 19.

[47] E. Tsotsas, "Lecture notes", *Product quality in process and chemical industry,* 2014.

[48] www.neutrium.net/fluid_flow/packed-bed-number/.

[49] Prof.Dr.-Ing.E.Specht, Lecture of Combustion Engineering,http://www.ltt.ovgu.de/Lehre

/Combustion+Engineering.html.

[50] Ali Alkhalaf, H. Woche, E. Specht, Experimental investigation of cross flow mixing in an unstructured packed bed, Journal of Chemical Technology and Metallurgy, 51, 6, 2016, 639-648.

[51] A. Alkhalaf and E. Specht, "Prediction of cross flow mixing in the structured packed bed through CFD simulation using (FBM and PMM) and validation with the experiments", Engineering Application of Computational Fluid Mechanics, vol. 11, No. 1, pp 1-14, 2017.

[52] A. Alkhalf, H. A. Refaey, Nabeh Al-durobi, E. Specht, "CFD Simulation and experimental validation of cross flow mixing in body center cubic packed bed and Comparison with PMM", Accepted in the (12 International Conference of Fluid Dynamics 19-20 December 2016, Le Meridin Pyramids Hotel, Cairo, Egypt).

[53] Alkhalaf, Ali; Refaey, H. A.; Al-durobi, Nabeh; Specht, Eckehard, "Influence of contact point treatment on the cross flow mixing in a simple cubic packed bed - CFD simulation and experimental validation", In: Granular matter - Berlin: Springer, Vol. 20.2018, 2, Art. 22, insgesamt 13 S.; http://dx.doi.org/10.1007/s10035-018-0793-2.

[54] A. Nirmolo, H. Woche, E. Specht, "Temperature homogenization of reactive and non-reactive flows after radial jet injections in confined cross-flow", Engineering Applications of Computational fluid mechanics, 12, 1, 2008, 85-95.

[55] Aryoso Nirmolo, "Optimization of radial jets mixing in cross-flow of combustion chambers using computational fluid dynamics", Ph.D. thesis, Otto Von Guericke University Magdeburg, Germany, 2007.

[56] CFD-online, Turbulent Intensity, http://www.cfd-online.com/wiki/Turbulence_intensity.

[57] W. H. Lam, D. J Robinson, G. A Hamill, H. T. Johnston, "An effective method for comparing the turbulence intensity from LDA measurement and CFD predictions within a ship propeller jet", Ocean Engineering, 52 (2012) 105-124.

[58] Gang Li, Makoto Tsubokura, "An implicit turbulence model for low-Mach Roe scheme using truncated Navier–Stokes equations", Journal of Computational Physics, 345 (2017), 462–474. https://www.researchgate.net/profile/Chung_Gang_Li.

[59] H.F.Elattar,Rayko Stanev,Eckehard Specht,A.Fouda," CFD simulation of confined non-premixed jet flames in rotary kilns for gaseous fuels",Computers & Fluids,102(2014)62-73.